Access to Electronic Thesis

Author:	Ryan Montague
Thesis title:	Control of Drive Trains Incorporating Magnetic Gears
Qualification:	PhD

CONTROL OF DRIVE TRAINS INCORPORATING MAGNETIC GEARS

Ryan Gary Montague

Ph.D. Thesis

Department of Electronic and Electrical Engineering

December 2011

A thesis submitted in partial fulfilment of the requirements for the degree of Doctor of Philosophy in Electrical and Electronic Engineering at The University of Sheffield.

Abstract

This is a thesis about the control of magnetic gears. A decade ago (2001) the first modern prototype magnetic gear box was constructed using rare earth magnets (NdFeB). Magnetic gear boxes have some desirable properties not found in their mechanical gear box counterparts, these include: contact-less torque transmission, lubrication-free, reduced noise and vibration, and non-destructive torque overload capability. Hitherto, no detailed investigation or analysis has been conducted on the effects of using a magnetic gear box in place of a mechanical gear box. As will be demonstrated in this thesis, magnetic gears possess a number of undesirable properties which must be given due consideration when designing speed and position controllers. In particular, unlike mechanical gear boxes, magnetic gear boxes have extremely low torsional rigidity. Furthermore, the torque transfer characteristic is fundamentally nonlinear and magnetic gear boxes have the potential to ‘slip’. On the one hand, ‘slipping’ is a great benefit as a non-destructive ‘torque fuse’; but on the other, this represents a consequential loss of control. This thesis examines the control issues that arise through the use of a specially constructed magnetic coupling integrated into an experimental test rig. The development of a linearized mathematical model of the experimental magnetic coupling is used to derive optimized classical controllers for speed and position, demonstrating outstanding theoretical and experimental results. To compensate for the possibility of ‘slip’, a methodology is presented for the detection and recovery from what is defined as ‘pole-slip’ in a magnetic coupling. To avert ‘pole-slip’, a model predictive control (MPC) scheme is developed that prevents over-torque pole-slipping. Feedback linearization is considered for a nonlinear model of the magnetic coupling and nonlinear control laws and state transformations are derived to produce perfect linearization, for both speed and position control, over the entire operating range of the experimental magnetic coupling.

List of Publications

Parts of the work contained in this thesis have been published in international journals and presented at international conferences. These publications are listed below.

R. G. Montague, C. Bingham, and K. Atallah, “Servo control of magnetic gears,” *Mechatronics, IEEE/ASME Transactions on*, vol. 17, pp. 269-278, April 2012.

R. G. Montague, C. Bingham, and K. Atallah, “Dual observer-based position-servo control of a magnetic gear,” *Electrical Power Applications, IET*, vol. 5, pp. 708-714, 2011.

R. G. Montague, C. Bingham, and K. Atallah, “Pole-slip prevention in a magnetic gear using explicit model predictive control,” *Mechatronics, IEEE/ASME Transactions on*, accepted in revision, Nov 2011.

R. G. Montague, C. Bingham, and K. Atallah, "Magnetic gear overload detection and remedial strategies for servo-drive systems," *Power Electronics Electrical Drives Automation and Motion (SPEEDAM), 2010 International Symposium on*, 2010, pp. 523-528.

R. G. Montague, C. Bingham, and K. Atallah, "Magnetic gear dynamics for servo control," *MELECON - 2010 15th IEEE Mediterranean Electrotechnical Conference*, 2010, pp. 1192-1197.

R. G. Montague, C. Bingham, and K. Atallah, "Characterisation and modelling of magnetic couplings and gears for servo control systems," *Power Electronics, Machines and Drives (PEMD 2010), 5th IET International Conference on*, 2010, pp. 1-6.

Acknowledgements

I would like to thank, first and foremost, Professor Chris Bingham who, unwittingly, gave me the opportunity to put to rest a deep regret of more than two decades standing. Over the past three years Professor Bingham has been an excellent supervisor, allowing me the time and space to find my own keel and get on with things, but always being there to provide encouragement, support and direction when needed. Dr Kais Atallah, co-inventor of the modern magnetic gear, provided valuable support and advice for which I am also grateful. This research was made possible with financial support provided by the UK Engineering and Physical Sciences Research Council (EPSRC). The final words of acknowledgement must however be reserved for my wife Nichola and son Ollie whose love, patience and understanding throughout this period of time is, ultimately, the only reason this enterprise has reached its culmination.

Dedicated To

Dr S. M. Lord
1942 - 2009

Table of Contents

5 Linearization and Nonlinear Effects: Further Considerations

6 Advanced Techniques: Model Predictive Control and Pole-Slip Prevention

7 Advanced Techniques: Observer-Based Servo Position Control

8 Nonlinear Approaches

9 Conclusions and Future Work

List of Figures

List of Tables

Nomenclature

θ_M	Motor-side angle	rad
θ_L	Load-side angle	rad
θ_S	Output angle with ferromagnetic pole pieces as rotor	rad
θ_O	Output angle with outer permanent magnets as rotor	rad
$\theta_D = \theta_M - \theta_L$	Relative mechanical displacement angle	rad
$\omega_D = \omega_M - \omega_L$	Relative angular velocity	rad/s
p_{M}	Number of magnetic pole-pairs on high-speed motor rotor	
p_{O}	Number of magnetic pole-pairs on low-speed outer rotor	
n_S	Number of ferromagnetic pole-pieces	
G_R	Gear ratio	
$B(\omega_D)$	Non-linear damping torque	N•m/(rad/s)
$K(\theta_D)$	Non-linear torsion	N•m /rad
ω_{ref}	Speed reference	rad/s
$\omega_M = \dot{\theta}_M$	Motor-side angular velocity	rad/s
$\omega_L = \dot{\theta}_L$	Load-side angular velocity	rad/s
T_{EM}	Motor-side electromagnetic torque	N•m
T_L	Load-side (disturbance) torque	N•m
T_C	Gear coupling torque	N•m
T_G	Maximum gear torque	N•m
J_M	Motor-side inertia	kg.m^2
J_L	Load-side inertia	kg.m^2
J_{EQ}	Equivalent inertia	kg.m^2
p	Number of pole pairs 1:1 coupling	
α	Percentage of maximum gear torque in damping function	%
β	Relative angular velocity for max damping torque	rad/s

K_{lin}	Linearized spring constant	N•m /rad
$K_{lin}^{\max}$	Maximum value of linearized spring constant	N•m /rad
$K_{lin}^{\min}$	Minimum value of linearized spring constant	N•m /rad
K_{lin}^{opt}	Optimum value of linearized spring constant	N•m /rad

Chapter 1

Introduction and Literature Review

1.1 Background

Mechanical gears have been around for a very long time, with the earliest known reference taking place almost 2000 years ago [1]. A mechanical gear is essentially a rotating part having teeth that mesh with another mechanical part, of possibly dissimilar size, also having teeth. Indeed so ubiquitous are mechanical gears that almost everyone would recognise figure 1.1, two toothed cogs, as part of a mechanical gear.

Figure 1.1 Mechanical spur gear

The simple mechanical spur gear of figure 1.1 can be used to convert rotational speed up or down. Over the past 100 years mechanical gears and gear boxes have progressed to some considerable sophistication with applications in the very small, such as the watch mechanism shown in figure 1.2 (a), to the somewhat larger and most omnipresent use as in the car gear box of figure 1.2 (b).

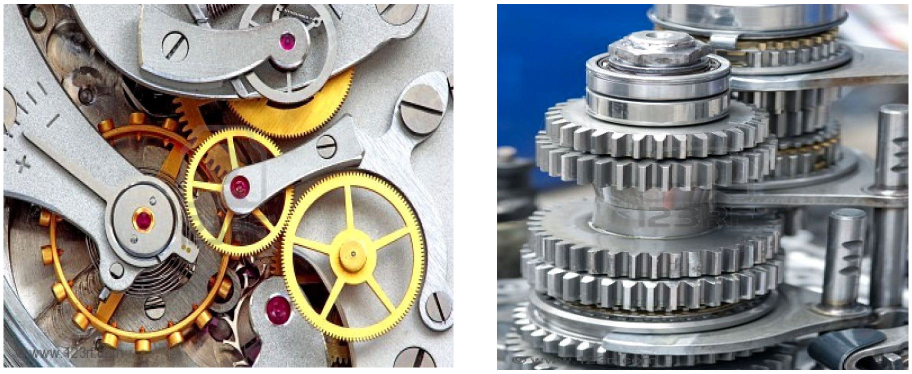

(a) (b)

Figure 1.2 Mechanical gearing (a) watch gears (b) car gears

Mechanical gears and gear boxes have been used extensively throughout the 20th century to translate rotational energy from a primary source (motor) to a load. Efficiencies and practicalities dictate the need for speed conversion via gear boxes. In the most simplified model, for example, the power output of an electrical machine is given by,

$$P = \tau\omega \tag{1.1}$$

where P is power in Watts (W), τ is torque in Newton-metres (N•m) and ω is angular velocity in rad/s. Another simplifying assumption is that the torque produced is also proportional to motor current, that is, $\tau = k\mathrm{I}$ (where k is a motor-specific constant, and I is the current), a determinant of a machine's weight and volume. For a given power P, possibilities are low speed with a high current, or high speed with a low current. From a practical point of view therefore, it may be more appropriate to use a high speed motor (smaller size) and reduce the output speed via a mechanical gear box. A common example would be an electric screwdriver where a direct drive (input and output speed equal) would be unrealizable. In this instance, the output speed must be geared substantially down from a high speed motor to a much lower speed output shaft to be of practicable use. Mechanical gear boxes are to be found in a huge number of applications, both domestic and industrial, that require speed changes both up and down. They come in a vast range of sizes and types, such as: spur, helical, bevel, hypoid, worm, planetary, and harmonic; some mechanically simple, others with complex construction and operation. All the aforementioned mechanical gear boxes have a common unifying factor: torque transmission takes place via physical contact at the surfaces of the materials from which they are constructed. In the simplest case of the steel spur gear (figure 1.1), torque is transferred from the meshing of the teeth cut into the steel. However, a number of inherent disadvantages accrue from such a physical contact-based scheme, particularly for rotating machinery of large scale and power. They are likely to need periodic servicing, require lubrication, support from bearings, and have contact issues such as friction, backlash, heat dissipation, noise and vibration which must all be taken into account [2].

The principal function, in general, of mechanical gear boxes is to transmit torque from a primary source (electric machine, motor, engine etc.) to a rotational load. But over the past decade considerable interest has been growing in the possible replacement of mechanical gear boxes, in certain applications, with *magnetic* gear boxes. Magnetic gear boxes are a form of contact-less torque transmission. The ability of magnets to transmit force/torque has of course been known for quite some time [3], but the introduction of high-energy permanent magnets (PMs) in the last two decades has allowed industrial-scale non-contact torque transmission to take place via interacting permanent magnets [4]. In comparison with mechanical gear boxes, Non Contacting Magnetic Gear boxes (NCMGs) have a number of favourable attributes, foremost of which is that torque transmission is contact-less via a magnetic field. This removes, or alleviates, many issues associated with contacting mechanical gears, viz: maintenance, friction, lubrication, vibration, noise, heat and myriad other issues. In addition, unlike their mechanical counterparts, magnetic gear boxes possess inherent non-destructive torque overload capabilities, because when overloaded magnetic gears *slip*. In effect, a NCMG behaves as a perfect *torque fuse*.

Over the past decade huge advances have been made in the analysis, design and construction of NCMGs to such an extent that they are now in commercial production and operation [5]. To date however, no consideration has been given to the effects, on an otherwise mechanically stiff drive train, when that drive train incorporates a magnetic gear box. Consequently, the central aim of this thesis is to investigate the effects of torque transmission via magnetic means on the *control* of a drive train that incorporates a magnetic gear box. Essentially, therefore, this work does not consider magnetic gear boxes from the perspective of *magnetics*, but does investigate the salient issues that arise for servo control of drive trains that utilize NCMGs. In the context of this work, it is the *mechanical* properties of NCMGs that sets the framework for investigating the control challenges faced for servo control of magnetically-geared drive trains.

1.2 Literature review

The aim of this thesis is to investigate the control issues that arise when using magnetic gears or magnetic couplings in an otherwise mechanically stiff drive train. This essentially leads to three principal subject areas for which literature searches were conducted, and existing research evaluated. For the subject areas identified, “Control of magnetic gears”; “Magnetic gears”; and for reasons to be expounded upon in Chapter 2, “Two-inertia servo drive systems”; a literature review and brief synopsis of the current state of knowledge is now presented.

The first topic, “control of magnetic gears”, in 2008, had no known or detectable published research output, this forming the entire ***raison d'être*** for conducting the work contained herein. Consequently, the work of this thesis and its concomitant journal and conference publications [6], [7], [8] & [9], represent the first original and new contribution to the nascent topic of interest, namely, the control of magnetically-geared drive trains. Magnetic gears themselves have a relatively small, but growing, number of published journal and conference papers, while the third of the identified topics, two-inertia servo drive systems, has a considerable number of research outputs over many years. A summary of the research literature for these two topics now follows.

1.2.1 Magnetic gears

Using magnets for gearing purposes is not a new idea, having been suggested as early as 1913 [10]. A quantitative analysis of the number of conference and journal research papers published over the past twenty years, from 1990 to 2010, indicates that there has been relatively little research activity in the field of magnetic gears. In figure 1.3, it can be seen that for the most part of the preceding twenty years, research output has been single-digit for conference and journal papers, with some years producing no published work at all. However, in the past three years (2007-2010), there has been a substantial (exponential) rise in the volume of published work on magnetic gears.

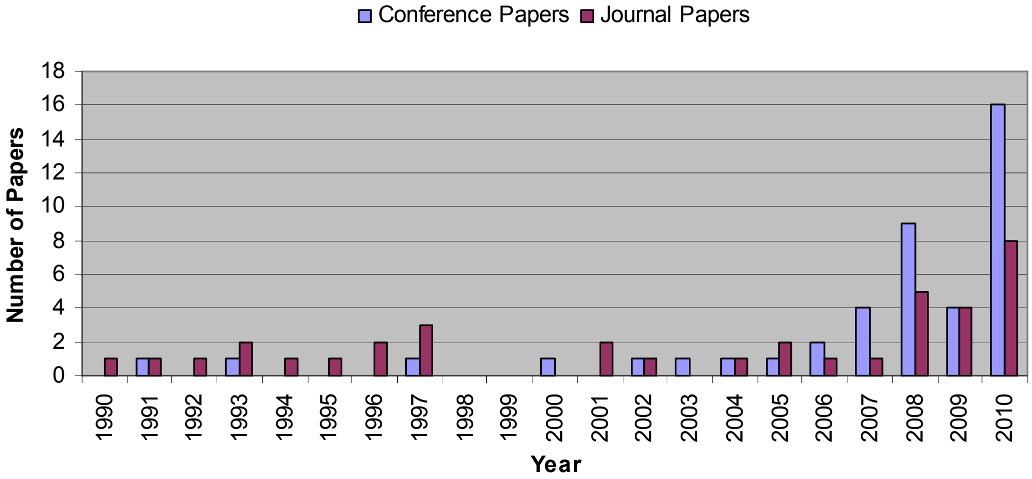

Figure 1.3. Magnetic gear published conference and journal papers 1990 to 2010

Although the concept of torque transmission using *ferrite* magnetic gears was patented as early as 1940 [10], it is only the relatively recent introduction of high energy permanent magnets (PMs) in the 1980’s that has re-ignited interest in the use of magnets for gearing purposes. On the other hand, it is quite clear that high energy rare-earth permanent magnets have had a significant impact on the construction of modern motors, giving rise to permanent magnet a.c. machines (PMSMs) [11]. Back in the 1940’s only ferrite magnets were available with very poor torque transmission capability, and a force per unit volume only one tenth of that available today from modern Neodymium-Iron-Boron (Nd-Fe-B) permanent magnets [12].

Unsurprisingly, the first attempt at constructing a magnetic gear was based on a topological copy of a traditional mechanical spur gear as shown in figure 1.4. This topology, however, is hampered by considerable inefficiency, as very few of the (expensive) permanent magnets take part in torque transmission at any specific time instant. Consequently, peak torque transmission capabilities and torque densities are very low.

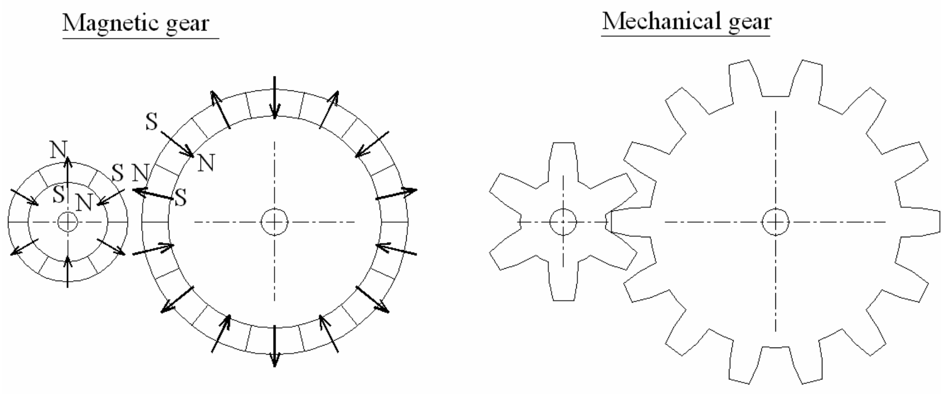

Figure 1.4 Permanent-magnet and mechanical spur gears (ref [1])

The spur gear topology therefore has limited, if any, practical application. Nevertheless, the principle of torque transmission between the non-contacting ‘cogs’ can be readily appreciated. To facilitate a successful paradigm shift from mechanical to magnetic gears, the peak torque transmission capability and torque per unit volume density of the constructed magnetic gear box must be comparable, or superior to, that of their mechanical counterparts. Take for instance magnetic couplings, which allow the separation of primary source and driven shaft, where non-contact is desirable (e.g. clean rooms, certain types of isolated liquid agitation). Torque densities can be in the range 300-400 kN•m/m^3, compared with only around 20 kN•m/m^3 for normal electrical machines.

At the turn of the millennium, Atallah & Howe [13] presented a novel high-performance magnetic gear employing rare earth magnets that promised high torque densities and high torque transmission capability. The topology of the proposed magnetic gear consists of a concentric inner high-speed rotor driven by the primary source (motor), an arrangement of ferromagnetic pole-pieces, and a further arrangement of permanent magnets to form the low speed outer rotor.

A schematic of this topology is shown in figure 1.5. Key parameters for the magnetic gear are presented in [13] viz. number of high speed rotor pole-pairs, $p_M = 4$, number of low speed rotor pole-pairs, $p_O = 22$, number of stationary steel pole-pieces $n_s = 26$. From [13], the rotational velocity of the low-speed rotor is determined from,

$$\Omega_l = \frac{p_M}{p_M - n_s}\Omega_h = \frac{4}{4 - 26}\Omega_h = -\frac{1}{5.5}\Omega_h \tag{1.2}$$

where Ω_h and Ω_l are the high speed and low speed rotational velocities and the negative sign indicates that the inner and outer rotors are contra-rotating. In this instance the magnetic gear provides a reduction ratio G_R = -5.5:1. The magnetic gear box theoretically investigated in [13] had a calculated torque per volume of more than 100 kN•m/m^3.

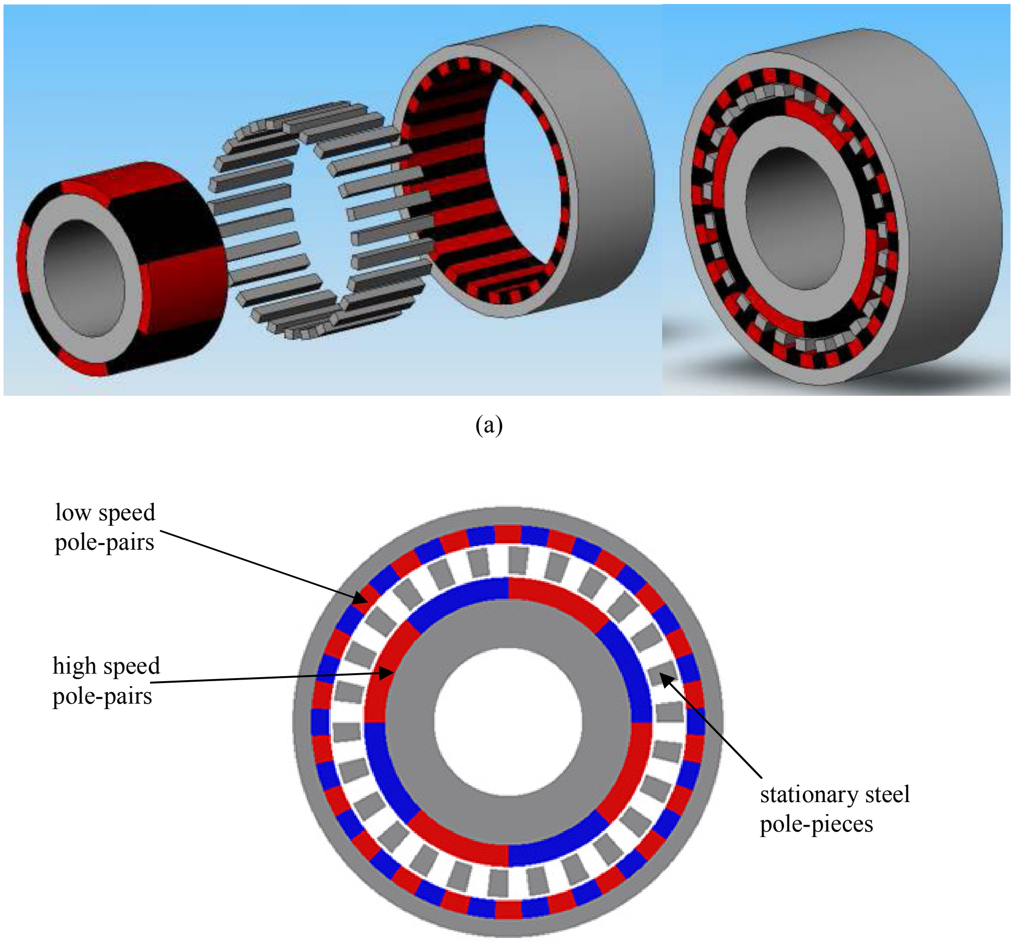
(a)

(b)

Figure 1.5 A coaxial or concentric magnetic gear (a) 3D rendered view (b) schematic

In 2003 Rasmussen *et al.* [14], reported on the development of a high-performance magnetic gear - the first modern practical magnetic gear using high energy magnets. The realised magnetic gear box had the same parameters as the one theoretically described in [13]. However, with a slightly modified structure, it was considered more suitable for a prototype build. Figure 1.6 shows a photograph of the prototype, which is claimed to be the first modern construction of a magnetic gear presented in a research paper in the public domain [14].

Atallah *et al.* [15], subsequently manufactured a high-performance magnetic gear, figure 1.7, with a gear reduction ratio of -5.75:1, pull-out torque 60 N•m and a torque density of 72 kN•m/m^3, and providing similar results to those obtained in [14]. Whilst in both cases the measured torque density results were somewhat lower than those theoretically calculated using Maxwell's stress tensor, high torque per volume density magnetic gears were, nonetheless, shown to be practically realizable and, with optimizations and refinements, could be a competitor technology for classical mechanical counterparts

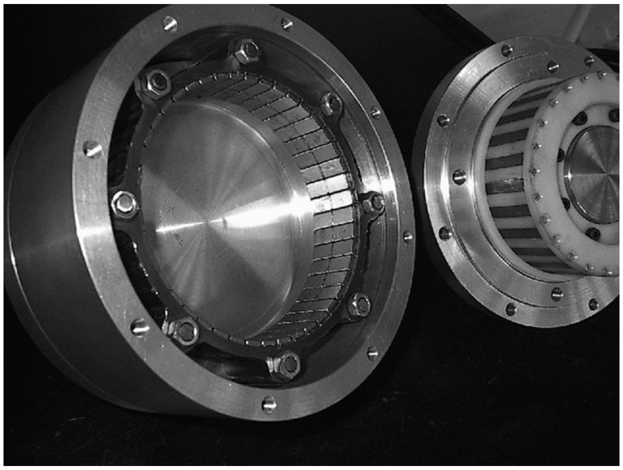

Figure 1.6 Prototype magnetic gear of Rasmussen *et al.* (ref. [14])

.

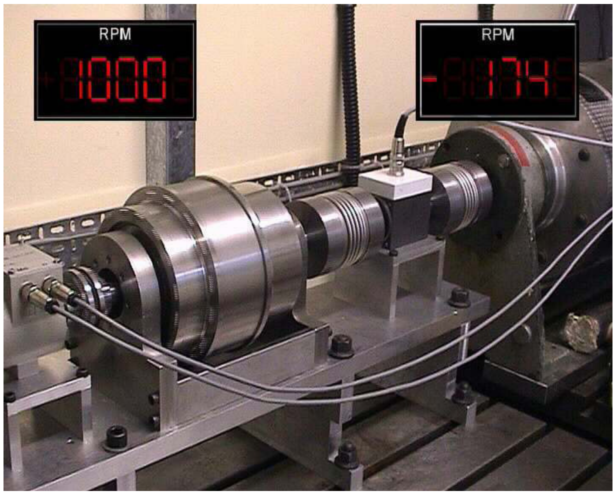

Figure 1.7 Atallah's prototype magnetic gear (ref. [15])

The works of Atallah *et al*. [15], and Rasmussen *et al*. [14], provide a proof-of-concept foundation for the introduction of practicable permanent magnet gears as replacements for classical mechanical gear boxes, for appropriate applications. This is evidenced in figure 1.4 where it can be seen that there has been a rapid rise in the number of published journal and conference papers devoted to research on magnetic gears since 2006. With the fundamental principle of torque transmission via magnetic means established, recent research output has focused on the structure and design of enhanced magnetic gear boxes, and the potential applications that will benefit from this new torque transmission technology.

Rasmussen *et al.* [16], and Atallah *et al.* [17], both proposed evolutions to the established concentric magnetic gear structure shown in figure 1.5. While in [16] this is referred to as the *cycloid* magnetic gear, in [17] it is called the *harmonic* magnetic gear. In both cases the objective is to overcome the relatively poor utilization of magnets when there is a large numerical difference in the number of pole-pairs between the inner and outer rotors. If the number of pole-pairs is almost equal, better utilization results but the gear ratio approaches unity, thereby creating a magnetic coupling. Whilst good magnetic interaction occurs, the gear-reduction capability is reduced. To provide better magnet utilization and high gearing ratios, the movement of inner and outer rotors follows a cycloid principle as indicated in figure 1.8.

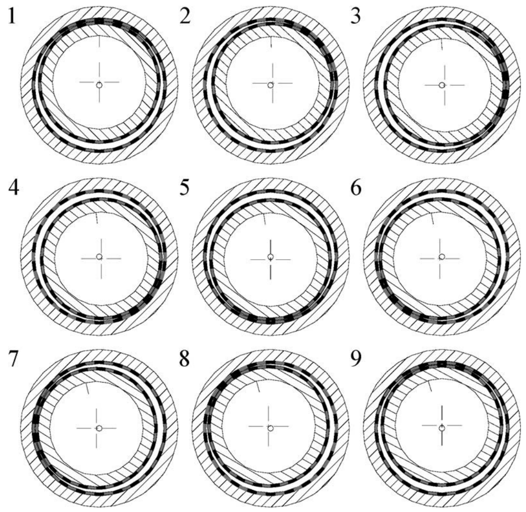

Figure 1.8 Cycloidal movement in a magnetic gear (ref [16])

For the example illustrated, the inner rotor contains 42 poles and the outer rotor 44 poles, yet provides a gear ratio of -1:21, far higher than the simple coaxial magnetic gear structure. Figure 1.9 illustrates a rendered view of the complex construction of the cycloid magnetic gear [16].

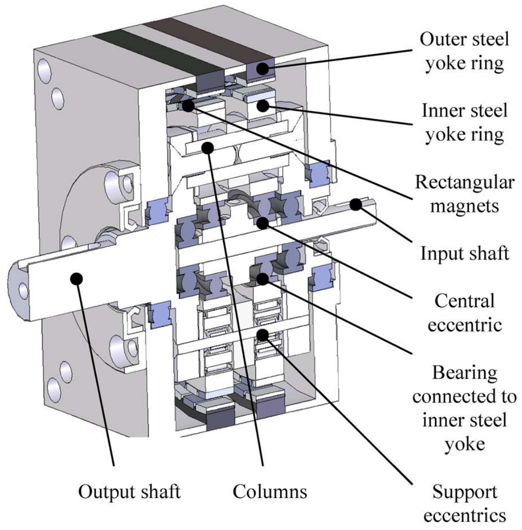

Figure 1.9 Physical construction of cycloid magnetic gear (ref [16])

The benefit of this complex design is an increase in torque per volume density, potentially up to 183 kN•m/m^3, purportedly 40% greater than a conventional coaxial design [16].

Another further new design for a magnetic gear box is reported in 2008 by Huang *et al.* [18], based on the principle of a mechanical planetary gear box, a schematic of which is shown in figure 1.10.

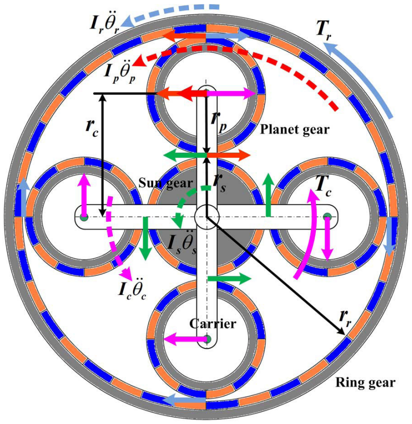

Figure 1.10 Magnetic planetary gear box (ref [18])

Like the mechanical planetary gear, its magnetic counterpart has three transmission modes, a high speed reduction ratio, high durability, and for the proof-of-concept magnetic planetary gear constructed in [18], a torque per volume density approaching 100 kN•m/m^3. In addition to the aforementioned magnetic gear designs, more esoteric developments include magnetic gears utilizing high temperature superconductors (HTS) and magnetic gears based on Halbach arrays, detailed descriptions of which are contained in [19] , [20].

Various researchers have also integrated magnetic gears with permanent magnet machines. For example Atallah *et al.* [19] integrated, both mechanically and magnetically, a permanent magnet brushless machine with a magnetic gear to create the *pseudo-direct drive (PDD)*. Similarly, Ho *et al.* [20], presents a novel magnetic gear integrated with a brushless permanent magnet machine, a rendered view of which is shown in figure 1.11.

Industrial applications for such magnetic gearing technologies range from electric motor vehicles, where in [21], [22] Chau *et al*. have designed a magnetically-geared in-wheel PM motor for use in electric vehicles, to uses in power generation by wind [23], [24] and tidal waves [25]. With magnetic gearing technologies still in their infancy, design sophistication is likely to improve significantly over the coming decade, and new application sectors will evolve to take full advantage of the potential benefits afforded by magnetic torque transmission techniques.

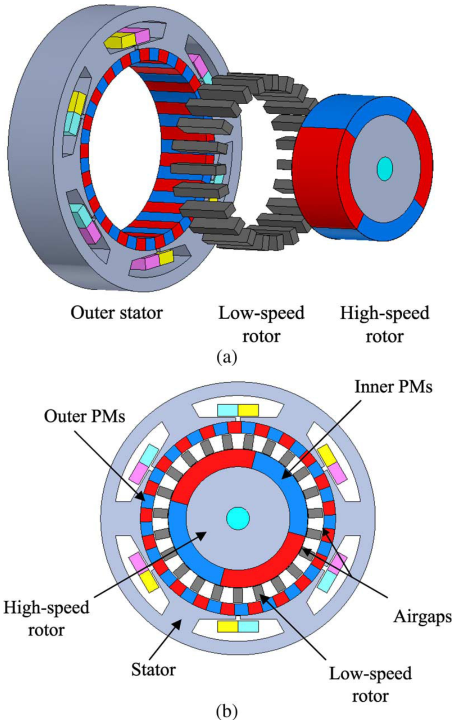

Figure 1.11 Integrated magnetic gear and PM brushless machine (ref. [20])

1.2.2 Two-inertia servo drive systems

In Chapter 2 it will be shown that, from a dynamics theory perspective, a magnetic gear or magnetic coupling can be considered as two inertias (either side of the magnetic gear) interconnected by a nonlinear torsional spring. Consequently, it becomes instructive to investigate the broad, and very large, body of research that exists on the control of two-inertia (two-mass) systems with flexible couplings. As will also be shown in Chapter 2, one of the ways in which magnetic gears manifest themselves is as extremely flexible couplings. Unlike "magnetic gears", and the "control of magnetic gears", the body of work relating to "two-inertia systems" is extremely large due to the prevalence of drive trains whose dynamics can be approximated by the coupling of two rotating inertias. A simplified model of this torque transmission system is shown in figure 1.12.

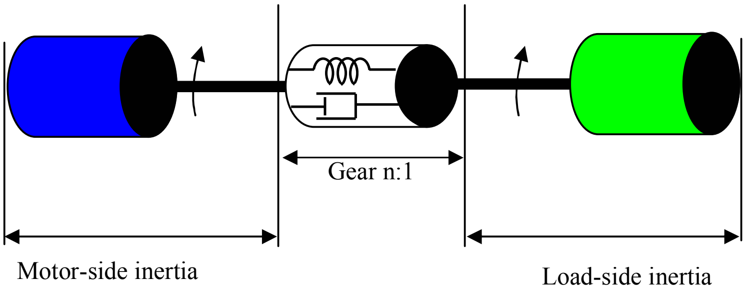

Figure 1.12 Torque transmission through a gear

As indicated in figure 1.12, the gear, mechanical or magnetic, is considered to have both compliance, in other words, it is not torsionally rigid; and, possibly, viscous damping (the interconnecting shafts are considered to be perfect, inertia-less and infinitely stiff). Although more sophisticated modelling of gear boxes could include enhanced models of friction and backlash and other nonlinearities, for present purposes the simplified model is sufficient. The scenario shown in figure 1.12, where the two inertias are connected via a gear that is not torsionally rigid, can also be presented as in figure 1.13.

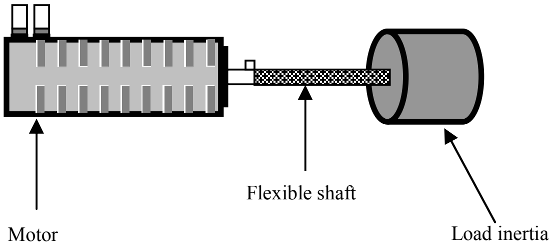

Figure 1.13 Torque transmission through a flexible shaft

From a mechanical modelling perspective the two scenarios presented in figures 1.12 and 1.13 can both be viewed, in the most simplified form, as two inertias connected by a *torsion spring*, where the spring twists when subjected to a torque input. The most commonly adopted model of the presented scenarios is shown in figure 1.14, and is widely adopted to model many electrically driven mechanical systems, such as: machine tools, metallurgical rolling mill, robot arms, antennas, hoists, elevators (lifts), printing machines, pointing and tracking systems [26], [27], [28], [29]. A common characteristic shared by these diverse applications is that they can all be modelled, as a first approximation, by the two-inertia/two-mass servomechanism, where torque/force is transmitted through a mechanically compliant component [30], [31]. For the examples cited above, the source of mechanical compliance is generally considered to be in the form of elastic shafts and joints [32].

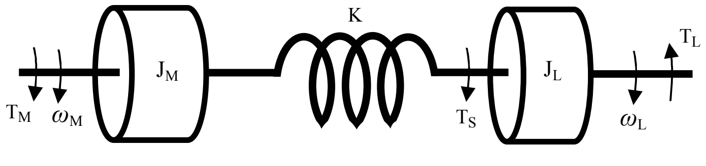

Figure 1.14 Model of servo drive system with flexible shaft

A number of consequences accrue from the elasticity of interconnecting shafts; first and foremost is the potential for torsional oscillations to be induced into the mechanical system as a result of both step demand changes and step load inputs to the system, e.g. figure 1.15. For instance, a typical rolling mill consists of large inertias connected via long shafts. Since a relatively small amount of input energy is required to excite mechanical resonances, control measures must be taken to minimize the possibility of torsional oscillations, thereby preventing poor quality outputs and potentially catastrophic failure of the overall mechanical system [33]. Furthermore, the frequency of the mechanical resonance is often within the bandwidth of the controller, such that the servo drive can readily excite the dominant resonant frequency if vibration suppression strategies are not adopted in the controller.

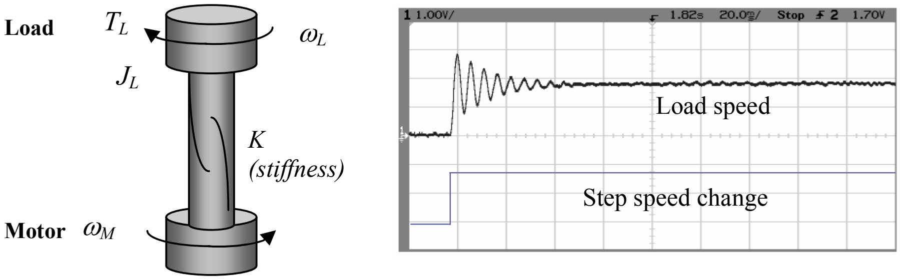

Figure 1.15 Torsional oscillations in two inertia system

Since two inertias are connected by a flexible shaft, the position and velocity of the primary (motor-side) inertia can be transiently different to the position and velocity of the secondary (load-side) inertia, due entirely to the compliance of the interconnecting component. This is referred to as the “stiffness problem” [34]. A further consequence of the finite elasticity is that, dynamically, the system order is doubled, generally requiring the measurement of additional state variables if precise control is desired. However, it is generally accepted that it is not economically feasible, or practical, to measure load-side variables. In addition, measurements of shaft torsional torque and external load torque are also problematic. As a consequence, a large body of the research literature devoted to the control of two-inertia systems makes the presumption that only motor-side variables are available for direct measurement. While a number of conventional techniques have been applied in speed control applications, e.g. PID, Speed Derivative Compensation (SDC), Simulator Following Compensation (SFC), more advanced techniques generally rely on some form or other of state and/or disturbance estimation; such methods include Resonance Ratio Control (RRC), State Feedback and Load Acceleration Control (SFLAC) [29]. A common feature of many of these techniques is that no systematic method exists for setting controller parameters, and trial and error tuning is adopted to determine the closed-loop dynamics [35]. To address the latter issue, Zhang and Furusho [36], developed a systematic design method based on PI speed control with three types of pole assignment; (i) identical radius, (ii) identical damping coefficient, and (iii) identical real part, each considered for different inertia ratios. It was shown that the load to motor inertia ratio dominates the damping characteristics, and that consideration to different pole-pattern assignments should be made on the basis of differing inertia ratios [36].

The majority of techniques proposed for high-performance speed servo drive systems can be subdivided into one of three categories; (i) techniques based on full motor- and load-side measurements, (ii) vibration suppression strategies based on conventional speed control structures with notch filtering and phase-lead compensation, and (iii) motor-side measurements from a single feedback sensor with an observer to determine unmeasured states [37]. The measurement of both motor-side and load-side speed/position is generally considered to be impracticable in an industrial environment, due to the added cost and reduction in overall system reliability. Techniques in the second category are based on the use of passive notch filters for suppression of torsional oscillations. Such passive approaches are predicated on the basis that, for high-performance high speed servo systems, state estimation becomes problematic inasmuch that it may not be sufficiently fast or have acceptable noise immunity, thereby substantially degrading overall closed-loop performance. However, with modern digital signal processing techniques and high-speed microcontrollers, techniques based on state estimation have become feasible [38], [39], [40], albeit not ‘tunable’ by on-site operatives.

More recently, significant advances have been made by O’Sullivan and Bingham [41] in high-performance control of dual-inertia servo drives with the use of low cost integrated surface acoustic wave (SAW) torque transducers. While a number of authors have proposed techniques based on feedback of torsional torque, its reliable, accurate and cost-effective measurement has imposed a significant impediment to implementation. However, SAW torque sensors have been proposed as they do not reduce system stiffness, have high sensitivity, high bandwidth, high noise immunity and low cost. Techniques based on resonance ratio control (RRC) and its derivatives (e.g. RRC+) are shown to be the preferred approach, especially if high-performance, low-cost SAW torque transducers can be employed [41].

As previously stated, a large body of work has been devoted to the control of two-inertia servo systems (predominantly speed control it should be noted). In addition to the techniques already discussed, there also exist methods based on neural networks [42], [43], [44], fuzzy logic [45], [46], sliding mode [47], [48], Kalman filters [49], [50], forced dynamic control [51], [52] and other variations on the above themes. A common thread in much of this published research is the requirement for some form of state estimator for load-side variables that are not measured for the reasons highlighted previously. For output regulation, a disturbance observer (DOB) is constructed to estimate unknown load torque perturbations.

The methods proposed in this thesis for control of drive trains incorporating magnetic gears are based on the assumption that a magnetic gear can be viewed as two inertias interconnected by a magnetic torsional spring. Furthermore, it is assumed that only a single feedback sensor at the motor-side of the magnetic gear is available for control purposes, so-called *collocated control*.

1.3 Summary of previous work

In 2008 an extensive literature search indicated that there had been, up to that date, no detectable published research that examines the control of drive trains that incorporate magnetic gear boxes. Furthermore, despite having been in widespread use for some 30 years, no published research on the control of magnetic couplings exists either. Consequently, the fundamental objective of this thesis can be considered to be a nascent topic of research; a topic that must inevitably grow in importance if magnetic gear boxes are to have any realistic chance of being adopted in high bandwidth servo control system applications.

While around 50 or so significant journal publications currently exist on *magnetic gears*, none consider the inherent control issues that ensue from their use in a purely mechanical drive train. Currently, no published works investigate the specific control issues that arise from the use of magnetic couplings or magnetic gears in otherwise mechanically stiff drive trains. The work contained in this thesis aims to remedy this situation by considering only *control* issues, from an entirely servo control system's perspective. It is the author's view that the first ever journal and conference publications to investigate control issues related to non-contact magnetic gears (NCMGs) are to be found in Montague, Bingham & Atallah [6, 7, 8, 9]. The aforementioned publications form the basis for detailed study of control system design for drive trains that incorporate magnetic couplings and magnetic gear boxes, in an otherwise mechanically stiff drive train.

1.4 Objective of this thesis

The principal objective of this research is to determine the issues that arise, and potential solutions, to *control* a drive train that incorporates a non-contact magnetic gear box (NCMG). In this context, the NCMG is considered to have replaced a mechanical counterpart that has, in comparison with a NCMG, effectively infinite torsional stiffness, linear torque transfer over its operating range, and is not subject to torque overload induced slip.

The unresolved control issues therefore centre on speed, position and load regulation when incorporating a magnetic gear within an otherwise mechanically stiff drive train, and the loss of control when the maximum applied torque is beyond that which can be developed by the magnetic gear. An overall framework for the issues that need to be addressed is formalized in figure 1.16 [8].

1.5 Outline of thesis

The remainder of this thesis is structured as follows: Chapter 2 presents detailed design of the experimental magnetic coupling used throughout this research. The construction of an experimental test rig allows relevant measurements to be made and controller designs to be evaluated. Chapter 3 examines speed control issues from a conventional control perspective using traditional controller structures (PI), while Chapter 4 investigates position control issues from the same conventional controller (PD) perspective. Chapter 5 considers more fully the linearization methodology adopted for conventional speed and position control of Chapters 3 and 4, and investigates the effects of nonlinearity on the overall performance when utilizing linear controllers. Chapter 6 considers more advanced control techniques for a speed controlled servomechanism utilizing model predictive speed control, while in Chapter 7 advanced position control is presented using a dual observer-based approach. In the former, MPC is used to ameliorate the possibility of 'pole-slipping' (see Chapter 3) in a speed controlled system, and in the latter to rectify torsion-induced position errors using load-side state estimation. Chapter 8 considers nonlinear approaches, in particular feedback linearization, to the control of a magnetically-geared drive train. Chapter 9 details the contributions of this thesis and suggests areas that may benefit from further research.

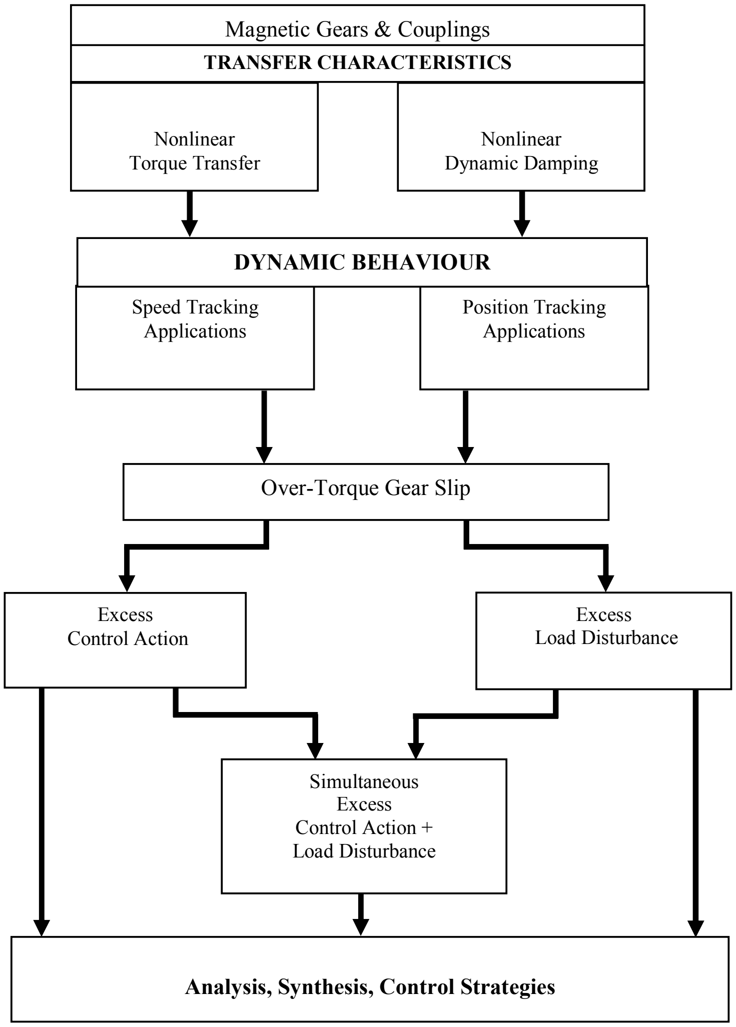

Figure 1.16 Magnetic gear research framework

1.6 Summary of contributions

This thesis will demonstrate that a magnetic gear box can be considered to have an internal nonlinear torsion spring that is characterized by extremely low torsional rigidity. Consequently, the high compliance and nonlinearity of the torque transfer characteristics must be given due consideration when designing speed and position controllers for drive trains that incorporate magnetic gears. Contributions resulting from this research are:

(i) Methodology for designing ITAE optimized speed and position controllers (Chapters 3 &4).

(ii) Demonstration of magnetic gear over-load conditions leading to 'pole-slip' and remediation with pole-slip detection and a reconfigurable controller (Chapter 3).

(iii) Performance assessment of the effects of nonlinear torque transfer characteristics when utilizing linear speed and position controller designs (Chapter 5).

(iv) Proposed advanced speed control based on explicit model predictive control methodology to obviate pole-slip due to under-torque pole-slipping phenomenon (Chapter 6).

(v) Proposed advanced position observer-based servo position control to provide load-side set-point tracking with torsion compensation from motor-side only feedback (Chapter 7).

(vi) Derivation of nonlinear control laws and nonlinear state transformations to produce perfect linear behaviour with implementation of feedback linearization plus state feedback control methodology (Chapter 8).

Chapter 2

Magnetic Coupling and Experimental Test Rig

2.1 Introduction

The principal objective in this chapter is to propose that the analysis of a magnetic gear can be reduced to an equivalent model consisting of idealized (perfect) gear boxes interconnected by a magnetic coupling (or 1:1 magnetic gear). It is on this basis that the subsequent study presented can focus on a purposely designed magnetic coupling. An experimental test rig is constructed to determine the torque transfer characteristic of the magnetic coupling, and, in succeeding chapters, to investigate the detailed control issues that arise with the use of a demonstrator drive train that incorporates the manufactured magnetic coupling.

2.2 Electromechanical modelling of magnetic gear

In Chapter 1 a number of magnetic gear topologies were reviewed from the available research literature. By far the most commonly used magnetic gear topology is shown in figure 2.1.

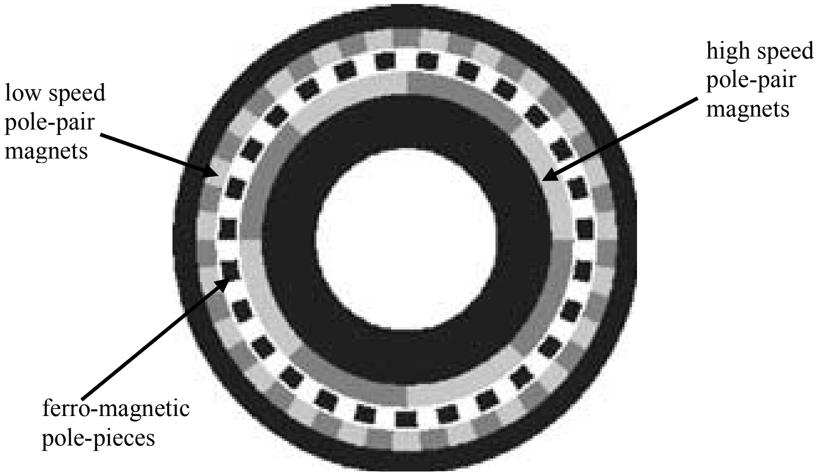

Figure 2.1 Concentric magnetic gear topology

For the topology of figure 2.1 the drive motor is connected to the inner rotor and the low speed rotor can be taken from either the ferro-magnetic pole-pieces or the outer pole-pairs with the other rotor ‘earthed’.

Figures 2.2(a) and 2.2(b) show examples of a magnetic gear consisting of a concentric inner high speed rotor with permanent magnet pole-pairs (p_M = 4), a low speed outer rotor with ferromagnetic pole-pieces (n_s = 27), and a low speed outer rotor with permanent magnet pole-pairs ($p_O = 23$). With this configuration there are two modes of operation (i) figure 2.2(a) with the outer permanent magnet rotor held stationary, or ‘earthed’, the pole-pieces become the low speed rotor, and (ii) figure 2.2(b) with the pole-pieces ‘earthed’, the outer permanent magnets form the low speed rotor. For the case shown in figure 2.2(a), the dynamics are described by the following system of equations,

$$J_M \frac{d^2\theta_M}{d\,t^2} = T_{EM} - T_G \frac{p_M}{n_s} \sin\left(p_M\,\theta_M - n_S\,\theta_S\right)$$

$$J_S \frac{d^2\theta_S}{d\,t^2} = T_L - T_G\ \sin\left(n_S\,\theta_S - p_M\,\theta_M\right) \tag{2.1}$$

where J_s represents the equivalent inertia of the load and rotating ferromagnetic pole-pieces, and the gear ratio for the example in figure 2.2(a) is,

$$G_R = \frac{n_S}{p_M} = \frac{27}{4} = 6.75:1 \tag{2.2}$$

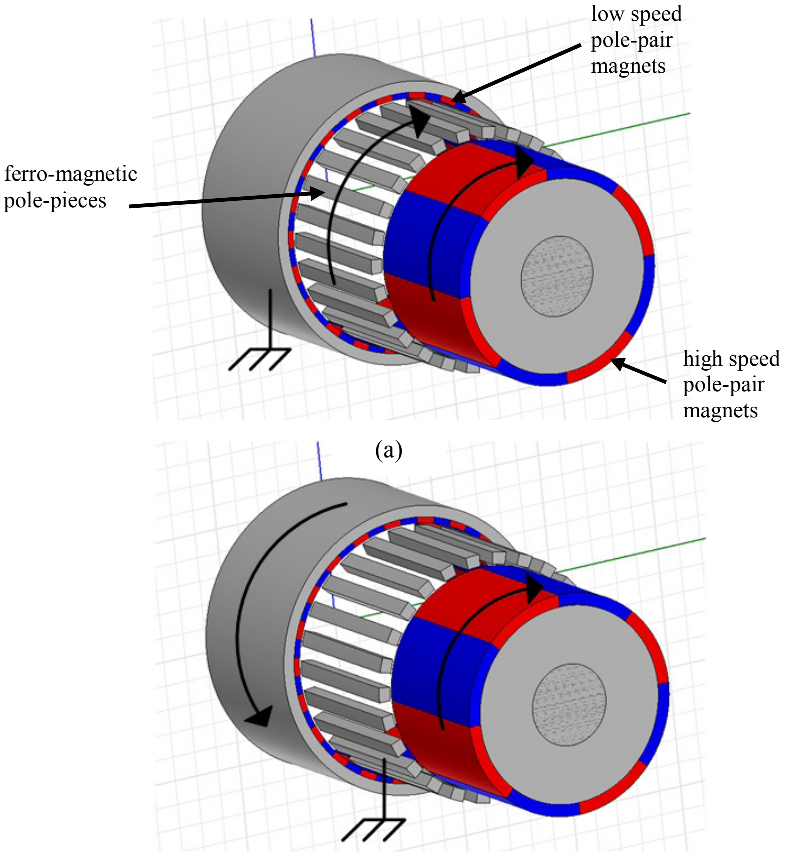

(a)

(b)

Figure 2.2 Magnetic gear topologies (a) outer rotor earthed (b) ferromagnetic pole-pieces earthed

An alternative arrangement is to have the ferromagnetic pole-pieces earthed as shown in figure 2.2 (b). For figure 2.2 (b), the dynamics are described by,

$$J_M \frac{d^2\theta_M}{dt^2} = T_{EM} - T_G \frac{p_M}{n_S} \sin(p_M\,\theta_M + p_O\,\theta_O)$$

$$J_O \frac{d^2\theta_O}{dt^2} = T_L - T_G \frac{p_O}{n_s} \sin(p_O\,\theta_O + p_M\,\theta_M) \tag{2.3}$$

where J_O represents the equivalent inertia of the load and outer rotor permanent magnet pole-pairs. The gear ratio is then,

$$G_R = \frac{p_M - n_S}{p_M} = \frac{4-27}{4} = -5.75:1 \tag{2.4}$$

Note: the negative sign indicates that the high speed and low speed rotors turn in opposite directions. This particular example of a magnetic gear is investigated in [15] and has a calculated torque per volume of 72 N•m/m^3. Moreover, this level of torque density is a typical continuous rating for magnetic gears with torque transmission capabilities of less than a few hundred N•m, and is comparable with mechanical counterparts, though these may exhibit significantly higher peak to continuous ratios [6].

For a magnetic gear operating as in figure 2.2(a), the system of equations defined in (2.1) is represented by the equivalent electromechanical model shown in figure 2.3, consisting of an ideal step-down gear box with gear ratio p_M:1 with transmission via a 1:1 magnetic gear (or magnetic coupling) to an ideal step-up gear box with ratio 1:n_s , the overall gear ratio being equivalent to (2.2). (By the same reasoning, a similar equivalent model can also be obtained for a magnetic gear operating as in figure 2.2 (b)).

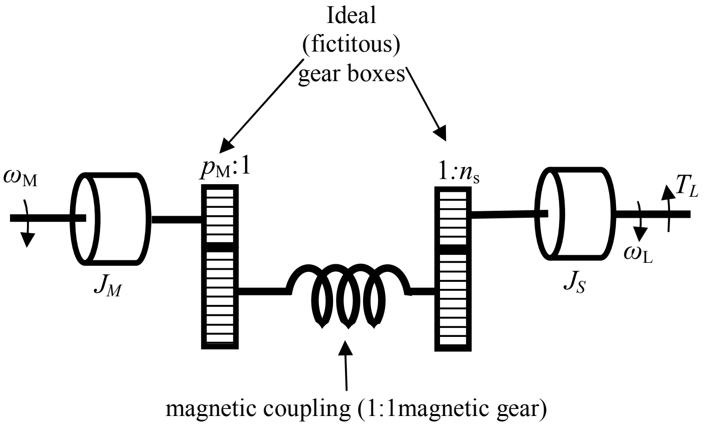

Figure 2.3 Equivalent model of magnetic gear

From figure 2.3, it can be seen that the magnetic torque transmission characteristics reduce to that of a 1:1 magnetic coupling (magnetic spring). Consequently, pertinent issues surrounding the use of magnetic gear systems, and their modelling and analysis, such as: high compliance, nonlinear torque transfer, nonlinear damping and over-torque pole-slipping, can be reduced to that of a 1:1 magnetic coupling, and this forms the basis for the remaining analysis.

2.3 Magnetic coupling and experimental test rig

To provide a focus to the research, an experimental magnetic coupling with a maximum transmitted torque of ~6 N•m has been designed and constructed. The experimental magnetic coupling has 3 pole-pairs on both the inner and outer rotors, giving a ‘gear ratio’ of 1:1. A simplified schematic of the magnetic coupling construction is shown in figure 2.4. (More detailed information relating to the construction of the magnetic coupling is contained in the Appendix.)

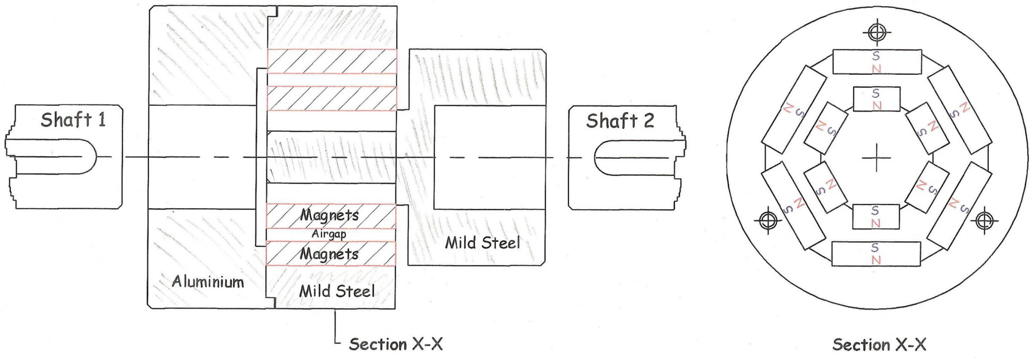

Figure 2.4 Schematic of experimental 3 pole-pair magnetic coupling (see also Appendix)

The prototype magnetic coupling is assembled into a static/dynamic test rig (cf. figure 2.5) comprised of two Control Techniques Unimotor FM PMSM machines and two Control Techniques Unidrive SP intelligent AC drives under the control of a Hardware-in-the-Loop (HIL) dSPACE DS1104 development platform. Pertinent details and key parameters for the two Unimotor machines and two Unidrives are detailed in table 2.1 below. Both machines are operated in pure torque mode, the motor-side (prime-mover) having speed/position controllers implemented in Simulink/dSPACE; the load-side is always in torque mode and imparts a programmable dynamic load. The only exception to this is in the measurement of the static torque transfer characteristic of the magnetic coupling (cf. section 2.3.1) where both motor-side and load-side machines make use of the Unidrive SP position controllers for convenience. These state-of-the-art intelligent IGBT inverter-based drives are designed for high speed, high performance servo applications. The inner current/torque control loop of the Unidrives, having a bandwidth more than ten times greater than the developed speed/position controllers, can be considered to have negligible effect on the overall system response [41]. Furthermore, for the experimental work undertaken, a maximum motor speed of 1500 rpm has been used, this being approximately 30% of maximum rated speed capability of the machines. A maximum load torque of 5.7 N•m represents approximately 37% of maximum stall torque of the utilized machines. Consequently, the drives' servo current amplifier is modelled as a unity gain and the Unidrive SP/Unimotor FM combination is considered to behave as an instantaneous torque actuator and therefore the internal dynamics of the machines are omitted from further analysis.

Speed and position measurements in the experimental set-up are obtained from the Unimotors' incorporated resolvers and the SM-Resolver ("Solutions Module") plug-in interface module for the Unidrive SPs. The module provides speed and position feedback via a simulated incremental encoder output which is connected directly to the incremental encoder interface of the dSPACE interface panel. Estimation of salient torques is accomplished with measurements of motor active currents provided by the Unidrives and the motor torque constant given in table 2.1. Estimated torques and controller output torque are obtained via 16-bit, 2μs ADC channels and 16-bit 10μs DAC channels on the dSPACE interface panel.

<table>
<tr><th colspan="2">Control Techniques 3 Phase PMSM AC Servo Motor
(Model 115U2E300VAAEA115240)</th></tr>
<tr><th>Key Parameters</th><th>Value</th></tr>
<tr><td>Maximum Speed</td><td>4800 rpm</td></tr>
<tr><td>Stall Torque</td><td>15.3 Nm @ 9.6 A</td></tr>
<tr><td>Rated Torque</td><td>12.6 Nm</td></tr>
<tr><td>Rated Power</td><td>3.96 kW</td></tr>
<tr><td>Back emf constant</td><td>98 V/ kRPM</td></tr>
<tr><td>Torque constant</td><td>1.6 Nm / A</td></tr>
<tr><td>Feedback device</td><td>6 pole resolver</td></tr>
<tr><td>Inertia</td><td>13.8 kg.cm^2</td></tr>
<tr><td>Motor poles</td><td>6</td></tr>
<tr><td>Max switching frequency</td><td>16 kHz</td></tr>
<tr><th colspan="2">Control Techniques Unidrive Intelligent AC Drive
(Model SP 2401)</th></tr>
<tr><td>Voltage</td><td>380 – 480V 3Θ</td></tr>
<tr><td>Frequency</td><td>50 – 60 Hz</td></tr>
<tr><td>Continuous current rating</td><td>15.3 A</td></tr>
<tr><td>Current controller sample rate</td><td>83μs</td></tr>
<tr><td>Nominal power</td><td>7.5 kW</td></tr>
<tr><td>Peak current</td><td>16.8 A</td></tr>
<tr><td>Solutions Module</td><td>SM-Resolver</td></tr>
<tr><td>User drive mode</td><td>Torque</td></tr>
</table>

Table 2.1 Unimotor and Unidrive key parameters

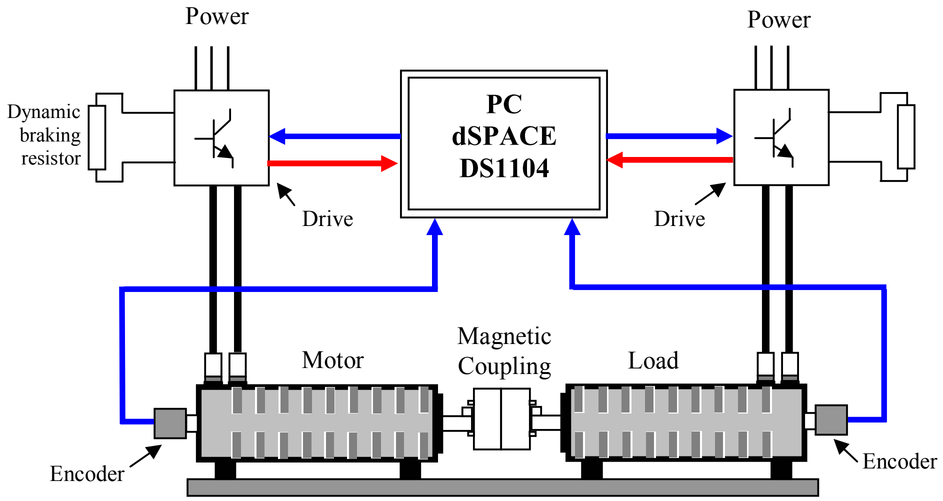

Figure 2.5 Schematic of experimental magnetic coupling test rig

Figure 2.6 shows photographs of the magnetic coupling separated, engaged and mounted within the complete experimental test rig.

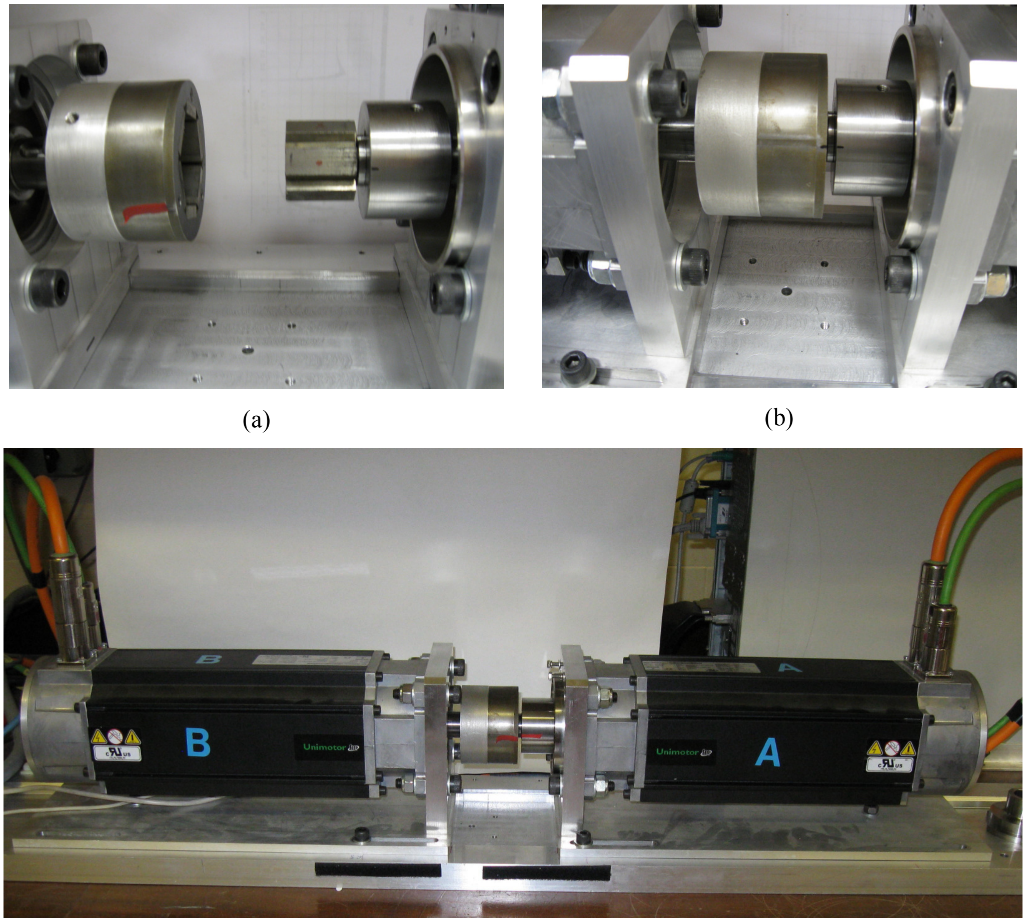
(a)
(b)
(c)

Figure 2.6 Experimental magnetic coupling and static/dynamic test facility
(a) magnetic coupling separated (b) magnetic coupling engaged (c) complete experimental test rig

2.3.1 Static torque transfer

The first objective following construction and assembly of the magnetic coupling is to determine the static torque transfer through the device. This is achieved by locking one side of the magnetic coupling and measuring the static holding torque as the other side is rotated through 360°. Similarly, the roles of locked and rotated sides of the magnetic coupling are reversed and the static holding torque from both sides of the coupling is determined. More specifically, by using internal position control available on the drives, the relative angular displacement, θ_D, between the two sides of the magnetic coupling can be controlled, and the static transmitted torque measured. The resulting graphs of torque versus relative mechanical angular displacement, from either side of the magnetic coupling, are shown in figure 2.7, from which a peak torque of 5.7 N•m (= T_G) is observed.

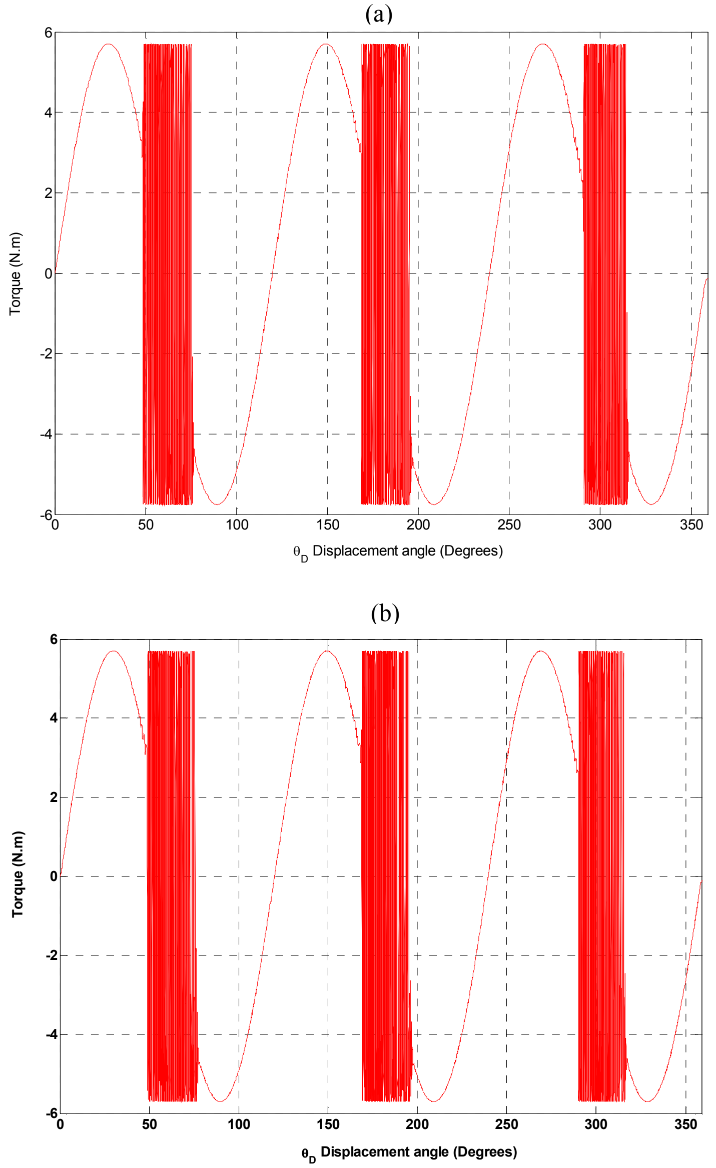

Figure 2.7 Experimentally measured results: static torque transfer
(a) inner rotor locked (b) outer rotor locked

Closer inspection of either torque transfer characteristic around mechanical displacement angles of 60°, 180° or 300° reveals a form of limit cycle response, shown in greater detail in figure 2.8[†], a function of the magnetic nature of the torque transfer. This is a consequence of the existence of unstable equilibrium points in the torque transfer characteristic, and will be considered further shortly. In terms of the measurement system, this effect occurs because the position controllers are unable to stabilize and hold the magnetic coupling around mechanical displacement angles of 60°, 180° or 300°.

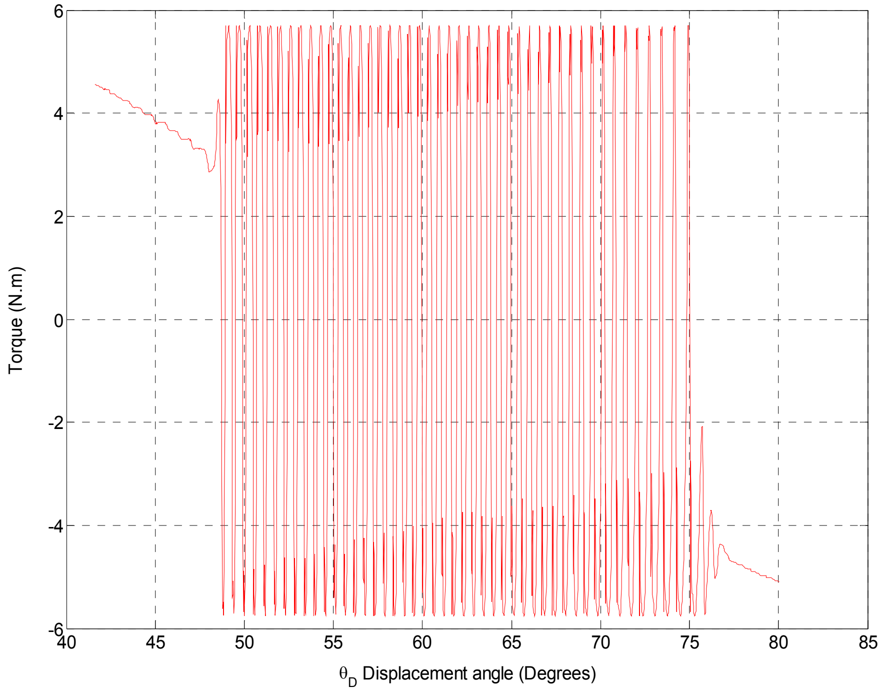

Figure 2.8 Measurement system ‘limit cycle’ near unstable equilibria

The theoretically expected torque versus displacement angle characteristic is described by,

$$T_C = T_G \sin(p\theta_D) \tag{2.5}$$

where T_C represents the magnetic coupling’s transmitted torque, T_G the peak (design) torque, p is the number of pole pairs (3 in this case) and $\theta_D = (\theta_M - \theta_L)$ is the mechanical displacement angle between the motor- and load-side of the magnetic coupling, respectively. A plot of the theoretically expected torque transfer characteristic is shown in figure 2.9.

[†] Throughout this thesis graphs plotted in red represent torque.

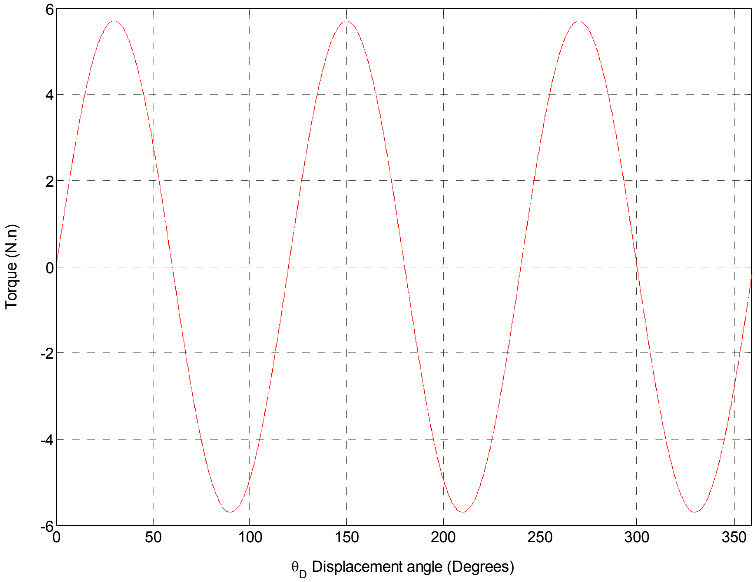

Figure 2.9 Simulated theoretical torque transfer characteristic of the designed magnetic coupling

What is not apparent from figure 2.9, but hinted at in figure 2.7, is that the magnetic coupling possesses 6 dynamic equilibrium points, 3 stable and 3 unstable, as depicted in figure 2.10.

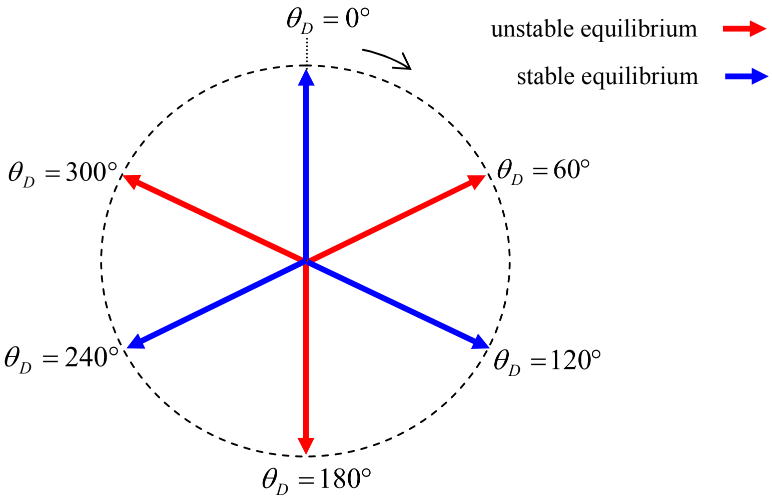

Figure 2.10 Equilibrium points for magnetic coupling with 3 pole-pairs

The dynamic equilibria indicated in figure 2.10 will be examined further in section 5.2.1.

2.3.2 Inertia tests

To construct a working model of the magnetic coupling it is necessary to determine the inertias of each half of the coupling, and, in addition, the inertias of the motor rotors connected to the low speed and high speed sides of the magnetic coupling. As indicated in figure 2.3, the coupling can be modelled as a magnetic spring interconnecting two inertias. To distinguish either side of the magnetic coupling the term ‘motor-side’ refers to the outer rotor, and ‘load-side’ refers to the inner rotor (note: this is an essentially arbitrary choice, but reflects the experimental system set-up). Moreover, the total inertias on either side of the magnetic spring are composed of motor rotor inertia plus the inertia of either inner or outer rotor of the magnetic coupling respectively.

The motor rotor inertias and the inertias of each half of the magnetic coupling are determined from a ‘Unidrive initiated’ auto-tune inertia test. During auto-tuning, the drive attempts to accelerate the motor to a known speed using *a priori* selected torque input and then decelerates it back to a standstill. Provided the motor and load can be accelerated to the desired speed, an estimate of the total inertia is then determined. For the experimental test rig, four separate inertia tests are conducted to determine the inertias of the two motor rotors (designated A and B), and two inertia tests with each half of the magnetic coupling mounted on to the relevant motor shafts, in this case motor A and magnetic coupling inner rotor, and motor B and magnetic coupling outer rotor. The outcomes of these tests are given in table 2.2 below.

Inertia test	**Averaged inertia**[††]
Motor A	$13.8 \cdot 10^{-4}$ kg.m^2
Magnetic coupling inner rotor	$1.2 \cdot 10^{-4}$ kg.m^2
Motor B	$14 \cdot 10^{-4}$ kg.m^2
Magnetic coupling outer rotor	$4.9 \cdot 10^{-4}$ kg.m^2

Table 2.2 Auto-tune inertia tests for motor rotors and magnetic coupling

2.4 Servo drive modelling of magnetic coupling

The magnetic coupling interconnecting a motor and load can be represented as a classical two-inertia servo-drive system, as shown in figure 2.11. The combined motor-side inertia is J_M, the combined load-side inertia is J_L, and the interconnecting magnetic spring has a nonlinear stiffness, $K(\theta_D)$, that is a function of the relative mechanical angular displacement between motor- and load-side of the magnetic coupling.

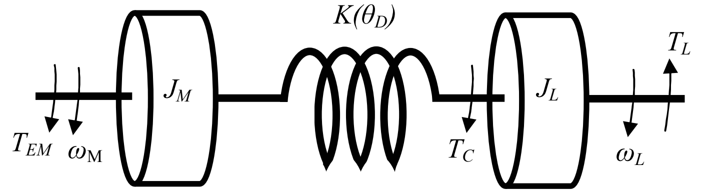

Figure 2.11 Dynamic representation of a dual inertia servo

[††] Averaged over five trials

In a classical two-inertia drive model the torsional stiffness is generally considered to be linear in the first instance [29]. For comparison purposes, figure 2.12 shows the torque transfer characteristic of an ideal linear torsion spring and the equivalent transfer characteristic of the magnetic coupling over the principal mechanical displacement angle, $-30° \leq \theta_D \leq 30°$.

For a conventional servo-drive system the inter-connecting drive shaft has stiffness K (N•m/rad) and is considered to function linearly within its operating range. That is,

$$T_C = K\,\theta_D = K\left(\theta_M - \theta_L\right) \tag{2.6}$$

and the transmitted torque is a linear function of the relative angular displacement between motor and load. The torsional stiffness of the drive shaft is considered to be constant with respect to mechanical displacement angle whilst operating within its maximum torque rating.

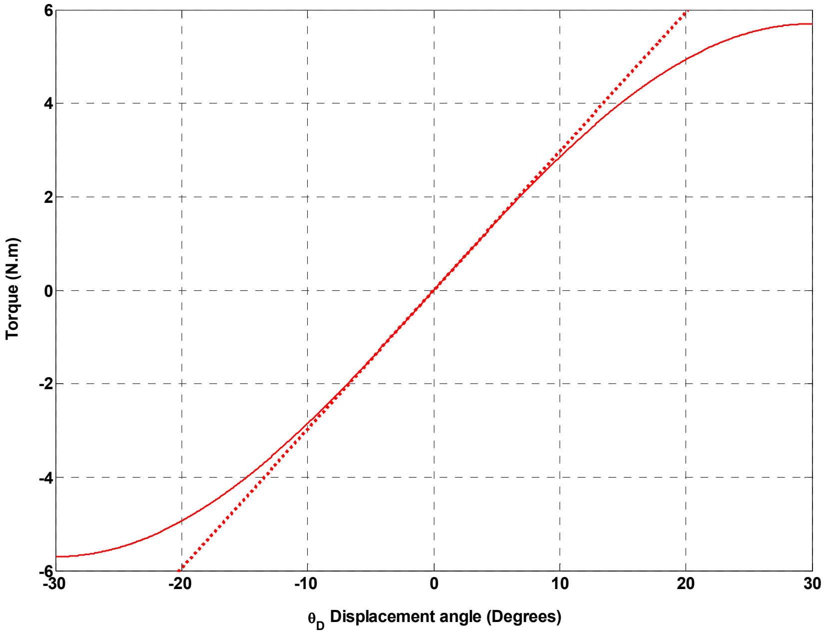

Figure 2.12 Simulated torque transfer (**solid line** magnetic coupling, **dashed line** linear spring)

When considering the magnetic coupling, the linear torsion spring stiffness of traditional systems is replaced by the nonlinear torque transfer function given in (2.5). Consequently, the torsional stiffness is no longer constant with mechanical displacement angle, and is given by,

$$K\left(\theta_D\right) = pT_G \cos\left(p\left(\theta_M - \theta_L\right)\right) \tag{2.7}$$

and is shown in figure 2.13 for the first principal mechanical displacement range, $\theta_D = \pm 30°$.

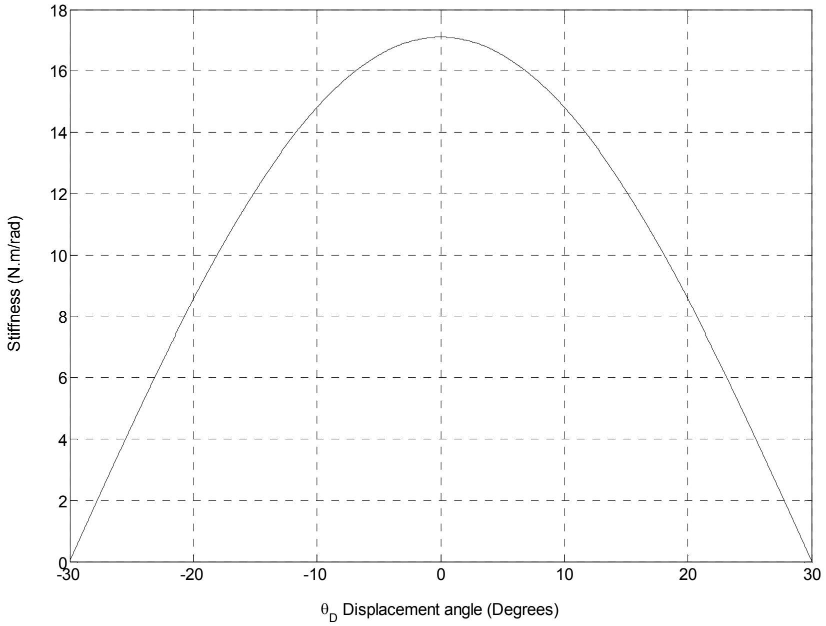

Figure 2.13 Simulated magnetic coupling torsional stiffness vs. mechanical displacement angle

Beyond this range of mechanical displacement angle, the magnetic coupling enters a pole-slipping regime (discussed more fully in Chapter 3), providing effective over-torque protection without jamming. However, just prior to the over-torque condition being reached the magnetic coupling behaves as a nonlinear soft torsional spring. When linearized about the origin, the torsional stiffness in this case is given by $K_{lin} = pT_G \approx 17$ N•m/rad. The linearized transfer characteristic is shown (dashed line) in figure 2.12. By way of comparison, a medium torsional stiffness coupling rated at 22 N•m has a torsional stiffness constant of 2500 N•m/rad [14].

Additionally, from a dynamics perspective, an effective damping torque may also be designed into the magnetic coupling characteristic. Damping torque is mainly caused by the eddy currents generated in the conducting components of the magnetic coupling, and these include the permanent magnets, the back-irons, metallic sleeves etc. The magnetic damping torque is described by,

$$B(\omega_D) = \alpha T_G \frac{2\beta\omega_D}{\omega_D{}^2 + \beta^2}, \; \omega_D = (\omega_M - \omega_L) \qquad (2.8)$$

where α represents a proportion of the coupling's maximum torque capability and β represents the relative angular velocity at which maximum damping torque occurs. Equation (2.8) has the same form as the equation for torque versus slip in an induction machine [1]. Example damping characteristics are shown in figure 2.14 for completeness.

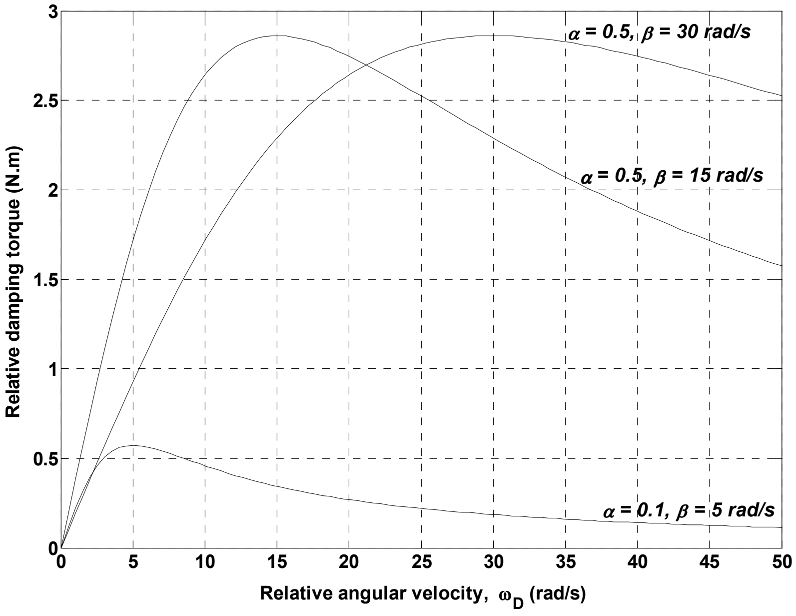

Figure 2.14 Simulated damping curves for $\alpha = 0.1, 0.5$, $\beta = 5$ rad/s, 15 rad/s & 30 rad/s

Whilst it is possible to include a damping torque $B(\omega_D)$, for the experimental magnetic coupling manufactured the damping torque has been designed to be negligible, that is, $\alpha \approx 0$, and is not considered further.

2.5 Summary

An equivalent model of a magnetic gear box has been proposed that allows the ‘magnetic’ part of the torque transfer characteristic to be located within a magnetic coupling (1:1 magnetic gear) that interconnects two ideal (fictitous) gear boxes. It is this transformation that provides the rationale for the construction and manufacture of a magnetic coupling (rather than a general *n*:1 magnetic gear). The manufactured magnetic coupling is incorporated into a static/dynamic experimental test rig consisting of two PMSM machines under the control of a dSPACE hardware-in-the-loop (HIL) development platform. Torque and stiffness characteristics of the designed magnetic coupling are determined. The constructed experimental test rig represents a demonstrator drive train that incorporates a 1:1 magnetic gear to be used for investigating salient control issues.

Chapter 3

Conventional Speed Control of Two-Inertia Drive Train

3.1 Introduction

Speed control of a drive train incorporating the magnetic coupling introduced in Chapter 2 is now considered. The method adopted, initially, is conventional PI control subject to the introduction of a suitable metric for performance assessment. Although myriad performance metrics are available (ISE, IAE, ITSE, ISTSE, ISTAE, for example), the Integral of Time multiplied by Absolute Error, or ITAE, metric has been adopted throughout as it is generally considered to be more selective than the other possible metrics.

A classical representation of a two-inertia servo-drive system is shown in figure 3.1. The interconnecting shaft has a stiffness K (N•m/rad) and is considered to be linear within its operating range, and the developed torque is a linear function of relative angular displacement between the prime-mover (motor in this case) and load [29].

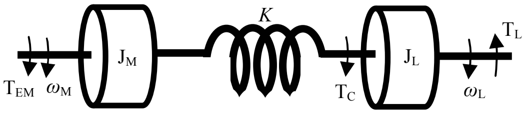

Figure 3.1 Dynamic representation of a dual inertia servo

For comparison purposes, figure 3.2 (repeated from Chapter 2 for convenience) shows the torque transfer characteristic of an 'ideal' linear torsion spring and the equivalent transfer characteristic of the magnetic coupling over the principal displacement angle, $-30° \le \theta_D \le 30°$.

It is apparent that in the region up to ≈ 50% of maximum rated torque T_G the magnetic coupling's torque transfer characteristic is essentially linear. Outside of this range (≈ 50% - 100%), the torque transfer characteristic begins to deviate, mildly, from that of an ideal linear torsion spring. As the magnetic coupling is only weakly nonlinear, it can be argued that a reasonable first order approximation is to investigate control of a linearized form of the magnetic coupling in a classical two-inertia servo drive model. (A more detailed discussion on the linearization of the magnetic coupling's nonlinear dynamics, and the effects of nonlinearity on system performance, is deferred until Chapter 5). To obtain a baseline for comparative performance between a linearized and nonlinear model, the magnetic coupling is put under idealized and optimized PI control and investigated through simulation (Simulink) and experimentation (dSPACE).

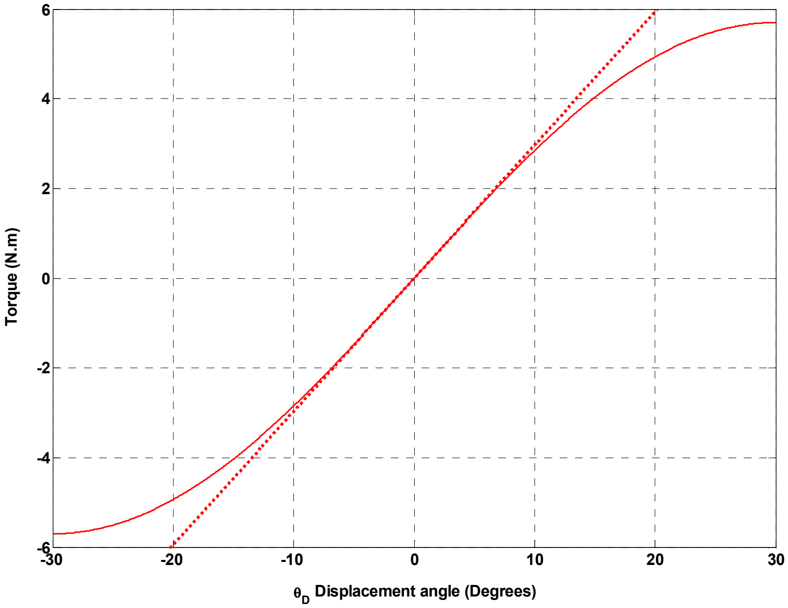

Figure 3.2 Simulated static torque transfer characteristics
(**solid line** ideal magnetic coupling, **dashed line** ideal linear spring)

Initially starting with a linearized approximation to the magnetic coupling's dynamics, a block diagram of the two-inertia mechanical system, is shown in figure 3.3 (electromagnetic dynamics of the motor-side and load-side machines are modelled as unity gains for the reasons outlined in section 2.3) .

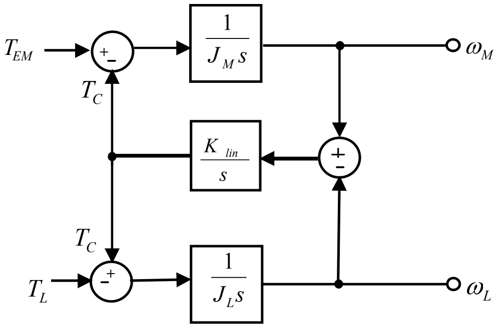

Figure 3.3 Two-inertia block diagram

Transfer functions between electromagnetic torque produced by the motor, T_{EM} , and the motor-side ω_M , and load-side ω_L, angular velocities will be derived from Mason's Gain Formula [53].

3.2 Open-loop analysis

From a signal flow graph describing the system dynamics, relevant transfer functions, T, can be obtained from Mason's formula, stated below (without proof [54]),

$$T = \frac{\sum P_K \Delta_K}{\Delta} \qquad (3.1)$$

where

1. P_K is transmittance of each forward path between input and output
2. Δ is the overall determinant of the signal flow graph and is given by

$$\Delta = 1 - \Sigma L_1 + \Sigma L_2 - \Sigma L_3 + \ldots \qquad (3.2)$$

and

a. L_1 is the transmittance of each closed loop
b. L_2 is the product of two non-touching loops. All possible combinations of non-touching loops are taken two at a time
c. L_3 is the product of three non-touching loops. All possible combinations of non-touching loops are taken three at a time

3. Δ_k is the cofactor of P_k obtained by removing loops from Δ that touch forward path P_k

The signal flow graph for figure 3.3, with no disturbance input, $T_L = 0$, is shown in figure 3.4,

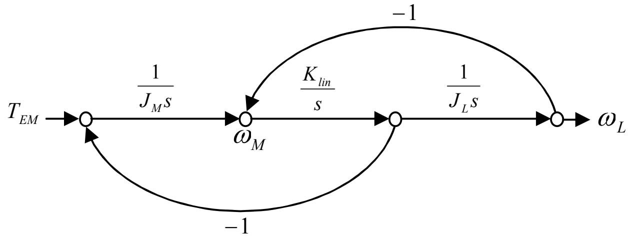

Figure 3.4 Signal flow graph of two-inertia block diagram

The open loop transfer function from input torque to load speed, that is, $\frac{\omega_L(s)}{T_{EM}(s)}$, is determined from Mason's Rule as follows.

Loops gains from left to right are given by,

$$L_1 = \frac{-K_{lin}}{J_M s^2} \qquad L_2 = \frac{-K_{lin}}{J_L s^2} \qquad (3.3)$$

As there are no non-touching loops in this signal flow graph (all loops touch the forward path) the cofactor $\Delta_K = 1$ and the determinant Δ becomes,

$$\Delta = 1 - \sum L_i = 1 + \frac{K_{lin}}{J_M s^2} + \frac{K_{lin}}{J_L s^2} \tag{3.4}$$

With only one forward path between input and output the forward transmittance is given by,

$$P_K = \frac{1}{J_M s}\frac{K_{lin}}{s}\frac{1}{J_L s} = \frac{K_{lin}}{J_M J_L s^3} \tag{3.5}$$

and the overall transfer function is then,

$$\frac{\omega_L(s)}{T_{EM}(s)} = \frac{P_K \Delta_K}{\Delta} = \frac{\dfrac{K_{lin}}{J_M J_L s^3}}{1 + \dfrac{K_{lin}}{J_M s^2} + \dfrac{K_{lin}}{J_L s^2}}$$

$$\frac{\omega_L(s)}{T_{EM}(s)} = \frac{\dfrac{K_{lin}}{J_L}}{J_M s^3 + sK_{lin} + \dfrac{sJ_M K_{lin}}{J_L}}$$

$$\frac{\omega_L(s)}{T_{EM}(s)} = \frac{\dfrac{K_{lin}}{J_L}}{J_M s^3 + J_M s\left(\dfrac{K_{lin}}{J_M} + \dfrac{K_{lin}}{J_L}\right)} \tag{3.6}$$

For notational convenience the following terms are defined:

Anti-resonant frequency $\omega_a^2 = \dfrac{K_{lin}}{J_L}$ *Inertia ratio* $R = \dfrac{J_L}{J_M}$ (3.7)

Resonant frequency

$$\omega_n^2 = \omega_a^2 (R+1)$$
$$\omega_n^2 = \frac{K_{lin}}{J_L}\left(\frac{J_L}{J_M} + 1\right) = \left(\frac{K_{lin}}{J_M} + \frac{K_{lin}}{J_L}\right) \tag{3.8}$$

Substituting the above definitions in (3.6) gives,

$$\frac{\omega_L(s)}{T_{EM}(s)} = \frac{\omega_a{}^2}{J_M s^3 + J_M \omega_n{}^2 s} \tag{3.9}$$

To determine the open loop transfer function between input torque and motor speed the forward path transmittance and cofactor become,

$$P_K = \frac{1}{J_M s} \qquad \Delta_K = 1 + \frac{K_{lin}}{J_L s^2} \tag{3.10}$$

(L_2 does not touch the forward path in this case and is not removed from the determinant.)

The open loop transfer function is determined as before by,

$$\frac{\omega_M(s)}{T_{EM}(s)} = \frac{P_K \Delta_K}{\Delta} = \frac{\frac{1}{J_M s}\left(1 + \frac{K_{lin}}{J_L s^2}\right)}{1 + \frac{K_{lin}}{J_M s^2} + \frac{K_{lin}}{J_L s^2}}$$

$$\frac{\omega_M(s)}{T_{EM}(s)} = \frac{s^2 + \frac{K_{lin}}{J_L}}{J_M s^3 + sK_{lin} + \frac{sJ_M K_{lin}}{J_L}}$$

$$\frac{\omega_M(s)}{T_{EM}(s)} = \frac{s^2 + \omega_a^2}{J_M s^3 + J_M \omega_n^2 s} \tag{3.11}$$

For the experimental coupling under consideration it is now possible to determine the open loop frequency responses of the motor- and load-side of the coupling. The relevant parameters are J_M = 19 x 10^{-4} kg.m^2, J_L = 15 x 10^{-4} kg.m^2 and K_{lin} = 17 N•m/rad, yielding the following transfer functions for motor- and load-side respectively,

$$\frac{\omega_M(s)}{T_{EM}(s)} = \frac{s^2 + 1.133\times10^4}{0.0019s^3 + 38.53s} \qquad \frac{\omega_L(s)}{T_{EM}(s)} = \frac{1.133\times10^4}{0.0019s^3 + 38.53s} \tag{3.12}$$

A Bode (magnitude) plot for motor- and load-side frequency responses of the magnetic coupling is shown in figure 3.5, where both the anti-resonant and resonant frequencies can be clearly seen with break frequencies given by,

$$\omega_a = \sqrt{\frac{K_{lin}}{J_L}} = \sqrt{\frac{17}{15\times10^{-4}}} = 106.45 \text{ rad/s} \tag{3.13}$$

$$R = \frac{J_L}{J_M} = \frac{15\times10^{-4}}{19\times10^{-4}} = 0.7895 \tag{3.14}$$

$$\omega_n = \omega_a\sqrt{(R+1)} = 106.45\times\sqrt{0.7895+1} = 142.41 \text{ rad/s} \tag{3.15}$$

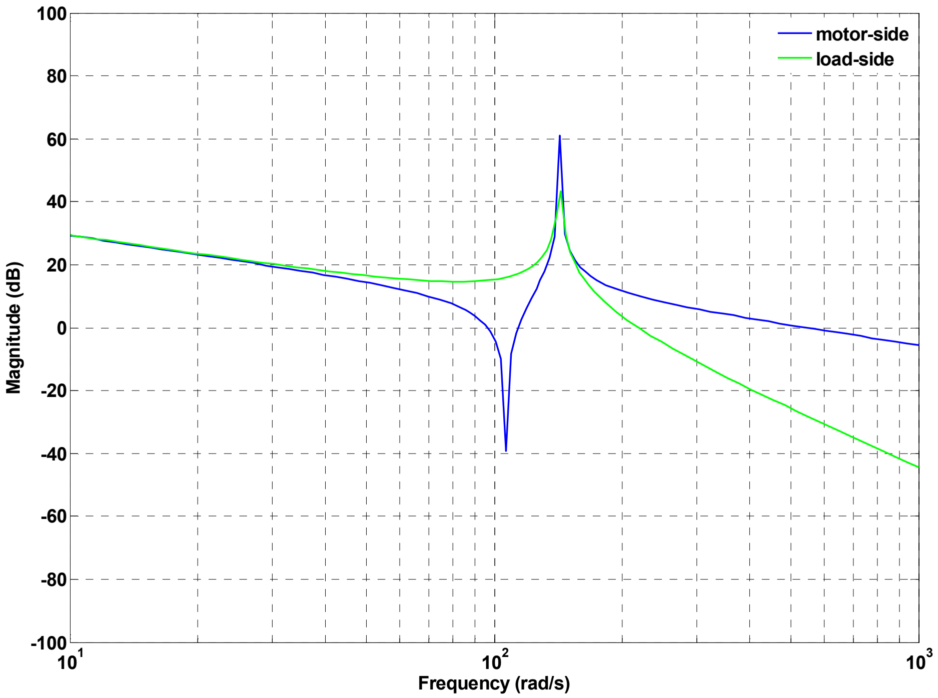

Figure 3.5 Simulated open loop Bode plot of two-inertia magnetic coupling model

3.3 Closed-loop control using PI controller

Figure 3.6 shows the block diagram of a classical PI control loop from which closed-loop transfer functions of interest can be derived [41]. Of particular interest are transfer functions from reference speed to motor speed and reference speed to load speed, i.e. speed tracking dynamics on either side of the magnetic coupling, respectively.

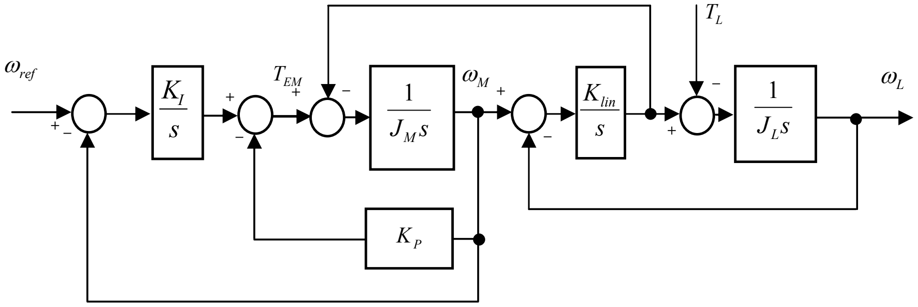

Figure 3.6 PI control of two-inertia mechanical system

As in section 3.2, it is more convenient to use the signal flow graph to derive the transfer functions of interest. The signal flow graph for the PI control block diagram of figure 3.6 is shown in figure 3.7, again with assumption of no disturbance torque, that is, $T_L = 0$.

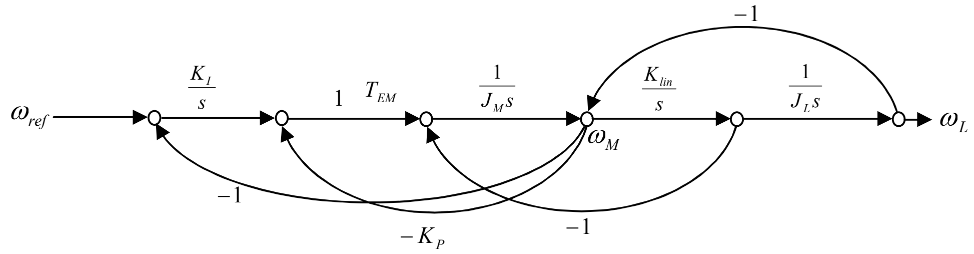

Figure 3.7 Signal flow graph of two-inertia block diagram

The closed loop transfer function from reference speed to load speed that is, $\frac{\omega_L(s)}{\omega_{ref}(s)}$, is again determined from Mason's Rule as follows.

Forward path transmittance from reference speed to load speed is,

$$P_K = \frac{K_I}{s}\frac{1}{J_M s}\frac{K_{lin}}{s}\frac{1}{J_L s} = \frac{K_{lin}K_I}{J_L J_M s^4} \tag{3.16}$$

and loops gains from left to right are given by,

$$L_1 = \frac{-K_I}{J_M s^2} \qquad L_2 = \frac{-K_P}{J_M s} \qquad L_3 = \frac{-K_{lin}}{J_M s^2} \qquad L_4 = \frac{-K_{lin}}{J_L s^2} \tag{3.17}$$

In this case loops L_1, L_2 and L_4 are non-touching and the signal flow graph determinant becomes,

$$\begin{aligned} \Delta &= 1-(L_1+L_2+L_3+L_4)+L_1L_4+L_2L_4 \\ \Delta &= 1+\frac{K_I}{J_M s^2}+\frac{K_P}{J_M s}+\frac{K_{lin}}{J_M s^2}+\frac{K_{lin}}{J_L s^2}+\frac{K_I K_{lin}}{J_M J_L s^4}+\frac{K_P K_{lin}}{J_M J_L s^3} \end{aligned} \tag{3.18}$$

and as all loops touch the forward path the cofactor $\Delta_k = 1$. Hence,

$$\frac{\omega_L(s)}{\omega_{ref}(s)} = \frac{P_K \Delta_K}{\Delta} = \frac{\dfrac{K_I K_{lin}}{J_M J_L s^4}}{1+\dfrac{K_I}{J_M s^2}+\dfrac{K_P}{J_M s}+\dfrac{K_{lin}}{J_M s^2}+\dfrac{K_{lin}}{J_L s^2}+\dfrac{K_I K_{lin}}{J_M J_L s^4}+\dfrac{K_P K_{lin}}{J_M J_L s^3}}$$

$$\frac{\omega_L(s)}{\omega_{ref}(s)} = \frac{\dfrac{K_I K_{lin}}{J_L}}{J_M s^4 + K_P s^3 + \left(K_I + K_{lin}\left(1 + \dfrac{J_M}{J_L}\right)\right)s^2 + \dfrac{K_P K_{lin}}{J_L}s + \dfrac{K_I K_{lin}}{J_L}} \tag{3.19}$$

Substituting from (3.7) and (3.8),

$$\frac{\omega_L}{\omega_{ref}} = \frac{K_I {\omega_a}^2}{J_M s^4 + K_P s^3 + \left((K_{lin}\left(1 + \dfrac{1}{R}\right) + K_I)\right)s^2 + K_P {\omega_a}^2 s + K_I {\omega_a}^2} \tag{3.20}$$

Further noting that,

$$K_{lin}\left(1 + \frac{1}{R}\right) = J_M\left(\frac{K_{lin}}{J_L}\right)\left(1 + \frac{J_L}{J_M}\right) = J_M \omega_a^2 (1 + R) \tag{3.21}$$

the closed-loop transfer function from reference speed to load speed is,

$$\frac{\omega_L}{\omega_{ref}} = \frac{K_I {\omega_a}^2}{J_M s^4 + K_P s^3 + \left(J_M \omega_a^2 (1 + R) + K_I\right)s^2 + K_P {\omega_a}^2 s + K_I {\omega_a}^2} \tag{3.22}$$

To determine the closed-loop transfer function between input reference speed and motor speed the forward path transmittance and cofactor become,

$$P_K = \frac{K_I}{J_M s^2} \qquad \Delta_K = 1 + \frac{K_{lin}}{J_L s^2} \tag{3.23}$$

and the closed-loop transfer function is determined similarly as,

$$\frac{\omega_M(s)}{\omega_{ref}(s)} = \frac{P_K \Delta_K}{\Delta} = \frac{\left(K_I s^2 + \dfrac{K_I K_{lin}}{J_L}\right)}{J_M s^4 + K_P s^3 + \left(K_I + K_{lin}\left(1 + \dfrac{J_M}{J_L}\right)\right)s^2 + \dfrac{K_P K_{lin}}{J_L}s + \dfrac{K_I K_{lin}}{J_L}}$$

$$\frac{\omega_M}{\omega_{ref}} = \frac{K_I (s^2 + {\omega_a}^2)}{J_M s^4 + K_P s^3 + (J_M {\omega_a}^2 (1 + R) + K_I)s^2 + K_P {\omega_a}^2 s + K_I {\omega_a}^2} \tag{3.24}$$

3.4 Controller parameter selection

Selection of the PI gains, K_I and K_P determine the closed-loop tracking performance of the drive train incorporating the magnetic coupling. A number of possible techniques are available for the selection of PI controller gains depending on the desired objective. For example, Zhang and Furusho [36] examined three kinds of pole assignment with identical radius/damping coefficient and real part for PI speed control of a two inertia system.

The method investigated here follows O'Sullivan and Bingham [41] in which the most suitable performance index is considered to be the integral of time multiplied by absolute error (ITAE) for a step reference input. The ITAE index generates s-domain polynomials that produce minimum overshoot and minimum rise time for a given polynomial of order *n*. A particular advantage of the ITAE metric is that it does not unduly penalize the inevitably large initial error that exists in the step response. It does, however, penalize long duration transient error with the explicit inclusion of time in metric's integral calculation. Many performance indices exist, for example, integral of squared error (ISE), integral of absolute error (IAE) and others. By way of comparison, consider a normalized standard second order system with damping coefficient ζ and $\omega_n = 1$. Figure 3.8 illustrates the performance index value for ITAE, ISE and IAE as a function of ζ.

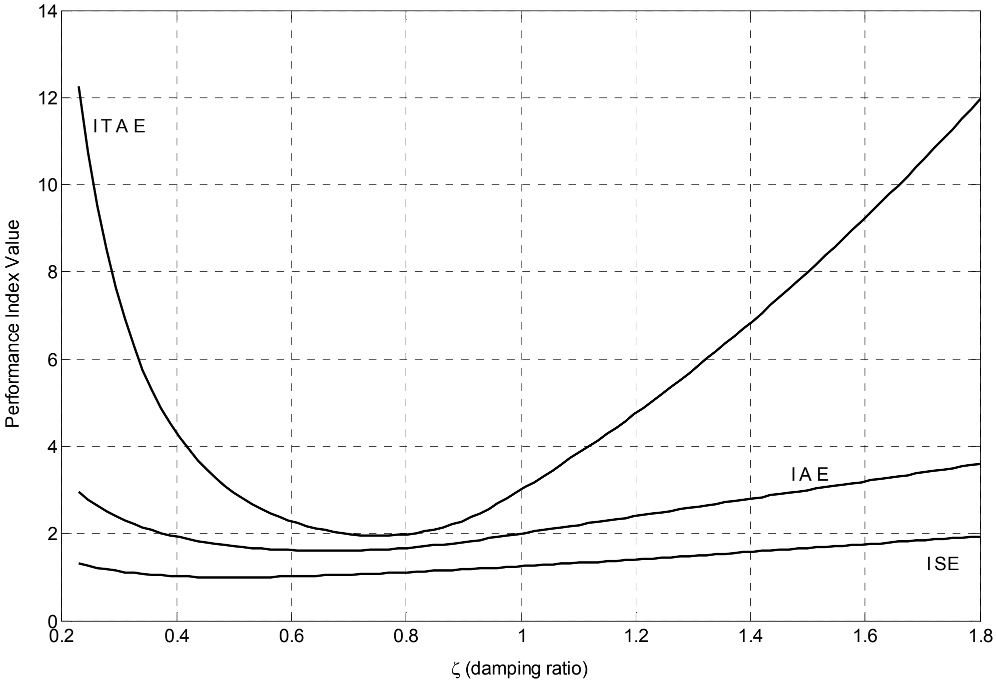

Figure 3.8 Performance indices ITAE, IAE and ISE for second order system

It is clear that in this case the ITAE index offers the best selectivity with a much more sharply defined minimum than either ISE or IAE [55]. It can also be noted that the value of the ITAE minimum is $\zeta = 0.7$, a well-known optimum setting for a standard second order system. As a further illustration, consider figure 3.9 which shows the normalized step responses for orders $n = 2, 3, 4, 5$, and 6. In each of these cases, the system has its closed-loop characteristics defined by optimum coefficients that result in the ITAE performance index being a minimum when subjected to a step reference input command. The ITAE step responses offer superior performance in terms of the key metrics such as percentage overshoot, rise time and settling time. Although to some extent a subjective term, 'optimum' in this sense implies that the relevant performance index is at a minimum. Standard tables for ITAE optimum step input response and ITAE optimum ramp input response are the most widely available, and most commonly used, for optimizing the step and ramp response of linear control systems [54].

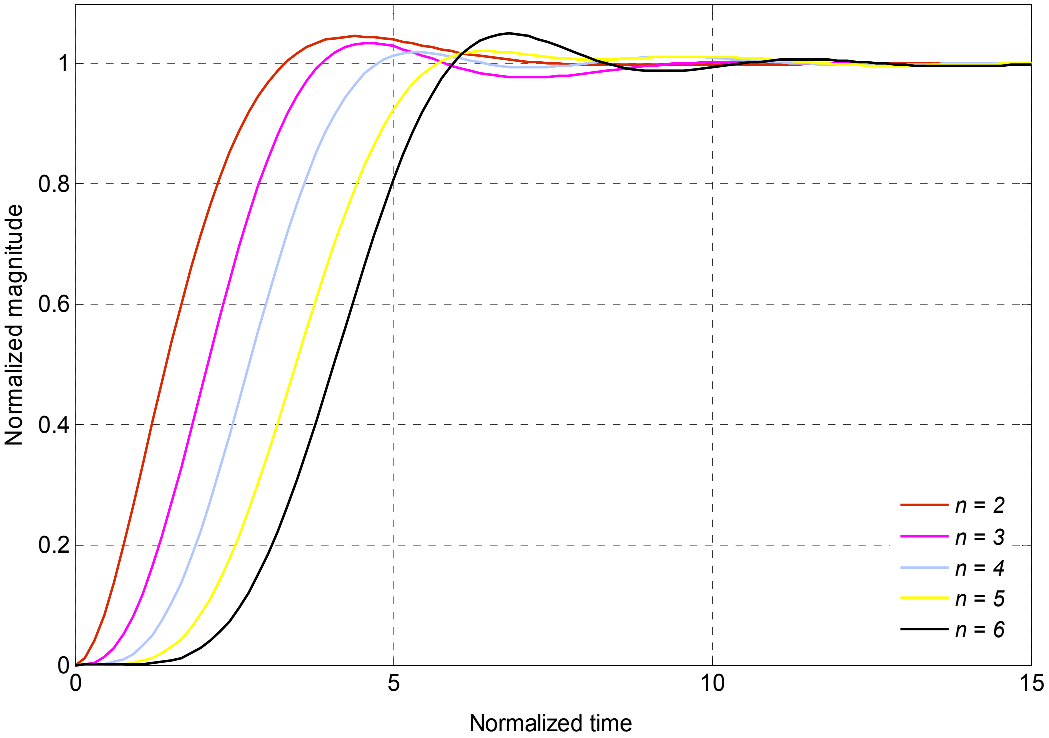

Figure 3.9 Optimum ITAE step responses (ref[54])

The principal objective in selecting the ITAE performance index is to provide an optimum step response for speed tracking on the load-side of the magnetic coupling, and as shown in (3.22) the load-side closed-loop transfer function is defined by a fourth order polynomial with no closed-loop zeros. Consequently, it is possible to equate the denominator of (3.22) with the optimized fourth order ITAE polynomial for a step response, given by,

$$s^4 + 2.1\omega_x s^3 + 3.4\omega_x{}^2 s^2 + 2.7\omega_x{}^3 s + \omega_x{}^4 \tag{3.25}$$

where ω_x = -3 dB bandwidth. Equating coefficients,

$$\begin{aligned}
\omega_x^4 &= \frac{K_I \omega_a^2}{J_M} \\
2.7\omega_x^3 &= \frac{K_P}{J_M}\omega_a^2 \\
3.4\omega_x^2 &= \frac{K_I + J_M \omega_a^2 (1+R)}{J_M} \\
2.1\omega_x &= \frac{K_P}{J_M}
\end{aligned} \tag{3.26}$$

solving for K_p,

$$\begin{aligned}
K_P &= 2.7\frac{\omega_x^3}{\omega_a^2} J_M = 2.1\omega_x J_M \\
\frac{\omega_x}{\omega_a} &= \sqrt{\frac{2.1}{2.7}} = 0.88
\end{aligned} \tag{3.27}$$

and K_I,

$$J_M \frac{\omega_x^4}{\omega_a^2} = 3.4\omega_x^2 J_M - J_M \omega_a^2 (1+R)$$

$$R = 3.4\frac{\omega_x^2}{\omega_a^2} - 1 - \frac{\omega_x^4}{\omega_a^4} = 3.4(0.88)^2 - 1 - (0.88)^4 = 1.03 \cong 1 \tag{3.28}$$

Hence for optimality, the inertia ratio, R = 1, and the ratio ω_x / ω_a = 0.88. Under these conditions the ITAE-derived optimum PI gains become,

$$\begin{aligned}
K_P &= 2.1\omega_x J_M = 2.1\frac{\omega_x}{\omega_a} J_M \omega_a = 2.1 \times (0.88) \times J_M \omega_a \\
K_P &= 1.85 J_M \omega_a
\end{aligned} \tag{3.29}$$

$$\begin{aligned}
K_I &= J_M \frac{\omega_x^4}{\omega_a^2} = J_M \frac{\omega_x^4}{\omega_a^4}\omega_a^2 = J_M (0.88)^4 \omega_a^2 \\
K_I &= 0.6\omega_a^2 J_M
\end{aligned} \tag{3.30}$$

As a consequence of (3.28), $J_M = J_L$, and the controller gains are also defined thus,

$$\begin{aligned} K_I &= 0.6\omega_a^2 J_L = 0.6\frac{K_{lin}}{J_L}J_L \\ K_I &= 0.6K_{lin} \end{aligned} \tag{3.31}$$

$$K_P = 1.85 J_L \omega_a \tag{3.32}$$

3.5 Simulation results for ITAE optimized PI speed controller

The linearized two-inertia mechanical model of the magnetic coupling, under ITAE optimized PI control, is constructed in Simulink. The closed-loop frequency response under optimized control is shown in figure 3.10† and comparison with figure 3.5 indicates how the optimized PI controller has substantially improved the load-side response, effectively removing the resonant peak.

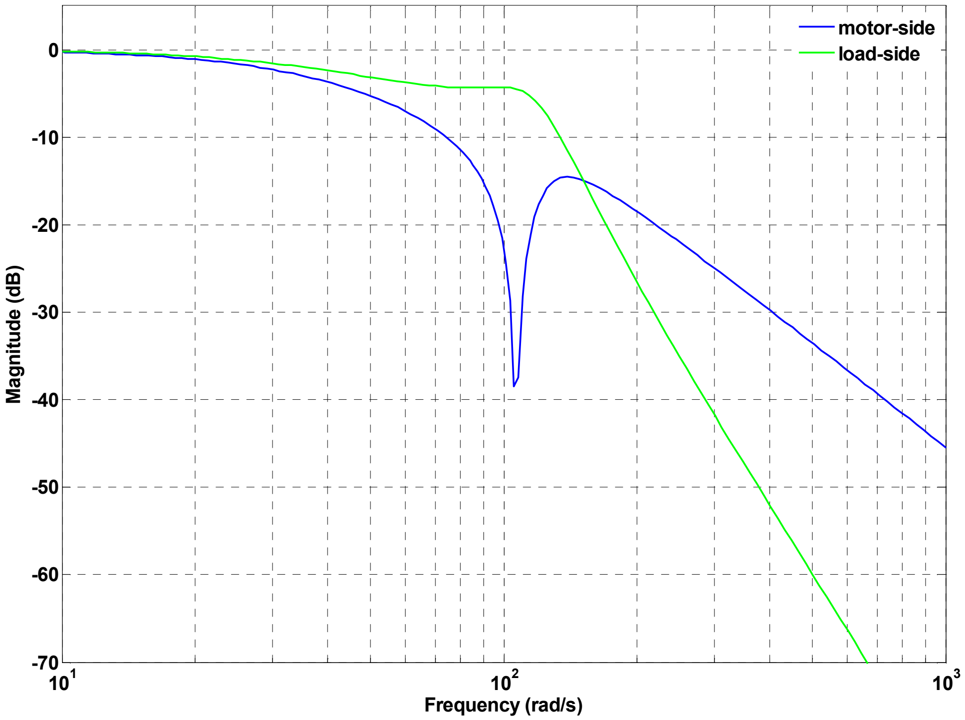

Figure 3.10 Simulated closed-loop Bode plot under ITAE optimised PI control

A simulated step response, figure 3.11, shows motor- and load-side responses plus the theoretically optimal response of the ITAE 4th order polynomial for an optimum step. Clearly, the load-side step response is identical to the required ITAE response.

---

† Throughout this thesis graphs plotted in <u>blue</u> represent <u>motor-side</u> frequency, speed or position responses and graphs plotted in <u>green</u> represent <u>load-side</u> frequency, speed or position responses.

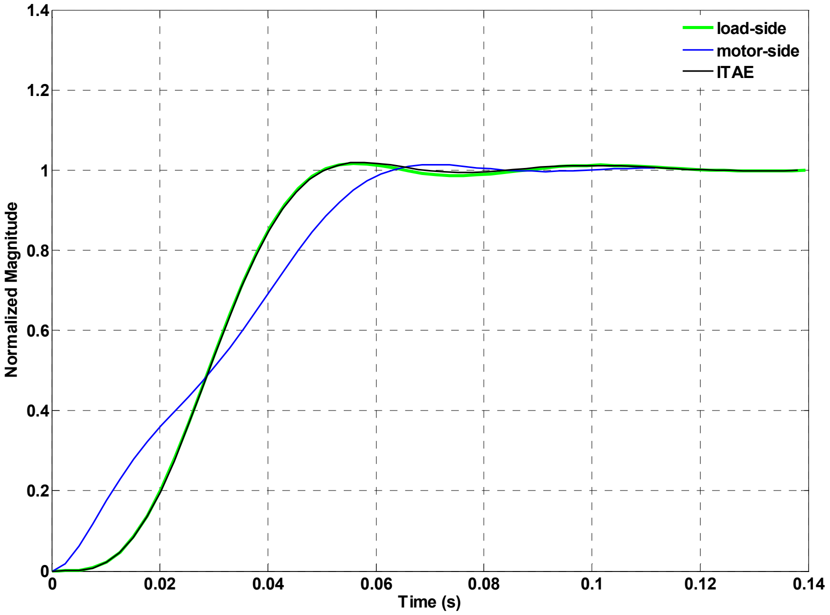

Figure 3.11 Simulated step responses (normalized): motor-side, load-side and 4th order ITAE

With a 4th order denominator in (3.22), and only two variable parameters K_I and K_P for the controller, it is not possible to arbitrarily place the poles of the closed-loop response. As shown by (3.27) and (3.28) the inertia ratio and ratio of -3dB bandwidth to anti-resonant frequency are already prescribed in order to select the optimum PI gains. A specific consequence is that the inertia ratio R must be equal to unity for optimality. The step responses indicated in figure 3.11 are simulated under the assumption that the motor-side and load-side inertias are identical at either side of the magnetic coupling. For the experimental system this is not true, and the actual inertia ratio is $R = 0.79$. Consequently, figure 3.12 indicates the simulated step responses under these sub-optimal conditions, where it is apparent that the load-side step response deviates somewhat from the theoretically expected response. This is an inevitable consequence of violating (3.28), a necessary condition for optimality.

3.6 Experimental results for ITAE optimized PI speed controller

The theoretically derived two-inertia model for the magnetic coupling, and optimum (in the ITAE sense) controller design, has been simulated and is now verified on the experimental test rig and a dSPACE hardware development platform. Figure 3.13 shows the simulated speed tracking responses of both the motor-side and load-side of the magnetic coupling for a 1500 rpm step reference speed demand, with the PI controller having gains optimally tuned to a fourth-order ITAE model.

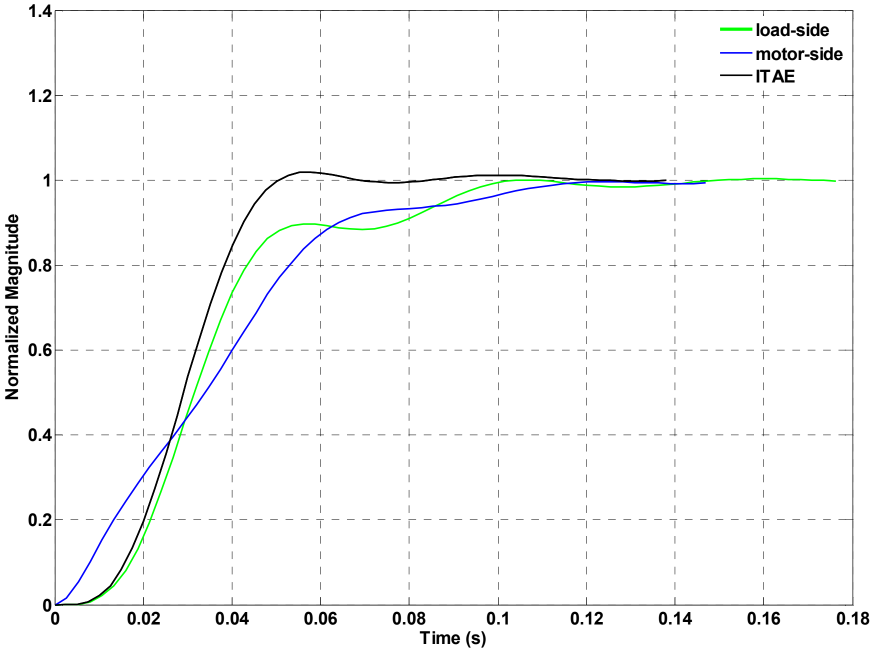

Figure 3.12 Simulated sub-optimal $R \neq 1$ step responses: motor-side, load-side and 4th order ITAE

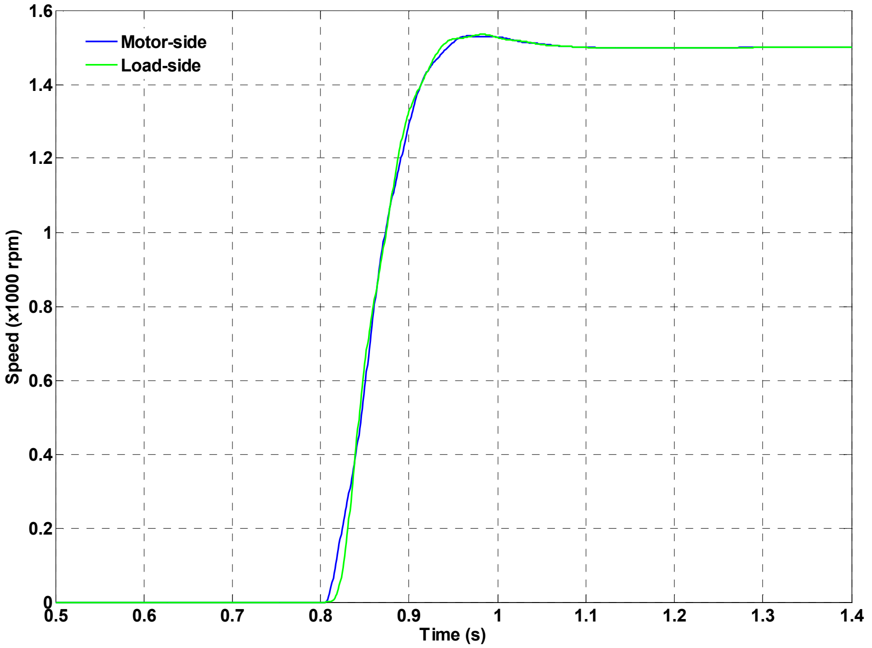

Figure 3.13 Simulated step response for ITAE PI controller

The experimentally measured response, shown in figure 3.14, shows excellent agreement between the measured ITAE optimised controller, and the simulated model.

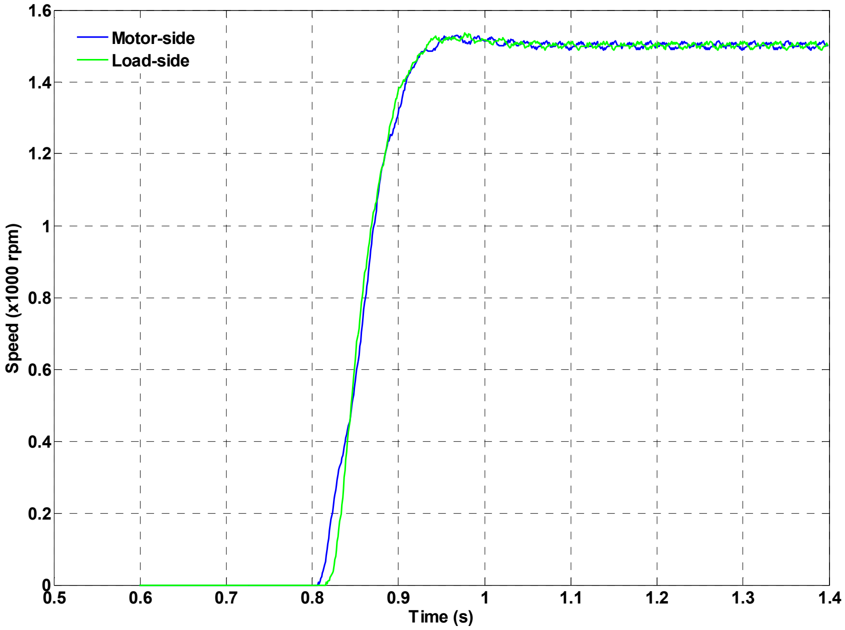

Figure 3.14 Experimentally measured step response for ITAE PI controller

Given the highly compliant nature of the torque transmission inherent in the magnetic coupling, with a maximum torsional stiffness of only 17 N•m / rad, it is of considerable interest to examine the regulation response to a step change in torque demand. A step torque disturbance input of 90% maximum design torque T_G is applied once the drive train is in steady state at $t = 3$ s. Figure 3.15 shows both motor- and load- side dynamics in response to step inputs.

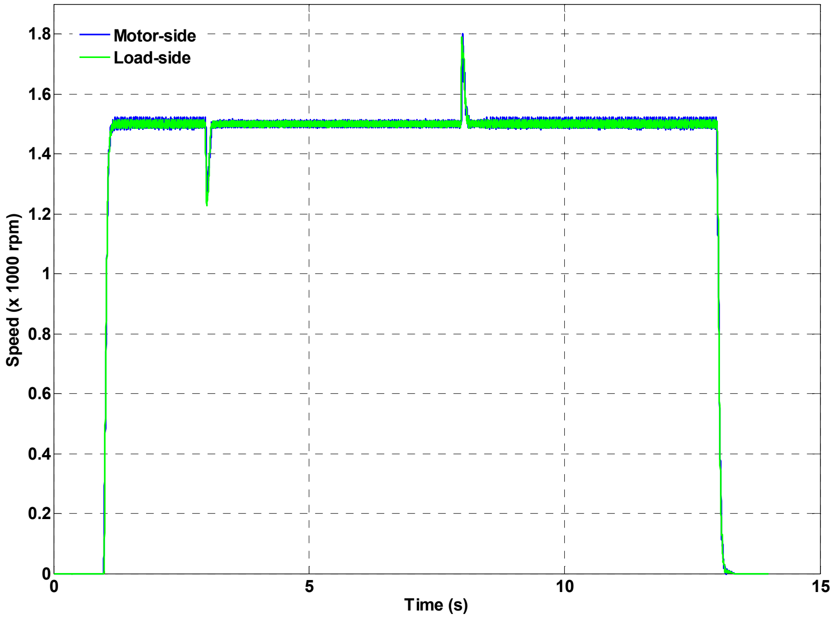

Figure 3.15 Experimentally measured load rejection, 5.1 N•m (90%) load torque at $t = 3$ s

From figure 3.15 it can be seen that, despite the high compliance of the magnetic coupling, excellent load rejection is possible using the optimised PI controller. However, at this magnitude of load disturbance the magnetic coupling is well outside of the range of reasonable approximation to a constant linear torsion spring. For load torques up to ≈ 50% of T_G, system performance can be considered linear if the damping term is not significant. Between 50-100% of T_G the coupling becomes increasingly compliant, resulting in underdamped responses when compared with systems with linear stiffness. However, excellent performance can still be obtained provided the controller is tuned to optimised ITAE calculated gains.

3.7 Over-torque pole-slipping

One of the principal advantages of magnetic gearing technologies is the potential to offer a completely non-destructive torque 'fuse'. Because torque transmission takes place through a magnetic field, with no mechanical contact between motor- and load-side of the gear, a torque load or disturbance that exceeds the capability of the magnetic gear results in 'pole-slipping'. Pole-slipping allows the magnetic gear to slip non-destructively in the event that either the produced motor torque, or the load torque, exceeds the magnetic gear's peak 'pull-out' torque T_G. As shown in Chapter 2, the peak torque capability of the experimental magnetic coupling is 5.7 N•m, and occurs when the mechanical displacement angle approaches 30°.

To investigate the effects of pole-slipping, simulation studies are conducted with a load torque demand that is beyond the maximum capability of the magnetic coupling. The simulation results in figure 3.16 show excess load torque applied at $t \approx 1.75$ s. The magnetic coupling immediately enters a pole-slipping regime and a zero-mean load-side speed is observed. Closer inspection of the motor-side speed signal shows a sinusoidal modulation that is indicative of a pole-slipping condition.

The experimental magnetic coupling is subjected to, (i) a load torque that is greater than the maximum design torque T_G, and (ii) excess control torque resulting from too aggressive control action from the prime-mover. Effectively, this induces pole-slipping from either side of the magnetic coupling. Figures 3.17 and 3.18 show measured results from both scenarios.

For the results in figure 3.17, at $t \approx 2$ s an over-load torque of 6 N•m is applied to the drive train, causing pole-slipping. Whilst the speed controller on the prime-mover attempts to maintain the 1000 rpm demanded, an effective zero-mean load speed is apparent. This represents over-torque pole-slipping due to excess load-side torque. The dual condition is from excessive control action and as indicated in figure 3.18, the initial controller torque is greater than the pull out torque of the coupling and instantaneous pole-slipping occurs.

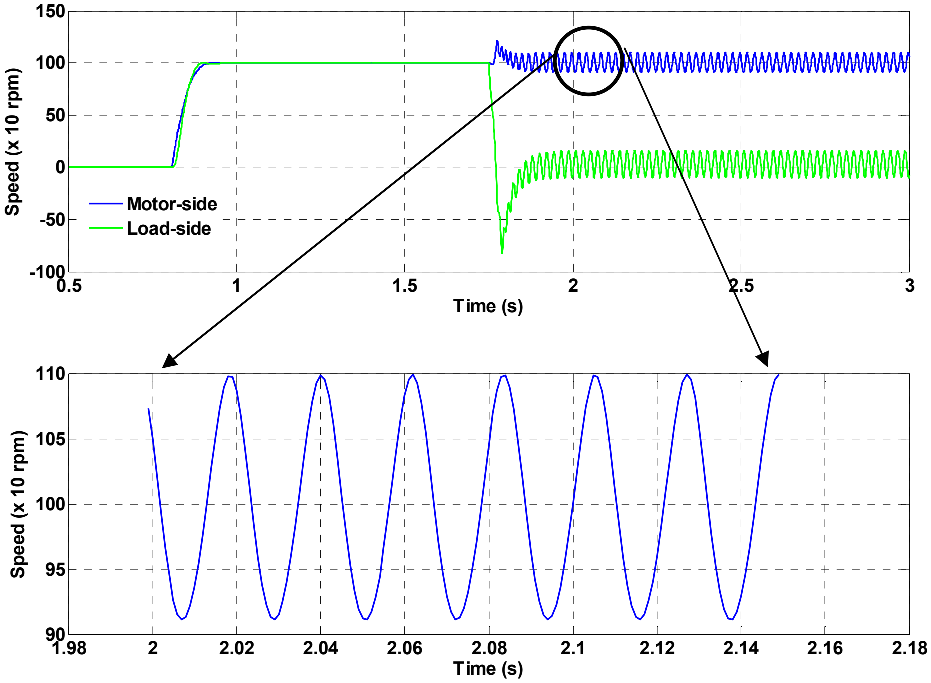

Figure 3.16 Simulated over-torque at $t = 1.75$ s leading to pole-slipping ($T_L = 6$ N•m)

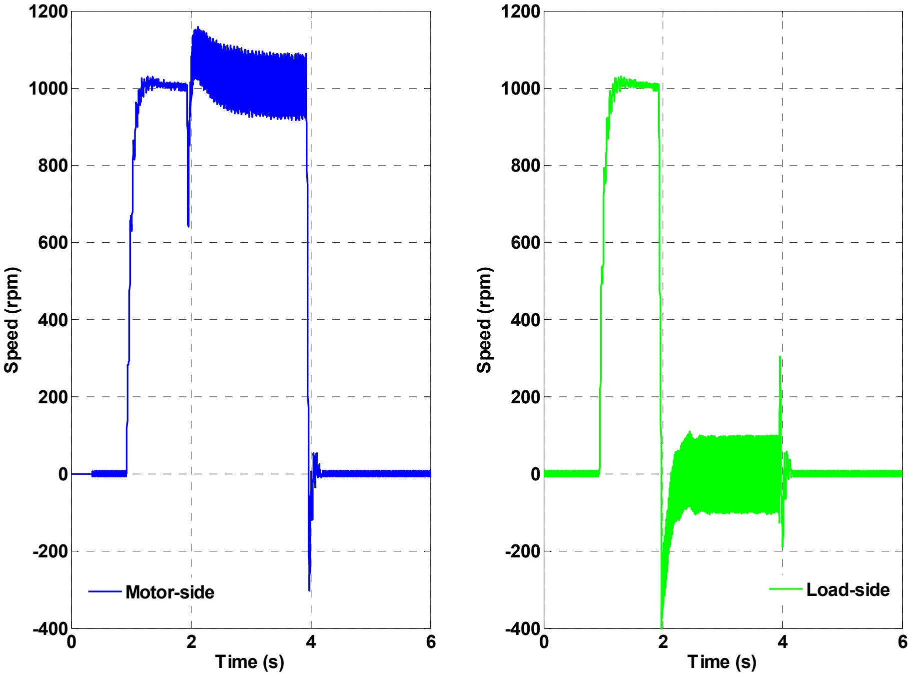

Figure 3.17 Experimentally measured speed response with excess load-side torque $T_L = 6$ N•m at $t \approx 2$ s

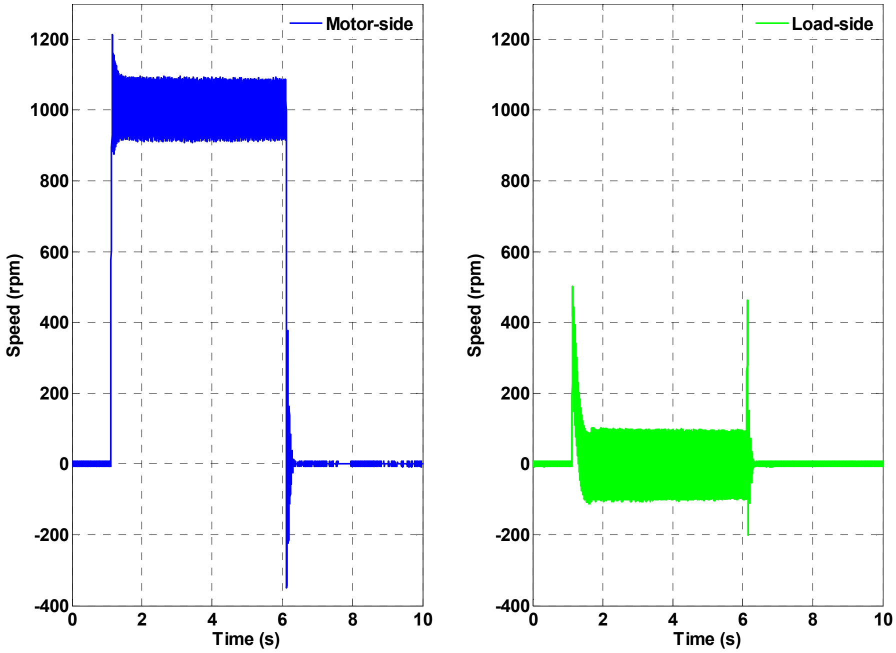

Figure 3.18 Experimentally measured speed response with excess motor-side controller torque leading to instantaneous pole-slipping

From a conventional perspective, the effect of pole-slipping constitutes a loss of control of the drive train. Consequently, it is necessary to provide pole-slip detection and recovery by some means if control is to be regained following a pole-slipping incident. By way of example, simulation and experimental studies have made it apparent that over-torque pole-slipping imposes a modulation onto the speed feedback signal (or error signal). Experimental responses from two example transient step demands, 1000 rpm and 1200 rpm, are shown in figure 3.19. In each case, the modulating sine wave indicates that the magnetic coupling has entered a pole-slipping regime. Further examination of the power spectral density (PSD) of the error signals reveal a clearly identifiable signature (in this instance a single sine wave), characterising the over-torque pole-slipping condition. This is shown clearly in the PSD estimates of figure 3.20.

The presence of a modulating sine wave on the speed feedback signal can therefore be used by the controller to detect magnetic coupling overload conditions. An opportunity then exists for the implementation of remedial action by the controller, allowing the magnetic coupling to be reset to normal power transmission within its operating range

To affect a recovery from pole-slipping, a controller sub-system has been developed that detects pole-slipping on the motor-side of the magnetic coupling. Once detected, it is necessary to attempt to re-engage power transmission through the coupling. The technique shown here undertakes two automatic reconfigurations by the controller.

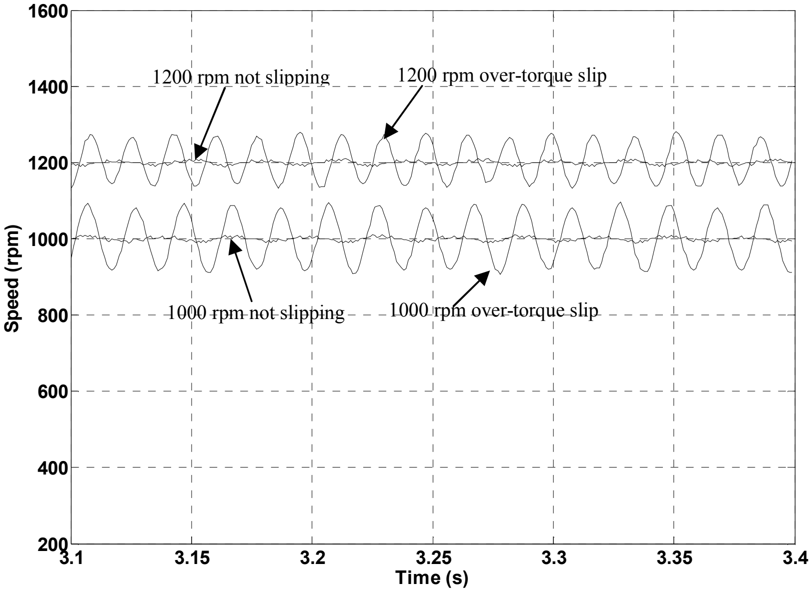

Figure 3.19 Experimentally measured sinusoidal modulation on feedback signal due to over-torque pole-slipping for 1000 rpm and 1200 rpm step demands

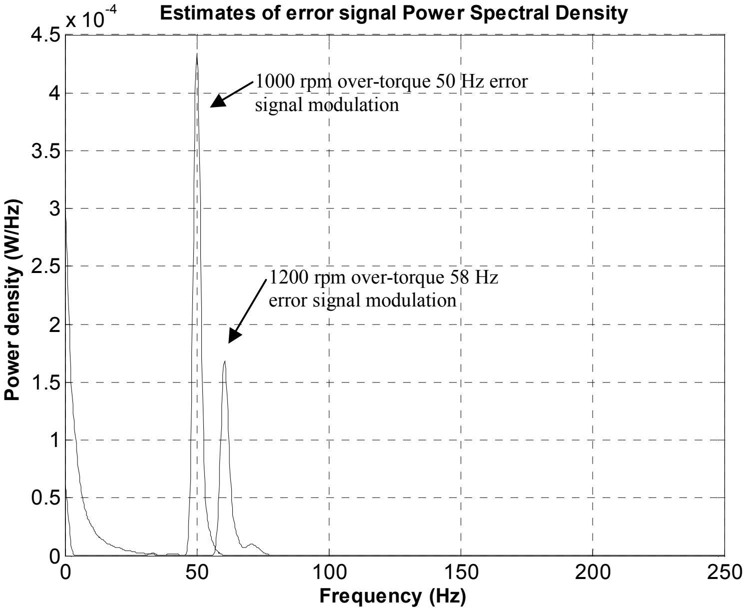

Figure 3.20 Experimentally measured PSD estimates pole-slipping for 1000 rpm & 1200 rpm demands

The first stage is to switch the speed command input to zero prior to attempting to re-engage the load-side of the magnetic coupling. The motor-side speed command input is held at zero for a short duration before being reset to the original speed command input. The second stage is a reconfiguration of the controller just prior to attempting a re-engagement of torque transfer.

Figure 3.21 provides a block diagram of how, upon detection of a pole-slipping signal, both command speed and controller parameters are reconfigured to allow the magnetic coupling to re-establish power transfer between motor- and load-side of the coupling.

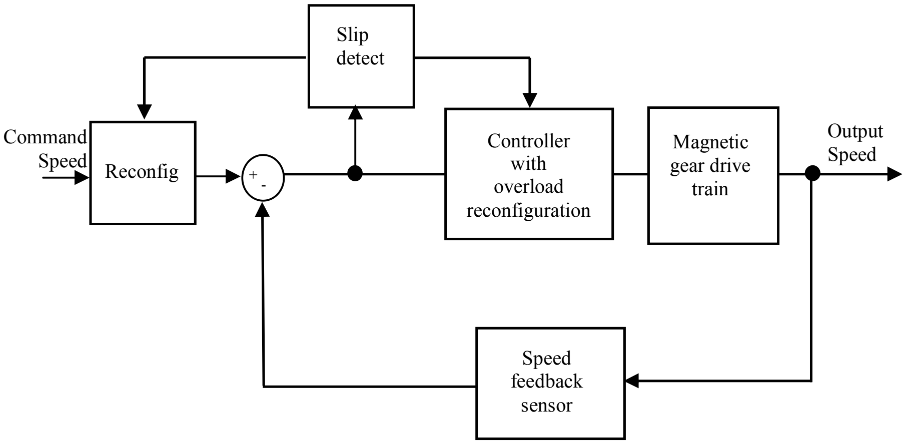

Figure 3.21 Reconfigurable controller to remediate over-torque pole-slipping in magnetic geared drive train

Slip detection is performed by an integrate-dump circuit (figure 3.22) that monitors the motor speed error signal. The threshold setting determines how fast the slip detection responds to a slip condition.

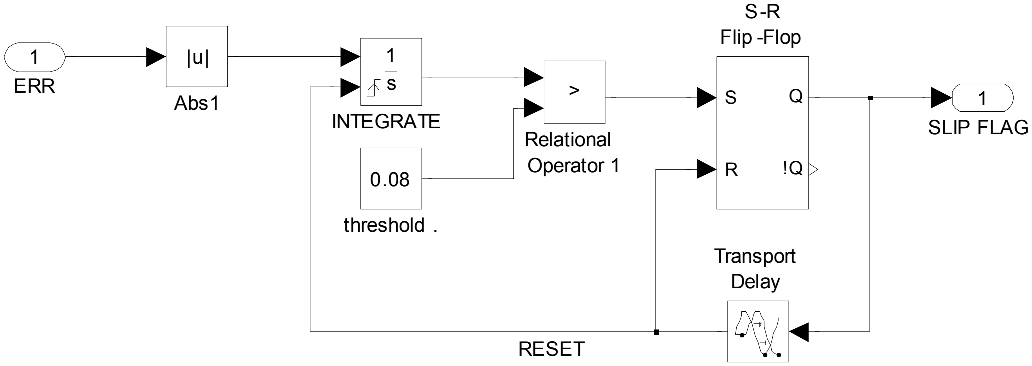

Figure 3.22 Slip detection sub-system

The output of the slip detection sub-system is the ‘slip flag’ which is utilized by two further sub-systems to produce re-configurations of the operating conditions. The command input is ‘run down’, i.e. pulsed low for a short period of time and the ‘slip flag’ causes the controller integral term to be reconfigured, via a flip-flop and an enabled sub-system, to an alternative setting. These two reconfigurable sub-systems are shown in figure 3.23 (a) & (b) respectively.

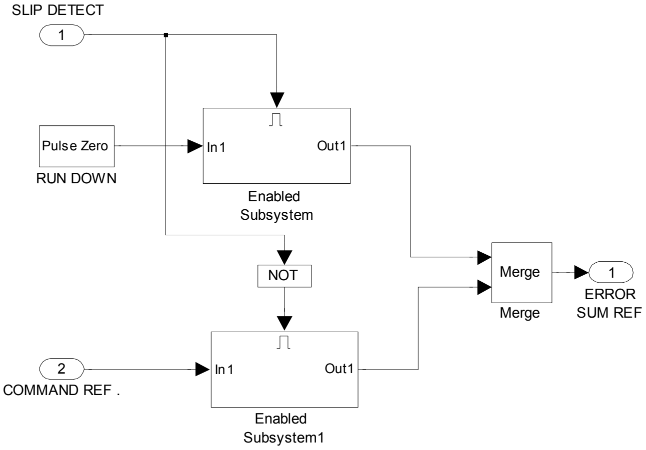

(a)

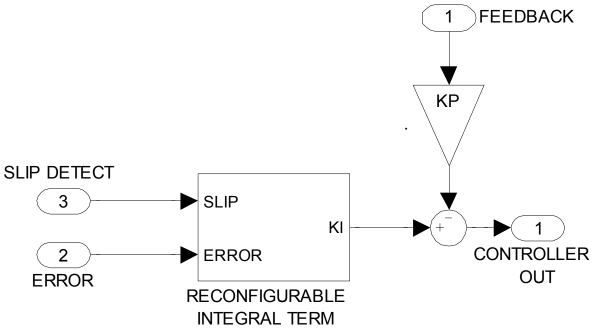

(b)

Figure 3.23 Sub-systems (a) command input reconfiguration (b) controller integral reconfiguration

As a demonstration, figure 3.24 shows a transient torque overload profile that induces pole-slipping at $t \approx 4.5$ s, resulting in a temporary disconnection of the motor- and load-side of the magnetic coupling.

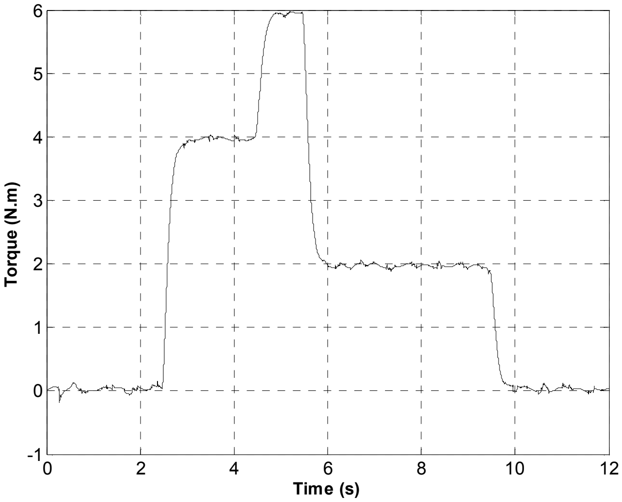

Figure 3.24 Experimental load torque profile to induce pole-slip

The experimentally measured response of the reconfigurable controller with slip detection is shown in figure 3.25, where pole-slip detection and recovery re-engages the magnetic coupling in around 100 ms. For clear illustration the initial controller transient response is deliberately under-damped. However, with a pole-slip condition detected, the controller has its integral term reconfigured (via the sub-system in 3.23 (b)) so as to produce a far less aggressive (over-damped) transient response when attempting to re-engage power transfer through the coupling. This is just an illustrative experimental example of how a controller might be re-configured if deemed necessary, but would ultimately depend on the application-specific context.

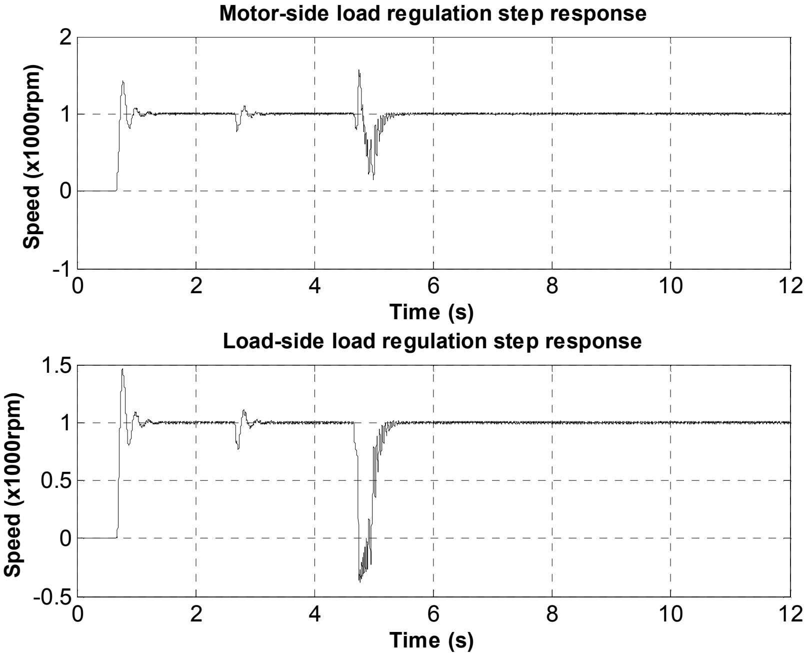

Figure 3.25 Experimentally measured over-torque detection & recovery of magnetic coupling subject to transient torque overload of fig. 3.24

3.8 Under-torque pole-slipping

The experimental responses in figures 3.17 and 3.18 show that when the magnetic coupling is subject to excess torque, that is, greater than the pull out torque, the magnetic coupling will enter a pole-slipping regime and the load becomes effectively disconnected from the motor. In this section a scenario in which it is also possible for the magnetic coupling to begin pole-slipping when the load torque is *below* the coupling's maximum rating is demonstrated. This scenario is termed 'under-torque pole-slipping' and will be demonstrated using specially constructed baseline speed and torque inputs.

Baseline speed and torque inputs are shown in figure 3.26 in which the speed command profile exhibits a transient change. The reference input consists of a step speed demand of 500 rpm, followed by a speed change (doubling) at t = 6 s. A step load torque demand of 75% of maximum torque capability occurs at t = 3 s and extends to t = 8 s. This speed/torque demand profile will be used to investigate under-torque pole-slipping. In this case the magnetic coupling experiences a speed change command whilst under a constant load torque. This means that the motor-side and load-side of the magnetic coupling are subject to a mechanical displacement angle which is a function of the applied load torque.

Experimental results for this scenario are shown in figure 3.27, where it can be seen that the magnetic coupling is able to transfer the 75% load torque at t = 3 s. However, at t = 6 s a doubling of the command speed to 1000 rpm produces sufficient additional controller-derived torque to make the magnetic coupling begin pole-slipping. Notably, the load torque is *substantially below* the magnetic coupling's maximum capability, but the combined load torque plus required controller torque for the speed change has exceeded the maximum pull out torque T_G.

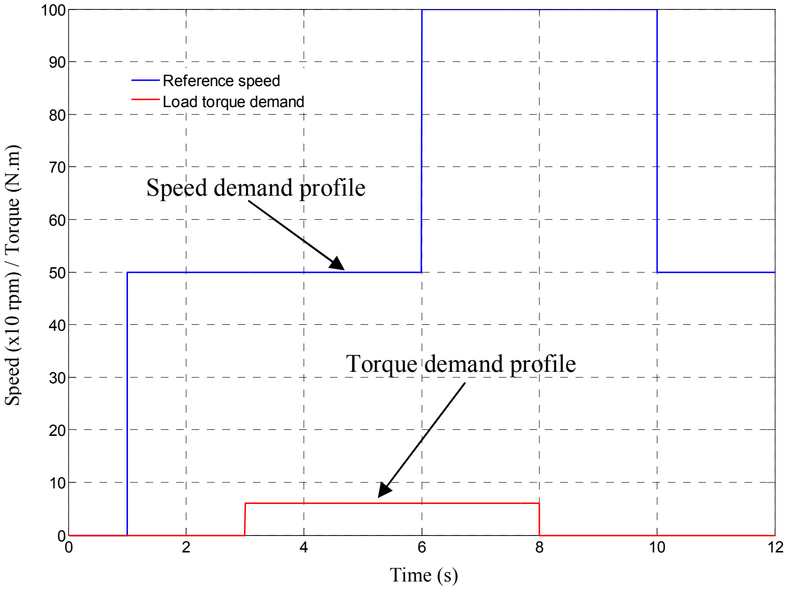

Figure 3.26 Reference speed and torque profiles

The ability to induce pole-slipping, despite being well within load torque capability, is a substantial impediment to successful control of the torque transfer between motor- and load-side of the magnetic coupling. As is clear from figure 3.27, at t = 6 s, the load has become effectively disconnected from the motor. This results from the fact that the controller does not take into consideration the instantaneously transmitted load torque, and what is required is a controller that can apply constraints to the overall *combined* controller-demanded torque and load torque. This is considered further in Chapter 6 through the application of model predictive control.

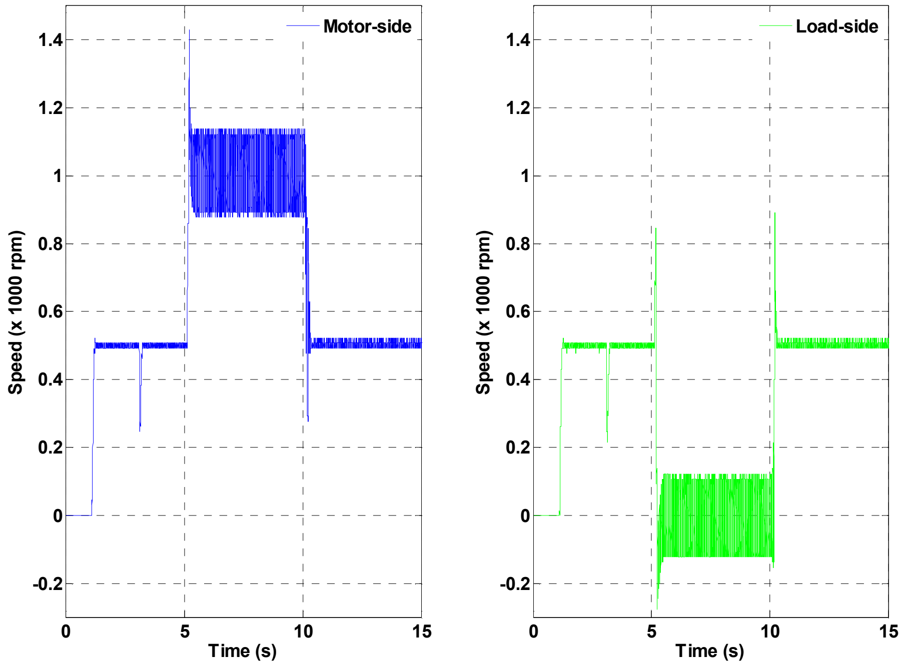

Figure 3.27 Experimentally measured speed response with under-torque pole-slipping with load torque $T_L =$ 4.2 N•m (75%)

3.9 Summary

The conditions for ITAE optimized PI speed control of the magnetic coupling have been derived. Simulated and experimental results exhibit excellent agreement for step input transient speed commands. Furthermore, the implemented controller demonstrates outstanding load torque rejection capability. The phenomenon of pole-slipping in a magnetic gear is introduced and investigated in the context of (i) over-torque induced pole-slip and, (ii) under-torque pole-slip, demonstrating the ability of a magnetic gear to function as a non-destructive torque fuse. A technique for the automatic detection and recovery from pole-slipping is presented, based on the detection of a pole-slip 'signature'. Detection of a pole-slip signature is utilized by a reconfigurable controller that attempts to re-engage a disconnected gear.

Chapter 4

Conventional Position Control of a Flexible Joint

4.1 Introduction

Consideration is now given to the effects of the magnetic coupling when incorporated into a servo *position* controlled drive train. In essence, the problem is similar to that of a flexible link robot joint. For example, manipulators using harmonic drives for torque transmission result in significant joint flexibility [56]. An idealized model of a single-link robot joint is given in figure 4.1, consisting of two inertias interconnected by a torsional spring.

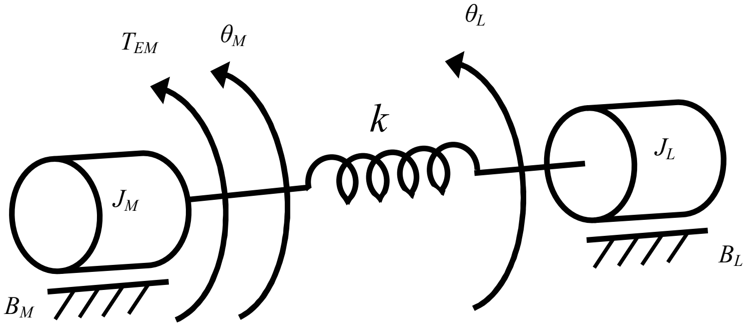

Figure 4.1 Idealized model of single-link robot joint with flexibility

This model is identical to that of figure 2.1, with the exception that the torsional spring k is nonlinear. However, as in the previous chapter a linearized model of the magnetic coupling is utilized and both motor-side (B_M) and load-side (B_L) friction coefficients are set to zero. It should be noted that it is usually extremely difficult to obtain an accurate friction *model*, let alone determine accurate parameter values [57].

Initially, the optimum ITAE rate feedback PD controller is derived for a step position command and, subsequently, load disturbance rejection for position control of the load-side (link) angle is investigated. While a conventional method for position control of industrial servo drives may rely on a cascade control structure, an alternative technique is the use of a two-term PD controller. The use of a multi-loop controller, with the requirement to set 3, 4 or 5 parameters is considered to be unnecessary for the context under investigation. For high-speed, high-precision servo position control, as typified by multi-axis robot joints, PD control offers superior performance [56]. Furthermore, as will be discussed in Chapter 6, for servo position control of the load-side of the magnetic coupling, with only motor-side measurements, there is an inherent requirement for state estimation of the load-side variables. Given the introduction of an observer to measure load-side states, it then becomes practicable to incorporate a load-torque estimator to compensate for the inherent steady-state position errors observed with PD control under a constant load-torque disturbance (see Chapter 7). In addition, the introduction of integral action leads to substantially degraded transient performance with increased overshoot, settling and rise times. Finally, as will be demonstrated, there are no noise issues within the experimental set-up that may, otherwise, require derivative action to be at best heavily filtered, or at worst, completely discounted. As in the speed control case, the effect of magnetic coupling pole-slip for a servo position control system is also investigated.

4.2 Open-loop analysis

For position control, it is assumed in the first instance that both motor-side and load-side friction (B_M and B_L) are negligible and the nonlinear magnetic coupling torque transfer can be replaced by a linearized torsional spring constant, K_{lin}. A block diagram of a single-link flexible joint for position control is shown in figure 4.2.

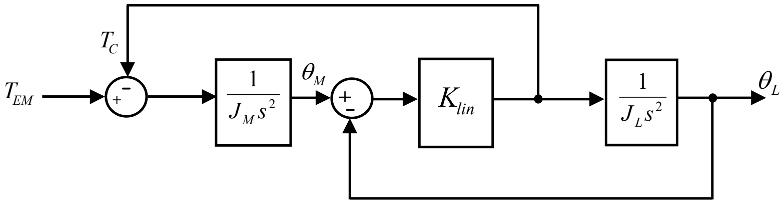

Figure 4.2 Single link flexible joint block diagram

Following the analysis presented in Chapter 3, for the derivation of motor-side and load-side angular velocities, the open loop transfer function from input torque T_{EM} to load angle is given by,

$$\frac{\theta_L(s)}{T_{EM}(s)} = \frac{\omega_a{}^2}{J_M s^4 + J_M \omega_n^2 s^2} \tag{4.1}$$

Similary, the open loop transfer function from input torque T_{EM} to motor angle is,

$$\frac{\theta_M(s)}{T_{EM}(s)} = \frac{s^2 + \omega_a^2}{J_M s^4 + J_M \omega_n^2 s^2} \tag{4.2}$$

where (4.1) and (4.2) are obtained from (1/s)*(3.9) and (1/s)*(3.11) respectively.

4.3 Closed-loop control using rate feedback PD controller

Figure 4.3 shows the block diagram of a rate feedback PD control loop from which closed-loop transfer functions of interest can be derived [41]. Of particular interest are those transfer functions from reference position to motor position and reference position to load position, i.e. set-point position tracking dynamics on either side of the magnetic coupling, respectively.

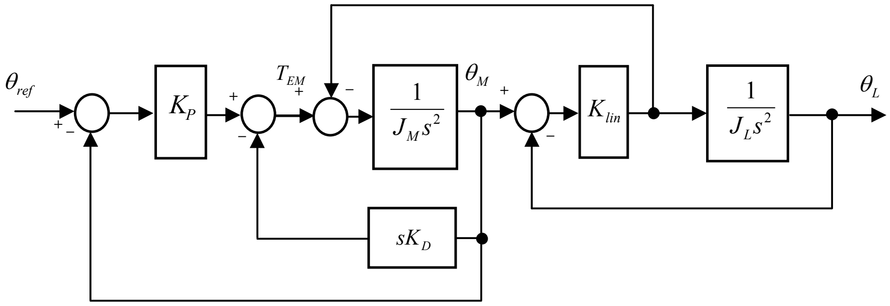

Figure 4.3 Rate feedback PD control of flexible joint

The closed loop transfer function from reference angle to load angle, that is, $\frac{\theta_L(s)}{\theta_{ref}(s)}$, can be determined from Mason's Rule, following the analysis presented in Chapter 3. The closed-loop transfer function from reference angle to load angle is then,

$$\frac{\theta_L(s)}{\theta_{ref}(s)} = \frac{K_P\omega_a{}^2}{J_M s^4 + K_D s^3 + \left(J_M \omega_a^2(1+R) + K_P\right)s^2 + K_D\omega_a{}^2 s + K_P\omega_a{}^2} \tag{4.3}$$

The closed-loop transfer function from reference angle to motor angle is determined similarly as,

$$\frac{\theta_M(s)}{\theta_{ref}(s)} = \frac{K_P(s^2 + \omega_a{}^2)}{J_M s^4 + K_D s^3 + (J_M \omega_a{}^2(1+R) + K_P)s^2 + K_D\omega_a{}^2 s + K_P\omega_a{}^2} \tag{4.4}$$

4.3.1 Controller parameter selection

Selection of the rate feedback PD gains, K_D and K_P determine the closed-loop tracking performance of the drive train incorporating the magnetic coupling. A number of possible techniques are available for the selection of rate feedback PD controller gains depending on the desired objective.

The method investigated here extends the results of O'Sullivan & Bingham [41] to the case of position control. In [41] the most suitable performance metric is considered to be the integral of time multiplied by absolute error (ITAE) for a step reference input. The principal objective is to provide optimum set-point position tracking dynamics on the load-side of the magnetic coupling, and as shown in (4.3), the closed-loop transfer function is defined by a fourth order polynomial with no closed-loop zeros. Consequently, it is possible to equate the denominator of (4.3) with the optimized ITAE polynomial for a step response given in (3.25)

Equating coefficients and solving for K_D and K_P (as with PI speed controller in Chapter 3, section 3.4), the optimum controller gains are given by,

$$K_P = 0.6K_{lin} \qquad K_D = 1.85 J_L \omega_a \tag{4.5}$$

4.3.2 Simulation of ITAE optimized rate feedback PD set-point position controller

The simulated step responses of figure 4.4 show motor- and load-side responses plus the theoretical response of the ITAE 4^{th} order polynomial for an optimum step. It can be seen that the load-side step response is identical to the required fourth order optimum ITAE response.

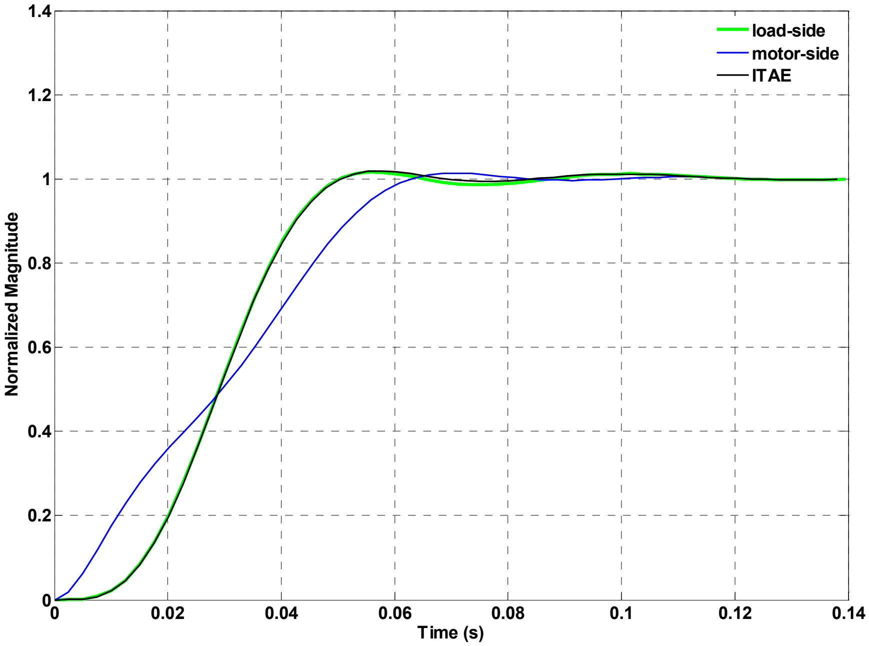

Figure 4.4 Simulated optimum ITAE normalized position step responses

The results obtained for the ITAE optimized rate feedback PD position controller are, of course, identical to those derived in Chapter 3 for the optimized ITAE PI speed controller, under condition of no load-side disturbance torque. However, the performance of the ITAE optimized PI and PD controllers diverge when subjected to a constant load-side disturbance torque. This is investigated further in section 4.4.

4.3.3 Experimental results for optimized rate feedback PD set-point position controller

The optimum (in the ITAE sense) set-point position tracking controller derived in Section 4.3.1 is now verified on the experimental test rig and the dSPACE hardware development platform. Figure 4.5 shows the simulated set-point position tracking response of both the motor-side and load-side of the magnetic coupling for $\theta_{ref} = 3$ rad step reference position command. The rate feedback PD controller has gains optimally tuned to a fourth-order ITAE model, as determined by (4.5).

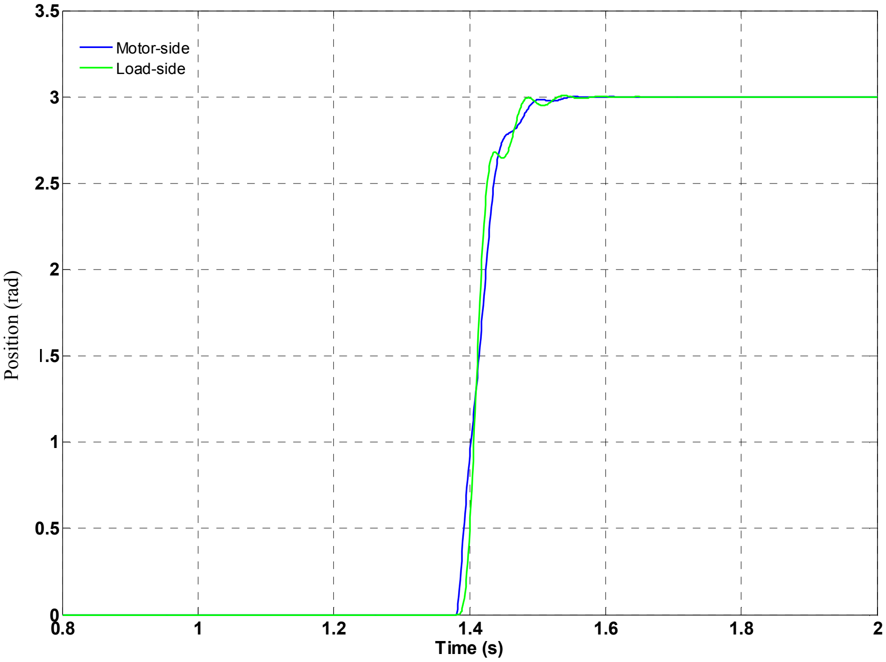

Figure 4.5 Simulated step response for ITAE optimum PD controller $\theta_{ref} = 3$ rad

The experimentally measured response, shown in figure 4.6, indicates a good agreement between the measured ITAE optimised controller and the theoretically simulated model.

4.4 Disturbance rejection

In section 4.3 the optimum ITAE rate feedback PD controller for servo position control of a drive train incorporating the magnetic coupling is derived. This section examines the performance of the ITAE rate feedback PD controller when subjected to a load-side disturbance torque. Figure 4.7 shows the simulated step response with no disturbance indicating perfect motor-side and load-side position tracking. With a small command position of $\theta_{ref} = 1$ rad, the magnetic coupling behaves in an entirely linear manner as the controller torque remains well within the linear range of the magnetic coupling's transfer characteristic.

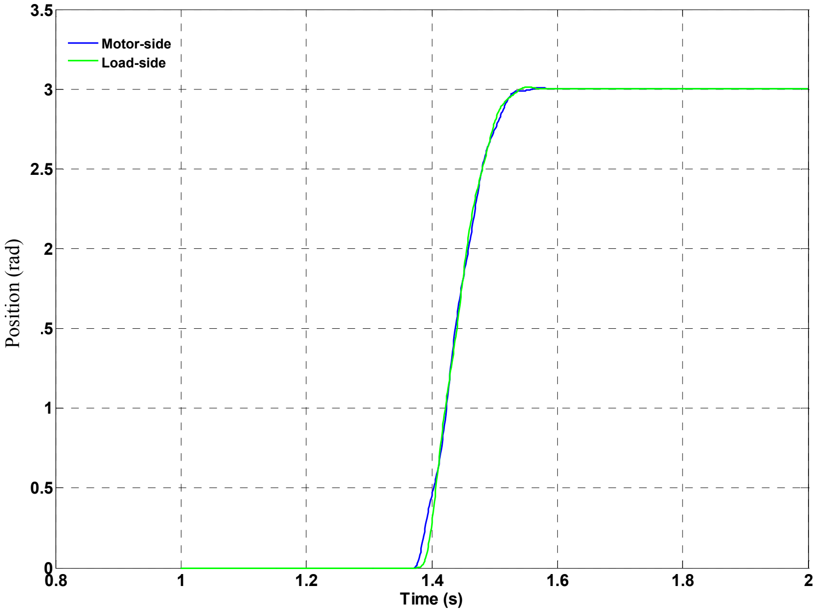

Figure 4.6 Experimentally measured step response for optimum ITAE PD controller θ_{ref} = 3 rad

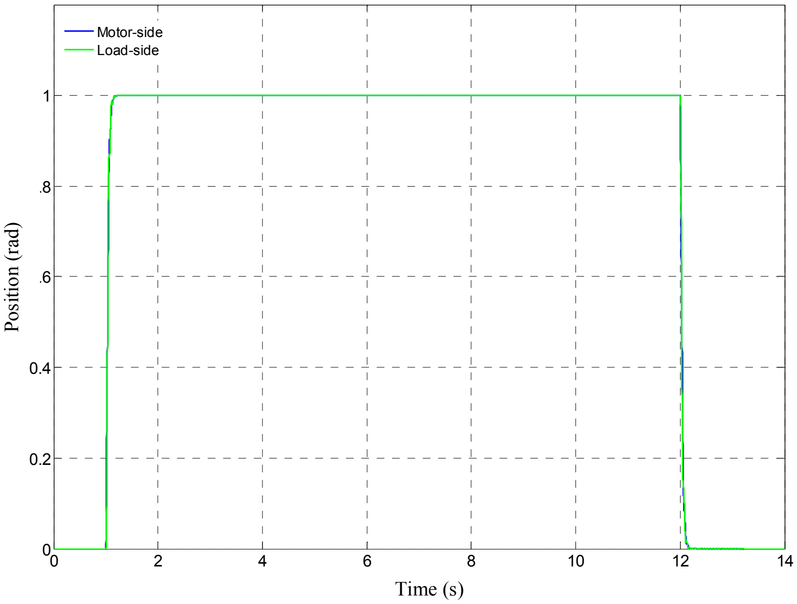

Figure 4.7 Simulated step response for ITAE rate feedback PD controller θ_{ref} = 1 rad

However, an increase in the command position to θ_{ref} = 4 rad excites the nonlinear portion of the torque transfer characteristic, resulting in small position overshoot transients as shown in figure 4.8.

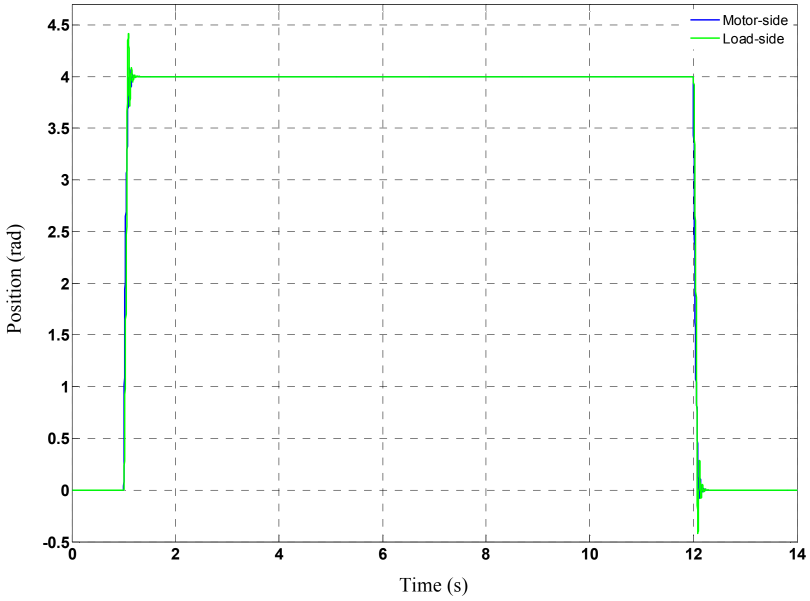

Figure 4.8 Simulated step response for ITAE rate feedback PD controller θ_{ref} = 4 rad

To investigate disturbance rejection properties, a load-side torque of approximately 50% rated torque (≈ 3 N•m) is applied at t = 4 s, and as shown in figure 4.9, both motor-side and load-side of the magnetic coupling have significant steady-state position errors.

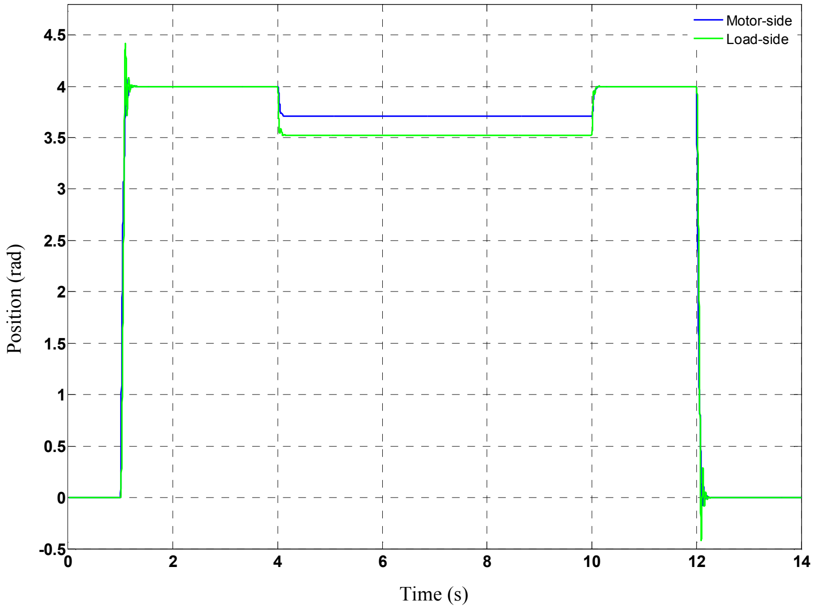

Figure 4.9 Simulated step response for ITAE PD controller with
T_L = 3 N•m (≈50%) load disturbance torque

The signal flow graph of the rate feedback PD controlled magnetic coupling with load-side torque disturbance is shown in figure 4.10, from which the transfer function between load position and disturbance torque can be determined.

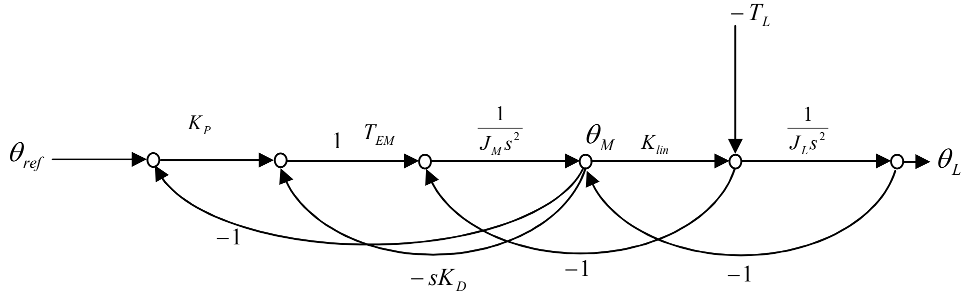

Figure 4.10 Signal flow graph of PD control of flexible joint with load-side disturbance

The transfer function from disturbance torque, T_L, to load position, $\frac{\theta_L(s)}{T_L(s)}$, can be determined from Mason's Rule as follows.

Forward path transmittance from load torque to load position is

$$P_K = -\frac{1}{J_L s^2} \tag{4.6}$$

and loops gains from left to right are given by,

$$L_1 = \frac{-K_P}{J_M s^2} \qquad L_2 = \frac{-K_D}{J_M s} \qquad L_3 = \frac{-K_{lin}}{J_M s^2} \qquad L_4 = \frac{-K_{lin}}{J_L s^2} \tag{4.7}$$

In this case loops L_1, L_2 and L_4 are non-touching and the signal flow graph determinant is,

$$\begin{aligned} \Delta &= 1-(L_1+L_2+L_3+L_4)+L_1L_4+L_2L_4 \\ \Delta &= 1+\frac{K_P}{J_M s^2}+\frac{K_D}{J_M s}+\frac{K_{lin}}{J_M s^2}+\frac{K_{lin}}{J_L s^2}+\frac{K_P K_{lin}}{J_M J_L s^4}+\frac{K_D K_{lin}}{J_M J_L s^3} \end{aligned} \tag{4.8}$$

and as only L_4 touches the forward path the cofactor becomes,

$$\Delta_K = 1+\frac{K_P}{J_L s^2}+\frac{K_D}{J_M s}+\frac{K_{lin}}{J_M s^2} \tag{4.9}$$

Hence,

$$\frac{\theta_L(s)}{T_L(s)} = \frac{\sum P_K \Delta_K}{\Delta} \tag{4.10}$$

$$\frac{\theta_L(s)}{T_L(s)} = \frac{P_K \Delta_K}{\Delta} = \frac{\left(\frac{-1}{J_L s^2}\right)\left(1 + \frac{K_P}{J_L s^2} + \frac{K_D}{J_M s} + \frac{K_{lin}}{J_M s^2}\right)}{1 + \frac{K_P}{J_M s^2} + \frac{K_D}{J_M s} + \frac{K_{lin}}{J_M s^2} + \frac{K_{lin}}{J_L s^2} + \frac{K_P K_{lin}}{J_M J_L s^4} + \frac{K_D K_{lin}}{J_M J_L s^3}}$$

$$\frac{\theta_L(s)}{T_L(s)} = \frac{\frac{-1}{J_L}\left(J_M s^4 + K_D s + \left(K_{lin} + K_p\right)\right)}{J_M s^4 + K_D s^3 + \left(J_M \omega_a^2 (1+R)\right)s^2 + K_D {\omega_a}^2 s + K_P \omega_a^2} \tag{4.11}$$

Applying the final value theorem and assuming the load-side disturbance is of Heaviside form then,

$$\left.\frac{\theta_L(s)}{T_L(s)}\right|_{s \to 0} = \frac{\frac{-1}{J_L}\left(K_{lin} + K_p\right)}{K_P \omega_a^2} T_L^* = \frac{-\left(K_{lin} + K_p\right)}{K_P K_{lin}} T_L^* \neq 0 \tag{4.12}$$

showing that the disturbance torque produces a steady-state position error, where T^*_L is the magnitude of the disturbance torque input. With a reference position of 0 rad, under optimized ITAE rate feedback PD control, and with a disturbance torque of 1 N•m, the steady-state position error is then,

$$\left.\frac{\theta_L(s)}{T_L(s)}\right|_{s \to 0} = \frac{-\left(17.1 + 10.26\right)}{10.26 * 17.1} = -0.156 rads \neq 0 \tag{4.13}$$

Figure 4.11 shows a simulation of this scenario indicating agreement between simulated and theoretically calculated steady-state error. For both motor-side and load-side of the magnetic coupling, significant steady-state position errors are obtained.

4.4.1 Experimental results for disturbance rejection of PD set-point position controller

The disturbance rejection capability of the rate feedback PD set-point position tracking controller is now verified on the experimental test rig and the dSPACE hardware development platform. Figure 4.14 shows the experimentally measured set-point position tracking response of both the motor-side and load-side of the magnetic coupling for θ_{ref} = 3 rad step reference position command, when subjected to a 50% load-side disturbance torque. Both motor-side and load-side of the magnetic coupling have significant steady-state positional errors due to the application of a constant load-side disturbance torque at $t \approx 7$ s.

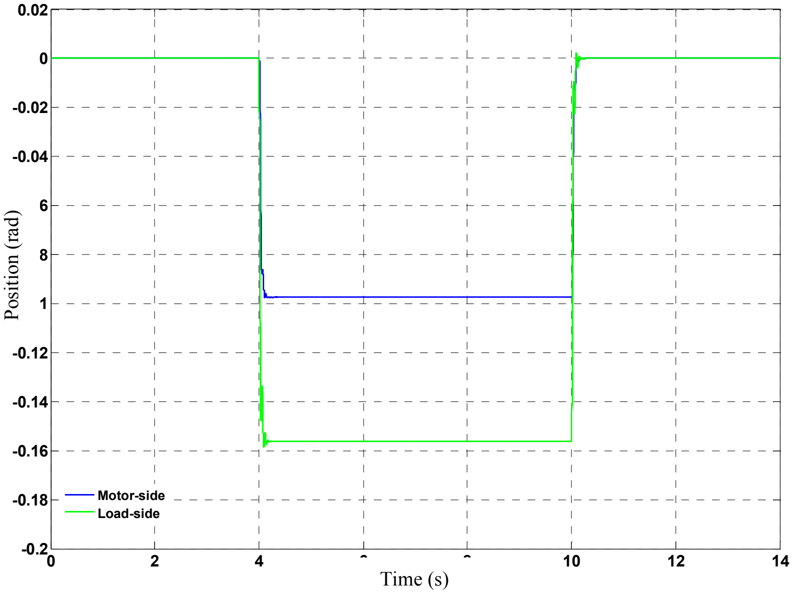

Figure 4.11 Simulated steady-state position $\theta_{ref} = 0$ rad
with position errors due to $T_L = 3$ N•m (≈50%) load-side disturbance torque

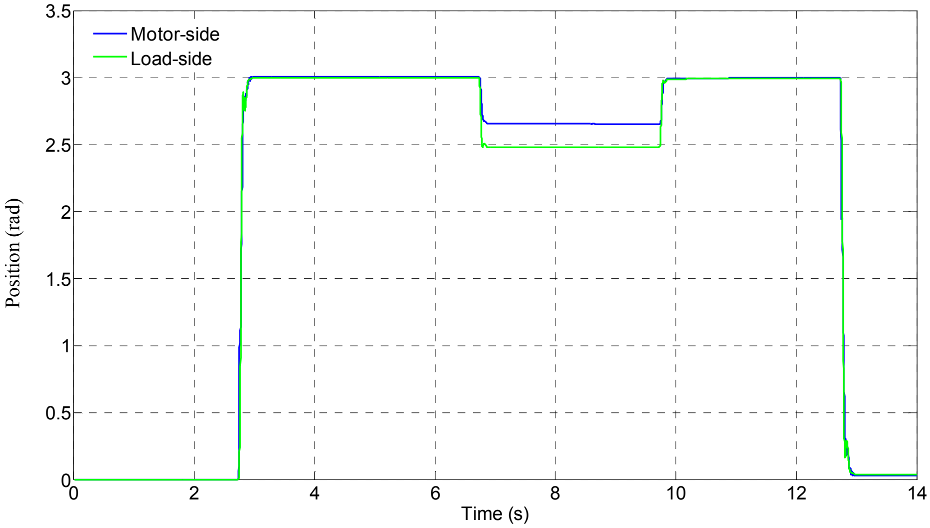

Figure 4.12 Experimentally measured steady-state position $\theta_{ref} = 3$ rad
with position errors due to $T_L = 3$ N•m (≈50%) load-side disturbance torque

In the simulation and experimental scenarios presented above, figure 4.11 and figure 4.12, the assumption made is that load-side disturbances can be represented by a Heaviside step-like response. Two possibilities for improving the disturbance rejection properties of the drive train are, (i) introduction of integral action in the form of PID control, or (ii) feedforward corrective action to eliminate steady-state position errors. With the assumption that the load torque disturbance can be estimated, the latter of the two possibilities is investigated in more detail in Chapter 7. In the event that the load torque is unpredictable, or that its estimation is of poor quality, it is then compulsory to incorporate integral action to remove steady-state disturbance position errors [57].

4.5 Pole-slip in a position controlled servo system

Chapter 3 demonstrated that pole-slipping can be caused by excessive motor-side controller action on a speed controlled system. In the speed control case induced pole-slipping results in an immediate loss of control of the drive train. In this section the effect of excessive controller torque on the performance of a position controlled system is investigated.

For a step-like position command, both motor-side and load-side of the magnetic coupling can be positioned precisely, provided the initial instantaneous controller torque does not exceed the coupling's maximum rating, T_G. In the following sections it is shown, via simulation and experimentation, how controller-induced pole-slip affects the magnetic coupling when incorporated into a position control servo system.

Pole-slip in a servo position controlled system can be induced on the motor-side of the magnetic coupling by increasing the position command step magnitude. For a command step of θ_{ref} = 1 rad the simulated outputs are shown in figure 4.13 and figure 4.14.

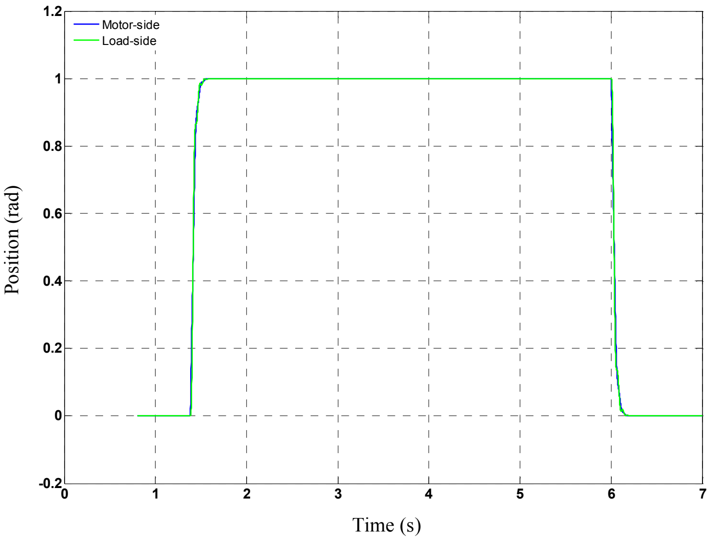

Figure 4.13 Simulated position step θ_{ref} = 1 rad with ITAE PD controller (no load)

With a small step command the magnetic coupling behaves in an entirely linear manner and no difficulties arise, with both motor-side and load-side positions showing perfect co-location (under no load conditions). If the torque transmitted through the magnetic coupling is examined, figure 4.14, the torsional torque is well below the maximum rated capability, T_G

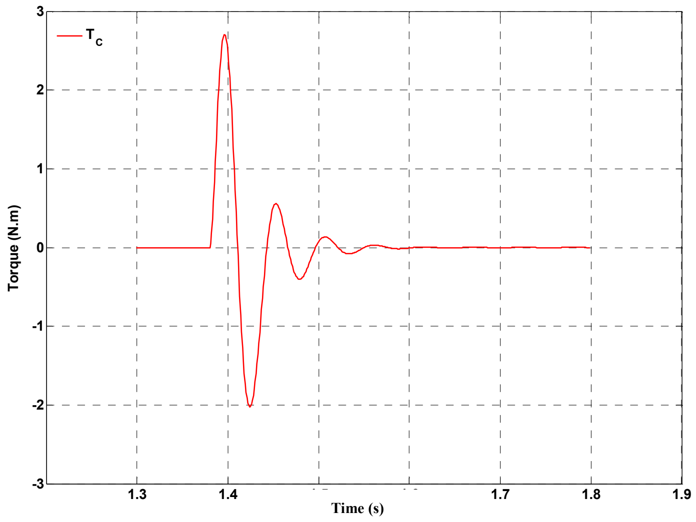

Figure 4.14 Simulated magnetic coupling torque with position step θ_{ref} = 1 rad for ITAE PD controller

By increasing the position step command to (arbitrarily) θ_{ref} = 9 rad, figure 4.15, the magnetic coupling has entered a pole-slip regime due to excessive initial controller torque. The consequence of pole-slipping in the position controlled system is that the load-side has reached a steady-state position, in this case, of just under θ_L = 5 rad. Meanwhile, the motor-side position is precisely as commanded, θ_M = 9 rad.

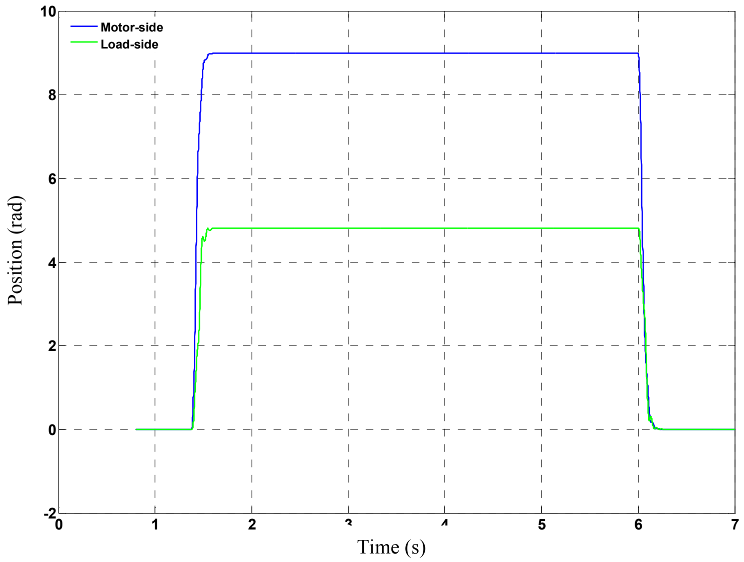

Figure 4.15 Simulated position step θ_{ref} = 9 rad with ITAE rate PD controller leading to pole-slip

Clearly, from figure 4.15 the load-side position is not tracking due to the magnetic coupling having entered a *pole-slip regime*. This can be further confirmed by examining the coupling torque, T_C. Figure 4.16 shows the defining signature of a pole-slip condition, an oscillatory torque response between the limits $\pm T_G$, induced by excessive controller-demanded torque.

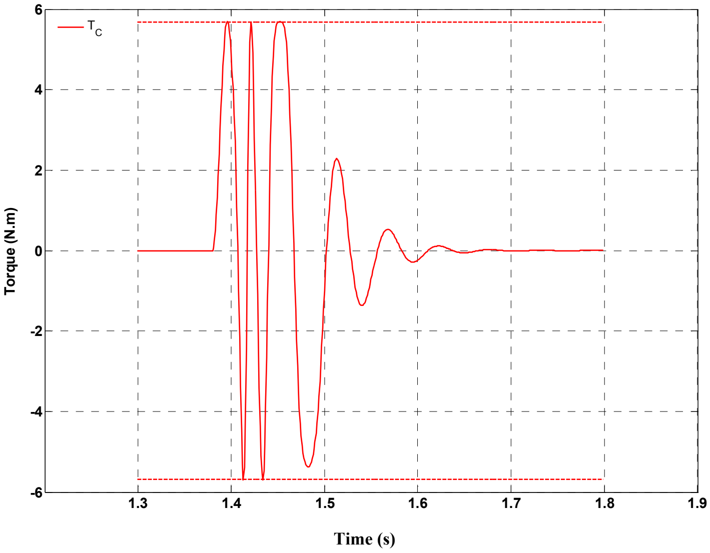

Figure 4.16 Simulated coupling torque T_C position step θ_{ref} = 9 rad with ITAE rate PD controller

4.5.1 Experimental results: servo position pole-slip

For the simulated command position step of θ_{ref} = 9 rad given in section 4.5, the experimental results of figure 4.17 demonstrate identical behaviour. The load-side position settles at just under θ_L = 5 rad as a result of excess controller-demanded torque inducing pole-slipping.

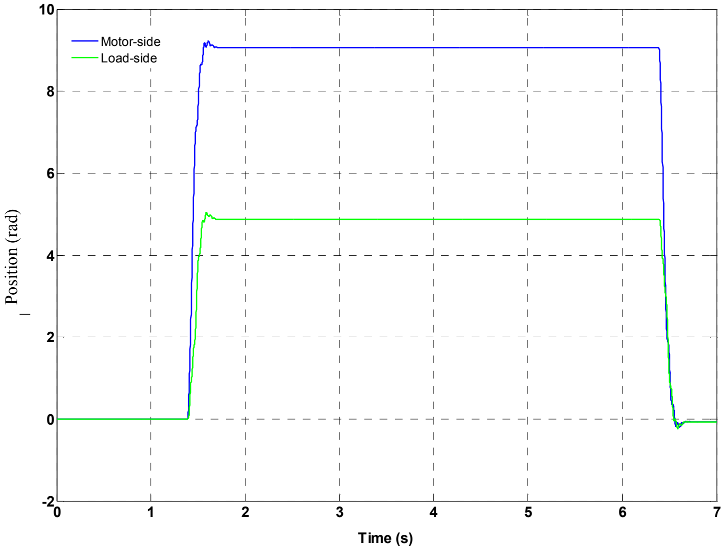

Figure 4.17 Experimentally measured position step response ITAE PD controller θ_{ref} = 9 rad (no load)

From the results of figure 4.17 it is clear that the ITAE PD controller can readily demand sufficient controller torque to force the magnetic coupling to pole-slip. As in the speed control case, there is therefore a requirement for controller action to take into account the maximum permissible torque, that is to say, it must observe the relevant *constraint*. However, unlike the speed control case, the position pole-slip phenomenon does not result in a loss of *control*, it results only in a steady-state position error between the motor- and load-sides of the magnetic coupling.

4.6 Summary

The conditions for ITAE optimized PD position control of the magnetic coupling have been derived. Simulated and experimental results exhibit excellent agreement for step input transient position commands. However, the implemented controller provides no load torque rejection capability. Pole-slipping in a position controlled servo system is investigated in the context of excess motor-side controller torque. Excess controller torque results in steady-state positional errors but does not result in a loss of control.

Chapter 5

Linearization and Nonlinear Effects: Further Considerations

5.1 Introduction

It might be argued that every dynamical system is nonlinear. All signals and systems must have defined limits beyond which some form of saturation (or breakdown) occurs, causing behaviour to become effectively nonlinear. Nonlinearities also occur quite naturally in electrical and mechanical systems. Electrical machines and transformers contain components with highly nonlinear magnetization curves; mechanical systems incorporate gear boxes with backlash and highly nonlinear friction forces [58].

In this chapter, the theoretically derived nonlinear model of the magnetic coupling is examined. The qualitative behaviour of the nonlinear model is investigated using phase portraits for two theoretical cases, (i) a nonlinear model without damping, and (ii) a nonlinear model with damping. It is then subsequently argued that, under certain conditions, the magnetic coupling is sufficiently weakly nonlinear to justify linearization. With a linearized model all the vast array of linear systems tools can be brought to bear on the analysis and design of controllers to satisfy specific criteria to be set down.

5.2 Nonlinearity of magnetic coupling

The underlying theoretical nonlinear dynamics of the magnetic coupling, including the damping term, are described by,

$$\begin{aligned} J_M \frac{d\omega_M}{dt} &= T_{EM} - K(\theta_D) - B(\omega_D) \\ J_L \frac{d\omega_L}{dt} &= K(\theta_D) + B(\omega_D) - T_L \end{aligned} \tag{5.1}$$

where,

$$K(\theta_D) = T_G \sin(p\theta_D) \tag{5.2}$$

$$B(\omega_D) = \alpha T_G \frac{2\beta\omega_D}{{\omega_D}^2 + \beta^2} \tag{5.3}$$

$$\theta_D = \theta_M - \theta_L \tag{5.4}$$

$$\omega_D = \omega_M - \omega_L \tag{5.5}$$

Substituting for the nonlinear torque transfer and nonlinear damping function, from (5.2) and (5.3) respectively, gives,

$$\begin{aligned}\dot{\omega}_M &= \frac{T_{EM}}{J_M} - \frac{T_G}{J_M}\sin(p\theta_D) - \frac{2T_G\alpha\beta}{J_M}.\frac{\omega_D}{\omega_D^{\;2}+\beta^2} \\ \dot{\omega}_L &= \frac{T_G}{J_L}\sin(p\theta_D) + \frac{2T_G\alpha\beta}{J_L}.\frac{\omega_D}{\omega_D^{\;2}+\beta^2} - \frac{T_L}{J_L}\end{aligned} \tag{5.6}$$

In terms of the relative mechanical displacement angle between the motor-side and load-side of the magnetic coupling,

$$\begin{aligned}\dot{\omega}_M - \dot{\omega}_L &= \ddot{\theta}_D = \frac{T_L}{J_L} + \frac{T_{EM}}{J_M} - \frac{T_G}{J_{EQ}}\left(\sin(p\theta_D) + \frac{2\alpha\beta\omega_D}{\omega_D^{\;2}+\beta^2}\right) \\ J_{EQ} &= \frac{J_M J_L}{J_M + J_L}\end{aligned} \tag{5.7}$$

or in state vector notation,

$$\begin{bmatrix}\dot{\theta}_D \\ \dot{\omega}_D\end{bmatrix} = \begin{bmatrix}\omega_D \\ \dfrac{T_L}{J_L} + \dfrac{T_{EM}}{J_M} - \dfrac{T_G}{J_{EQ}}\left(\sin(p\theta_D) + \dfrac{2\alpha\beta\omega_D}{\omega_D^{\;2}+\beta^2}\right)\end{bmatrix} \tag{5.8}$$

which is of the form $\dot{x} = f(x)$, a generalized representation of a nonlinear system [59].

5.2.1 Zero-input response of un-damped and damped system

Consider initially the free response of the system with no damping term included. From (5.6) the equations of motion reduce to,

$$J_M\frac{d\omega_M}{dt} = -T_G\sin(p\theta_D),\; J_L\frac{d\omega_L}{dt} = T_G\sin(p\theta_D) \tag{5.9}$$

or, in terms of $\theta_D = (\theta_M - \theta_L)$,

$$\ddot{\theta}_D = \frac{-T_G}{J_{EQ}}\sin(p\theta_D) \tag{5.10}$$

giving,

$$\dot{x} = f(x) \quad or \quad \begin{bmatrix}\dot{\theta}_D \\ \dot{\omega}_D\end{bmatrix} = \begin{bmatrix}\omega_D \\ \dfrac{-T_G}{J_{EQ}}\sin(p\theta_D)\end{bmatrix} \tag{5.11}$$

To explore the dynamics, the experimental test-rig has the following parameters:

Mechanical Parameters	**Value**
Motor-side inertia J_M	19×10^{-4} kgm^2
Load-side inertia J_L	15×10^{-4} kgm^2
Maximum design torque T_G	5.7 N•m
Pole-pairs p	3

Table 5.1 Experimental test rig mechanical parameters

A phase portrait of the dynamics of (5.11) is shown in figure 5.1, where the equilibrium points illustrated in figure 2.10 are clearly evident. Notably, the dynamics are consistent with those of the free un-damped pendulum problem [60].

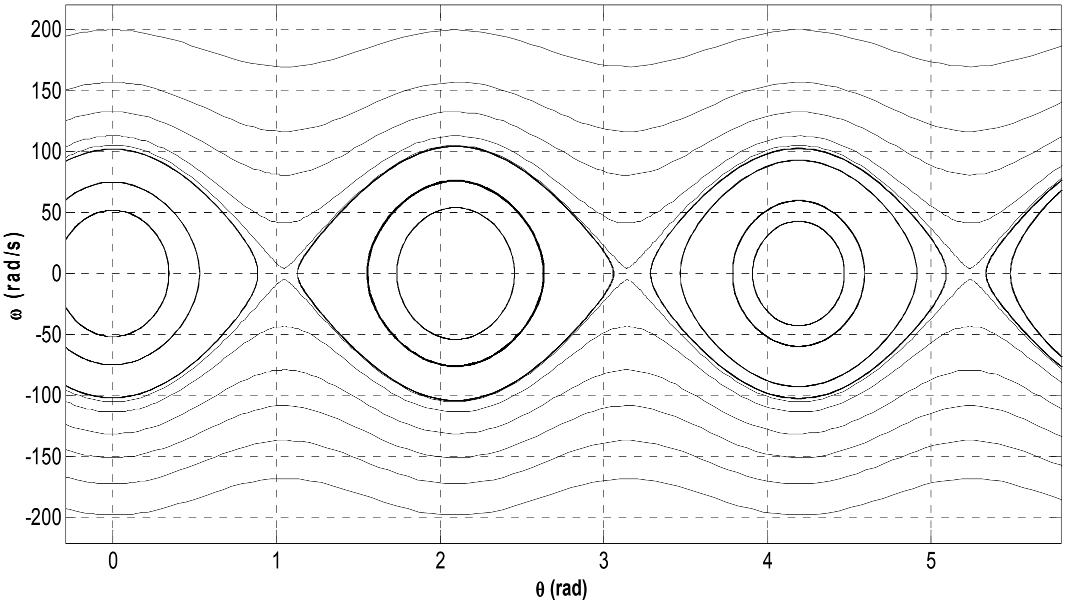

Figure 5.1 Phase portrait of un-damped free system

With the inclusion of damping torque, (5.6) becomes,

$$\begin{bmatrix} \dot{\theta}_D \\ \dot{\omega}_D \end{bmatrix} = \begin{bmatrix} \omega_D \\ \dfrac{-T_G}{J_{EQ}}\left(\sin(p\theta_D) + \dfrac{2\alpha\beta\omega_D}{\omega_D{}^2 + \beta^2} \right) \end{bmatrix} \tag{5.12}$$

and the resulting phase portrait is shown in figure 5.2.

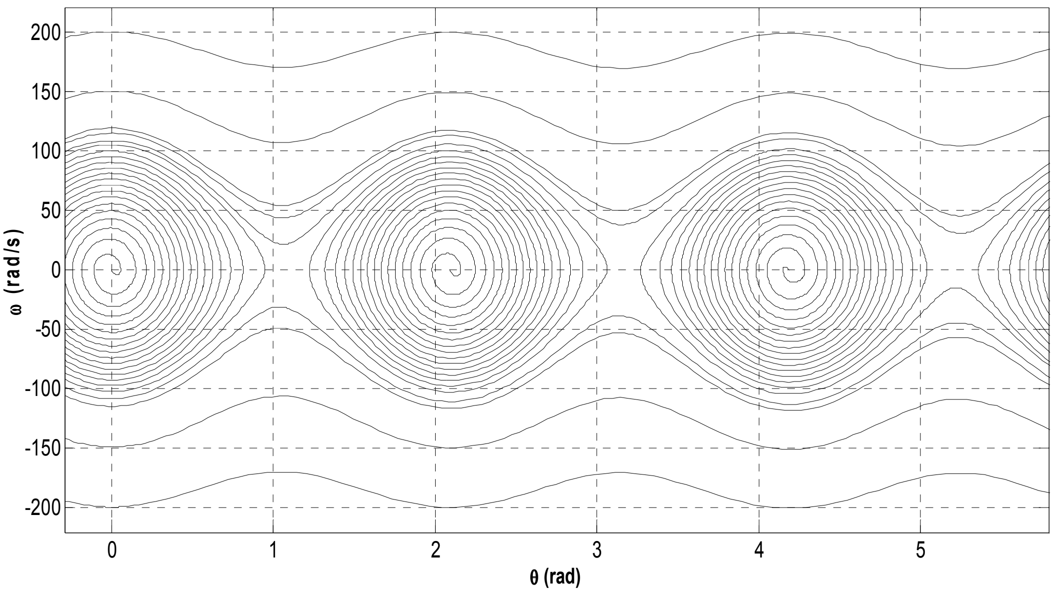

Figure 5.2 Phase portrait of damped system with $\alpha = 0.1$, $\beta = 5$ rad/s

5.3 Linearization: justification and effects of nonlinearity

The system of equations in (5.6) is inherently nonlinear and, as such, superposition cannot be applied, and the myriad tools for linear analysis and control methodologies, such as: convolution, Laplace transforms, transfer functions, root-locus, Mason's rule, Nyquist, Bode, Nichols etc. cannot be directly applied. With a mathematical model that contains nonlinearities three options present themselves, (i) determine a linear approximation that can be analyzed and is reasonably accurate, (ii) solve the differential equations directly, (iii) use computer simulation for specific numerical cases [61].

The invoking of the principle of *lex parsimoniae* practically mandates the implementation of option (i), the construction of a linearized model of the magnetic coupling. Moreover, as the torque transfer characteristic is a smoothly differentiable function, obtaining a 'good' linear approximation becomes straightforward. As is clear from figure 5.3, a tangent line through the origin gives $K_{lin} = pT_G \approx 17$ N•m/rad.

5.3.1 Torque de-rating of magnetic coupling

For the experimental magnetic coupling, the torque transfer characteristic for the first principal mechanical displacement angle is defined as $-30^\circ < \theta_D < 30^\circ$ and is shown in figure 5.3, this being repeated from Chapter 2 for convenience.

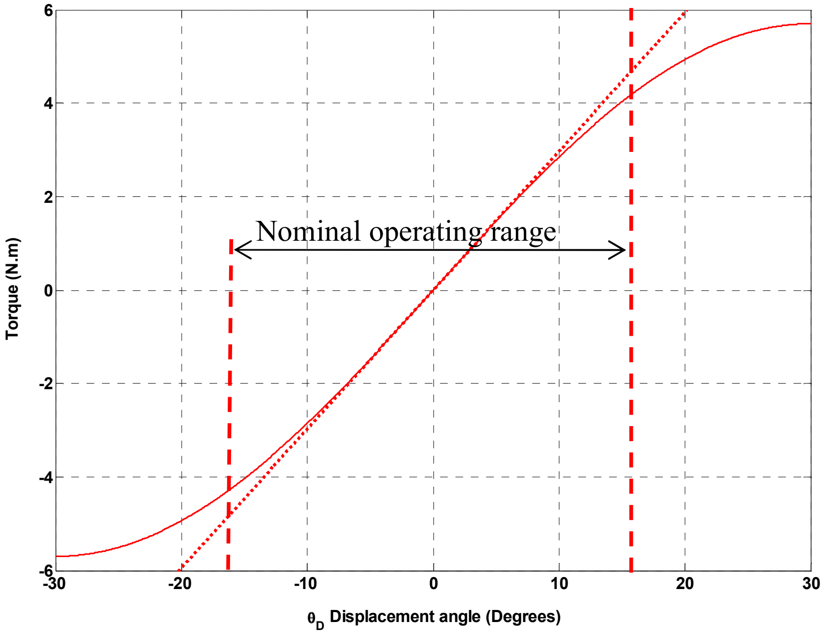

Figure 5.3 Torque-angle characteristic first principal mechanical displacement angle

This range is so defined because outside of this level of mechanical displacement angle, the magnetic coupling will begin to pole-slip due to either excess motor-side or excess load-side torque input. However, the need to take into consideration manufacturing tolerances, variations in magnetizations due to temperature, safe operating limits, etc. the permissible operating range is deemed by the manufacturer to be 80% of pull out torque at 20° C. As with any commercial product, it is necessary to include some degree of acceptable tolerance and maximum defined limit in the overall operating characteristics of the device. Consequently, the effective safe maximum torque operating range is considered to be between the dashed red lines shown in figure 5.3. Evidently within these limits the magnetic coupling is essentially *linear*, with a linearized spring constant $K_{lin} = pT_G \approx$ 17 N•m/rad. The linearized transfer characteristic (dotted line) is also shown in figure 5.3.

For the 3-pole pair magnetic coupling considered herein, this provides three ‘operating bands’ over the 360° of mechanical rotation. These stable operating bands are shown in figure 5.4, where the (faint) grey line indicates the full displacement range, and the overlaid red shows the *de-rated* safe operating ranges. It can be reasonably concluded from figure 5.4 that linearization around the origin of the full torque-angle curve is justifiable.

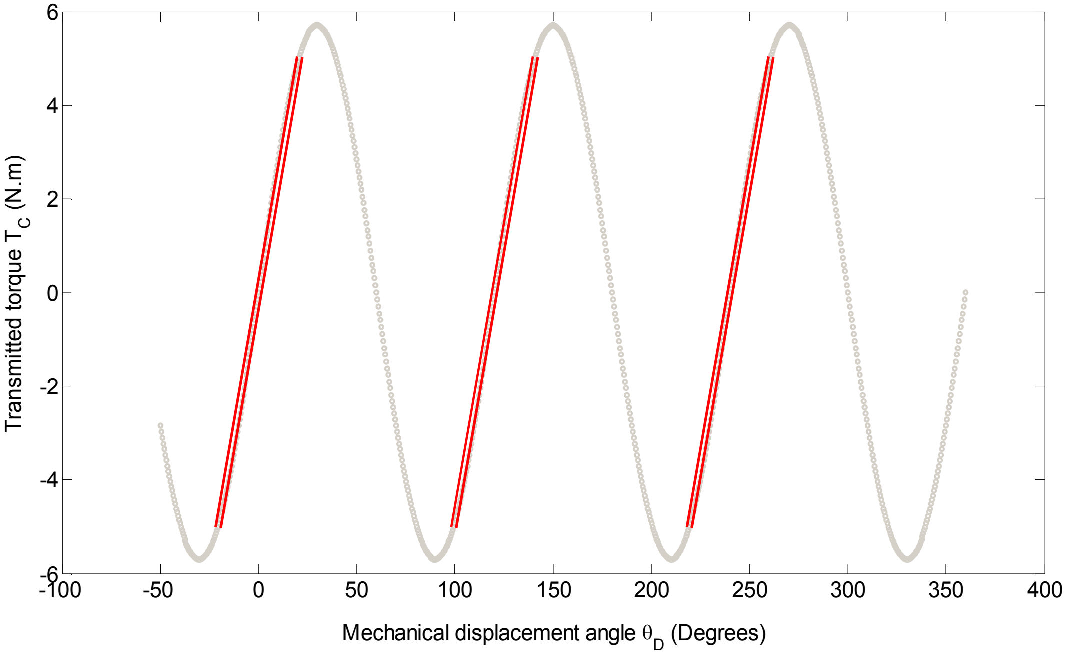

Figure 5.4 Magnetic coupling's three safe operating bands

5.3.2 Linearization around zero - $K_{lin}^{\max}$

The magnetic coupling can be modelled as two-inertias, motor-side and load-side, interconnected by a torsion spring representing torque transfer via a magnetic field. From figure 2.13, linearization at the origin gives a torsion constant of $K_{lin}^{\max} = pT_G = 17$ N•m/rad. With optimized controllers, PI$^{\text{ITAE}}$ for speed control and PD$^{\text{ITAE}}$ for position control, the closed-loop load-side dynamics are given by,

$$\frac{\omega_L}{\omega_{ref}} = \frac{K_I \omega_a{}^2}{J_M s^4 + K_P s^3 + \left(J_M \omega_a^2 (1+R) + K_I\right) s^2 + K_P \omega_a{}^2 s + K_I \omega_a{}^2} \tag{5.13}$$

$$\frac{\theta_L(s)}{\theta_{ref}(s)} = \frac{K_P \omega_a{}^2}{J_M s^4 + K_D s^3 + \left(J_M \omega_a^2 (1+R) + K_P\right) s^2 + K_D \omega_a{}^2 s + K_P \omega_a{}^2} \tag{5.14}$$

where $K_I = 10.26$, $K_P = 0.375$ for the optimized speed controller and $K_D = 0.375$, $K_P = 10.26$ for the optimized position controller. As can be seen from (5.13) and (5.14) this results in identical closed-loop load-side dynamics for both speed and position. This also applies to the closed-loop motor-side dynamics. Consequently, normalized closed-loop motor-side and load-side responses for both speed and position can now be considered.

The simulated step responses (normalized) of the linear model and nonlinear models, using an optimized controller (PI^{ITAE} or PD^{ITAE}) with $K_{lin}^{\max}$, for 0.5 and 1 p.u. reference are shown in figures 5.5(a) and 5.5(b) respectively. (Note: only load-side responses are shown as this represents the worst-case scenario).

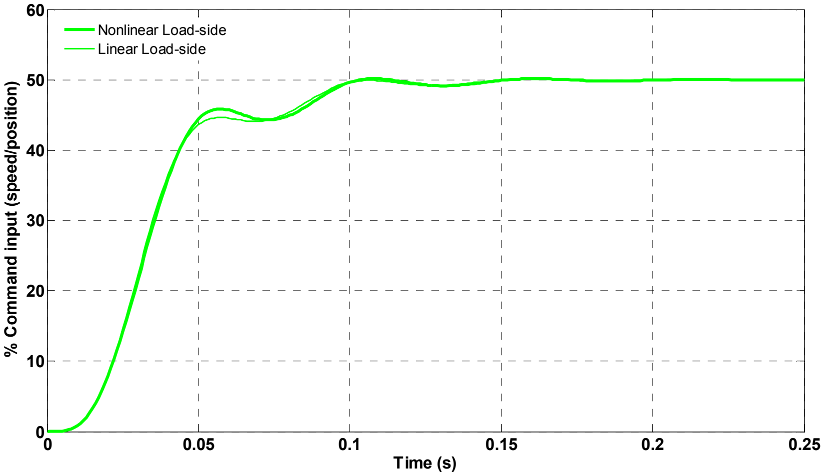

(a)

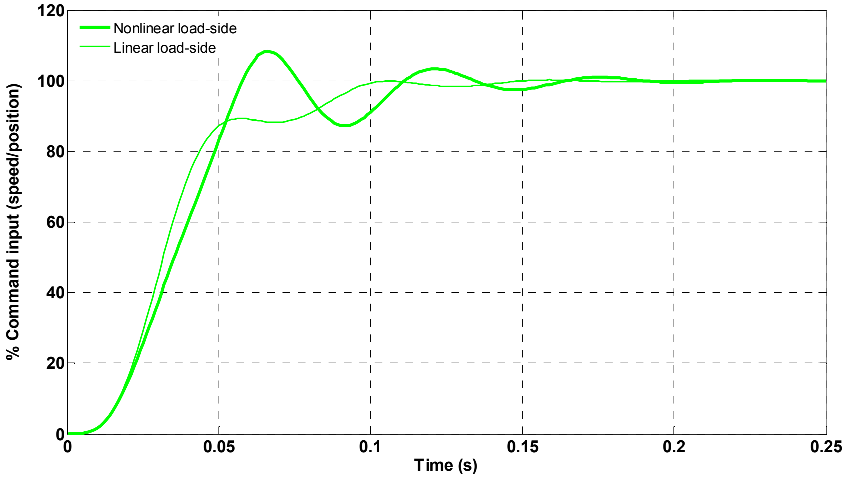

(b)

Figure 5.5 Simulated load-side step responses for linear model using $K_{lin}^{\max}$ and nonlinear model
(a) 50% command input (b) 100% command input

From figure 5.5(a) it can be seen that at 50% command input the linear and nonlinear responses are almost identical. At 100% command input the nonlinear response becomes under-damped, with small (<10%) increases in overshoot, settling and rise times. By simulating over the full command input range (speed/position) and calculating the instantaneous percentage error between the linear and nonlinear step responses the error surfaces of figure 5.6(a) motor-side step error, and figure 5.6(b) load-side step error, are obtained.

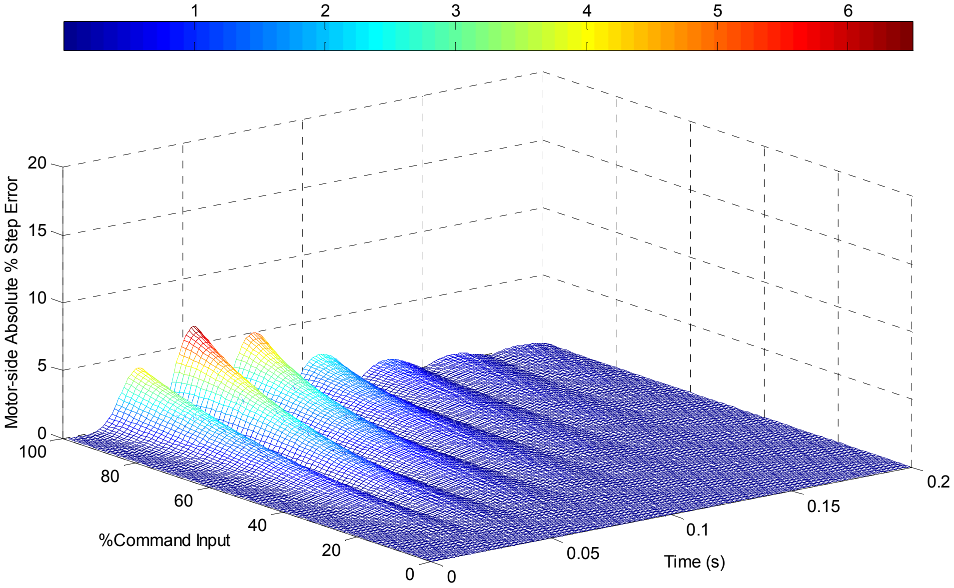

(a)

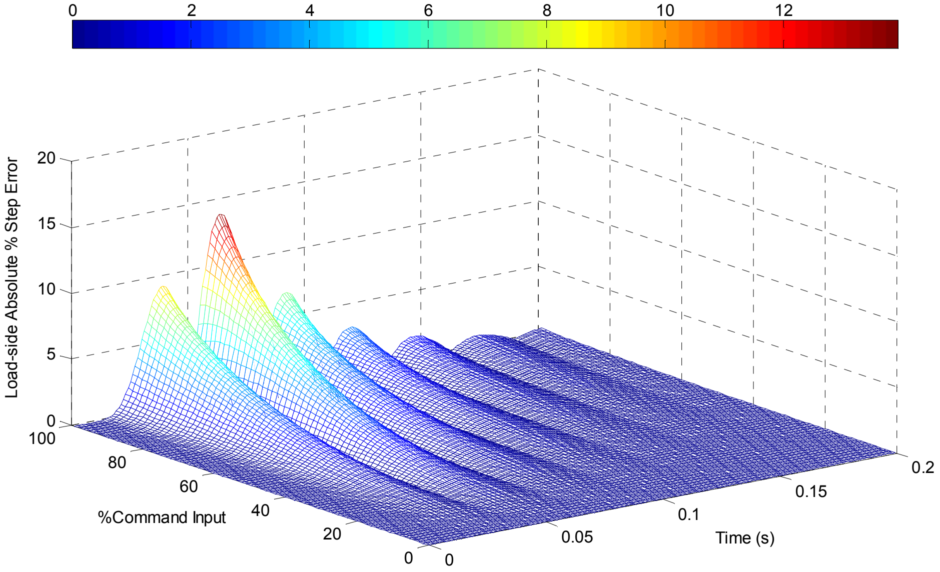

(b)

Figure 5.6 Linear ($K_{lin}^{\max}$) vs. nonlinear step error surfaces
(a) motor-side % error from linear (b) load-side % error from linear

Figures 5.6(a) & 5.6(b) illustrate that as the command input approaches the maximum allowable, a small error exists between the linear and nonlinear models. At the motor-side the error is very small, while at the load-side the error, though larger, still remains small (maximum less than 15%). It should be noted that 100% command input limit is set by the point at which the magnetic coupling begins to pole-slip. Consequently, this defines the range over which the comparisons are performed.

In addition to the step errors calculated in figure 5.6, a number of commonly used performance metrics can also be calculated, these include: overshoot, rise time and settling time. For each of the aforementioned metrics, figure 5.7 (a-c) plots the percentage change that occurs between the linear and nonlinear models for both motor- and load-sides of the magnetic coupling. This presents a graphical illustration of how each particular metric changes as the command input is increased from zero to 100%.

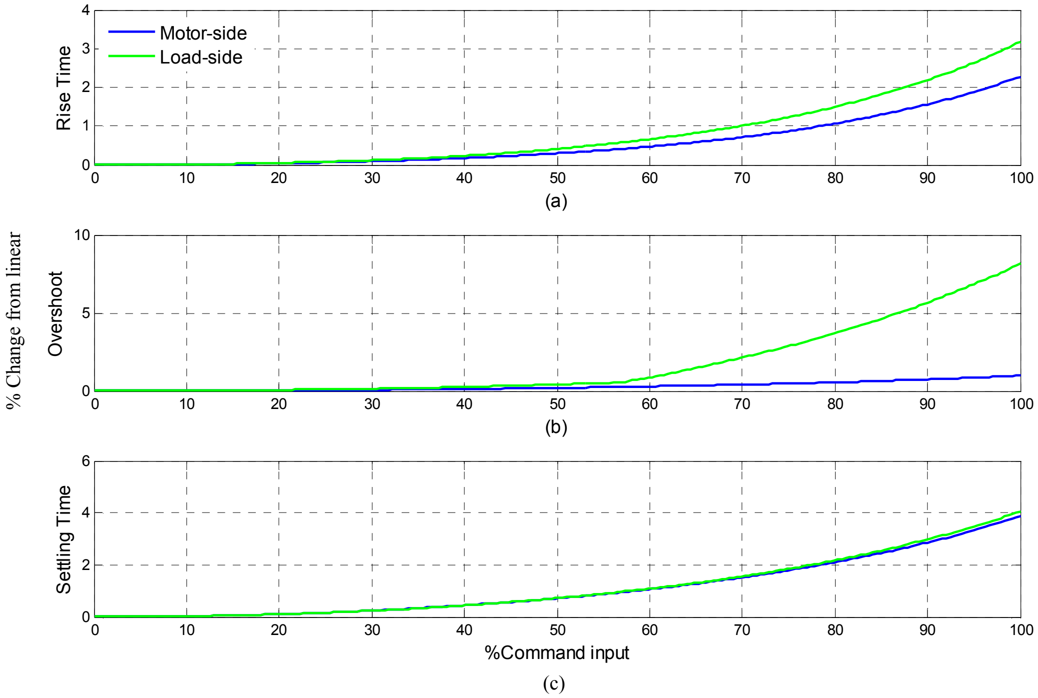

Figure 5.7 Percentage change from linear using $K_{lin}^{\max}$
(a) rise time (b) overshoot (c) settling time

5.3.2 Linearization around de-rated pull out torque - $K_{lin}^{\min}$

Section 5.3.1 indicated that the de-rated torque limit of 80% maximum pull-out torque is utilized for safety and operational reasons. Furthermore, Chapter 2 showed that the effective stiffness of the magnetic coupling reduces as the applied torque increases toward the maximum design torque T_G. Specifically, the nonlinear stiffness function is shown to be

$K(\theta_D) = pT_G \cos(p\theta_D)$, and in (5.13) and (5.14) linearization around zero is assumed. An alternative view is to linearize at the 80% pull out point, representing the worst-case scenario in the sense that the linearized stiffness constant is at a minimum, defined herein as $K_{lin}^{\min}$. From figure 2.13 it can be seen that the effective stiffness reduces to $K_{lin}^{\min} \approx 10$ N•m/rad.

With the linearized spring constant defined to be at 80% pull out level, the performance of the linearized and nonlinear models can be compared through simulation studies. The new controller gains are calculated to be $K_I = 6$ and $K_P = 0.287$ for PI speed control and $K_D = 0.287$ and $K_P = 6$ for PD position control. Simulation results for 50% and 100% command input step are shown in figures 5.8(a) and 5.8(b), respectively.

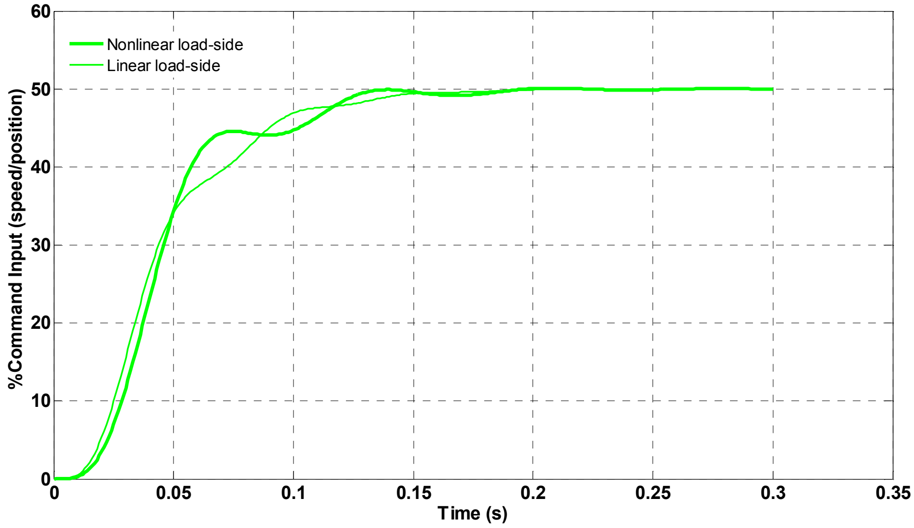

(a)

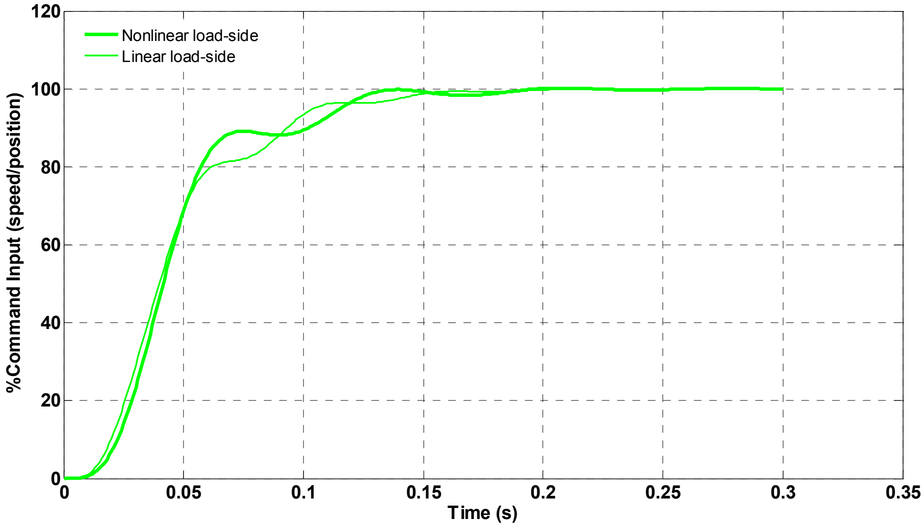

(b)

Figure 5.8 Simulated load-side step responses for linear model using $K_{lin}^{\min}$ and nonlinear model
(a) 50% command input (b) 100% command input

With the reduction in linearized spring constant to $K_{lin}^{\min}$, there is almost no perceptible change in response between 50% and 100% of command input. However, a comparison between the linear and nonlinear responses shows that they are effectively out of 'phase' (loose definition of phase) with each other during the initial transient. Unlike the previous case using $K_{lin}^{\max}$, the linear and nonlinear transient responses are never identical; whereas in figure 5.6 a portion of each error surface has a 'zero flat' on the initial transient when the command input is 'small', no such area exists for the case of $K_{lin}^{\min}$. As shown in figure 5.9, no transient zero flat area exists with the step error surfaces for either motor- or load-side step responses.

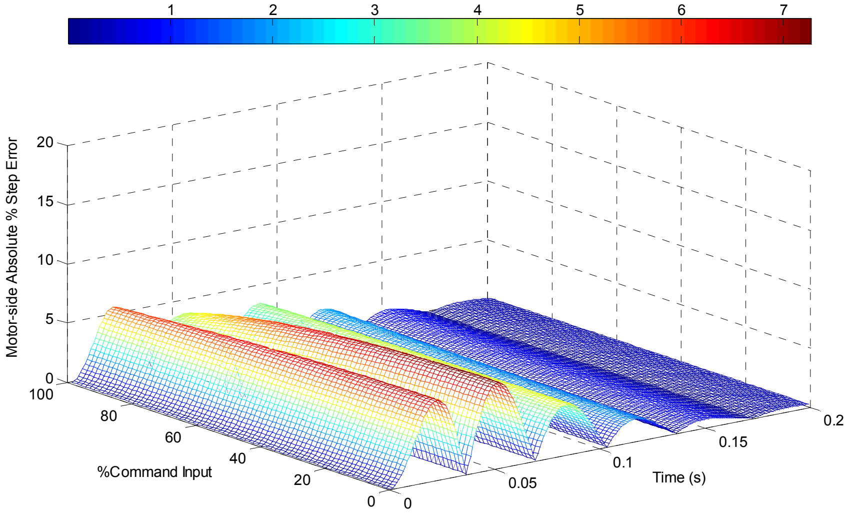

(a)

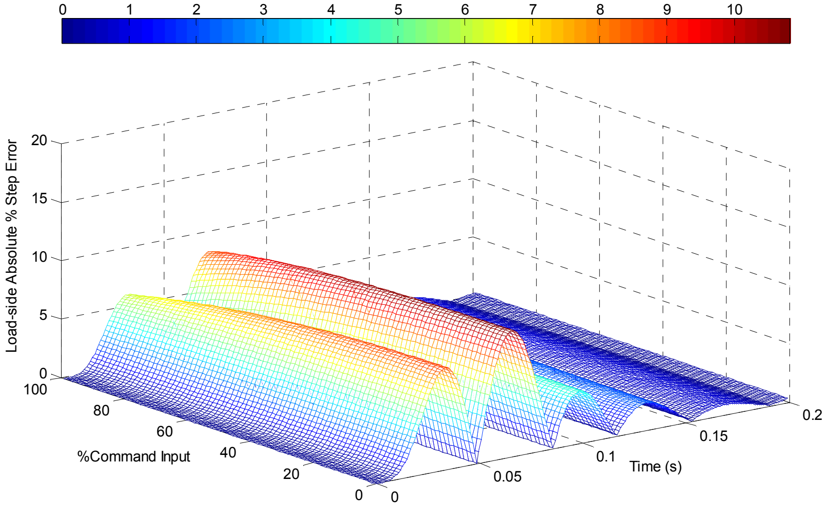

(b)

Figure 5.9 Linear ($K_{lin}^{\min}$) vs. nonlinear step error surfaces
(a) motor-side % error from linear (b) load-side % error from linear

However, what is clear from the error surfaces in figures 5.9(a) and 5.9(b) is that the instantaneous step error is extremely small for both motor- and load-side of the magnetic coupling.

As in the previous case it is now possible to calculate performance metric changes for $K_{lin}^{\min}$ and these are plotted in figure 5.10 (a-c). It can be noted that the motor-side overshoot is zero throughout the input command range, the response never overshooting the set-point.

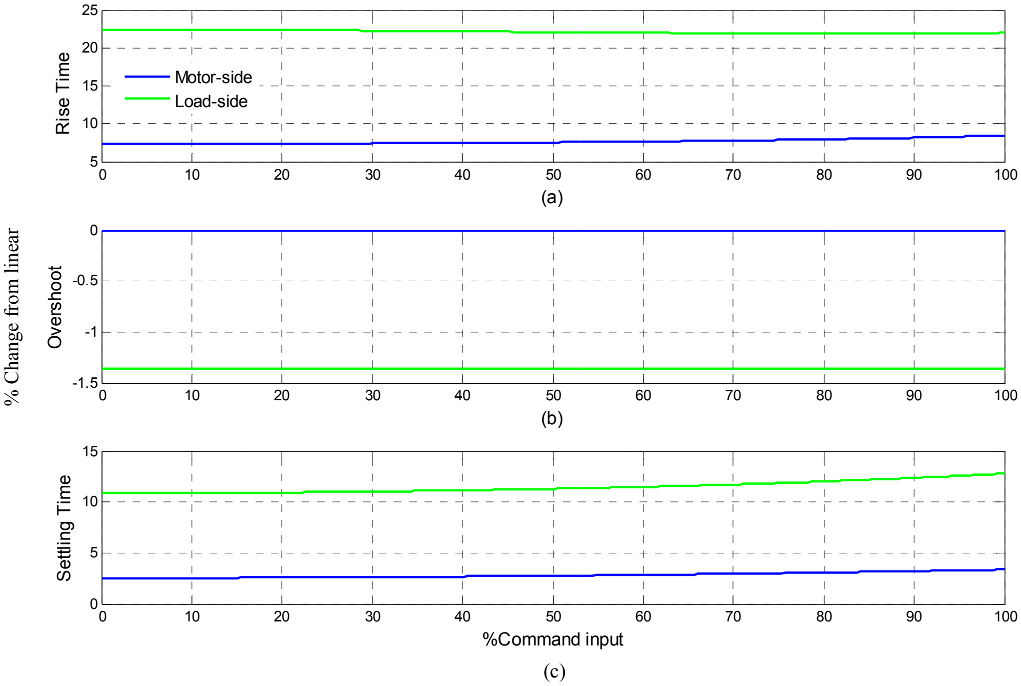

Figure 5.10 Percentage change from linear using $K_{lin}^{\min}$
(a) rise time (b) overshoot (c) settling time

5.4 Optimum linearization point

Empirically, it is possible to suggest an optimum linearization value for K_{lin}^{Opt}. The criterion for choosing such an optimum is the parameter value that produces the smallest perturbation of the instantaneous absolute step error response surfaces. This value, following simulation studies is determined to be $K_{lin}^{Opt} = 13.5$ N•m /rad, this being the mid-way point between the minimum and maximum values of the linearized spring constant. The error surfaces for motor-side and load-side percentage step error are shown in figure 5.11(a) and 5.11(b). The main performance metrics, overshoot, settling and rise times are indicated in figure 5.12 (a-c), and all demonstrate smooth and small (<10%) deviations suggesting that this value of linearized torsional spring constant could be considered optimum.

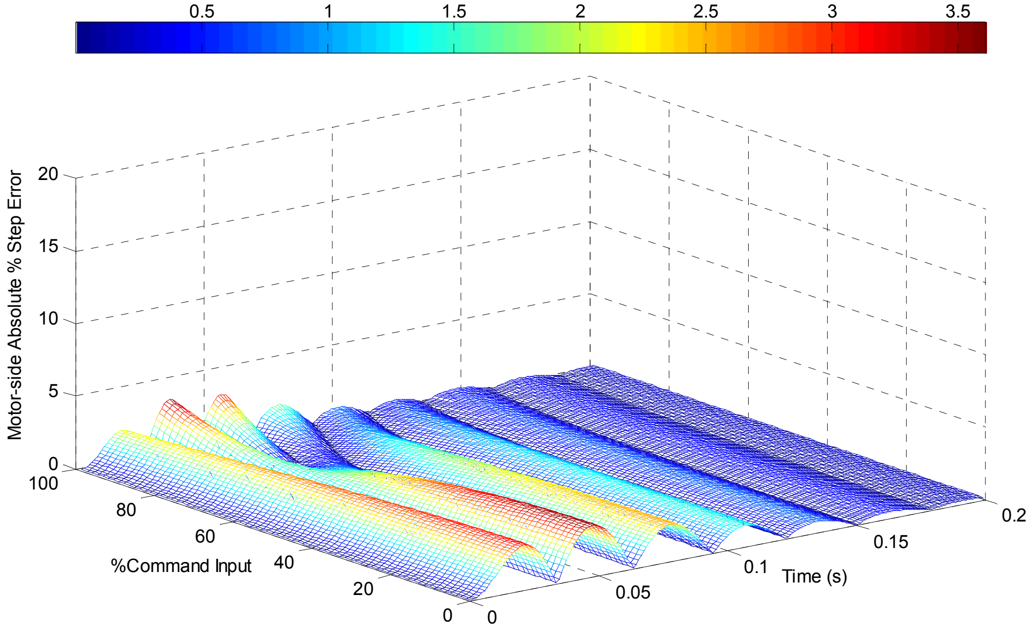

(a)

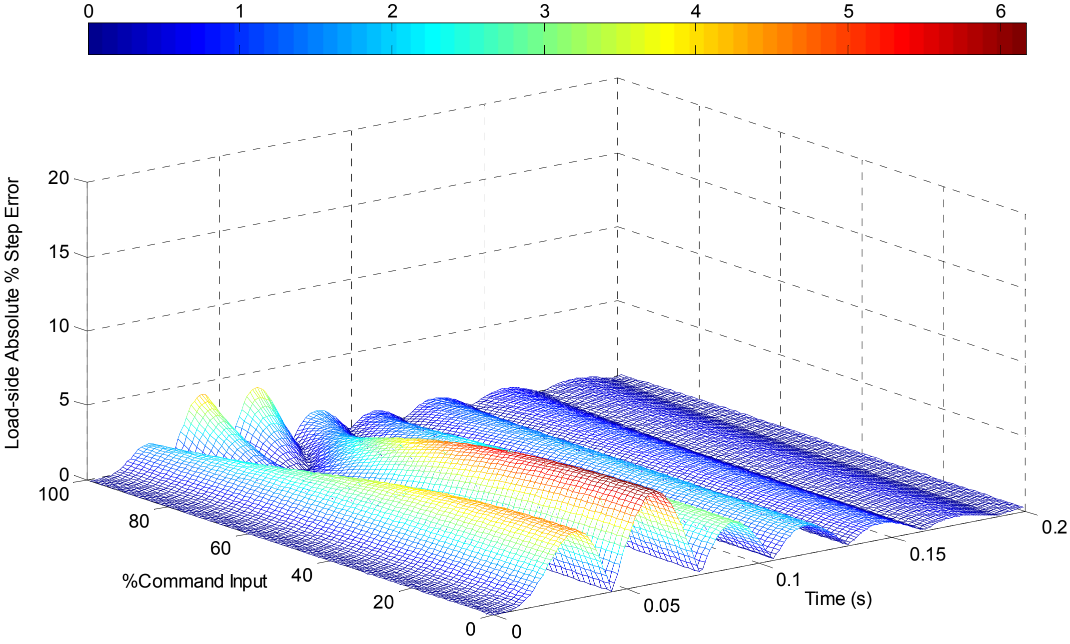

(b)

Figure 5.11 Linear (K_{lin}^{Opt}) vs. nonlinear step error surfaces
(a) motor-side % error from linear (b) load-side % error from linear

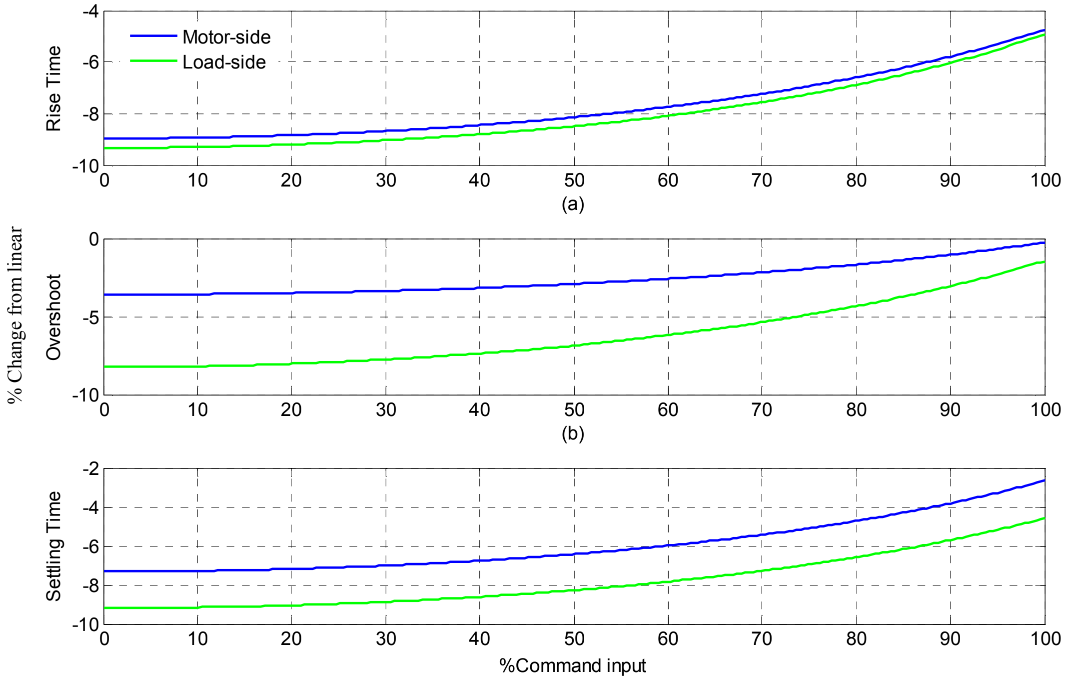

(c)

Figure 5.12 (a) Percentage change from linear using K_{lin}^{Opt}
(a) rise time (b) overshoot (c) settling time

5.5 Summary

In this chapter consideration has been given to the effects of linearizing the fundamentally nonlinear torque transfer characteristic of the manufactured magnetic coupling. Through simulation studies, the ITAE optimized speed and position control of linearized models and a nonlinear model have been examined. The use of step error response surfaces quantifies the effect of the magnetic coupling's inherent nonlinearity on controller performance. Three different linearization points have been considered with an empirically-determined optimum linearization point suggested.

Chapter 6

Advanced Techniques: Model Predictive Control and Pole-Slip Prevention

6.1 Introduction

In Chapter 3 it was shown that PI control of the magnetic coupling is ineffectual under loaded conditions, even though the implemented controller is optimal in the ITAE sense. While good speed and load regulation can be achieved under certain conditions, it is too easy to induce pole-slip. In the presented scenario, with the magnetic coupling operating well below maximum rated torque, a simple change in speed causes the combined load and controller torque to exceed the capability of the coupling, and consequently the PI controller loses control as a pole-slipping regime is induced. During this transient operation, the controller takes no account of the limitations imposed by the nature of the torque transfer via a magnetic field. In essence the design torque is an inviolable *hard constraint* on the maximum permissible torsional torque T_C; violation of this constraint results in instantaneous pole-slipping. It seems sensible, therefore, to use a control design that can fully incorporate the magnetic coupling's design torque as a hard constraint, and the most obvious candidate is *Model Predictive Control - MPC*.

MPC has had a huge impact on process control where large scale multi-input multi-output (MIMO) systems, with multifarious constraints, can be handled in a unified and systematic way [62]. Although a number of variants exist, model predictive control falls into three principal categories, depending on how the model structure is handled. Early implementations were formulated with Finite Impulse Response (FIR) models, favoured by process control engineers because of the ability to incorporate process time delay, a significant issue in such systems. Dynamic Matrix Control (DMC), a first generation MPC algorithm, was introduced by Cutler and Ramaker more than thirty years ago [63], followed shortly after by the quadratic DMC formulation of Garcia and Morshedi [64]. In the late 1980's Clarke *et al.* [65], introduced transfer function model-based predictive control under the acronym GPC, or generalized predictive control. More recently, model predictive control has been formulated on the basis of state space design methods. These include the works of Ricker [66], Rawlings and Muske [67], and Maciejowski [68]. The remainder of this chapter will only consider the formulation of model predictive control from a state space perspective. Moreover, with implementation of a model predictive controller on a dSPACE hardware development platform, a discrete-time state space representation is applicable.

The following section develops a discrete-time state space formulation that closely follows [69]. Having developed a methodology that optimizes a control input sequence on the basis of a model prediction (hence formerly, Model-Based Predictive Control), it becomes necessary to introduce *constraints* into the optimization procedure. It is the systematic handling of constraints that gives model predictive control its considerable attraction for the control of processes where constraint handling is essential. The interpretation of MPC in this particular context is the control of a SISO system with just two constraints, (i) maximum allowable drive torque T_{EM} (an unavoidable physical constraint), and (ii) maximum coupling torsional torque T_C which must be less than the design torque T_G. The main objective of the MPC controller is to prevent excessive magnetic coupling torsion from inducing pole-slipping.

As in the case of PI controller design, the initial MPC formulation is based on the most widely studied linear model of an elastically coupled servo drive system. In its simplest linear form, assuming no friction,

$$\begin{aligned} J_M \frac{d\omega_M}{dt} &= T_{EM} - T_C \\ J_L \frac{d\omega_L}{dt} &= T_C - T_L \\ \frac{dT_C}{dt} &= K_{lin}(\omega_M - \omega_L) \end{aligned} \tag{6.1}$$

In this case J_M represents the motor inertia plus motor-side coupling inertia, and J_L the load inertia plus load-side coupling inertia, with K_{lin} the linearized magnetic spring constant.

6.2 Model predictive control: discrete-time state space formulation

A model predictive control system is predicated on the basis of a known mathematical model of the process to be controlled. The model considered for the remainder of this chapter is a discrete-time state space model of the form,

$$\begin{aligned} x[k+1] &= A_m x[k] + B_m u[k] \\ y[k] &= C_m x[k] \end{aligned} \tag{6.2}$$

where $x[k] \in \mathrm{R}^n$, is the state vector, $u[k] \in \mathrm{R}^m$, input vector, and $y[k] \in \mathrm{R}^p$, the output vector. The time-invariant system matrices of the model (m), A_m, B_m, C_m, are known with dimensions, (n **x** n), (n **x** m) and (p **x** n) respectively.

The design methodology adopted here is to embed an integrator into the process model so as to create a predictive control system able to track constant references while rejecting constant steady-state disturbances. In the context of servo speed control, this is accomplished in Chapter

3 with the use of an ITAE optimized proportional plus integral (PI) controller. However, as shown in figure 3.27 a conventional PI controller is not able to readily accommodate the constraints that must be imposed upon the magnetic coupling's torsional torque, T_C. Consequently, a discrete-time state space model predictive control methodology, incorporating constraints and an embedded integrator, is now developed.

To embed an integrator, a difference operation is taken on both sides of (6.2), thus,

$$x[k+1]-x[k]=A_m\big(x[k]-x[k-1]\big)+B_m\big(u[k]-u[k-1]\big) \tag{6.3}$$

Define the following incremental variables,

$$\begin{aligned}\Delta x[k+1]&=x[k+1]-x[k]\\ \Delta x[k]&=\big(x[k]-x[k-1]\big)\\ \Delta u[k]&=\big(u[k]-u[k-1]\big)\end{aligned} \tag{6.4}$$

so that the state-space model can be represented in incremental form as,

$$\Delta x[k+1]=A_m\Delta x[k]+B_m\Delta u[k] \tag{6.5}$$

The control input to the state space model is now $\Delta u[k]$ and it is necessary to relate this to the output, $y[k]$. A new state variable vector is defined as,

$$z[k]=\begin{bmatrix}\Delta x[k]^T & y[k]\end{bmatrix}^T \tag{6.6}$$

and noting that,

$$\begin{aligned}y[k+1]-y[k]&=C_m x[k+1]-C_m x[k]\\ y[k+1]-y[k]&=C_m\big(A_m x[k]+B_m u[k]\big)-C_m\big(A_m x[k-1]+B_m u[k-1]\big)\\ y[k+1]&=C_m A_m\Delta x[k]+C_m B_m\Delta u[k]+y[k]\end{aligned} \tag{6.7}$$

Combining (6.5) and (6.7) the augmented state space model is then,

$$\begin{aligned}\begin{bmatrix}\Delta x[k+1]\\ y[k+1]\end{bmatrix}&=\begin{bmatrix}A_m & 0_m^T\\ C_m A_m & 1\end{bmatrix}\begin{bmatrix}\Delta x[k]\\ y[k]\end{bmatrix}+\begin{bmatrix}B_m\\ C_m B_m\end{bmatrix}\Delta u[k]\\ y[k]&=\begin{bmatrix}0_m & 1\end{bmatrix}\begin{bmatrix}\Delta x[k]\\ y[k]\end{bmatrix}\end{aligned} \tag{6.8}$$

In terms of the new state vector $z[k]$, this is more compactly expressed as,

$$\begin{aligned} z[k+1] &= Az[k] + B\Delta u[k] \\ y[k] &= Cz[k] \end{aligned} \tag{6.9}$$

where,

$$A = \begin{bmatrix} A_m & 0_m^T \\ C_m A_m & 1 \end{bmatrix}, \qquad B = \begin{bmatrix} B_m \\ C_m B_m \end{bmatrix}, \qquad C = \begin{bmatrix} 0_m & 1 \end{bmatrix}$$

now form the discrete-time state space model with embedded integrator. Note the control input is now the incremental variable $\Delta u[k]$.

6.2.1 State and output prediction over an optimization window

To calculate the predicted state, output and optimum control variables an optimization problem is formulated in which the prediction takes place over N_p samples, referred to as the prediction horizon. Similarly, the control trajectory is defined as,

$$\begin{bmatrix} \Delta u[k] & \Delta u[k+1]....., & \Delta u[k+N_c-1] \end{bmatrix} \tag{6.10}$$

where N_c is the control horizon that determines how many control 'moves' are calculated within the optimization procedure.

Given the current state vector at sample time [k], that is, $z[k]$, the future state variables are predicted for the length of the prediction horizon N_p as,

$$\begin{bmatrix} z[k+1|k] & z[k+2|k]....., & z[k+N_p|k] \end{bmatrix} \tag{6.11}$$

where $z[k+j|k]$ is the prediction of state vector at sample time $[k+j]$ based on the current measurement of the state vector at sample time $[k]$. From the state space model of (6.9) future state variables can be calculated recursively based on the future control input,

$$\begin{aligned} z[k+1|k] &= Az[k] + B\Delta u[k] \\ z[k+2|k] &= Az[k+1] + B\Delta u[k+1] \\ z[k+2|k] &= A(Az[k] + B\Delta u[k]) + B\Delta u[k+1] \\ z[k+2|k] &= A^2 z[k] + AB\Delta u[k] + B\Delta u[k+1] \\ &. \\ &. \\ z[k+N_p|k] &= A^{N_p} z[k] + A^{N_p-1} B\Delta u[k] + A^{N_p-2} B\Delta u[k+1] \\ &\quad + ... \quad + A^{N_p-N_c} B\Delta u[k+N_c-1] \end{aligned} \tag{6.12}$$

Similarly, the predicted output variables are obtained by substitution,

$$\begin{aligned}
&y[k] = Cz[k] \\
&y[k+1|k] = Cz[k+1] = CAz[k] + CB\Delta u[k] \\
&y[k+2|k] = CA^2 z[k] + CAB\Delta u[k] + CB\Delta u[k+1] \\
&Y[k+3|k] = CA^3 z[k] + CA^2 B\Delta u[k] + CAB\Delta u[k+1] + CB\Delta u[k+2] \\
&. \\
&. \\
&y[k+N_p|k] = CA^{N_p} z[k] + CA^{N_p-1} B\Delta u[k] + CA^{N_p-2} B\Delta u[k+1] \\
&\qquad\qquad + \ldots\ldots \quad + CA^{N_p-N_c} B\Delta u[k+N_c-1]
\end{aligned} \tag{6.13}$$

To present the optimization in a more compact form the following vectors are defined,

$$\begin{aligned}
\Delta U &= \left[\Delta u[k] \quad \Delta u[k+1] \ldots\ldots, \quad \Delta u[k+N_c-1]\right]^T \\
Y &= \left[y[k+1|k] \quad y[k+2|k] \ldots\ldots, \quad y[k+N_p|k]\right]^T
\end{aligned} \tag{6.14}$$

and the compact matrix representation then becomes,

$$Y = Fz[k] + \Phi\Delta U \tag{6.15}$$

where,

$$F = \begin{bmatrix} CA \\ CA^2 \\ CA^3 \\ . \\ . \\ CA^{N_p} \end{bmatrix}; \quad \Phi = \begin{bmatrix} CB & 0 & 0 & . \ . & 0 \\ CAB & CB & 0 & . \ . & 0 \\ CA^2 B & CAB & CB & & 0 \\ . & & & & \\ . & & & & \\ CA^{N_P-1} & CA^{N_p-2}B & CA^{N_p-3}B & & CA^{N_p-N_c}B \end{bmatrix}. \tag{6.16}$$

6.2.2 Optimization

The compact matrix representation (6.15) of the discrete-time state space model is defined over the prediction horizon N_P, and the control horizon N_C with $N_C \le N_P$. For a given set-point, the purpose of the model predictive control system is to bring the predicted output to the set-point by calculating the optimal control vector $\Delta u[k]$. The set-point information is constant throughout the optimization window and defined by $R_S^T = [1 \quad 1 \quad .. \quad 1] r[k]$, and the optimization cost function is defined as,

$$J = \left(R_S - Y\right)^T \left(R_S - Y\right) + \Delta U^T R \Delta U \tag{6.17}$$

In (6.17) the first term measures the error between the predicted output Y and the set-point R_s, while the second term weights the amount of control effort that is expended bringing the output to the desired set-point. The matrix R is diagonal such that $R = I_{N_c \times N_c} r_w \ (r_w \geq 0)$ where the closed-loop performance can be tuned by appropriate choice of r_w. Substituting (6.15) into (6.17) the cost function then becomes,

$$J = \left(R_S - Fz[k] - \Phi \Delta U\right)^T \left(R_S - Fz[k] - \Phi \Delta U\right) + \Delta U^T R \Delta U \tag{6.18}$$

Noting the following matrix properties $(A+B)^T = (A^T + B^T)$, $(AB)^T = (B^T A^T)$ and expanding (6.18),

$$\begin{aligned} J &= \left(R_S^T - z^T[k]F^T - \Delta U^T \Phi^T\right) \left(R_S - Fz[k] - \Phi \Delta U\right) + \Delta U^T R \Delta U \\ J &= \left(R_s - Fz[k]\right)^T \left(R_s - Fz[k]\right) - 2\Delta U^T \Phi^T \left(R_s - Fz[k]\right) + \Delta U^T \left(\Phi^T \Phi + R\right) \Delta U \end{aligned} \tag{6.19}$$

To minimize the cost function J and find the optimal incremental control sequence $\Delta u[k]$, the first derivative of (6.19) is set to zero, that is,

$$\begin{aligned} \frac{\partial J}{\partial \Delta U} &= 0 = -2\Phi^T \left(R_s - Fz[k]\right) + 2\left(\Phi^T \Phi + R\right) \Delta U \\ \Delta U^{opt} &= \left(\Phi^T \Phi + R\right)^{-1} \Phi^T \left(R_s - Fz[k]\right) \end{aligned} \tag{6.20}$$

and the optimal control vector can be calculated provided $\left(\Phi^T \Phi + R\right)^{-1}$ exists.

6.2.3 Introducing constraints

The principal benefit of model predictive control comes from its ability to handle *constraints*. This section systematically introduces constraint handling in the formulation of the model predictive control optimization problem.

For control of the magnetic coupling, the maximum torsion when under load must not exceed the designed pull out torque if the magnetic coupling is to be prevented from pole-slipping. Similarly, the maximum input torque from the motor is determined by the physical capabilities of the drive electronics. In terms of the model predictive framework thus far developed, these constraints must be translated into linear inequalities in terms of the optimization performed in (6.18). Constraints must be articulated as a set of linear inequalities based on the optimal control vector ΔU. The optimization problem is then subject to a set of constraints, for which an optimal control vector is determined over each optimization window. Although it is feasible to impose constraints on the calculation of each element in the optimal control vector, i.e. $\Delta U = [\Delta u[k] \quad \Delta u[k+1] \ldots\ldots, \quad \Delta u[k+N_c-1]]$, the receding horizon principle requires only the first element be used to excite the plant. Furthermore, imposing constraints on every element of the optimal control vector can significantly increase the computational burden of the optimization. As a consequence, the remainder of this section considers only the first element of the control vector as being subject to constraint. A more detailed exposition of constraint handling over the entire control vector is given in [69].

The simplest form of constraint that can be applied to the predictive control model developed thus far is to limit the magnitude of the incremental control ΔU such that,

$$\Delta U^{\min} \le \Delta u[k] \le \Delta U^{\max} \tag{6.21}$$

Optimization of (6.18) subject to constraints is undertaken via *quadratic programming* and, as such, the constraints must be expressed in a slightly different (but equivalent) form as,

$$\begin{bmatrix} -1 & 0\ldots\ldots0 \\ 1 & 0\ldots\ldots0 \end{bmatrix} \Delta U \le \begin{bmatrix} -1 & 0\ldots\ldots0 \\ 1 & 0\ldots\ldots0 \end{bmatrix} \begin{bmatrix} \Delta U^{\min} \\ \Delta U^{\max} \end{bmatrix} \tag{6.22}$$

where in matrix form the leading 1 selects only the first element in the incremental control vector for optimization, the remaining (N_c-1) elements in each row being zero.

To incorporate constraints on the actual control vector U this must be expressed in terms of the incremental control vector ΔU as this is the decision variable in the quadratic programming optimization. Since $\Delta u[k] = u[k] - u[k-1]$ the control variable constraint then takes the form,

$$\begin{bmatrix} -1 & 0\ldots0 \\ 1 & 0\ldots\ldots0 \end{bmatrix} \Delta U + \begin{bmatrix} -1 \\ 1 \end{bmatrix} u[k-1] \le \begin{bmatrix} -U^{\min} \\ U^{\max} \end{bmatrix} \tag{6.23}$$

From (6.15) the output and state constraints can be similarly formulated as,

$$\begin{bmatrix} -\Phi \\ \Phi \end{bmatrix} \Delta U \le \begin{bmatrix} -Y^{\min} + Fz[k] \\ Y^{\max} - Fz[k] \end{bmatrix} \tag{6.24}$$

$$\begin{bmatrix} F^{-1}\Phi \\ -F^{-1}\Phi \end{bmatrix} \Delta U \le \begin{bmatrix} -z[k]^{\min} - F^{-1}Y \\ z[k]^{\max} + F^{-1}Y \end{bmatrix} \tag{6.25}$$

In all cases, the constraints are defined in the form $M\Delta U \le \lambda$ where M and λ are relevant matrices/vectors dependent upon which constraints are active.

6.3 Simulation of constrained model predictive control

As a basis to demonstrate the relative merits of constrained model predictive control (MPC), consider the simplified case in which the torsional stiffness of the magnetic coupling is infinitely stiff. For this scenario, assuming a lumped parameter approximation, the simplified and linearized model for position control is then,

$$G(s) = \frac{1}{(Js+b)s} \tag{6.26}$$

with J representing the equivalent inertia, and b the viscous friction. To illustrate the performance of constrained model predictive control on the continuous-time model of (6.26), the transfer function $G(s)$ is discretized with a sampling time of 10 milliseconds and parameter values arbitrarily set as $J = 20\times10^{-4}$ kg.m^2 and b = 0.01 N•m/(rad/s). Initially the performance of MPC is simulated with no active constraints on input, output, or state. The 'closed-loop' performance is determined by the value of the weighting matrix, $R = r_w I$, where R is a diagonal matrix with scalar parameter r_w that determines the penalty cost on the magnitude of the control input. Figure 6.1 illustrates three cases, (i) no weighting on the control input, $r_w = 0$; (ii) $r_w = 0.1$, and (iii) $r_w = 1$ for a step command input of 10 units.

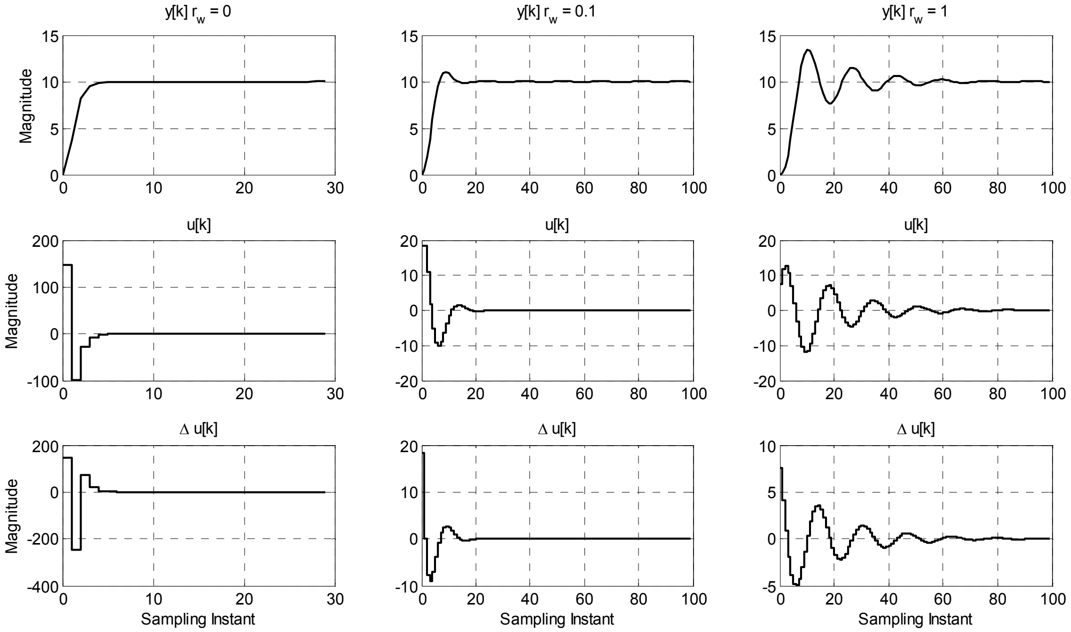

Figure 6.1 Unconstrained MPC step responses for (6.25) with scalar weighting parameter r_w = 0, 0.1 & 1

It is clear from figure 6.1(a) that having no weighting on the control input in the cost function of (6.18) leads to very large control input amplitudes with high dynamic rates of change. This may be unrealistic for a real plant, and hence, even a small scalar weighting, $r_w = 0.1$, as in figure 6.1(b), readily reduces the magnitude and rate of change of the control input to more realistic values. However, suppose the absolute magnitude of the control input, $u[k]$, must be limited to, say, ±10 units in magnitude. In this scenario the optimum solution of (6.18) is subject to the following constraints,

$$\begin{bmatrix} -1 & 0....0 \\ 1 & 0.....0 \end{bmatrix} \Delta U + \begin{bmatrix} -1 \\ 1 \end{bmatrix} u[k-1] \leq \begin{bmatrix} 10 \\ 10 \end{bmatrix} \tag{6.27}$$

The results of a simulation of the system of (6.26) under *constrained* model predictive control with the constraints defined in (6.27), and control weighting scalar $r_w = 0.1$, are shown in figure 6.2. It can be seen that while the control input is never allowed to exceed ±10 units in magnitude, as specified by the constraint conditions in (6.27) and within the dashed red lines of figure 6.3, the constrained output (solid line) deviates only slightly from the unconstrained output case (dashed line) in figure 6.3.

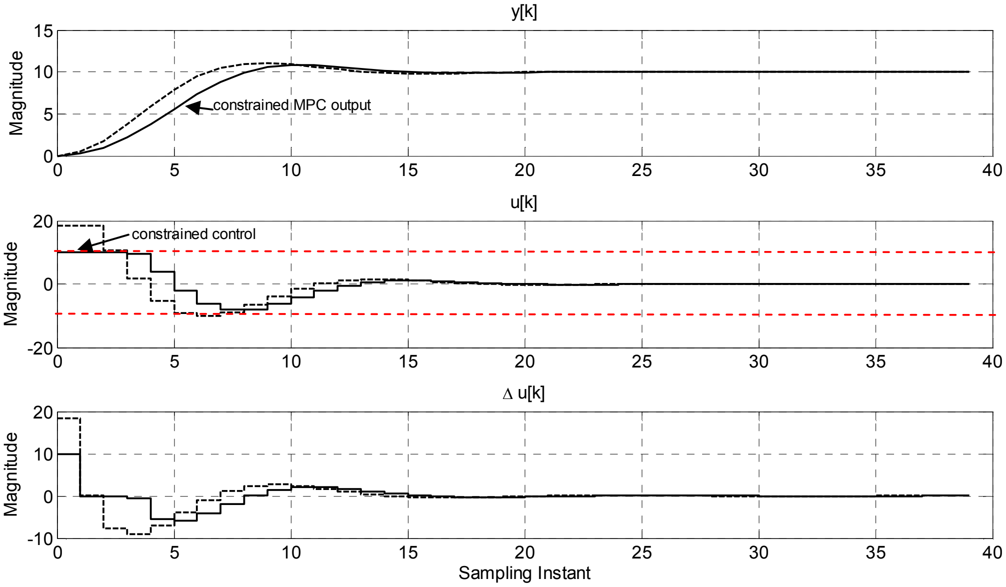

Figure 6.2 Constrained $u[k]$ MPC step responses (solid line) and unconstrained (dashed line)

While the example of figure 6.2 placed constraints on the absolute amplitude of the control input $u[k]$, a more likely situation is constraints not only on the amplitude, but also on the rate of change $\Delta u[k]$, of the control input since all real physical systems are subject to slew rate limiting of one form or another. To incorporate both control amplitude $u[k]$, and rate of change $\Delta u[k]$, constraints on the example of (6.26) the optimization of (6.18) proceeds with the constraints as defined in (6.28),

$$\begin{bmatrix} 1 & 0 & .. & 0 \\ -1 & 0 & .. & 0 \\ 1 & 0 & .. & 0 \\ -1 & 0 & .. & 0 \end{bmatrix} \Delta U \leq \begin{bmatrix} 2 \\ 2 \\ 4-u[k-1] \\ 4+u[k-1] \end{bmatrix} \tag{6.28}$$

For illustrative purposes, the control amplitude limits are set to ±4 units, and control rate of change to ±2 units, representing significant constraints compared with the unconstrained control input indicated by the dashed line plots in figure 6.2. The simulated constrained model predictive output for this scenario is shown in figure 6.3, where the dashed red lines represent the constraint limits imposed on both the control amplitude $u[k]$, and control rate of change $\Delta u[k]$. As can be seen in figure 6.3, the model predictive controller successfully constrains the rate of change and limits the maximum absolute magnitude of the control input. With both constraints active, the output from the constrained system differs somewhat from the unconstrained case, with a significant increase in rise time and settling time. However, this may be considered a reasonable trade-off for a well-defined, and well-behaved constrained system.

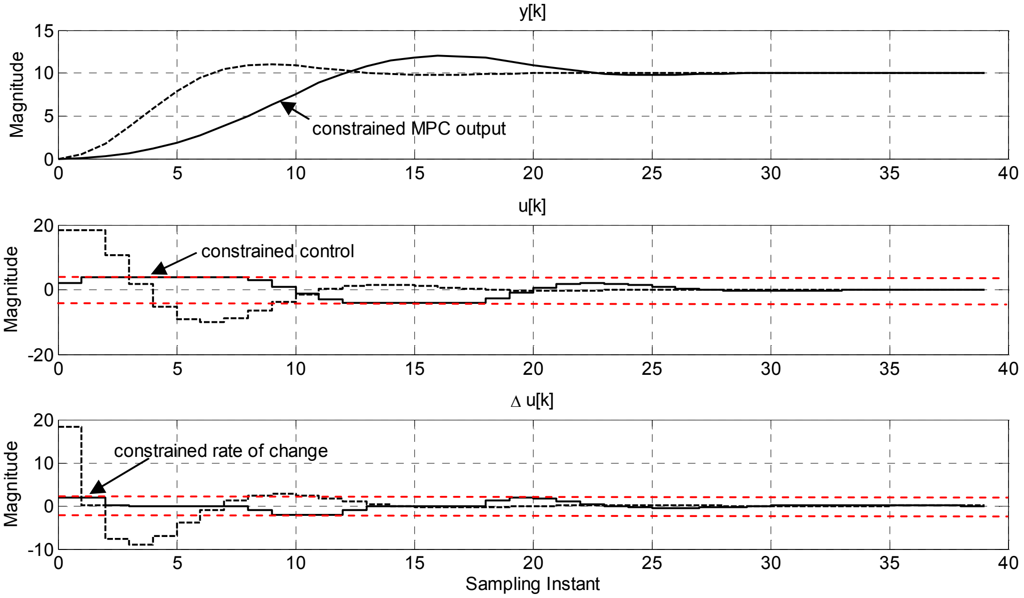

Figure 6.3 Constrained $u[k]$ and $\Delta u[k]$ MPC step responses (solid line) and unconstrained (dashed line)

As indicated in (6.24), the model predictive control problem can also be formulated with constraints on the *output* of the plant. Two cases are now considered, both having identical constraint formulations, given below,

$$\begin{bmatrix} 1 & 0 & .. & 0 \\ -1 & 0 & .. & 0 \\ 1 & 0 & .. & 0 \\ -1 & 0 & .. & 0 \\ \Phi & 0 & .. & 0 \\ -\Phi & 0 & .. & 0 \end{bmatrix} \Delta U \le \begin{bmatrix} 2 \\ 2 \\ 4-u[k-1] \\ 4+u[k-1] \\ 9.9-Fx[k] \\ 0+Fx[k] \end{bmatrix} \tag{6.29}$$

The constraints imposed on the control input and its rate of change are identical to the scenario presented in figure 6.3, but for the two cases now considered an additional constraint is that the output, $y[k]$, must remain 10% below the step input command. Consequently, the output is constrained to be a maximum of 9.9 units and minimum of 0; this being incorporated into the constraint handling via the last two entries of the right-hand side of the inequality vector (6.29). For case (i) the control input weighting remains identical to the previous examples, $r_w = 0.1$. Figure 6.5 shows the output of the constrained model predictive simulation with all constraints active, that is, control input amplitude $u[k]$, control input rate of change $\Delta u[k]$, and output $y[k]$, all indicated on figure 6.4.

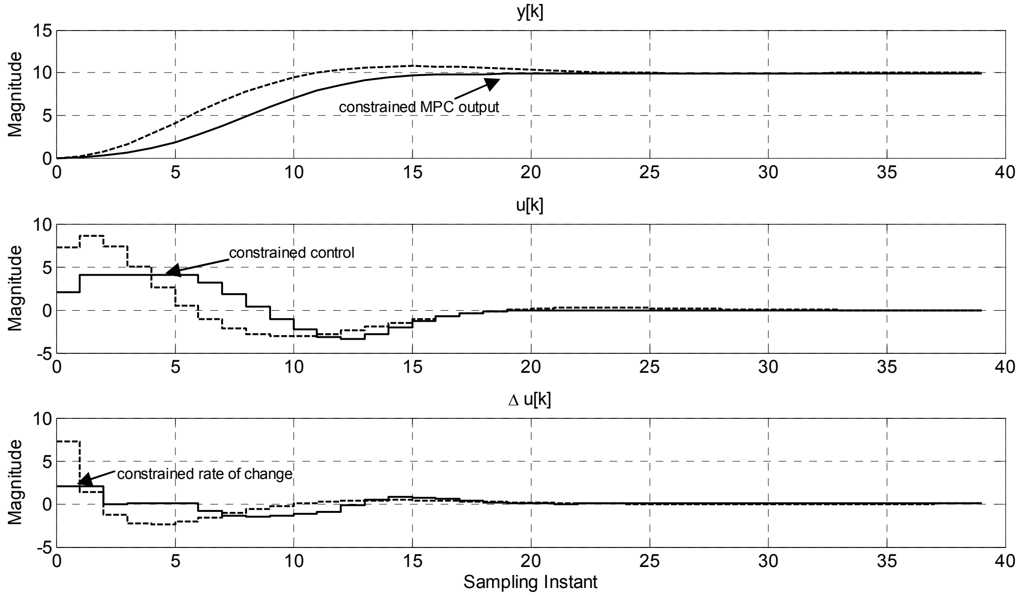

Figure 6.4 MPC with output constraint, control amplitude and control rate of change constraints

It is clear from figure 6.4 that all active constraints perform satisfactorily for the presented scenario with $r_w = 0.1$. The second case to be considered is (ii) $r_w = 1$, in which the control penalty is increased while the constraints are those defined in (6.29). The simulation results for this constrained model predictive control scenario are presented in figure 6.5.

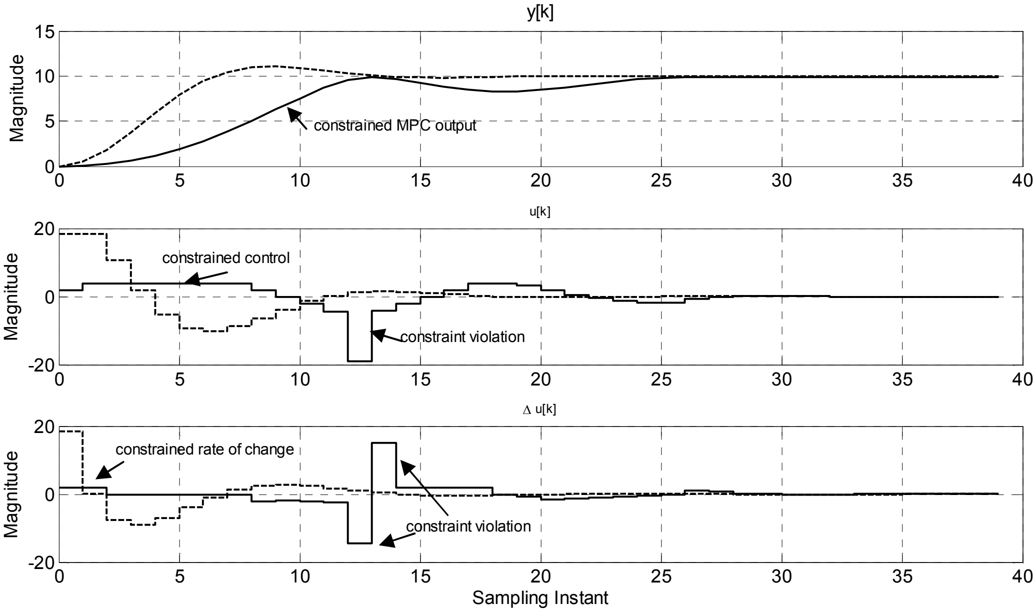

Figure 6.5 MPC with output constraints and induced constraint violation

Figure 6.5 illustrates a potential problem with imposing *hard constraints* on the output $y[k]$ in a model predictive control framework. Initially, control amplitude and control rate of change constraints are active until $[k] = 13$ when the output constraint becomes active in an attempt to limit the output to 9.9 units. In so doing, large constraint violations on the control amplitude and control rate of change of the control input occurs at $[k] = 13$. In this situation the solution to (6.18), subject to (6.29), effectively becomes *infeasible* and so the constraints on the control input are relaxed [69]. For situations where it would not be acceptable to have input constraint violations it is necessary to re-formulate the output as a *soft constraint* with the introduction of a slack variable [70].

6.4 Real-time implementation of model predictive control

The cost function of (6.17) is re-formulated in terms of the constrained finite-time optimal control (CTFOC) regulator problem (set-point $R_s = 0$), with cost function J defined in (6.30) and subject to the constraints defined in (6.31), for which the constrained optimization problem must be solved. This representation can be recognized as the classical cost function for the discrete-time linear quadratic regulator (DLQR), linking directly to model predictive control.

$$J = \min_{U} \sum_{i=0}^{N_P} x[k+i|k]^T Q x[k+i|k] \; + \sum_{i=0}^{N_C-1} u[k+i|k]^T R u[k+i|k] \tag{6.30}$$

$$
\begin{aligned}
&s.t.\\
&u_{\min} \le u[k+i] \le u_{\max}, i = 0,...N_C - 1\\
&x_{\min} \le x[k+i] \le x_{\max}, i = 0...N_P\\
&y_{\min} \le y[k+i] \le y_{\max}, i = 0..N_p
\end{aligned}
\tag{6.31}
$$

The solution to (6.30), with linear inequality constraints (6.31) on the optimal control input $u[k]$, output $y[k]$, and state vector $x[k]$, can be viewed as the optimal solution to a *quadratic programming* (QP) problem [71]. The burden of computational overhead when attempting to implement a QP solver in real-time for highly dynamic processes, typically requiring sampling rates in the micro/millisecond range, is well documented [72]. In addition, it is possible that at given time step $[k]$ the QP solver may return an *infeasible solution*. For the control of high speed electrical drives, these limitations pose substantial impediments to the use of traditional MPC.

Recently however, theoretical advances have led to the development of *explicit* MPC in which the solution to (6.30) is conducted ‘offline’. With the use of multi-parametric programming, it is shown that the state vector can be used as a parameter vector to determine a piece-wise affine (PWA) state feedback law from a partition of the optimized solution space based on polyhedral sets. Polyhedral partitioning of the state space, and determination of the PWA control laws, can be accomplished through the use of MATLAB Multi-Parametric Toolbox (MPT) [73], for instance. This facilitates the creation of real-time controller blocks for applications with sample times in the micro/millisecond range. The development of explicit MPC is primarily due to the seminal work of Bemporad *et al*. [74].

6.4.1. Explicit model predictive control using multi-parametric programming

To illustrate the operation of *explicit* model predictive control via multi-parametric programming, the model of (6.26) is used with identical parameters. In the framework of model predictive control it is more convenient to re-cast (6.26) as a discrete-time state space representation. Choosing, as in the previous case, a sampling time of 10 milliseconds, $J = 20\times10^{-4}$ kg.m^2, and b = 0.01 N•m/(rad/s), a discrete-time state space representation is then,

$$
\begin{aligned}
&x[k+1] = \begin{bmatrix} 1 & 0.009754 \\ 0 & 0.95122 \end{bmatrix} x[k] + \begin{bmatrix} 0.0245 \\ 4.877 \end{bmatrix} u[k]\\
&y[k] = \begin{bmatrix} 1 & 0 \end{bmatrix} x[k]\\
&\begin{bmatrix} x_1[k] \\ x_2[k] \end{bmatrix} \equiv \begin{bmatrix} \theta[k] \\ \omega[k] \end{bmatrix}
\end{aligned}
\tag{6.32}
$$

For the system model of (6.26) an explicit model predictive controller is determined using the Multi-Parametric Toolbox (MPT) in MATLAB with the following (arbitrary) parameter settings: Q = I, R = 1; $N_p = 5$, $N_c = 2$, constraints on the control input $u[k]$ and state vector $x[k]$ as follows,

$$-0.5 \le u[k] \le 0.5$$
$$\begin{bmatrix} -10 \\ -5 \end{bmatrix} \le \begin{bmatrix} x_1[k] \\ x_2[k] \end{bmatrix} \le \begin{bmatrix} 10 \\ 5 \end{bmatrix} \tag{6.33}$$

The polyhedral partition of the state space for the explicit model predictive controller, with parameters as defined above, is shown in figure 6.6. To facilitate visualization, a state regulator is specified to reduce the number of MPT generated partitions. The objective of the derived controller is to force the state vector to zero, subject to the constraints given in (6.33). As shown in figure 6.6 the polyhedral partition of the state space consists of 7 distinct, non-overlapping regions or polytopes. For each region there exists a piecewise affine control law given by,

$$u[k] = F_i^r x[k] + G_i^r \tag{6.34}$$

where the superscript r represents the active region and i the active dynamics for that region.

For the controller partition shown in figure 6.6 the control laws are:

$$\begin{aligned}
u[k]^1 &= [-0.3548 \quad -0.0101]x[k] \\
u[k]^2 &= [-0.246 \quad -0.0366]x[k] - 0.1911 \\
u[k]^3 &= [-0.246 \quad -0.0366]x[k] + 0.1911 \\
u[k]^4 &= [0 \quad -0.195]x[k] + 1.0252 \\
u[k]^5 &= [0 \quad -0.195]x[k] - 1.0252 \\
u[k]^6 &= [0 \quad 0]x[k] - 0.5 \\
u[k]^7 &= [0 \quad 0]x[k] + 0.5
\end{aligned} \tag{6.35}$$

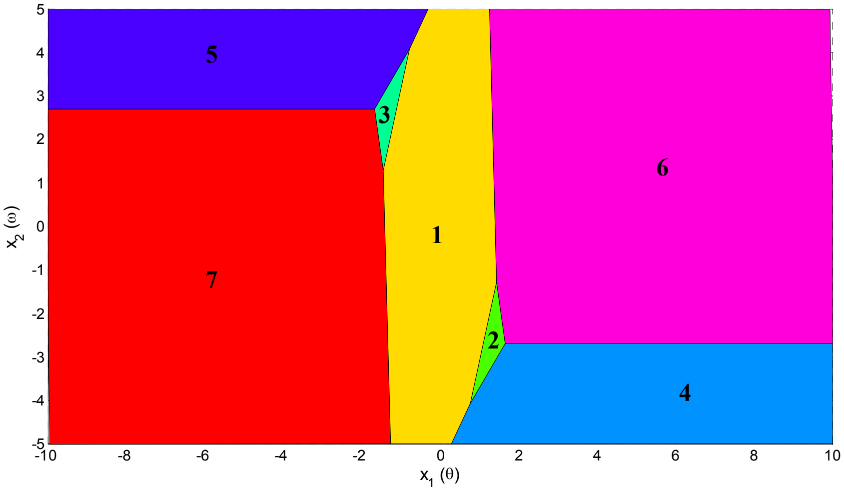

Figure 6.6 Polyhedral partition of the state space for (6.30) with constraints (6.31)

The explicit MPC controller's response is shown in figures 6.7 and 6.8 for initial state $x0 = [7 \quad 1]^T$.

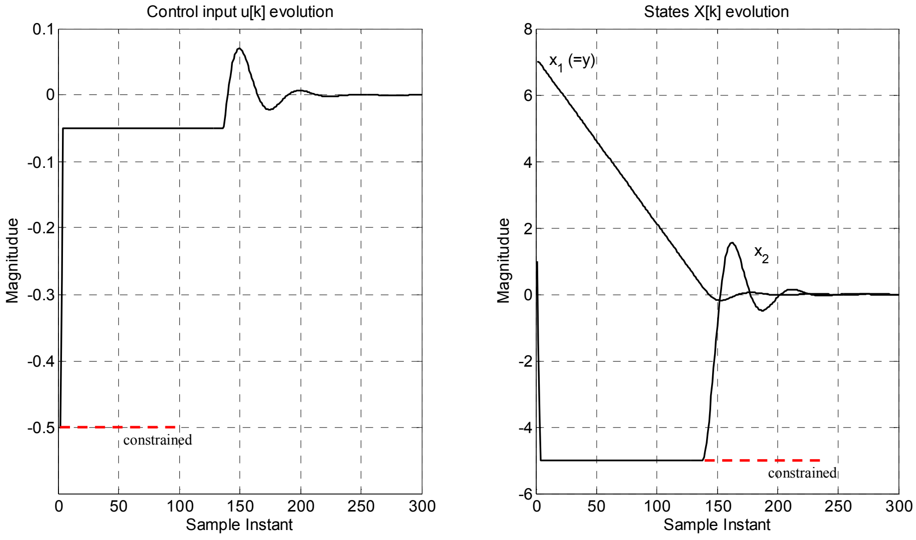

(a) (b)

Figure 6.7 Simulated response of explicit MPC controller for initial state $x0 = [7 \quad 1]^T$.
(a) control input $u[k]$ (b) state vector evolution $X[k]$

In figure 6.7(a) the initial control input $u[k]$ is constrained to -0.5 and figure 6.7(b) state x_2 is also held for a period at its constraint value of -5. To illustrate the state trajectory from $x0 = [7 \quad 1]^T$ to the origin, figure 6.8 plots the control evolution on top of the polyhedral partition.

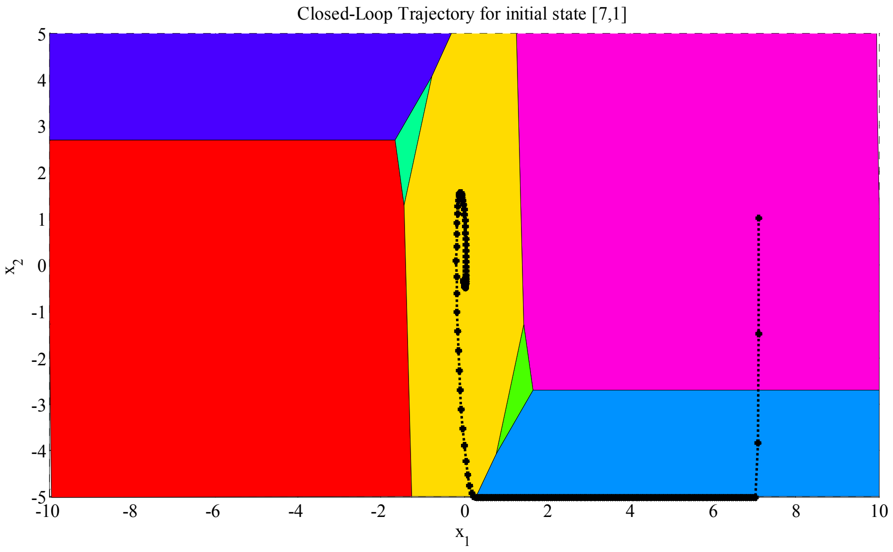

Figure 6.8 Simulated closed-loop trajectory for initial state $x0 = [7 \quad 1]^T$.

As can be seen from figure 6.8, in this instance the trajectory traverses three regions of the polyhedra, utilizing three PWA control laws. As a concluding example, an explicit MPC controller for (6.32) is designed for prediction horizon $N_p = 10$, control horizon $N_c = 3$, with the following modified constraints,

$$-0.05 \le u[k] \le 0.5$$

$$\begin{bmatrix} -5 \\ -3 \end{bmatrix} \le \begin{bmatrix} x_1[k] \\ x_2[k] \end{bmatrix} \le \begin{bmatrix} 5 \\ 2 \end{bmatrix} \tag{6.36}$$

The resulting controller partition, control input and state evolutions are shown in figure 6.9(a)-(c) respectively, where it can be seen that the number of PWA control laws (partitions) has increased to 13, and the polyhedral partition has lost its symmetry due to the 'asymmetrical' constraint definitions of (6.36). However, the resulting controller performs as required observing all constraints defined in (6.36) while regulating the initial state to zero.

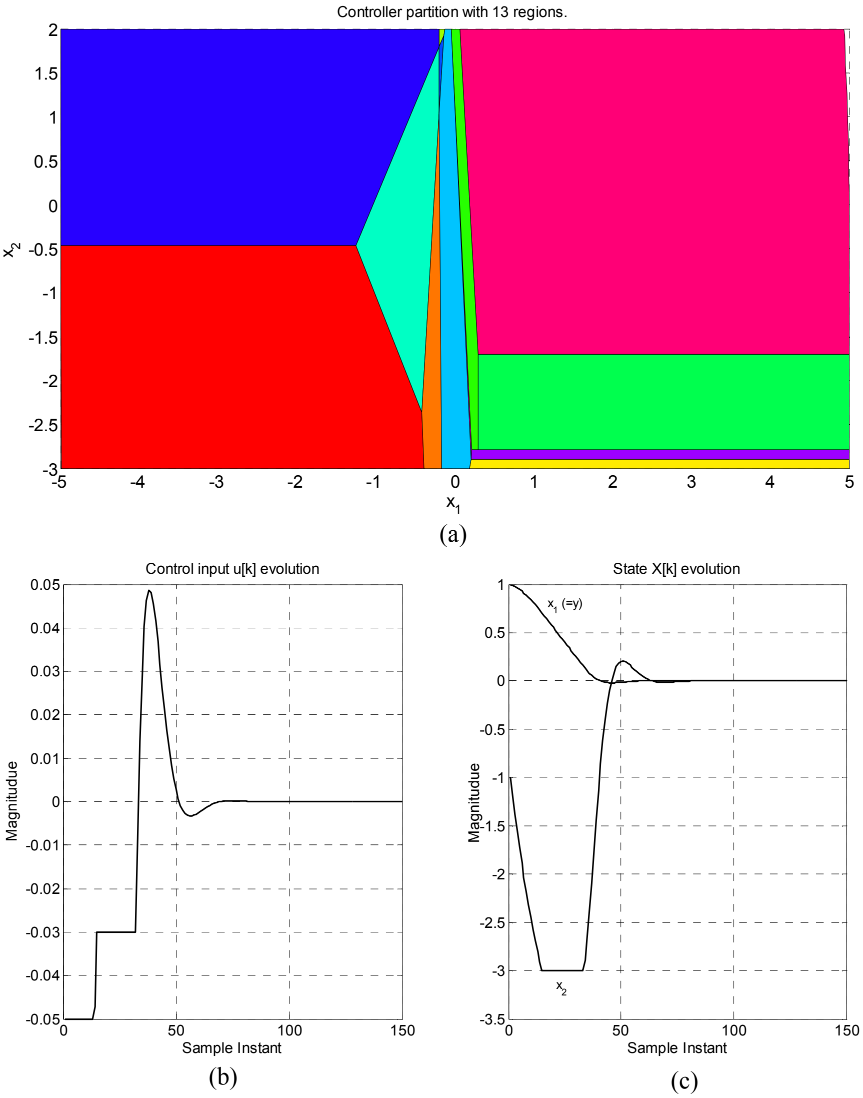

(a)

(b) (c)

Figure 6.9 Simulated response of explicit MPC controller for initial state $x0 = \begin{bmatrix} 1 & -1 \end{bmatrix}^T$.
(a) controller partition (b) control input evolution (c) state evolution

6.4.2 Formulation of model predictive control for speed control and pole-slip prevention

Chapter 3 showed that PI control of the magnetic coupling is ineffectual under lightly loaded conditions, even though the implemented controller is optimal in the ITAE sense. While good speed and load regulation can be achieved under certain conditions, pole-slip can be readily induced. In the presented scenario, with the magnetic coupling operating well below maximum rated torque, a simple change in speed causes the combined load and controller torque to exceed the capability of the magnetic coupling, and consequently the PI controller loses control as a pole-slipping regime is induced. During this transient operation, the controller takes no account of the limitations imposed by the nature of the torque transfer via a magnetic field. In effect the design torque T_G is an inviolable *hard constraint* on the permissible torsional torque T_C , as violation results in instantaneous pole-slipping.

The principal objective of the MPC controller is to therefore prevent excessive magnetic coupling torsion from breaking torque transfer, that is, to prevent *pole-slipping*. As with the PI controller design, the initial MPC formulation is based on the most widely studied linear model of an elastically coupled servo drive system.

A continuous-time state space model for the linearized magnetic coupling is then,

$$\frac{d}{dt}\begin{pmatrix}\omega_M\\ \omega_L\\ T_C\end{pmatrix}=\begin{pmatrix}0 & 0 & -\frac{1}{J_M}\\ 0 & 0 & \frac{1}{J_L}\\ K_{lin} & -K_{lin} & 0\end{pmatrix}\begin{pmatrix}\omega_M\\ \omega_L\\ T_C\end{pmatrix}+\begin{pmatrix}\frac{1}{J_M}\\ 0\\ 0\end{pmatrix}\left(T_{EM}\right)+\begin{pmatrix}0\\ \frac{-1}{J_L}\\ 0\end{pmatrix}\left(T_L\right) \tag{6.37}$$

As T_L represents an unknown load torque demand, and not a control input, the state-space formulation in (6.37) is re-cast with T_L as an extended state. Furthermore, the speed demand (set-point), ω_{ref}, is also incorporated as an extended state, which results in the augmented state space representation (6.38) [75],

$$\frac{d}{dt}\begin{pmatrix}\omega_M\\ \omega_L\\ T_C\\ T_L\\ \omega_{ref}\end{pmatrix}=\begin{pmatrix}0 & 0 & \frac{-1}{J_M} & 0 & 0\\ 0 & 0 & \frac{1}{J_L} & \frac{-1}{J_L} & 0\\ K_{lin} & -K_{lin} & 0 & 0 & 0\\ 0 & 0 & 0 & 0 & 0\\ 0 & 0 & 0 & 0 & 0\end{pmatrix}\begin{pmatrix}\omega_M\\ \omega_L\\ T_C\\ T_L\\ \omega_{ref}\end{pmatrix}+\begin{pmatrix}\frac{1}{J_M}\\ 0\\ 0\\ 0\\ 0\end{pmatrix}\left(T_{EM}\right) \tag{6.38}$$

This representation assumes that both the speed and load torque demands are step-like inputs such that,

$$\frac{dT_L}{dt} = \frac{d\omega_{ref}}{dt} = 0 \tag{6.39}$$

In addition, to achieve speed set-point tracking with no steady-state error, the output is defined as,

$$y_1 = \omega_M - \omega_{ref} \tag{6.40}$$

and to accommodate the available torsional torque that can be utilized by the controller when the magnetic coupling is under load, a further output incorporates the torque equilibrium as,

$$y_2 = T_C - T_L \tag{6.41}$$

The output equation of (6.42) accounts for speed tracking of the motor, y_1; and y_2 determines the maximum available controller torque, given that the aggregate load torque plus controller torque must be no greater than T_G.

$$Y = \begin{pmatrix} 1 & 0 & 0 & 0 & -1 \\ 0 & 0 & 1 & -1 & 0 \end{pmatrix} \begin{pmatrix} \omega_M \\ \omega_L \\ T_C \\ T_L \\ \omega_{ref} \end{pmatrix} \tag{6.42}$$

The model predictive control methodology solves the optimization problem of (6.30), subject to the constraints of (6.31), to determine the optimal control input ***U,*** at each sampling instant [*k*]. A key objective of the controller is to provide good load-side speed tracking. However, in the case of the magnetic coupling it can be posed that the primary objective is to ensure that the coupling does not *pole-slip*, as this represents a total loss of control. The need to obviate over-torque pole-slip, which can occur well before the maximum load torque capability, can be accommodated by enforcing hard constraints on the torsional torque T_C experienced by the magnetic coupling. It is prudent, therefore, to also incorporate the limitations of the motor's power converter directly into the model predictive controller formulation. Both the motor torque limit and the magnetic coupling torque limit constraints are defined thus,

$$\begin{gathered} -12\ \text{N}\bullet\text{m} < T_{EM} < 12\ \text{N}\bullet\text{m} \\ -5.7\ \text{N}\bullet\text{m} < T_C < 5.7\ \text{N}\bullet\text{m} \end{gathered} \tag{6.43}$$

with the assumption that $|T_{EM}|>|T_G|$ in what follows, implying that the motor-side can readily induce pole-slipping of the magnetic coupling.

To realize an MPC controller, the continuous-time system of (6.38) and (6.42) is discretized to allow real-time hardware implementation. Substituting for the relevant parameters from the experimental test rig, and utilizing a sampling rate of 10 milliseconds, the augmented discrete-time state space representation is then,

$$x[n+1] = \begin{bmatrix} 0.6176 & 0.377 & -3.6383 & -0.9001 & 0 \\ 0.4775 & 0.5161 & 4.6046 & -5.5047 & 0 \\ 0.1182 & -0.1181 & 0.1437 & 0.4784 & 0 \\ 0 & 0 & 0 & 1 & 0 \\ 0 & 0 & 0 & 0 & 1 \end{bmatrix} x[n] + \begin{bmatrix} 4.5384 \\ 0.9001 \\ 0.3779 \\ 0 \\ 0 \end{bmatrix} u[n]$$

$$\mathrm{y}[n] = \begin{bmatrix} 1 & 0 & 0 & 0 & -1 \\ 0 & 0 & 1 & -1 & 0 \end{bmatrix} x[n] \tag{6.44}$$

6.5 Simulation study: optimized PI vs. explicit MPC via MPT

To compare the performance of the MPC control strategy with conventional optimized PI control, a simulation study is initially undertaken, presenting the scenario shown in figure 3.21 to both types of control scheme. The control law determined from the optimization problem of (6.30) and (6.31), is piece-wise affine (PWA) and given by,

$$u^r[k] = F^r x[k] + G^r \tag{6.45}$$

where the polyhedral sets, *r,* represent active regions in a partition of the state space *X,* and [*k*] the current time index. F^r, G^r are obtained from the optimization algorithm detailed in [74]. The feedback control law determined from (6.30) and (6.31) is *implicit* and must be calculated, online, at each time step [*k*]. In (6.45) the feedback control law is *explicit* and calculated offline via a multi-parametric QP (mp-QP) program (Multi-Parametric Toolbox – MPT in MATLAB). Importantly, the feedback control laws, whether determined *implicitly* or *explicitly,* are *equivalent* [74]. Consequently, standard MPC tools (QP solvers, simulation software) can be used to evaluate and tune the MPC control strategy.

To show the performance of the proposed solution, figure 6.10 gives the underlying simulation structure. The speed demand and torque demand time profiles are given in figure 3.26 (p.52, Chapter 3) where the load torque is set between 20% and 95% of maximum permissible load torque (1.15 N•m – 5.4 N•m). In constructing the MPC controller, the constraints defined in (6.43) must be incorporated. In terms of the state-space formulation, this represents constraints on the control input $u[k]$, limited by the maximum capability of the drive, and on the state $[x_3] = T_C$, the torsional torque of the magnetic coupling, which must not exceed the designed pull out torque T_G. The remaining states are not subject to any constraints.

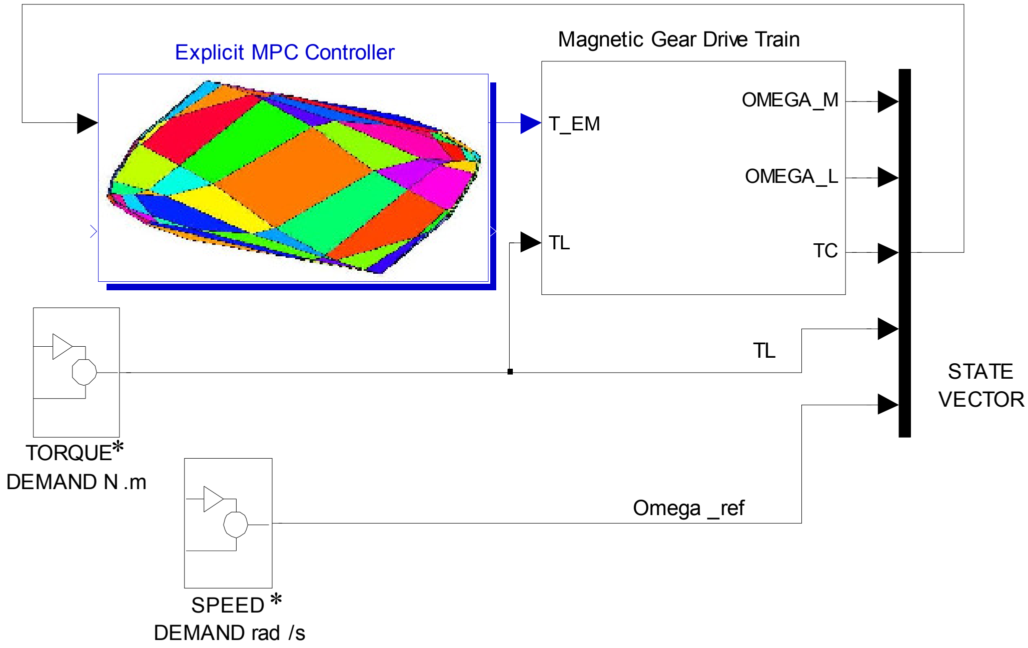

Figure 6.10 Simulation model of explicit model predictive controller

The required state constraint on $[x_3]$ ($= T_C$) to prevent the magnetic coupling from pole-slipping is formally defined as,

$$\begin{pmatrix} -\infty \\ -\infty \\ -T_G \\ -\infty \\ -\infty \end{pmatrix} < \begin{pmatrix} \omega_M \\ \omega_L \\ T_C \\ T_L \\ \omega_{ref} \end{pmatrix} < \begin{pmatrix} \infty \\ \infty \\ T_G \\ \infty \\ \infty \end{pmatrix} \tag{6.46}$$

For the explicit controller the prediction horizon, $N_P = 15$, control horizon, $N_C = 2$, $Q = \mathrm{I}$, $R = 1$, and a sample time $T_s = 10$ milliseconds are chosen. This produces an explicit MPC controller consisting of 245 regions over 5D space.

The performance of the constrained MPC controller is compared with that of the classical optimized PI controller using the baseline speed and torque reference profiles defined in Chapter 3, Section 3.7.1 (figure 3.21). The left-hand side of figure 6.11 demonstrates the performance of the optimized PI controller, while the right-hand side demonstrates the performance of the MPC controller. In this case, a small nominal load torque demand, $T_L = 20\%$

---

* see figure 3.26, p.52 for speed and load torque profiles

of T_G , is applied at t = 3 s, this causing an almost imperceptible perturbation on the speed outputs of both PI and MPC controllers.

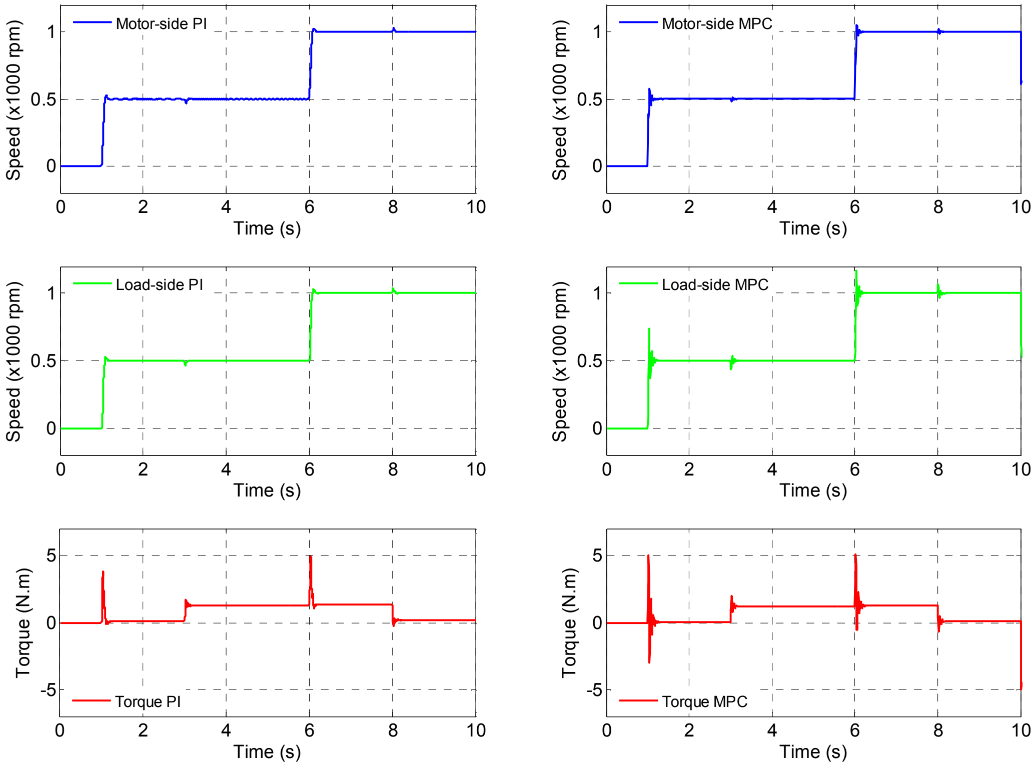

(a)

(b)

Figure 6.11 Performance comparisons T_L = 1.14 N•m (20% T_G) (a) optimized PI (b) constrained MPC

It is evident that no significant differences are apparent between the induced responses of the two controllers for this level of load torque demand. With an increase in load torque demand to just 30% of the maximum rated coupling torque, the outputs are different. As shown in figure 6.12, the PI controller demands too high a torque at t = 6 s when a doubling of output speed is requested. In this case, the magnetic coupling has clearly gone into a pole-slipping mode, as indicated by the load-side speed response and the coupling torque T_C. However, there is no discernible change in the performance of the constrained MPC controller.

As a final illustration, both controllers are now subjected to a load torque demand of 95% of rated design torque, with the dynamics shown in figure 6.13. The performance of the PI controller induces pole-slipping immediately upon application of the torque demand at t = 3 s, despite being less than the maximum rated torque of the magnetic coupling. Meanwhile, the constrained MPC performance is outstanding, and prevents the magnetic coupling from pole-slipping by constraining the torsional torque T_C to just below the ‘break point’ of the coupling.

The trade-off, however, for this constraint is a substantial increase in the settling time of the speed change request at t = 6 s. It is instructive to consider the dynamics of the coupling torque T_C in greater detail. As can be seen from figure 6.14, at the speed change command time t = 3 s, the torque limits at 5.6 N•m (constraint value), just below the breaking torque of the coupling. Once the output speed has reached the set-point the coupling torque settles to the steady-state load demand torque of 5.5 N•m. This example illustrates the outstanding constraint handling capabilities of model predictive control and demonstrates how controller action can prevent unwanted pole-slipping when the load torque is just below the maximum design torque.

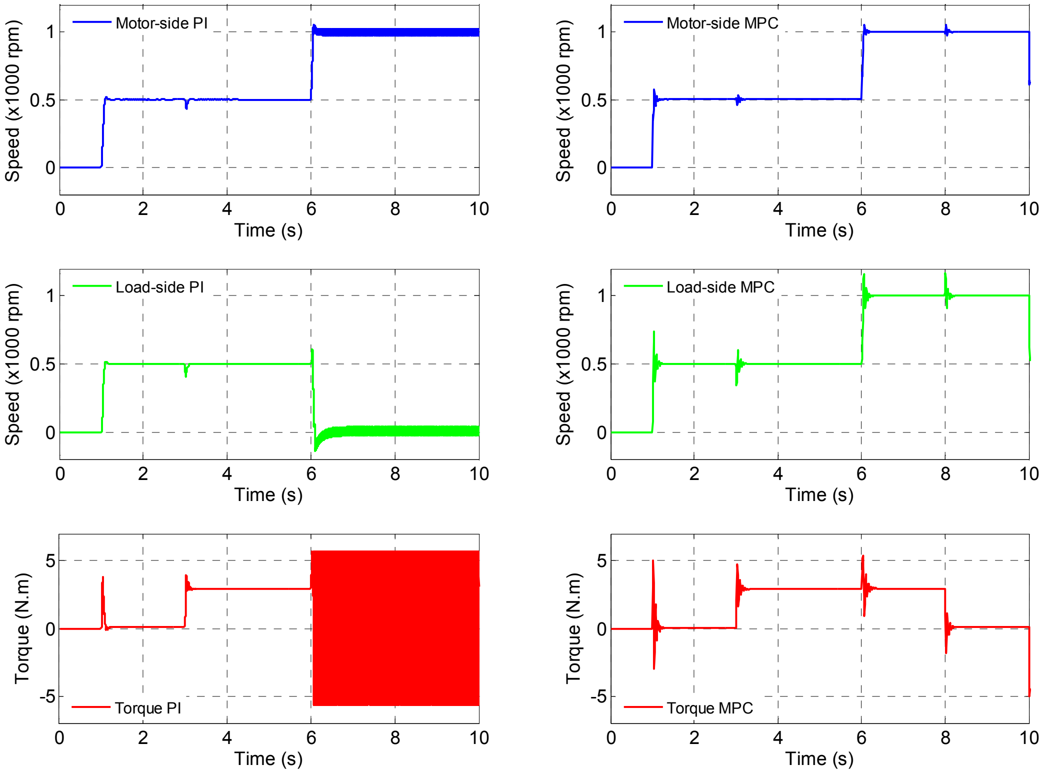

(a) (b)

Figure 6.12 Performance comparisons T_L = 1.71 N•m (30% T_G) (a) optimized PI controller (b) constrained MPC controller

The outstanding simulation results for the model predictive controller demonstrated by the above Simulink results may appear too good to be true. And indeed they are. In figure 6.10 it will be noted that the MPC controller has complete and perfect state feedback. This is unworkable on two counts, (i) it is unlikely that all states needed in the MPC formulation can be measured, (ii) any states that are measured will be subject to noise and other artefacts that are a function of the measurement system. Consequently, it is necessary to provide some form of state estimation to determine the unmeasured state variables and, additionally, to provide an *estimate* of the load torque. The issue of state estimation is considered in the next section. Prior to addressing the problem of state estimation, one final simulation study is presented. To illustrate the efficacy of the explicit model predictive controller formulation, an identical model is formulated in MATLAB's standard Model Predictive Control Toolbox. In effect this simulates MPC as an 'online' optimization process where the closed-loop control is implicit, that is, in the conventional understanding of model predictive control. A comparative plot of both MPC using the traditional implicit approach and MPC via MPT using the explicit formulation is shown in figure 6.15. Identical qualitative behaviour gives a significant degree of validation to the efficacy of the explicit MPC/MPT approach

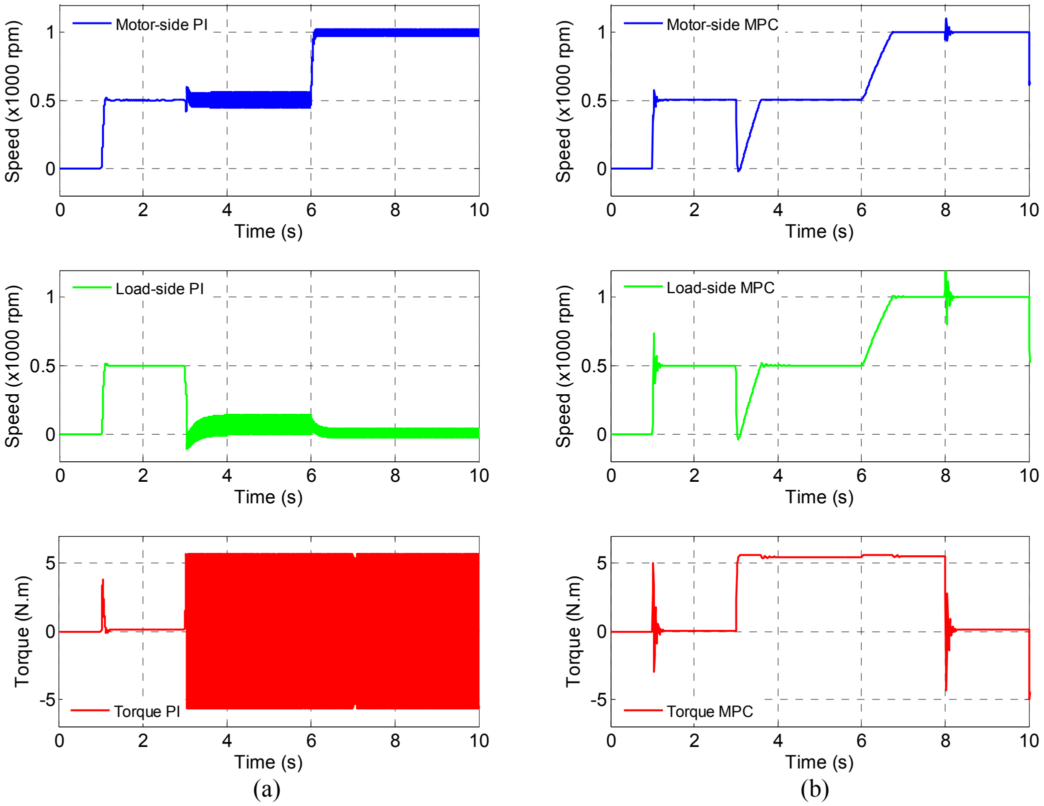

Figure 6.13 Performance comparisons T_L = 5.42 N•m (95% T_G) (a) optimized PI (b) constrained MPC

6.6 State estimation for real-time explicit MPC implementation

The preceding section demonstrated how the use of model predictive control, with a hard constraint on the allowable torsional torque T_C, can prevent the magnetic coupling from pole-slipping when subjected to a speed change under very heavy torque loading. However, in figure 6.10 the input to the MPC controller is the complete state vector as defined in (6.42). The results demonstrated in simulation, e.g. figure 6.13, can only be obtained with perfect state feedback. A particular feature of the approach taken thus far is that only motor-side measurements are available for control purposes. This problem becomes particularly acute for applications where it is prohibitive to use load-side feedback sensors, by virtue of their proximity, reliability, connection, specification, cost or load-side working environment. Applications such as those for aircraft flight control surface actuators, future all-electric automotive power trains and off-shore wind-turbines often fall into this category [67].

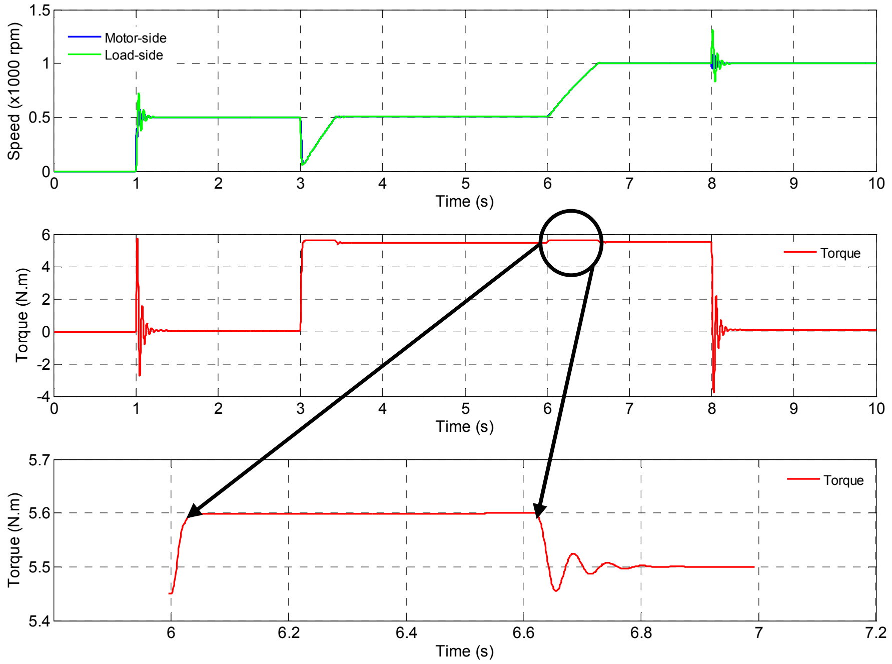

Figure 6.14 State constraint active during speed change command $T_L = 5.42$ N•m (95% T_G)

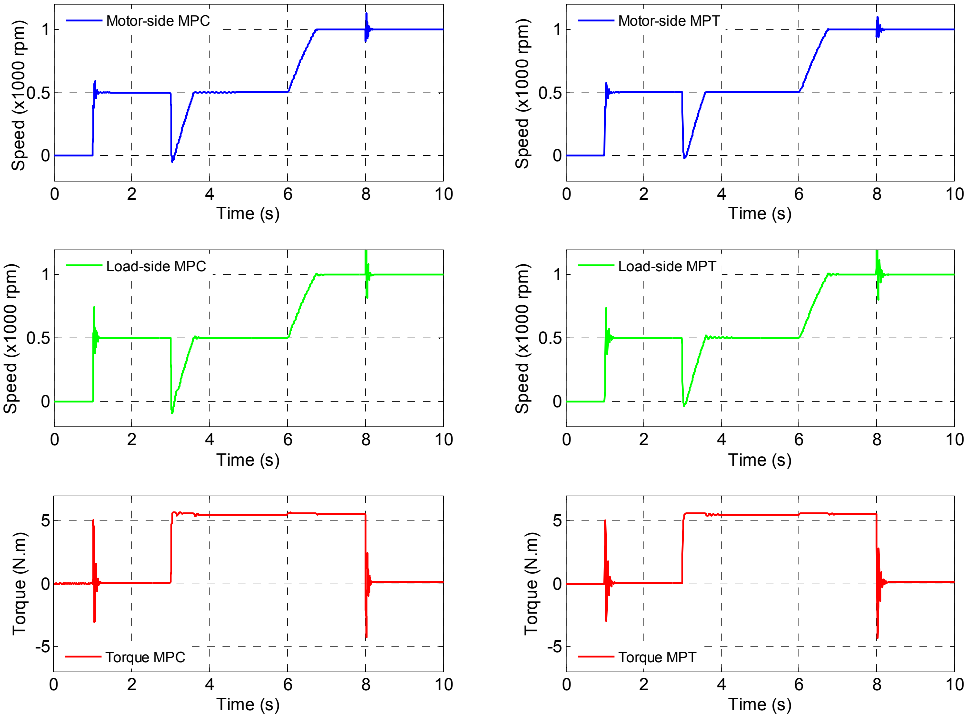

(a) (b)

Figure 6.15 Comparative responses between MPC and MPT Toolboxes at $T_L = 5.42$ N•m (95% T_G)

(a) MPC Toolbox (b) MPT Toolbox

Consequently, with only motor-side variables measured, the remainder of the state vector must be constructed from a state estimator. Furthermore, since the unknown load-torque disturbance is required in the model predictive control formulation, some form of disturbance observer is also a pre-requisite.

To implement the controller of figure 6.10 the state vector must be reconstructed from available inputs and output measurements, and a state estimator used for unmeasured states and load disturbance torque. For the experimental study it is assumed that only motor-side measurements are available for control purposes. Although from the experimental test rig position and velocity measurements are available on both motor- and load-side of the magnetic coupling, load-side measurements are only used for experimental verification and not control purposes.

For the current discussion, it is sufficient that a simple discrete-time Luenberger-type state estimator is used [76]. This is constructed from the state space observation model of (6.47) below, in which the load disturbance torque becomes an augmented state under the assumptions given in (6.39).

$$\frac{d}{dt}\begin{pmatrix}\omega_M\\ \omega_L\\ T_C\\ T_L\end{pmatrix}=\begin{pmatrix}0 & 0 & \frac{-1}{J_M} & 0\\ 0 & 0 & \frac{1}{J_L} & \frac{-1}{J_L}\\ K_{lin} & -K_{lin} & 0 & 0\\ 0 & 0 & 0 & 0\end{pmatrix}\begin{pmatrix}\omega_M\\ \omega_L\\ T_C\\ T_L\end{pmatrix}+\begin{pmatrix}\frac{1}{J_M}\\ 0\\ 0\\ 0\\ 0\end{pmatrix}(T_{EM}) \tag{6.47}$$

Discretization of (6.47) is accomplished using a sampling time of 10 milliseconds with observer poles being placed at the origin, and the observer gain matrix calculated via Ackerman's formula [53]. A block diagram of the real-time hardware implementation of the explicit MPC controller, including discrete-time observer, is shown in figure 6.16, where the discrete-time observer produces estimates for $\hat{\omega}_L$, $\hat{T}_C$, $\hat{T}_L$.

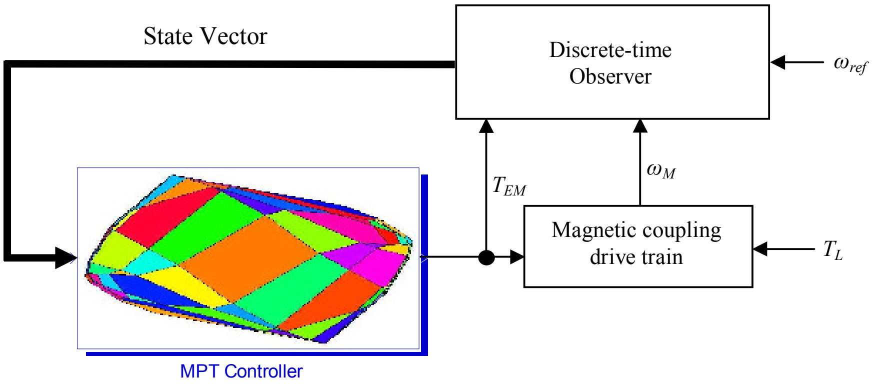

Figure 6.16 Real-time MPC implementation with discrete-time observer

6.7 Experimental results: explicit model predictive speed controller

The model predictive controller simulated in section 6.5 is experimentally tested using on the dSPACE hardware development platform. Figure 6.17 shows the Simulink real-time model used for performance assessment.

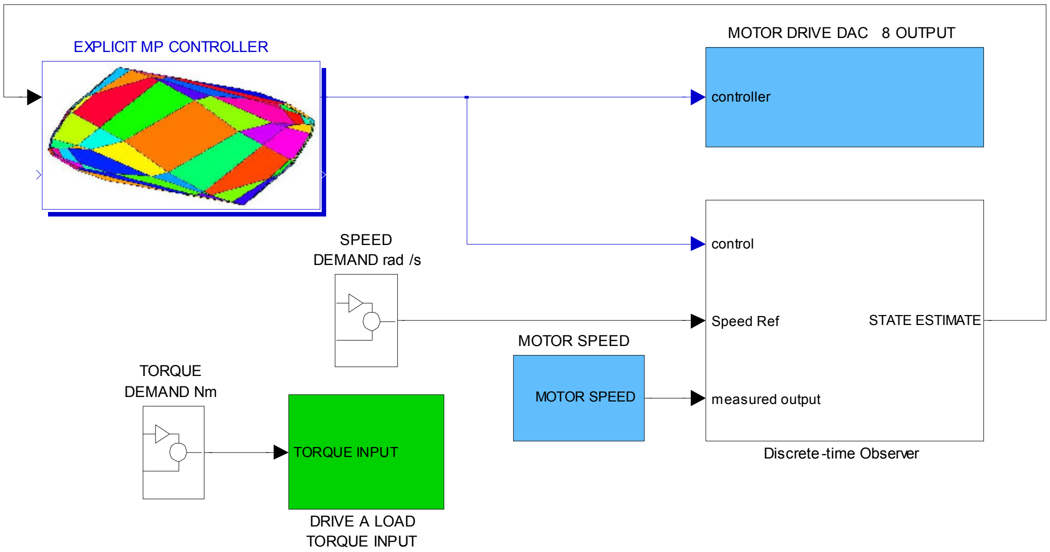

Figure 6.17 Experimental Simulink real-time dSPACE explicit MPC Controller implementation

The scenario simulated in figure 6.12 is now tested experimentally. A constant load torque disturbance of 1.7 N•m (30%) is applied between $t \approx 2.75$ s and $t \approx 7.75$ s, and as indicated in figure 6.18, there is only just perceptible perturbations in both motor-side and load-side speed responses. Notably, at this level of load torque the optimized PI controller was forced immediately into a pole-slipping regime at the speed change command at $t \approx 4.75$ s.

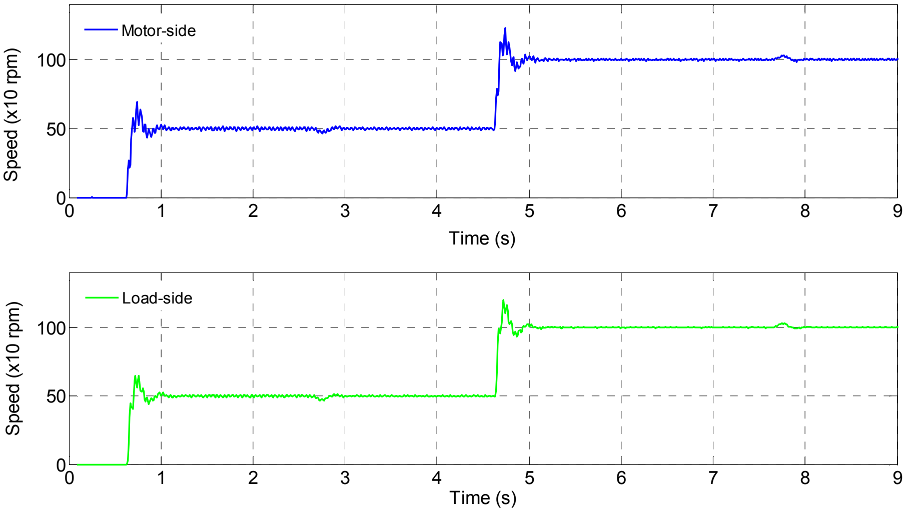

Figure 6.18 Experimental results for explicit MPC with observer and 1.71 N•m (30%) load torque

With the need to accommodate the effects of manufacturing tolerances, variations in magnetic properties due to temperature, safe operating limits etc., a maximum permissible operating range is deemed to be 80% of the pull-out torque T_G, at 20° C. At this level of load torque the optimized PI controller is unable to maintain control, readily resulting in pole-slipping. For the explicit MPC controller the performance at 80% load torque is shown in figure 6.19. Although motor-side and load-side speed perturbations due to load torque are now clearly evident, the model predictive controller invokes constraints on the torsional torque T_C at the speed change ($t \approx 5.5$ s) to successfully prevent pole-slipping. Figure 6.19 shows the superior performance exhibited by the explicit model predictive controller (MPC), compared with the optimized PI controller of figure 3.22, in preventing the magnetic coupling from pole-slipping, even when subjected to maximum permissible load torque. However, it must be noted that while preventing the magnetic coupling from slipping, at this level of constant load torque there is an approximate -5% error in the steady-state motor-side and load-side speeds observed during the application of load torque between $t \approx 3.5$ s and $t \approx 8.5$ s. It is possible that this small error could be eradicated with careful 'tuning' of the MPC controller's parameters, particularly R the control weighting.

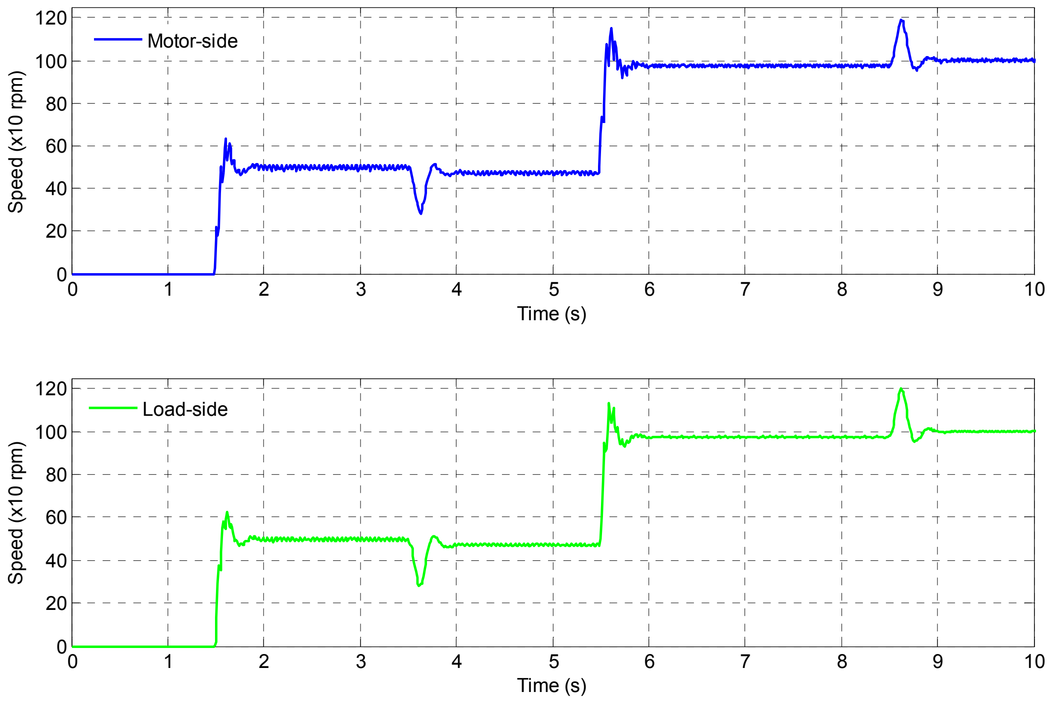

Figure 6.19 Experimental results for explicit MPC with observer and 4.6 N•m (80%) load torque

The experimental results demonstrate significant improvements are obtained with the use of constrained model predictive control, thereby preventing a magnetically-geared drive train from pole-slipping due to combined controller and load torque overload. While conventional model predictive control (MPC) requires online computation of the optimal control input (limiting its use to relatively low bandwidth processes), the use of a mathematically equivalent explicit form of MPC (via multi-parametric programming), which can be calculated offline, combined with a state estimation scheme, requires only a simple look-up table for evaluating the piecewise affine (PWA) controller output.

6.8 Model Predictive Control: Position control case

Model predictive control is now considered for the case of servo position control. Following the same analysis as for the case of MPC speed control, a simulation model of the MPC position controller with state estimation (observer) is illustrated in figure 6.20.

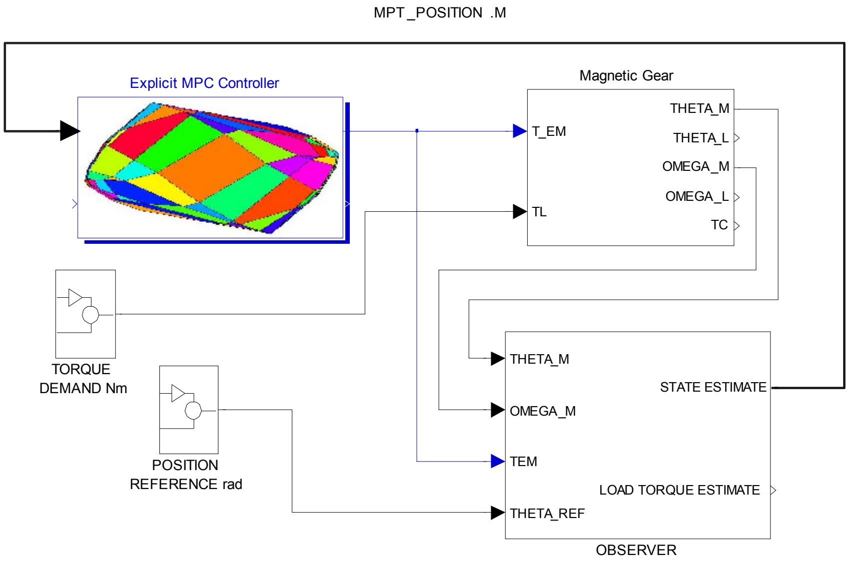

Figure 6.20 MPC Position controller with state estimation

The transient performance of the MPC position controller for a reference position of $\theta_{ref} = 1$ rad and constant load-side torque of 2 N•m (approx 35% of T_G) is shown in figure 6.21. It is clear from figure 6.21 that the transient response due to the onset of load torque is completely unacceptable demonstrating massive, and intolerable, overshoots in both motor-side and load-side positions. Furthermore, once in steady-state both motor-side and load-side have unacceptable steady-state position errors. This can be seen more clearly in figure 6.22, where neither motor-side nor load-side positions obtain the desired set-point. Worse still, with an increase of load torque to just 2.5 N•m (43%) the simulated controller becomes totally unstable. Consequently, further investigation of the MPC position controller is discarded and an alternative approach to set-point load-side position tracking is presented in Chapter 7.

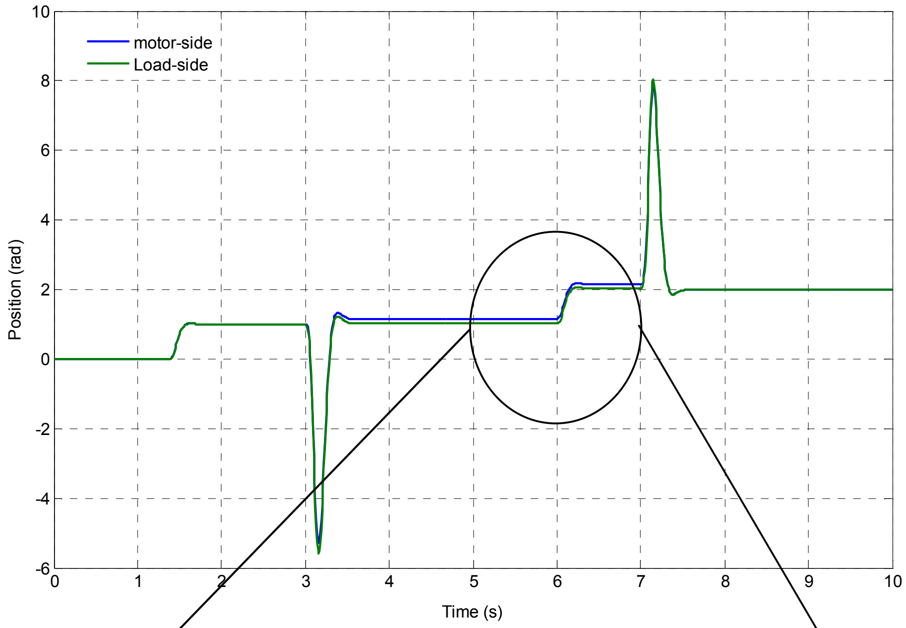

Figure 6.21 MPC Position step response $\theta_{ref} = 1$ rad load torque = 2 N•m (35%)

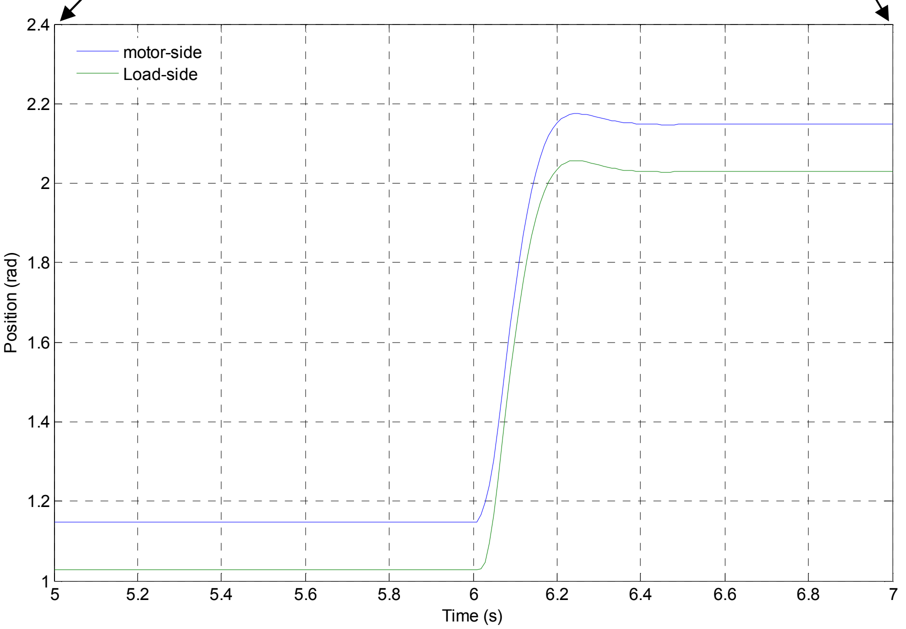

Figure 6.22 MPC Position step response steady-state position errors

6.8 Summary

With conventional PI speed control the magnetic coupling can be forced into a pole-slipping condition when operating with a load torque well below the maximum designed pull-out torque. To obviate under-torque pole-slipping, a model predictive control (MPC) framework has been presented that imposes constraints on the torque through the coupling, thus preventing pole-slip. Explicit MPC via multi-parametric programming produces off-line computation of the control laws, thus allowing implementation on high-speed, real-time hardware. The excellent results obtained using constrained model predictive speed control (MPC) further extends the potential for mechanical gears to be replaced by their magnetic gear counterparts.

Chapter 7

Advanced Techniques: Observer-Based Servo Position Control

7.1 Introduction

Although the optimized ITAE PI and MPC servo *speed* controllers demonstrated excellent set-point tracking and disturbance rejection capabilities, the optimized ITAE rate feedback PD servo *position* controller provided excellent set-point tracking but with ineffectual load-side disturbance torque rejection capabilities. The simulated MPC position controller suffered from exceptionally poor performance and was therefore discarded. In both cases, motor-side and load-side of the magnetic coupling had large positional errors when the drive train was subjected to a constant load torque. This is demonstrated clearly in the experimental results of figure 4.12, in which significant steady-state errors result from a constant load-side torque disturbance. To obviate load disturbance position errors, feedforward corrective action is investigated further in this chapter, under the assumption that good estimates of the load-side disturbance torque can be obtained from a state or disturbance observer. Consequently, this chapter is principally focused on obtaining a high-performance servo position controller with the capability to eradicate steady-state position errors due to a constant load-side torque disturbance. It should be noted that the issue of pole-slip for the position control scenario is not considered specifically herein, but is discussed further in section 9.3 of Chapter 9. The principal aim of this chapter is to consider servo position control utilizing state and load torque disturbance estimation under the assumption that only motor-side variables are measured.

7.2 Load-side disturbance torque estimation via state observer

With the servo position drive train under optimized ITAE PD control excellent set-point position tracking is obtained. However when the drive train is subjected to a constant load torque, significant motor- and load-side position errors result, as shown in figure 7.1.

The results of figure 7.1 show good set-point position tracking under no-load conditions, but with a load-side disturbance torque of 95% of T_G, very large position error occurs. Furthermore, the significant effects of the magnetic coupling's high compliance can be observed in the large position differential between the load-side and motor-side of the coupling. Consequently, both the load-torque disturbance steady-state position error, and the load-side torsion error must be corrected by the controller

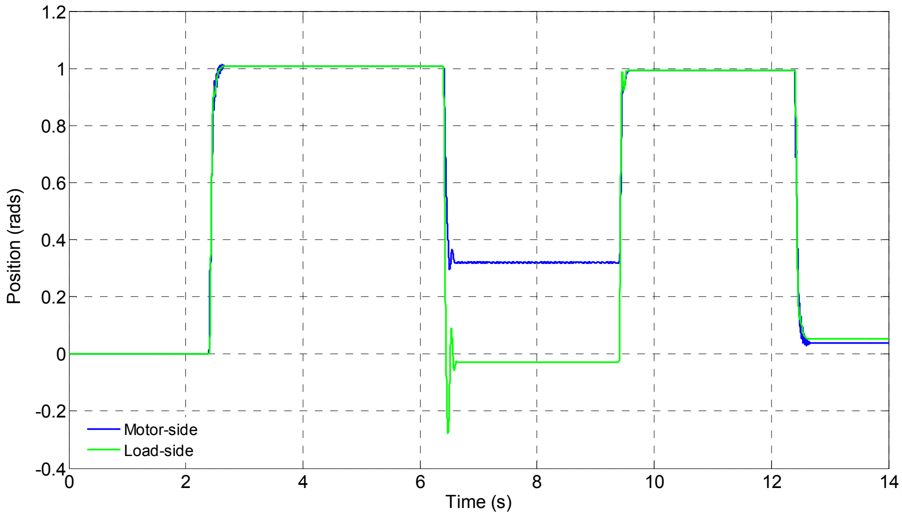

Figure 7.1 Experimentally measured results: position step $\theta_{ref} = 1$ rad $T_L = 5.42$ N•m (95%) load torque .

To remove the steady-state position error caused by the load-side disturbance, an *estimate* of the load-side disturbance is added to the position controller output and fed directly to the torque actuator. One technique to remove the steady-state error, at least on the motor-side, is to feed forward an estimate of the load torque. For this purpose, a simple practical disturbance observer can be designed using standard input/output state estimation, in effect, a Luenberger-type observer [77]. Furthermore, since both motor-side position and angular velocity are measured, the use of a reduced-order observer becomes applicable.

From the equations of motion, a linearized state-space representation of the magnetic coupling is given by,

$$\frac{d}{dt}\begin{pmatrix}\theta_M\\ \omega_M\\ \theta_L\\ \omega_L\end{pmatrix}=\begin{pmatrix}0 & 1 & 0 & 0 & 0\\ \frac{-K_{lin}}{J_M} & 0 & \frac{K_{lin}}{J_M} & 0 & 0\\ 0 & 0 & 0 & 1 & 0\\ \frac{K_{lin}}{J_L} & 0 & \frac{-K_{lin}}{J_L} & 0 & 0\end{pmatrix}\begin{pmatrix}\theta_M\\ \omega_M\\ \theta_L\\ \omega_L\end{pmatrix}+\begin{pmatrix}0\\ \frac{1}{J_M}\\ 0\\ 0\end{pmatrix}(T_{EM})+\begin{pmatrix}0\\ 0\\ 0\\ \frac{-1}{J_L}\end{pmatrix}(T_L) \tag{7.1}$$

where T_L represents the unknown disturbance torque at the load-side of the magnetic coupling. The disturbance torque estimation is predicated on the basis of an augmented state-variable description, where the disturbance torque is considered to be a slowly time varying input that satisfies the following requirement,

$$\frac{dT_L}{dt}\approx 0 \tag{7.2}$$

An augmented state-variable description for load torque estimation then becomes,

$$\frac{d}{dt}\begin{pmatrix}\theta_M\\ \omega_M\\ \hdashline \theta_L\\ \omega_L\\ T_L\end{pmatrix}=\left(\begin{array}{cc:ccc}0 & 1 & 0 & 0 & 0\\ \frac{-K_{lin}}{J_M} & 0 & \frac{K_{lin}}{J_M} & 0 & 0\\ \hdashline 0 & 0 & 0 & 1 & 0\\ \frac{K_{lin}}{J_L} & 0 & \frac{-K_{lin}}{J_L} & 0 & 0\\ 0 & 0 & 0 & 0 & 0\end{array}\right)\begin{pmatrix}\theta_M\\ \omega_M\\ \hdashline \theta_L\\ \omega_L\\ T_L\end{pmatrix}+\begin{pmatrix}0\\ \frac{1}{J_M}\\ \hdashline 0\\ 0\\ 0\end{pmatrix}\left(T_{EM}\right) \tag{7.3}$$

A linear state estimator (observer) for the system of (7.3) is given by,

$$\dot{\hat{x}} = A\hat{x} + Bu + L\left(y - C\hat{x}\right) \tag{7.4}$$

where L represents the Luenberger observer gain matrix. The closed loop poles of the system in (7.4), and consequently error dynamics, are calculated using the pole-placement technique and the MATLAB commands `place` or `acker` (an implementation of Ackerman's formula).

To obtain an estimate of load torque $\hat{T}_L$, a reduced order observer based on Gopinath's method is adopted for simplicity [78]. As shown in (7.3), the state vector is partitioned into measured x_m (with both motor-side position and motor-side velocity available from the dSPACE hardware), and unmeasured (estimated) x_e, parts. This partition is more compactly expressed as,

$$\begin{bmatrix}\dot{x}_m\\ \hline \dot{x}_e\end{bmatrix}=\left[\begin{array}{c|c}A_{11} & A_{12}\\ \hline A_{21} & A_{22}\end{array}\right]\begin{bmatrix}x_m\\ \hline x_e\end{bmatrix}+\begin{bmatrix}B_1\\ \hline B_2\end{bmatrix}\left(T_{EM}\right) \tag{7.5}$$

where A_{11}, $\mathbf{B}_1$ etc are indicated by the dotted lines in (7.3). Figure 7.2 shows the dynamic structure of the reduced-order observer including all estimated states, where L_{MIN} is the minimum-order observer gain matrix.

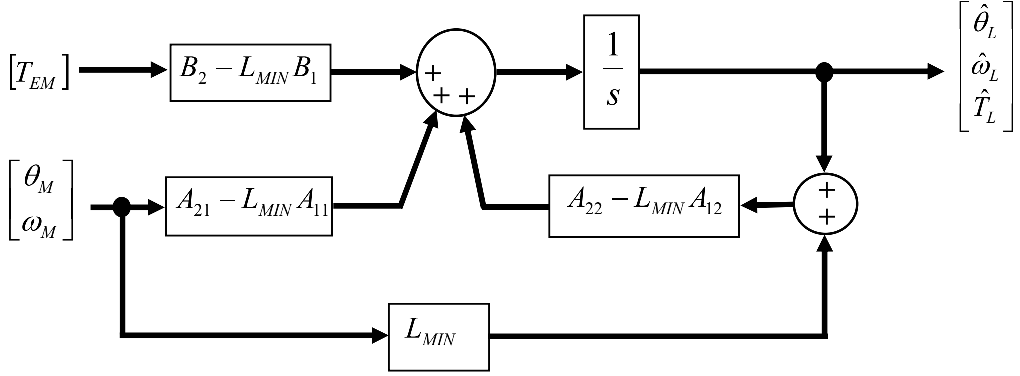

Figure 7.2 Dynamic structure of reduced order observer

With an estimate of the load-side disturbance, feedforward corrective action becomes feasible. A block diagram of this feedforward technique is shown in figure 7.3, where the controller plus disturbance torque observer is shown inside the red (dashed line) box.

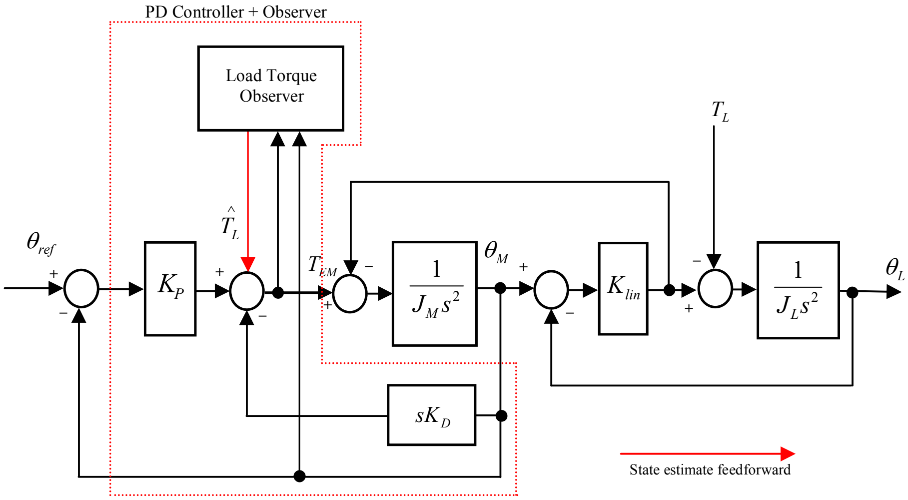

Figure 7.3 Load disturbance torque feedforward compensation using state observer

To illustrate the efficacy of this approach, a simulation study is conducted with ideal disturbance torque feedback for a command position θ_{ref} = 4 rad and disturbance torque of 3 N•m, shown in figure 7.4.

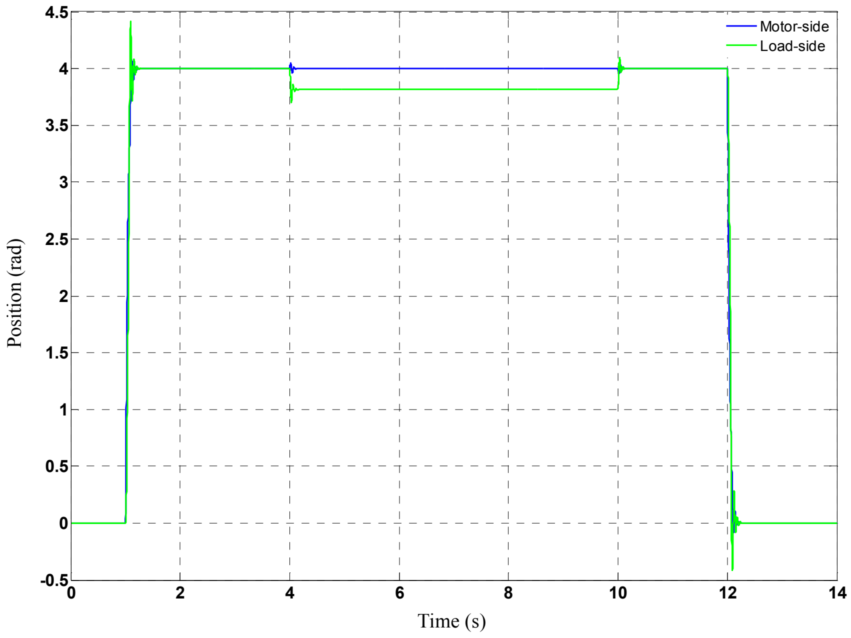

Figure 7.4 Simulated load disturbance feedforward compensation using *actual* load torque position θ_{ref} = 4 rad and disturbance torque T_L = 3 N•m (≈50%)

As shown in figure 7.4 perfect load disturbance torque rejection occurs resulting in zero motor-side position error. However, at the load-side significant positional error results from the inherent torsion of the magnetic coupling, due to the highly compliant nature of the torque transmission via magnetic means. If the position controlled servo system is referenced to the position of the *load-side* of the coupling, then additional torsion angle compensation is also required. This is considered further in Section 7.3. A simulation of disturbance torque feedforward compensation utilizing an *estimate* of the load torque, $\hat{T}_L$, is shown in figure 7.5 where the load-side disturbance is successfully rejected.

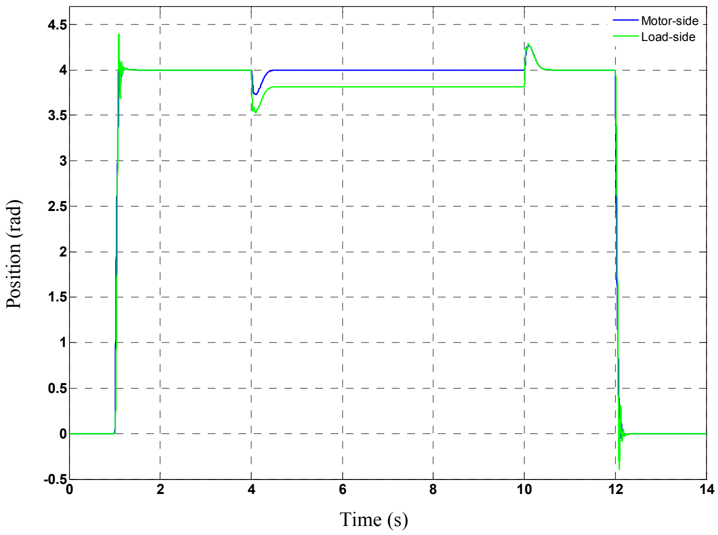

Figure 7.5 Simulated disturbance torque feedforward compensation with load torque observer position θ_{ref} = 4 rad and disturbance torque T_L = 3 N•m (≈50%)

Figure 7.6, $\hat{T}_L$ and $\hat{\theta}_L$, demonstrate the high integrity of the states estimates from the observer.

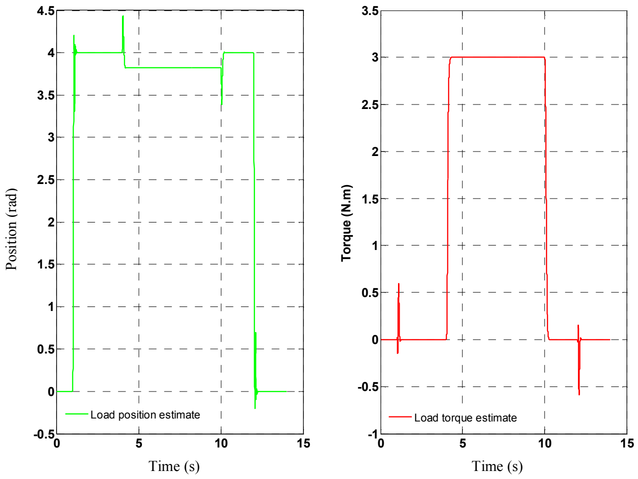

(a) (b)

Figure 7.6 Simulated state estimates for observer poles at -50 (a) $\hat{\theta}_L$ (b) $\hat{T}_L$

7.3 Load-side position referenced system

In a motion control positioning system with significant torsional flexibility there exists the possibility for a large positional difference between the motor-side and load-side of the drive train. In extremis, under maximum permissible load torque, the mechanical displacement angle approaches 30° (0.59 rad) and for accurate positioning of the load-side of the magnetic coupling additional torsion angle compensation is also required. In situations where both a motor-side and load-side position sensor exists no significant difficulty arises. However, the assumption is made that only motor-side measurements are available, and therefore torsion angle compensation must be provided from an estimate of the load-side angle when the magnetic coupling is subjected to a load disturbance torque.

In section 7.2 an observer was developed to provide an estimate of the load torque used for feedforward corrective action in the presence of a load-side disturbance. As shown in figure 7.5 this provides disturbance torque rejection resulting in zero motor-side position error. Since the observer also provides an estimate of the load-side position, this can be used as the position reference, instead of the motor-side position measurement, providing torsion angle correction at the load-side of the drive train. This modification is implemented within the controller structure as shown in figure 7.7

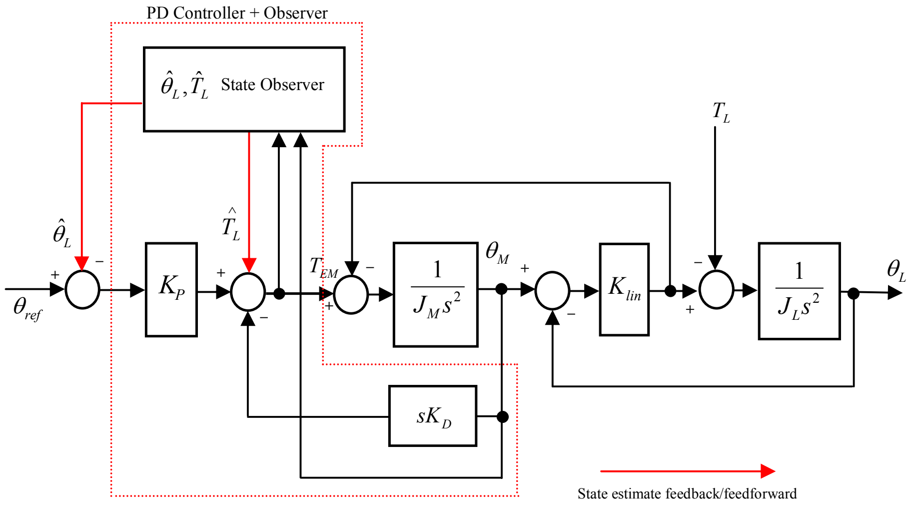

Figure 7.7 Load disturbance and torsion angle compensation using state observer

A simulation of the controller structure in figure 7.7 is shown in figure 7.8 for a reference step of θ_{ref} = 4 rad and load torque disturbance of 1 N•m. The results show that both load torque disturbance and torsion angle error have been fully compensated for and the load has no steady-state position error.

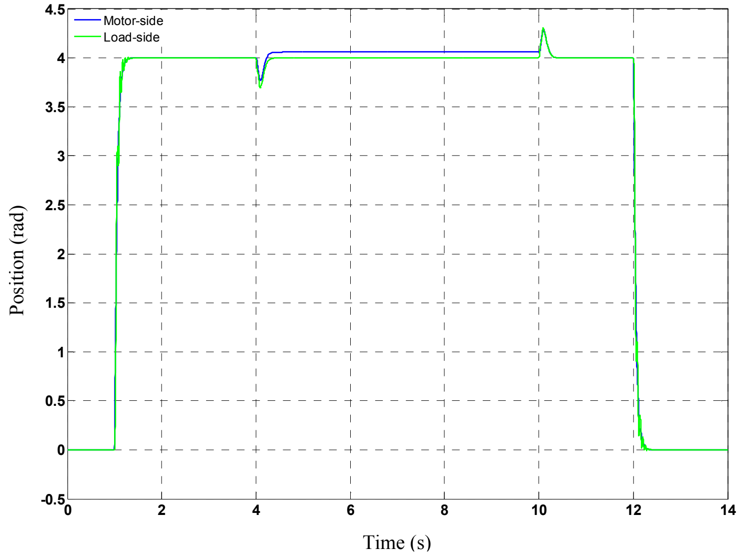

Figure 7.8 Simulated load disturbance and torsion angle compensation using an observer position $\theta_{ref} = 4$ rad and disturbance torque $T_L = 1$ N•m (≈20%)

7.3.1. Load-side angle observation error and correction

The results shown in figure 7.8 indicate excellent torsion angle correction and load disturbance rejection when using state estimate feedforward and feedback compensation. However, what is not indicated in figure 7.8 is the observer load position error due to the nonlinearity of the magnetic coupling's torque transfer characteristic. With a load disturbance torque of only 1 N•m, the magnetic coupling behaves in an entirely linear way. To illustrate the nonlinearity error inherent in an observer constructed from a linear model, consider the simulation results of figure 7.9 with a reference position of $\theta_{ref} = 0$ rad and disturbance of 75% of rated torque T_G.

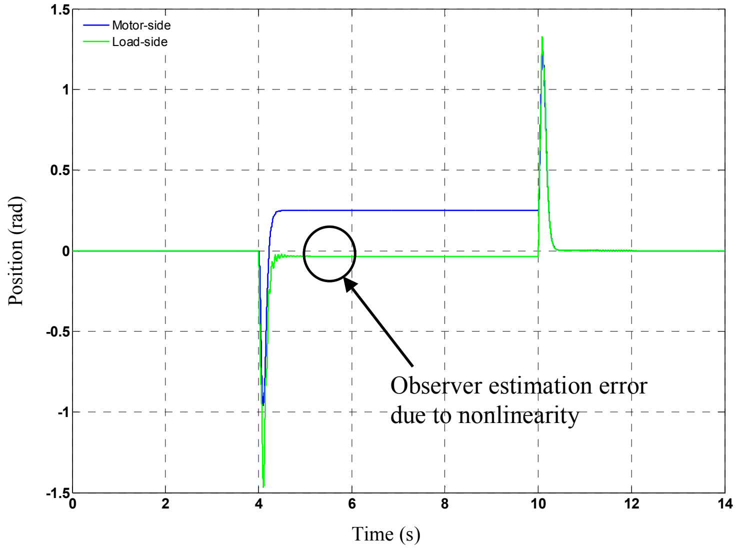

Figure 7.9 Simulated observer estimation error due to nonlinear torque transfer

The observed load-side position differs from the true position because the state estimation is predicated on the basis of a *linearized* two-inertia model. Consequently, a modification of the load-side position estimate is necessary. In steady-state the linear load-side position estimate is given by,

$$\hat{\theta}_L = \frac{\hat{T}_L}{K_{lin}} \tag{7.6}$$

For the magnetic coupling the torsion angle estimate is,

$$\hat{\theta}_L = \frac{\sin^{-1}\left(\frac{\hat{T}_L}{T_G}\right)}{p} \tag{7.7}$$

Consequently, the correction angle is the difference between the linear and nonlinear estimates thus,

$$\begin{aligned} \Delta\hat{\theta}_L &= \frac{\hat{T}_L}{K_{lin}} - \frac{\sin^{-1}\left(\frac{\hat{T}_L}{T_G}\right)}{p} = \frac{\hat{T}_L}{pT_G} - \frac{\sin^{-1}\left(\frac{\hat{T}_L}{T_G}\right)}{p} \\ \Delta\hat{\theta}_L &= \frac{1}{p}\left(\frac{\hat{T}_L}{T_G} - \sin^{-1}\left(\frac{\hat{T}_L}{T_G}\right)\right) \end{aligned} \tag{7.8}$$

The observer estimate must be corrected such that the *true* load-side position estimate becomes,

$$\hat{\theta}_L^{true} = \Delta\hat{\theta}_L + \hat{\theta}_L^{obs} \tag{7.9}$$

and the observer is modified as follows,

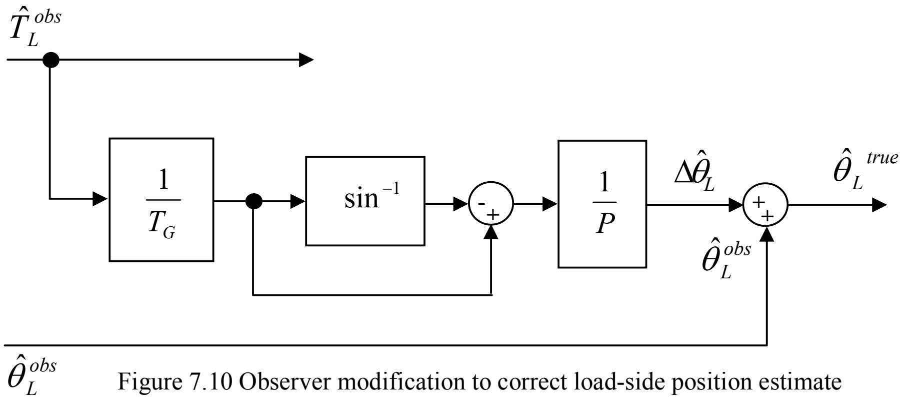

Figure 7.10 Observer modification to correct load-side position estimate

With the inclusion of the observer modification in figure 7.10, the load-side position error due to nonlinearity is eradicated, as shown in the simulation results of figure 7.11.

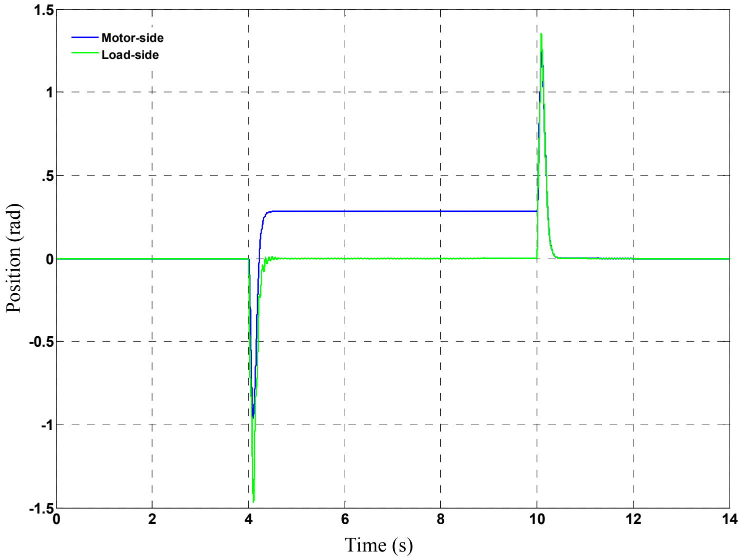

Figure 7.11 Simulation of load disturbance with observer nonlinearity correction

7.4 Experimental results: observer-based disturbance rejection

The controller structure of figure 7.7 is now verified on the dSPACE hardware development platform with the position demand profile and the load torque profile shown in figure 7.12.

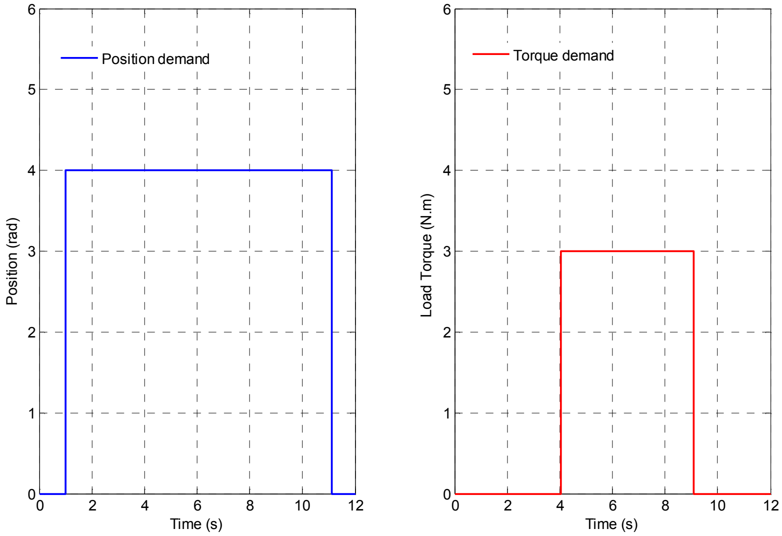

Figure 7.12 Test profiles (a) reference position demand (b) load torque demand

Results for the experimental implementation of the controller structure given in figure 7.7, including the observer modification of figure 7.10, are shown in figures 7.13 and 7.14.

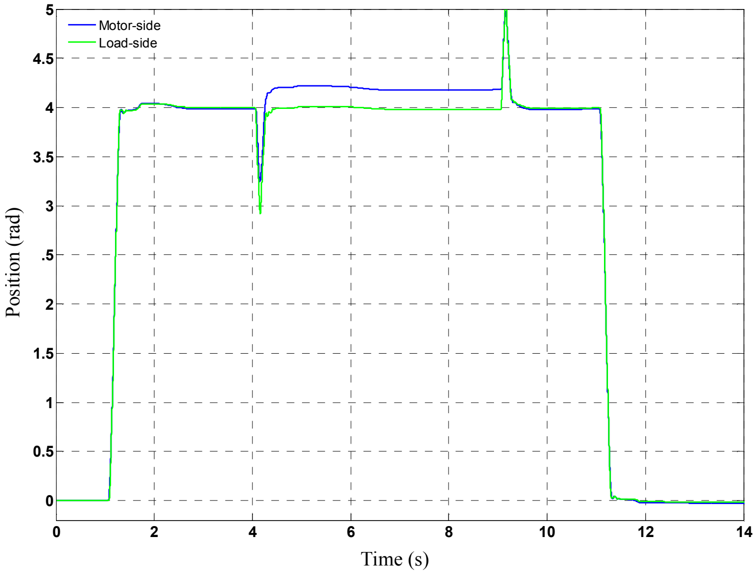

Figure 7.13 Experimentally measured results: load torque & torsion angle compensation via an observer position θ_{ref} = 4 rad and disturbance torque T_L = 3 N•m (≈50%)

The load-side position control of the experimental system shows excellent agreement with the simulated results. However, small variations in load-side position are due to the somewhat poor integrity of the estimated load torque. Figure 7.13 shows experimental measurements of the estimates of load-side position and load-side disturbance torque. While the estimate of load-side position is excellent, the estimate of disturbance torque is poor. This should be contrasted with the simulated load torque estimate which produces a perfect pulse.

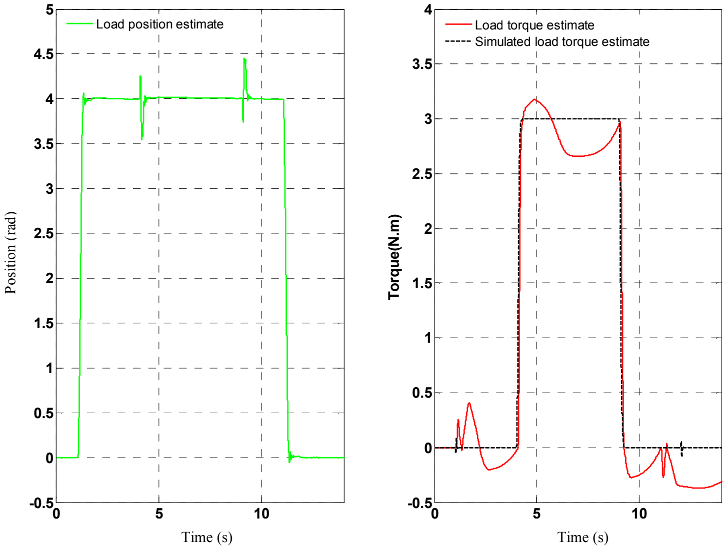

(a) (b)

Figure 7.14 Experimental results state observer (a) $\hat{\theta}_L^{obs}$ (b) $\hat{T}_L^{obs}$

To effect some improvement in the estimated load-side disturbance torque, state estimation is split over two separate observers, a fast observer for estimation of the load-side position and a slow observer for estimation of the load-side disturbance and nonlinearity correction. The modified controller structure is shown in figure 7.15.

The performance of the experimental system incorporating the dual observer approach is outstanding as can be seen from figure 7.16. Both steady-state disturbance and torsion angle error have been compensated for providing perfect load-side set-point position tracking.

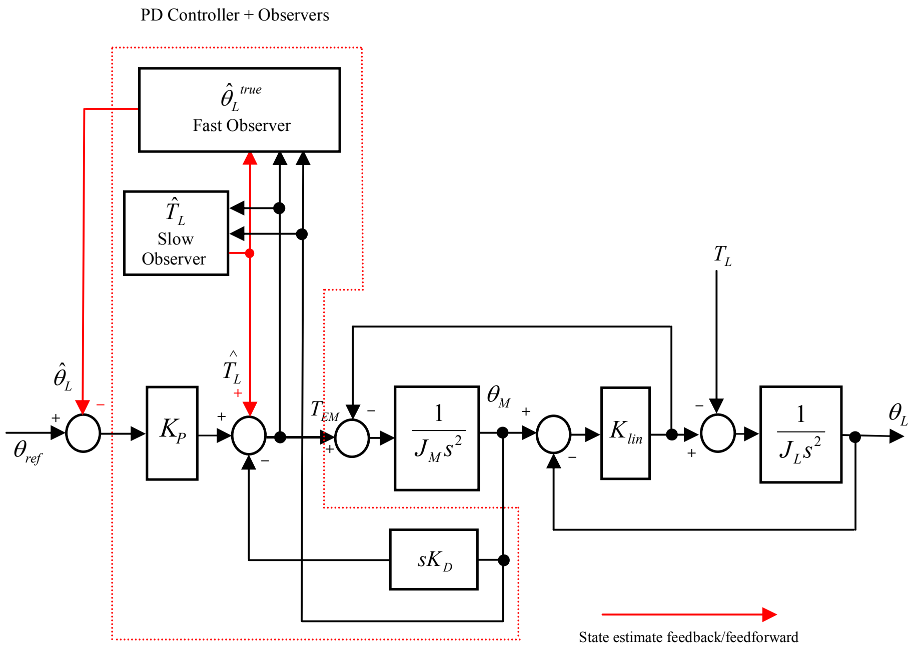

Figure 7.15 Modified controller with dual fast and slow observers

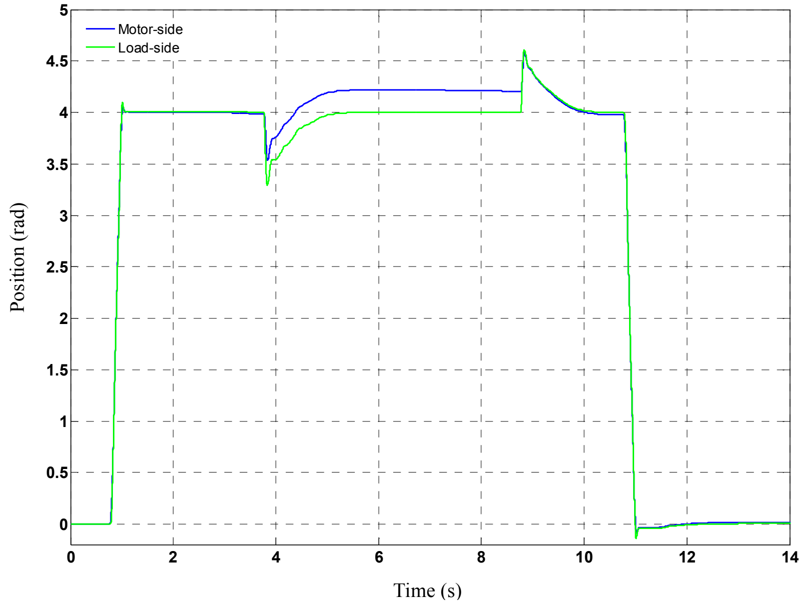

Figure 7.16 Experimentally measured results: dual observer controller of figure 7.15 position θ_{ref} = 4 rad and disturbance torque T_L = 3 N•m (≈50%)

In terms of observer poles, the slow disturbance torque observer has its poles located ten times slower than the load position (fast) observer's poles. Consequently, as can be seen in the experimental observer estimates, figure 7.17, the disturbance torque estimate is considerably improved over the single observer case (see figure 7.17(b)).

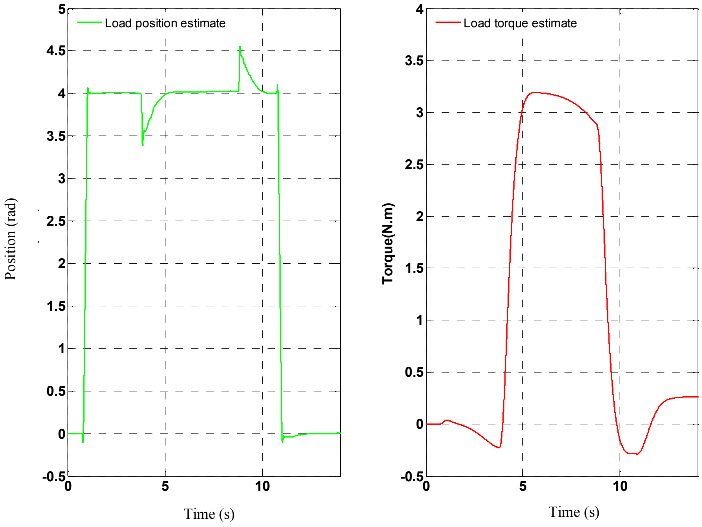

(a) (b)

Figure 7.17 Experimentally measured results: dual observers (a) $\hat{\theta}_L^{true}$ (b) $\hat{T}_L^{obs}$

The price to be paid for the improved load-side disturbance rejection is an increase in the rise time at the start and end of the load-side disturbance. In this scenario there exists a trade-off between the speed of the transient response and the stability of the load torque estimate. To illustrate this further, with the observer poles of the slow observer moved to be twice as fast as previously, the experimental results are shown in figures 7.18 & 7.19.

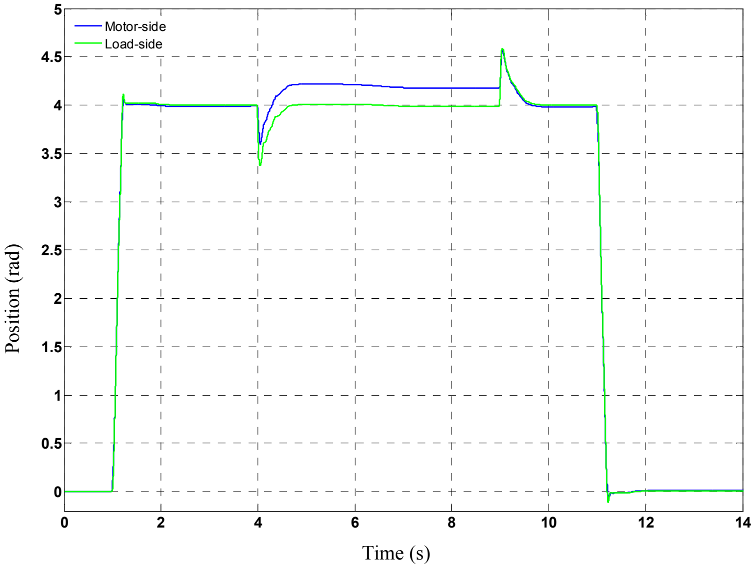

Figure 7.18 Experimentally measured results: dual observer with faster disturbance torque observer position θ_{ref} = 4 rad and disturbance torque T_L = 3 N•m (≈50%)

As can be seen in figure 7.18 a significant improvement in the transient response is accompanied by a slight deterioration in the load-side position tracking. This is confirmed by the experimental load torque estimate, figure 7.19(b), showing a somewhat degraded estimate of the load-side disturbance torque.

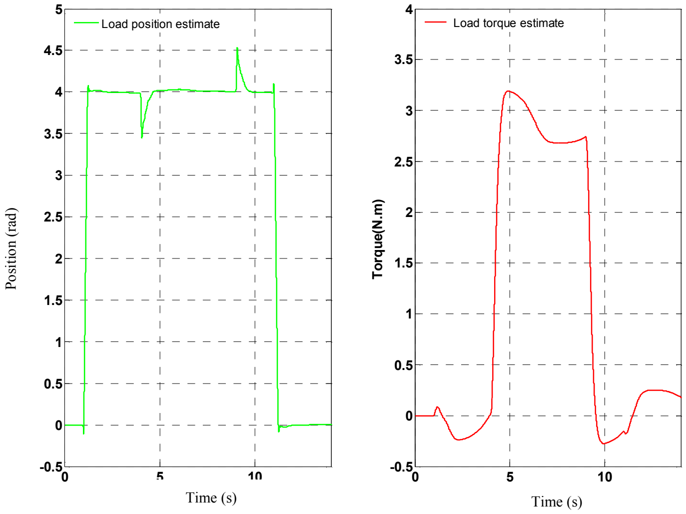

(a) (b)

Figure 7.19 Experimentally measured state estimates for dual observer (a) $\hat{\theta}_L^{obs}$ (b) $\hat{T}_L^{obs}$

Load-side torque disturbances produce significant set-point position tracking errors due to inherent steady-state error in the PD controller and further exacerbated by the torsion of the magnetic coupling. To prevent steady-state load-torque disturbance error and torsion angle error, an enhanced dual observer, with nonlinearity error correction, can be adopted to compensate for both sources of position inaccuracy utilizing only motor-side measurements.

7.5 Summary

Optimized ITAE PD position control provides excellent set-point position tracking provided there is no external disturbance torque. To compensate for a constant load-side disturbance torque feedforward corrective action is implemented via a state observer. In addition, the inherent compliance of the magnetic coupling introduces significant torsion-induced positional errors if a load-side referenced position system is considered. With the introduction of a disturbance observer and state estimator both types of positional error are compensated for. The effect of nonlinearity in the observer estimates is also considered, and a nonlinearity error correction term incorporated into the state estimation scheme.

Chapter 8

Nonlinear Approaches

8.1 Introduction

The preceding chapters have considered approaches to the control problem of the magnetic coupling from a predominantly linear perspective, adopting a linearized (approximated) model of the nonlinear characteristics. Conventional linearization of this form is an approximation and is mostly valid at, or close to, the chosen operating point. In Chapter 5 the effects of linearization about different operating points have been investigated, leading to qualitatively different behaviours. In this chapter, nonlinear approaches to the control of the magnetic coupling are considered, in particular, feedback linearization, an entirely different approach to traditional system approximation using Jacobian linearization [79]. The objective of feedback linearization is to determine both a nonlinear control law and a nonlinear state transformation that produces an *exact* linearization, either from an input-output or input-state of the originating nonlinear system. However, the analysis in this chapter is circumscribed by two important considerations: (i) no account is taken of external load-side torque disturbances in the first instance, this essentially restricts the nonlinear model to a single input single output (SISO) nonlinear system, (ii) the condition of pole-slipping, either controller-induced or load-induced (or both) is also not considered herein, definitively restricting the operating characteristics of the magnetic coupling to be within the principal mechanical displacement angle range, that is, $-30° < \theta_D < 30°$. These issues are returned to briefly in section 9.3. For the present discussion, the stated objective is to provide a control methodology that will allow the magnetic coupling to demonstrate entirely *linear* behaviour throughout its entire operating range, with load disturbance torque and pole-slipping issues deferred for future consideration and analysis.

It is now shown that the derived nonlinear control law and state transformation results in a linear system when input-output feedback linearization is applied. Furthermore, the introduction of an outer loop state variable control structure allows the optimized ITAE step response to be obtained throughout the entire speed or position input range. This results in ‘zero flat’ step response error surfaces for the entire input range space for both position and speed control. In addition, a further derived benefit of feedback linearization is excellent robustness to parameter variations in terms of modelled inertias and friction coefficients.

8.2 Nonlinear modelling of magnetic coupling

In Chapter 3 it was shown that the magnetic coupling possesses a torque transfer characteristic described by $T_C = T_G \sin(p\theta_D)$, a plot of which is shown in figure 2.12. Consideration is now given to a nonlinear state space representation of the magnetic coupling as a single-input single-output (SISO) nonlinear system, under the initial assumptions of zero friction, zero damping and disturbance free, as follows,

$$\begin{bmatrix} \dot{\theta}_M \\ \dot{\omega}_M \\ \dot{\theta}_L \\ \dot{\omega}_L \end{bmatrix} = \begin{bmatrix} \omega_M \\ \dfrac{-1}{J_M}\sin(p(\theta_M - \theta_L)) \\ \omega_L \\ \dfrac{1}{J_L}\sin(p(\theta_M - \theta_L)) \end{bmatrix} + \begin{bmatrix} 0 \\ \dfrac{1}{J_M} \\ 0 \\ 0 \end{bmatrix} T_{EM} \tag{8.1}$$

For notational convenience and consistency with conventional nonlinear systems theory, the following substitutions are made for the remainder of this chapter,

$$\begin{bmatrix} \theta_M \\ \omega_M \\ \theta_L \\ \omega_L \end{bmatrix} \equiv \begin{bmatrix} x_1 \\ x_2 \\ x_3 \\ x_4 \end{bmatrix}$$

$$\theta_D = (\theta_M - \theta_L) \equiv x_D = (x_1 - x_3) \tag{8.2}$$

A further constraint on the subsequent analysis is that the magnetic coupling is restricted to its principal mechanical displacement angle, $-30^\circ < \theta_D < 30^\circ$, and therefore does not enter a pole-slipping regime. From (2.5) the transmitted torque is a trigonometric (sin) function of the difference between two states. To simplify the subsequent analysis, a finite polynomial approximation is determined for the torque transfer characteristic over the first principal mechanical displacement angle, shown in figure 8.1.

The approximated torque transfer characteristic of figure 8.1 is indistinguishable from figure 2.12 over the principal displacement angle and is described by,

$$T_C = \gamma\theta_D - \psi\theta_D^3 \equiv \gamma x_D - \psi x_D^3 \tag{8.3}$$

where $\gamma = 16.9$ and $\psi = 22.4$.

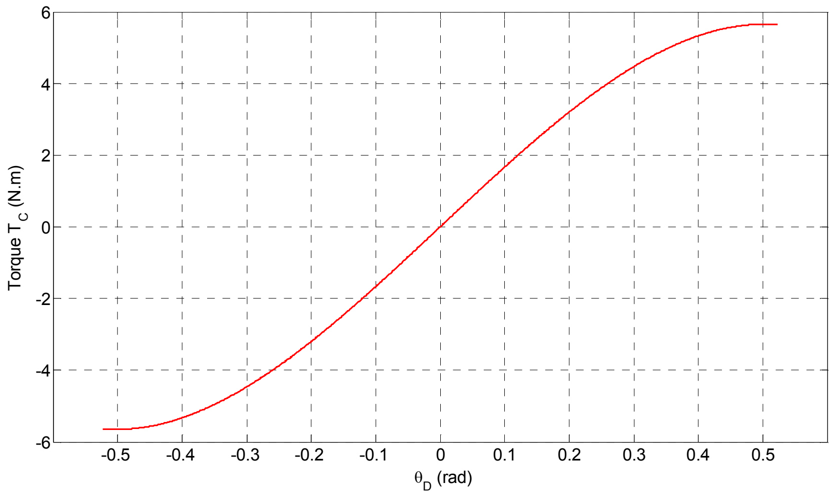

Figure 8.1 Cubic approximation to torque transfer characteristic for principal displacement angle

To demonstrate the absolutely local (principal displacement angle) dependence of this cubic approximation, figure 8.2 shows both the original torque characteristic T_C, and its cubic approximation over the entire 2π radians of displacement angle.

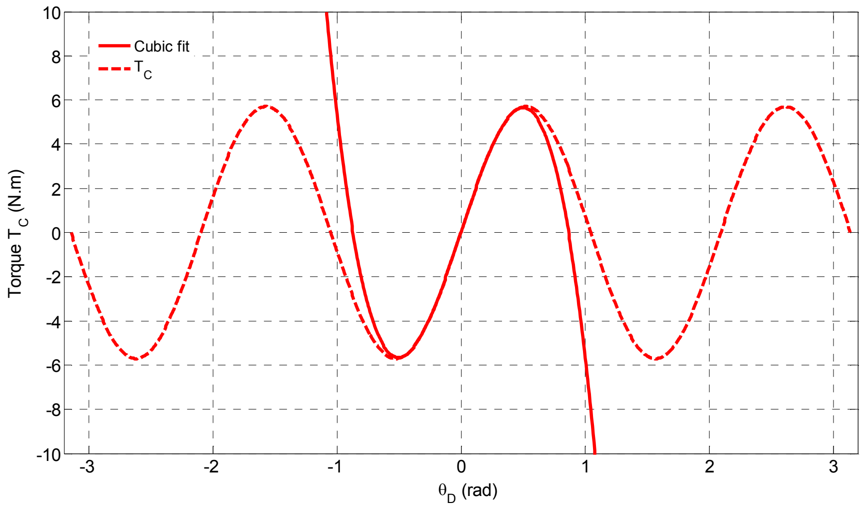

Figure 8.2 Torque characteristic over 2π radians and cubic approximation

With the simplified torque transfer function the nonlinear state space model of (8.1) is now described by,

$$\begin{bmatrix}\dot{x}_1\\ \dot{x}_2\\ \dot{x}_3\\ \dot{x}_4\end{bmatrix} = \begin{bmatrix} x_2 \\ \frac{-1}{J_M}\left(\gamma x_D - \psi x_D^3\right) \\ x_4 \\ \frac{1}{J_L}\left(\gamma x_D - \psi x_D^3\right)\end{bmatrix} + \begin{bmatrix}0\\ \frac{1}{J_M}\\ 0\\ 0\end{bmatrix} T_{EM} \tag{8.4}$$

The nonlinear SISO system of (8.4) is now represented in *control-affine* form defined by,

$$\begin{aligned} \dot{x} &= f(x) + g(x)u \\ y &= h(x) \end{aligned} \tag{8.5}$$

with,

$$f(x) = \begin{bmatrix} x_2 \\ \frac{-1}{J_M}\left(\gamma x_D - \psi x_D^3\right) \\ x_4 \\ \frac{1}{J_L}\left(\gamma x_D - \psi x_D^3\right) \end{bmatrix}$$

$$g(x) = \begin{bmatrix} 0 \\ \frac{1}{J_M} \\ 0 \\ 0 \end{bmatrix} \tag{8.6}$$

$$u \quad = T_{EM}$$

8.3 Feedback linearization

While excellent results using Jacobian linearization were shown to be achievable in Chapters 3 and 4, Chapter 5 highlighted some of the effects of the inherent nonlinearity, shown particularly in the step response error surfaces, (cf. figure 5.6). Here, feedback linearization is adopted to fully account for the intrinsic nonlinearity of the magnetic coupling. Prior to its detailed study however, a number of pre-requisite mathematical tools and preliminary results are now considered.

8.3.1 Mathematical tools

For the analysis of nonlinear systems, a number of mathematical results from differential geometry and topology become pre-requisite, and are stated here, without proof, and with considerable brevity. More detailed, and mathematically rigorous expositions, can be found in Isidori [80] and Nijmeijer [81].

Definition 8.1 (Scalar and Vector Gradients) For a scalar function $h(x)$ of state vector x, the gradient of h is given by ∇h,

$$\nabla h = \frac{\partial h}{\partial x} \tag{8.7}$$

representing a row-vector of elements $(\nabla h)_j = \partial h / \partial x_j$. The Jacobian of vector field *f*(*x*) is denoted by ∇f,

$$\nabla f = \frac{\partial f}{\partial x} \tag{8.8}$$

representing an *n* x *n* matrix of elements $(\nabla f)_{ij} = \partial f_i / \partial x_j$.

(Note: With slight abuse of notation, the symbol x without subscript denotes the state vector, while x_i refers to the i^{th} element of the state vector).

Definition 8.2 (Lie Derivatives) Let *h*(*x*) be a smooth scalar function of vector *x*, and *f*(*x*) be a smooth vector field, the derivative of *h* with respect to *f*(*x*) is called the Lie Derivative and is denoted by,

$$L_f h(x) = \frac{\partial h(x)}{\partial x} f(x) = \nabla h f(x) \tag{8.9}$$

and is a scalar function. Lie derivatives are defined recursively such that,

$$\begin{aligned} L_f{}^0 h(x) &= h(x) \\ L_f{}^i h(x) &= L_f\left(L_f{}^{i-1} h(x)\right) \end{aligned} \tag{8.10}$$

Also, if *g*(*x*) is a vector field the scalar function $L_g L_f h(x)$ is given by,

$$L_g L_f h(x) = \frac{\partial\left(L_f h(x)\right)}{\partial x} g(x) \tag{8.11}$$

Given a single input single output (SISO) nonlinear system of the form,

$$\begin{aligned} \dot{x} &= f(x) + g(x)u \\ y &= h(x) \end{aligned} \tag{8.12}$$

differentiating the output gives,

$$\dot{y} = \frac{dh}{dt} = \frac{\partial h}{\partial x}\frac{dx}{dt} = L_f h(x) + L_g h(x) u \tag{8.13}$$

and consequently Lie derivatives become the principal tool for calculating derivatives of the output of nonlinear systems.

Definition 8.3 (Relative Degree) For the nonlinear system of (8.12) the relative degree is the smallest integer *r* for which the following holds true,

$$\begin{aligned} L_g L_f^{\,r-1} h(x) &\neq 0 \\ L_g L_f^{\,r-2} h(x) &= 0 \end{aligned} \tag{8.14}$$

$\forall\ x$ in the neighbourhood of a given operating point x_0.

Definition 8.4 (Diffeomorphism and State Transformation) A function $\Phi(x): \Re^n \longrightarrow \Re^n$ is called a diffeomorphism if its inverse $\Phi^{-1}(x)$ exists and is smooth.

A diffeomorphism is used to transform the set of states of a nonlinear system to a new nonlinear or linear coordinate system. Coordinate transformations are important for input-state feedback linearization and state feedback control. (Note: 'smooth' in this sense means that continuous partial derivatives exist for function and inverse function).

8.3.2 Preliminary results

The following results are required for the determination of the linearizing feedback law and the state transformation (diffeomorphism) necessary to establish the conditions for exact input to output feedback linearization and optimized state feedback. Mechanical displacement angle, and its powers, are defined thus,

$$\begin{aligned} x_D &= (x_1 - x_3) \\ x_D^2 &= x_1^2 - 2x_1x_3 + x_3^2 \\ x_D^3 &= x_1^3 - 3x_1^2x_3 + 3x_1x_3^2 - x_3^3 \end{aligned} \tag{8.15}$$

Certain required vector derivatives are given by,

$$\nabla x_D = [1 \quad 0 \quad 0 \quad -1]$$

$$\nabla x_D^2 = [2x_D \quad 0 \quad -2x_D \quad 0]$$

$$\nabla x_D^3 = [3x_D^2 \quad 0 \quad -3x_D^2 \quad 0]$$

$$\nabla[x_2 x_D^2] = \begin{bmatrix} 2x_2 x_D & x_D^2 & -2x_2 x_D & 0 \end{bmatrix}$$
$$\nabla[x_4 x_D^2] = \begin{bmatrix} 2x_4 x_D & 0 & -2x_4 x_D & x_D^2 \end{bmatrix} \tag{8.16}$$

where $\nabla x_D = \dfrac{\partial x_D}{\partial x_i}$ for $i = 1..n$.

8.3.3 Input to output feedback linearization for position control

For position control of the load-side of the magnetic coupling, the SISO nonlinear state space model is given by,

$$\dot{x} = \begin{bmatrix} x_2 \\ -\dfrac{1}{J_M}\left(\gamma x_D - \psi x_D^3\right) \\ x_4 \\ \dfrac{1}{J_L}\left(\gamma x_D - \psi x_D^3\right) \end{bmatrix} + \begin{bmatrix} 0 \\ \dfrac{1}{J_M} \\ 0 \\ 0 \end{bmatrix} T_{EM}$$
$$y = h(x) = x_3 = \{\theta_L\} \tag{8.17}$$

The methodology of input-output feedback linearization is to successively differentiate the output until the input T_{EM} appears. Differentiating (8.17) gives,

$$\dot{y} = \frac{\partial h}{\partial x} f(x) + \frac{\partial h}{\partial x} g(x) T_{EM}$$
$$\dot{y} = L_f h(x) + L_g h(x) T_{EM} \tag{8.18}$$
$$\dot{y} = x_4 + (0) T_{EM} = x_4$$

and the Lie derivative $L_g h(x) = 0$. Consequently, it is necessary to differentiate until $L_g h(x) \neq 0$, repeated differentiation of the output results in the following.

Second derivative,

$$\ddot{y} = \frac{\partial \left\lfloor L_f h(x) \right\rfloor}{\partial x} f(x) + \frac{\partial \left\lfloor L_f h(x) \right\rfloor}{\partial x} g(x) T_{EM}$$
$$\ddot{y} = L_f{}^2 h(x) + L_g L_f h(x) T_{EM}$$
$$\ddot{y} = \frac{1}{J_L}\left(\gamma x_D - \psi x_D^3\right) + (0) T_{EM} = \frac{1}{J_L}\left(\gamma x_D - \psi x_D^3\right) = L_f{}^2 h(x) \tag{8.19}$$
$$L_g L_f h(x) = 0$$

third derivative,

$$\begin{aligned}
\dddot{y} &= \frac{\partial\left\lfloor L_f{}^2 h(x)\right\rfloor}{\partial x} f(x) + \frac{\partial\left\lfloor L_f{}^2 h(x)\right\rfloor}{\partial x} g(x) T_{EM} \\
\dddot{y} &= L_f{}^3 h(x) + L_g L_f{}^2 h(x) T_{EM} \\
\dddot{y} &= \frac{1}{J_L}(x_2 - x_4)(\gamma - 3\psi x_D^2) + (0)T_{EM} = \frac{1}{J_L}(x_2 - x_4)(\gamma - 3\psi x_D^2) = L_f{}^3 h(x) \\
L_g L_f{}^2 h(x) &= 0
\end{aligned} \tag{8.20}$$

fourth derivative,

$$\begin{aligned}
\ddddot{y} &= \frac{\partial\left[L_f{}^3 h(x)\right]}{\partial x} f(x) + \frac{\partial\left[L_f{}^3 h(x)\right]}{\partial x} g(x) T_{EM} \\
\ddddot{y} &= L_f{}^4 h(x) + L_g L_f{}^3 h(x) T_{EM} \\
\ddddot{y} &= \frac{-6\psi x_2 x_D}{J_L}(x_2 - x_4) - \frac{1}{J_M J_L}(\gamma x_D - \psi x_D^3)(\gamma - 3\psi x_D^2) + \frac{6\psi x_4 x_D}{J_L}(x_2 - x_4) \\
&\quad - \frac{1}{J_L^2}(\gamma x_D - \psi x_D^3)(\gamma - 3\psi x_D^2) + \frac{1}{J_M J_L}(\gamma - 3\psi x_D^2) T_{EM} \\
L_g L_f{}^3 h(x) &= \frac{1}{J_M J_L}(\gamma - 3\psi x_D^2)
\end{aligned} \tag{8.21}$$

As T_{EM} appears at the fourth derivative, the nonlinear SISO system of (8.17) has relative degree $r = 4$ (Definition 8.3). The linearizing control law is given by,

$$T_{EM} = \frac{1}{L_g L_f{}^3 h(x)}\left(v - L_f{}^4 h(x)\right) \tag{8.22}$$

where v is a ‘synthetic input’, and the feedback linearized dynamics from input v to output y is,

$$\ddddot{y} = v \tag{8.23}$$

For the output $y = h(x) = x_3$ the relative degree $r = n = 4$, the system order, and input-output feedback linearization results in *complete* linearization of the original nonlinear SISO system defined in (8.17). Complete in this sense means that all the system dynamics are linearized and no zero (or internal) dynamics need to be taken into consideration. Furthermore, the linearization (8.23) is not in any sense an approximation, but results in a totally linear system between the output y and the synthetic input v. In general, a feedback linearizing law can be formed from,

$$u = \frac{1}{L_g L_f^{\,r-1} h(x)} \left(v - L_f^{\,r} h(x) \right)$$

$$L_g L_f^{\,r-1} h(x) \neq 0 \qquad (8.24)$$

$$r \leq n$$

and the fully linearized ($r = n$), or partially linearized ($r < n$), nonlinear system is reduced to,

$$\overset{r}{y} = v \qquad (8.25)$$

Figure 8.3 illustrates how feedback linearization acts as an ‘inner loop’ creating a linear relationship between the output *y* and the synthetic input *v*. It then becomes feasible to apply many of the well-known linear control techniques for the ‘outer loop’ control to generate *v*.

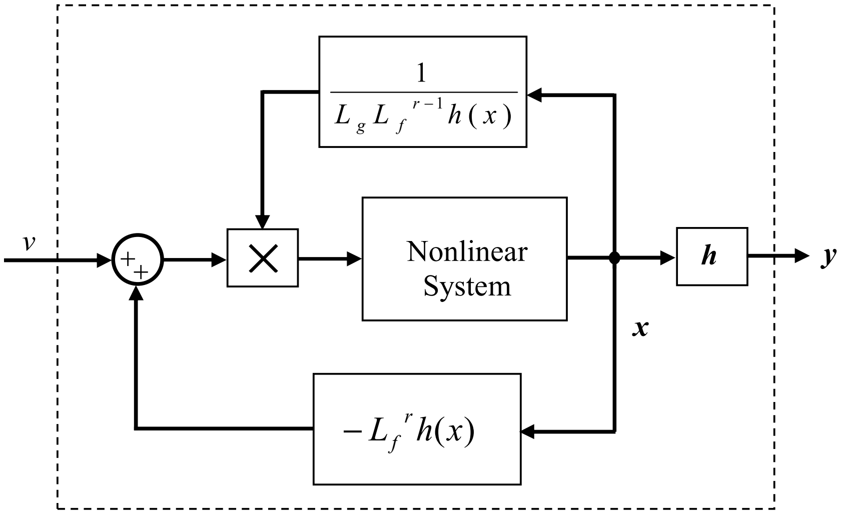

Figure 8.3 Feedback linearization of a nonlinear system

A consequence of (8.25) is that the system of (8.5) appears as a linear chain of integrators, as demonstrated in figure 8.4.

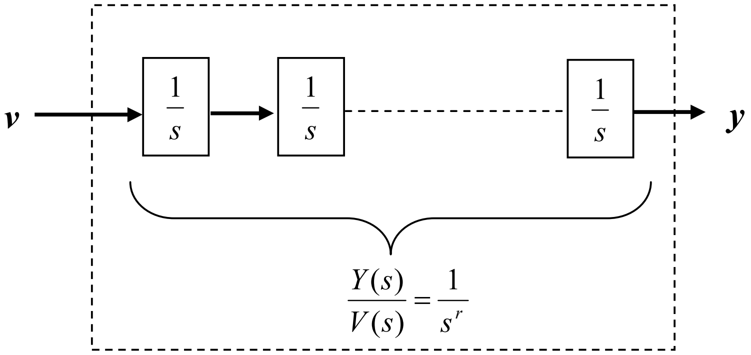

Figure 8.4 Linear chain of *r*-integrators after feedback linearization

The feedback linearized system of figure 8.3 has a particularly simple canonical linear state space structure which can be obtained by adopting the Byrnes-Isidori normal form [82]. It is possible to transform the nonlinear system to normal form via a diffeomorphism in the following manner. For a SISO nonlinear system with relative degree $r \le n$ the normal form is,

$$\left.\begin{array}{l} \phi_1(x) := h(x) \equiv z_1 \\ \phi_2(x) := L_f h(x) \equiv z_2 \\ . \\ . \\ \phi_r(x) := L_f{}^r h(x) \equiv z_r \end{array}\right\} \begin{array}{l} \textit{r states which depend} \\ \textit{on the output y and its} \\ \textit{derivatives – chain of} \\ \textit{integrators} \end{array}$$

$$\left.\begin{array}{l} \eta_1(x) \\ . \\ . \\ \eta_{n-r}(x) \end{array}\right\} \begin{array}{l} \textit{n-r further states if} \\ \textit{relative degree less than} \\ \textit{system order} \end{array} \tag{8.26}$$

However, as derived in (8.21), $r = n$ and additional η states are not necessary for the position control under discussion. (The issue of η_i dynamics will be considered further in section 8.4). The diffeomorphism $\Phi(x) : \Re^n \longrightarrow \Re^n$ is defined thus,

$$\Phi(x) \to \begin{bmatrix} \phi_1 \\ \phi_2 \\ \phi_3 \\ \phi_4 \end{bmatrix} \tag{8.27}$$

and provided its Jacobian is full rank, the diffeomorphism is a valid state transformation [83], [84]. As a consequence of the relative degree $r = n$, the z_i dynamics possess the simple form,

$$\begin{bmatrix} \dot{z}_1 \\ \dot{z}_2 \\ \dot{z}_3 \\ \dot{z}_4 \end{bmatrix} = \begin{bmatrix} 0 & 1 & 0 & 0 \\ 0 & 0 & 1 & 0 \\ 0 & 0 & 0 & 1 \\ 0 & 0 & 0 & 0 \end{bmatrix} \begin{bmatrix} z_1 \\ z_2 \\ z_3 \\ z_4 \end{bmatrix} + \begin{bmatrix} 0 \\ 0 \\ 0 \\ 1 \end{bmatrix} v \tag{8.28}$$

$$\dot{z} = Az + bv$$

where A, b are defined obviously, and the system of (8.28) is linear and controllable.

The z states can be viewed as the (fictitious) internal states of the integrator chain shown in figure 8.4, and these states are obtained via the state transformations below,

$$z = \begin{bmatrix} L_f{}^0 h(x) \\ L_f{}^1 h(x) \\ L_f{}^2 h(x) \\ L_f{}^3 h(x) \end{bmatrix} = \begin{bmatrix} y \\ \dot{y} \\ \ddot{y} \\ \dddot{y} \end{bmatrix} = \begin{bmatrix} x_3 \\ x_4 \\ \frac{1}{J_L}\left(\gamma x_D - \psi x_D^3\right) \\ \frac{1}{J_L}\left(x_2 - x_4\right)\left(\gamma - 3\psi x_D^2\right) \end{bmatrix} \tag{8.29}$$

8.3.4 Simulation of feedback linearization for position control

The derivation of (8.21) leads to the following nonlinear control law for feedback linearization of the magnetic coupling's load-side position,

$$\begin{aligned} T_{EM} = \frac{J_M J_L}{\left(\gamma - 3\psi x_D^2\right)}\Bigg(& \frac{6\psi x_2 x_D}{J_L}\left(x_2 - x_4\right) + \frac{1}{J_M J_L}\left(\gamma x_D - \psi x_D^3\right)\left(\gamma - 3\psi x_D^2\right) - \frac{6\psi x_4 x_D}{J_L}\left(x_2 - x_4\right) \\ & + \frac{1}{J_L^2}\left(\gamma x_D - \psi x_D^3\right)\left(\gamma - 3\psi x_D^2\right) + v \Bigg) \end{aligned} \tag{8.30}$$

$$x_D = \left(x_1 - x_3\right)$$

resulting in the linear relationship $\ddddot{x}_3 = \ddddot{\theta}_L = v$, a fourth order integrator chain. The outer control loop is now selected to satisfy the ITAE optimized linear results of Chapters 3 and 4. Specifically, the entire closed loop dynamics satisfies the optimal fourth order ITAE polynomial (3.25). With the state transformation (diffeomorphism) of (8.29) the closed-loop poles of (8.28) can be relocated to (3.25) via state feedback (with gains determined using Ackerman's formula), the completed model used in the simulation study being shown in figure 8.5. Figure 8.6 shows both motor-side and load-side position step responses, with the load-side position being characterized by a fourth order ITAE response.

For comparison purposes, figure 8.7 shows the load-side position and the output of a pure integrator chain under identical state feedback; the theoretical ITAE 4th order step is also included. Clearly, all three outputs are identical, validating the feedback linearization with state feedback approach.

The principal aim of the feedback linearization and state feedback scheme thus far derived is to ensure that the optimized step response remains linear throughout the entire input range, but prior to pole-slipping. Consequently, a plot of the step response error surface over the input range of interest is shown in figure 8.8.

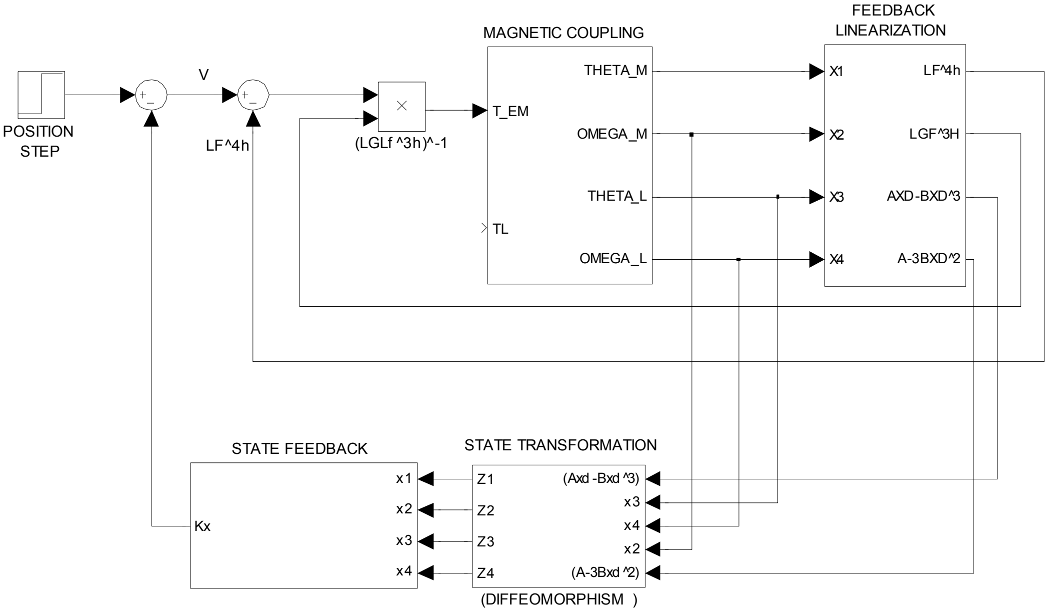

Figure 8.5 Simulation model position control feedback linearization with state feedback

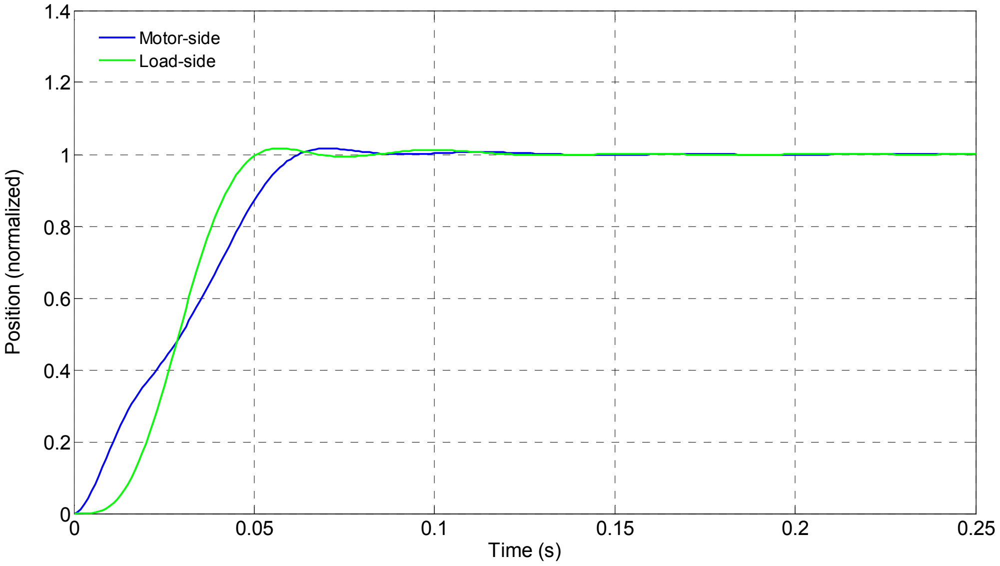

Figure 8.6 Simulated position step response with feedback linearization and state feedback

As indicated in figure 8.8, perfect linearity is obtained for the entire input operating range with the load-side percentage step error between the linearized model and feedback linearized nonlinear model with state feedback being identically zero throughout the entire range space. (Note: the initial small non-zero region indicated in the mesh plot is a function of numerical considerations in the simulation and the mesh plot within MATLAB – the response is entirely *linear* within the computational bounds of the software.)

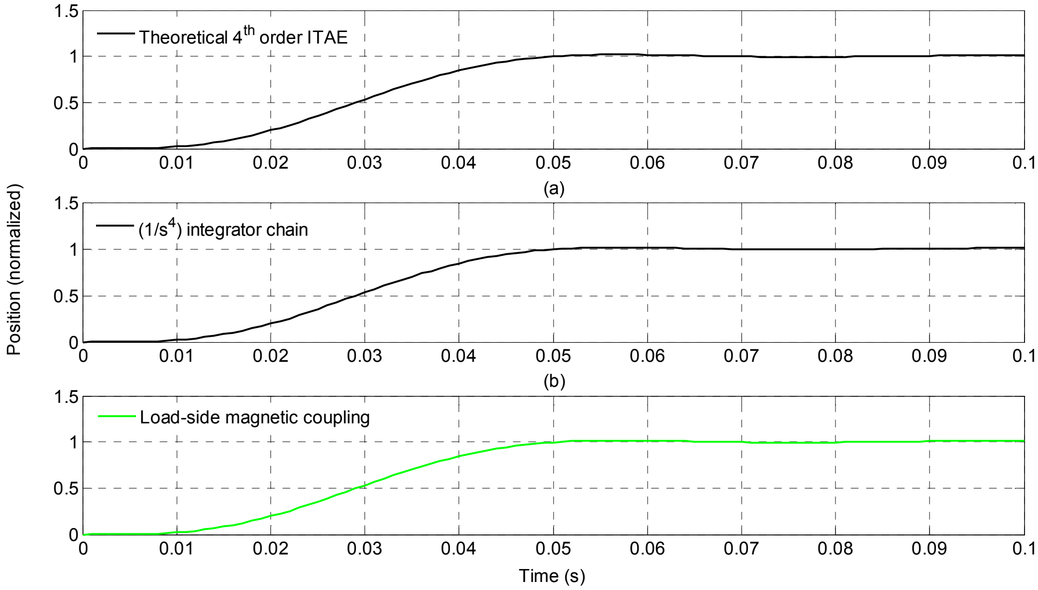

(c)

Figure 8.7 (a) ITAE step response (b) integrator chain with state feedback
(c) magnetic coupling with feedback linearization and state feedback

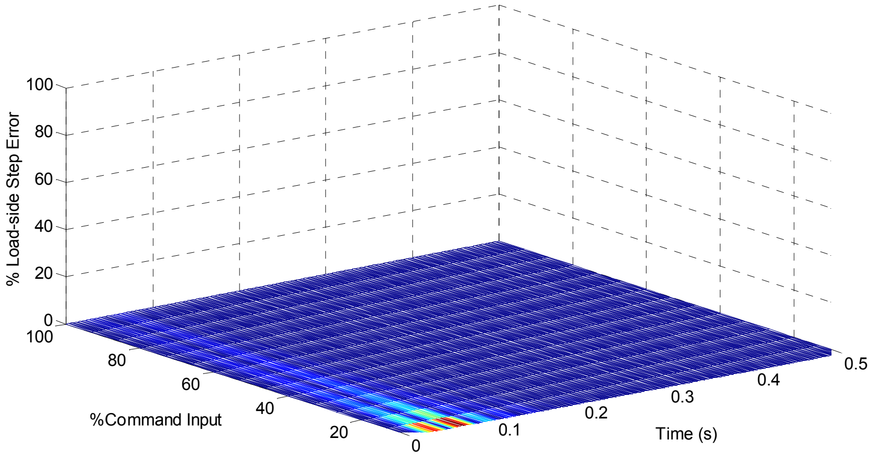

Figure 8.8 Position step response error surface with feedback linearization and state feedback

8.3.5 Simulation of feedback linearization for speed control

In Definition 8.3 the relative degree of a nonlinear system is defined to be the value of r for which,

$$\begin{aligned} L_g L_f^{r-1} h(x) &\neq 0 \\ L_g L_f^{r-2} h(x) &= 0 \end{aligned} \tag{8.31}$$

For linear systems the relative degree is defined as the number of excess poles over zeros and as there is a derivative relationship between position and speed, it is clear that the change in relative degree must be one. Consequently, adopting the analysis of Section 8.3.3 the relative degree for the speed control case is $r = 3$, with the output derivative being,

$$\dddot{y} = L_f{}^3 h(x) + L_g L_f{}^2 h(x) T_{EM} \tag{8.32}$$

and,

$$L_f{}^3 h(x) = \frac{-6\psi x_2 x_D}{J_L}\left(x_2 - x_4\right) - \frac{1}{J_M J_L}\left(\gamma x_D - \psi x_D^3\right)\left(\gamma - 3\psi x_D^2\right) + \frac{6\psi x_4 x_D}{J_L}\left(x_2 - x_4\right)$$
$$-\frac{1}{J_L^2}\left(\gamma x_D - \psi x_D^3\right)\left(\gamma - 3\psi x_D^2\right)$$

$$L_g L_f{}^2 h(x) = \frac{1}{J_M J_L}\left(\gamma - 3\psi x_D^2\right) \tag{8.33}$$

and the resulting linearization is a third order integrator chain $\dddot{x}_4 = \dddot{\omega}_L = v$. The necessary state transformation is given by,

$$z = \begin{bmatrix} x_4 \\ J_L^{-1}\left(\gamma x_D - \psi x_D^3\right) \\ J_L^{-1}\left(x_2 - x_4\right)\left(\gamma x - 3\psi x_D^2\right) \end{bmatrix} \tag{8.34}$$

where the symmetry with (8.29) is clear. However, as noted in (8.26) an additional ($n - r$) states are required in the diffeomorphism as the relative degree is less than the nonlinear system order. In general, the dynamics left over are $\dot{\eta} = \left(z, \eta\right)$ and are termed the zero or driven dynamics. Most importantly, these dynamics must satisfy,

$$\frac{\partial \eta}{\partial x} g(x) = 0 \Rightarrow \begin{bmatrix} \dfrac{\partial \eta_1}{\partial x_1} & \cdots\cdots & \dfrac{\partial \eta_1}{\partial x_n} \\ & \cdots & \\ \dfrac{\partial \eta_{n-r}}{\partial x_1} & \cdots\cdot & \dfrac{\partial \eta_{n-r}}{\partial x_n} \end{bmatrix} \begin{bmatrix} g_1(x) \\ .. \\ g_n(x) \end{bmatrix} = 0 \tag{8.35}$$

from which a set of simultaneous partial differential equations must be solved (a nontrivial proposition). This necessitates the use of the Frobenius Theorem, the detailed proof of which can be found in [85]. In any event, the 'left over' dynamics not 'reached' by the feedback linearization must be asymptotically stable for the overall linearization to be effective. For the nonlinear system under present discussion, the 'left over' dynamics are described by,

$$\frac{\partial \eta}{\partial x_2}\frac{1}{J_M} = 0 \tag{8.36}$$

and consequently, the zero dynamics are stable.

Feedback linearization for the speed control case produces a third order linear integrator chain, and the outer loop state feedback is optimized to the 3rd order ITAE polynomial,

$$s^3 + 1.75\omega_n s^2 + 2.15\omega_n^2 s + \omega_n^3 \tag{8.37}$$

As with the position control case, state feedback provides the ITAE optimized step response for a third order system. Simulation results for the feedback linearized system are provided in figures 8.9 and 8.10, where, as previously, comparison is made with identical state feedback for an integrator chain, and the theoretical ITAE optimized step response.

8.4 Robustness to uncertain parameters

The nonlinear SISO model of (8.4) is predicated on the basis of accurate model parameters. In general most physical systems are subject to uncertainties including, model errors, disturbances, parameter variations and unmodelled dynamics [86]. The outcome of the input-output feedback linearization in the previous section is a linear model that does not directly depend upon model parameters. It is instructive therefore, to examine the effects of uncertainties in the inertia parameters J_M and J_L on the overall closed-loop performance under feedback linearization.

The simulation studies of figures 8.11 & 8.12 indicate step error surfaces as J_M (J_L) is varied ±50% from nominal with J_L (J_M) held constant at nominal value. As indicated in both cases, the overall closed-loop response demonstrates good robustness to wide parameter variations, a valuable benefit of feedback linearization.

8.5 Experimental results for feedback linearization

The feedback linearizing control law of (8.32) and state transformation of (8.33) are implemented on the dSPACE hardware development platform for experimental testing of the speed controller. Figure 8.13 shows the speed transient responses for 25%, 50%, 75% and 100% of speed command request, up to the maximum permissible input before instability occurs. Reiterating section 8.1, experimental results are obtained under no load torque conditions, i.e. $T_L = 0$, and the system is considered as purely single input single output.

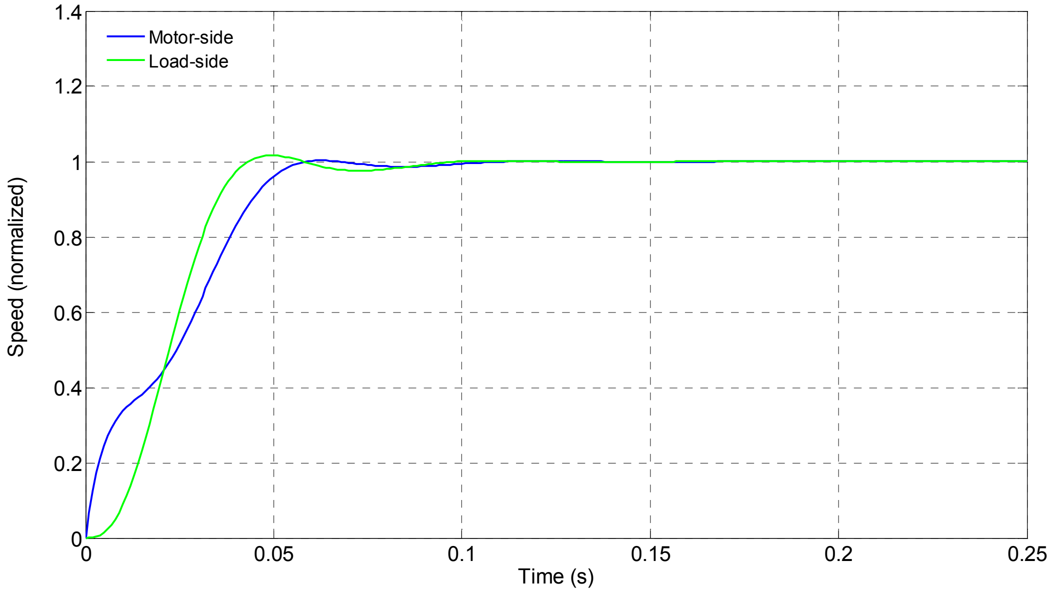

Figure 8.9 Simulated speed step response with feedback linearization and state feedback

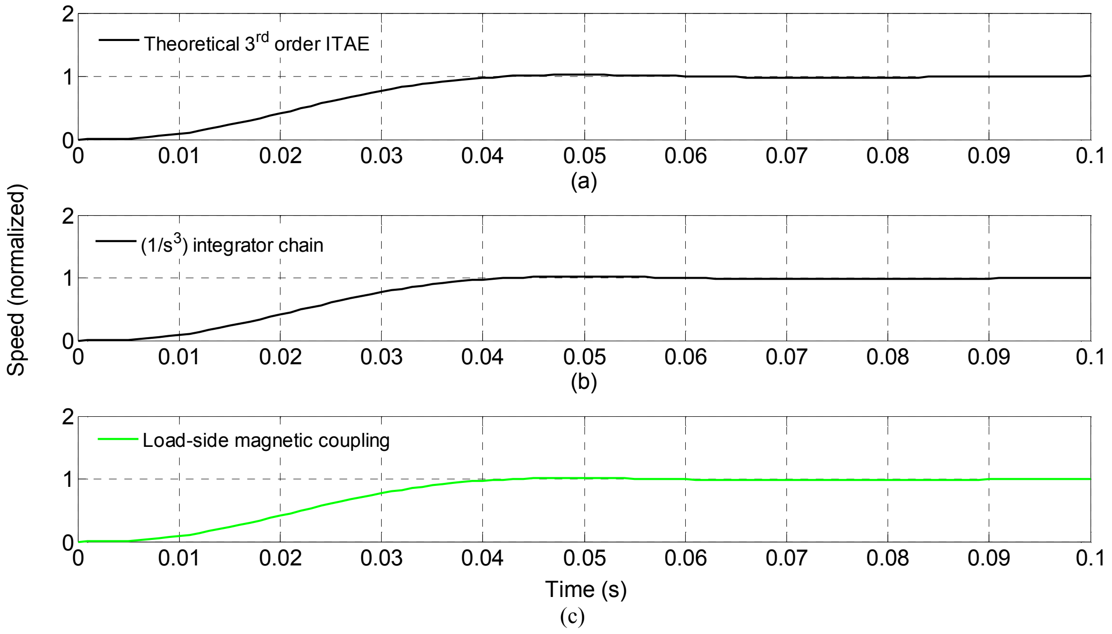

Figure 8.10 (a) ITAE speed step response (b) integrator chain with state feedback
(c) magnetic coupling with feedback linearization and state feedback

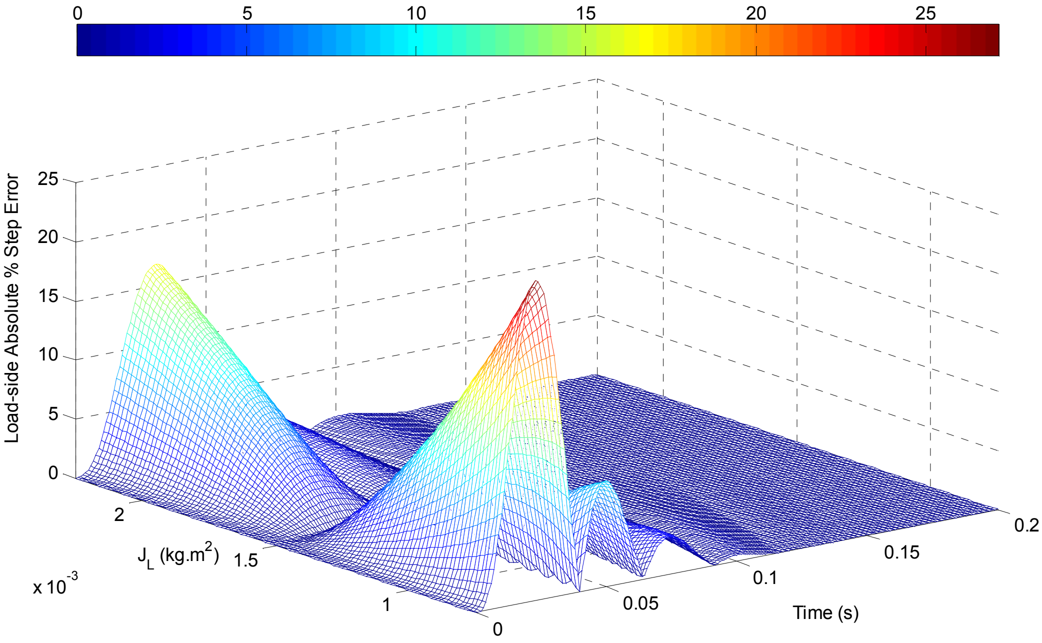

Figure 8.11 Percentage step error from nominal for ± 50% variation in J_L load inertia

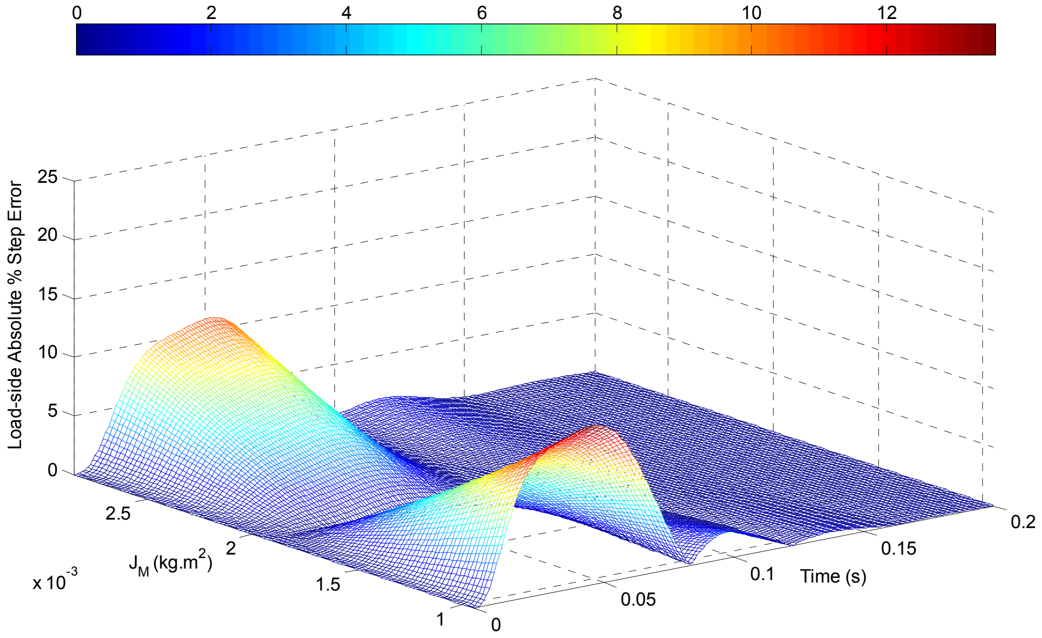

Figure 8.12 Percentage step error from nominal for ± 50% variation in J_M load inertia

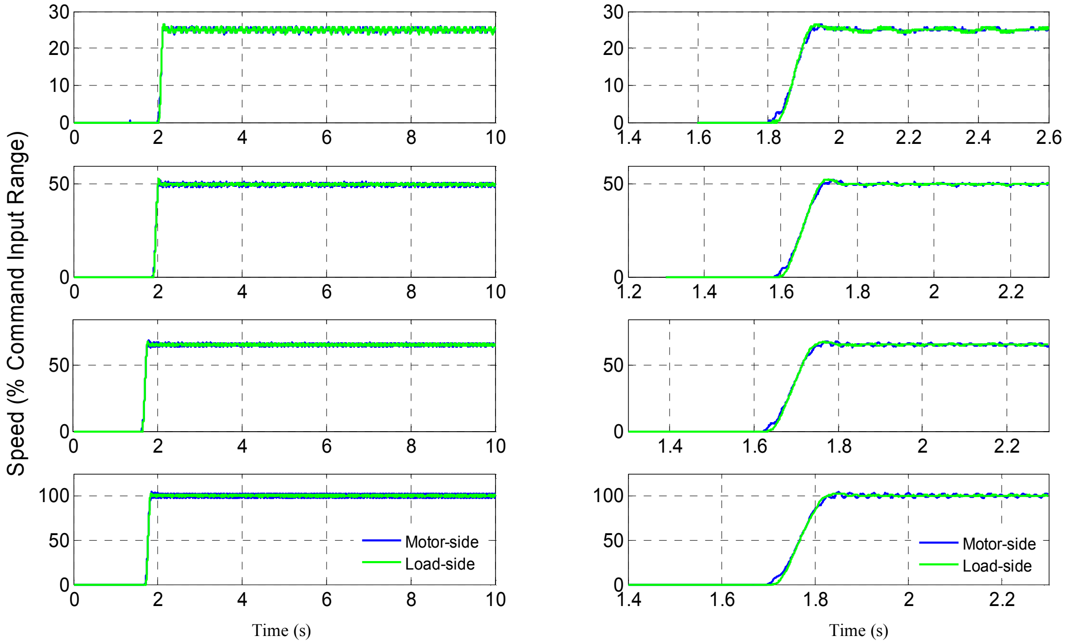

Figure 8.13 Experimentally measured transient responses 25%, 50%, 75% & 100% Speed command

It is clear from figure 8.13 that the transient response is essentially identical for all levels of speed command input. It should be noted, however, that despite noisy signals within the experimental system, outstanding results are achieved. Furthermore, the required diffeomorphism (state transformation) and linearizing control law have a significant degree of complexity, particularly when compared with the classical PI case. Ultimately, this complexity manifests itself in severe instability as the speed command input crosses a pre-determined threshold. To illustrate the effect of instability, a speed command input of 110% is applied to the feedback linearizing controller, and as shown in figure 8.14, the transient response becomes unstable very readily.

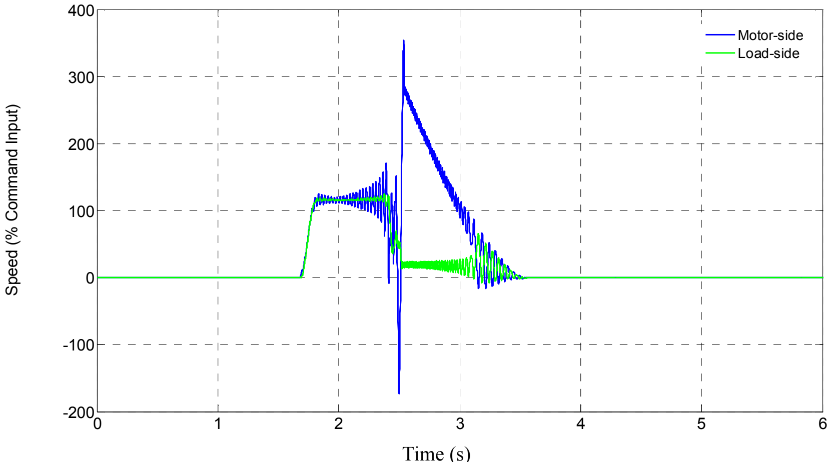

Figure 8.14 Experimentally measured transient response 110% speed command

The feedback linearizing position controller, (8.21) and (8.29), is implemented in dSPACE with experimental results obtained for transient position commands of θ_{ref} = 1, 2, 3 & 4 rad respectively. Figure 8.15 shows the results obtained, illustrating good agreement with the theoretically expected outputs. However, it is observed that increases in the position command produce noticeable ripple on the motor-side transient position. Although this deviates somewhat from the simulated results, the overall set-point position tracking is excellent, particularly when considering the complexity of the control law, which contains over 50 products of states, and the relatively low resolution and noisy nature of the state measurements.

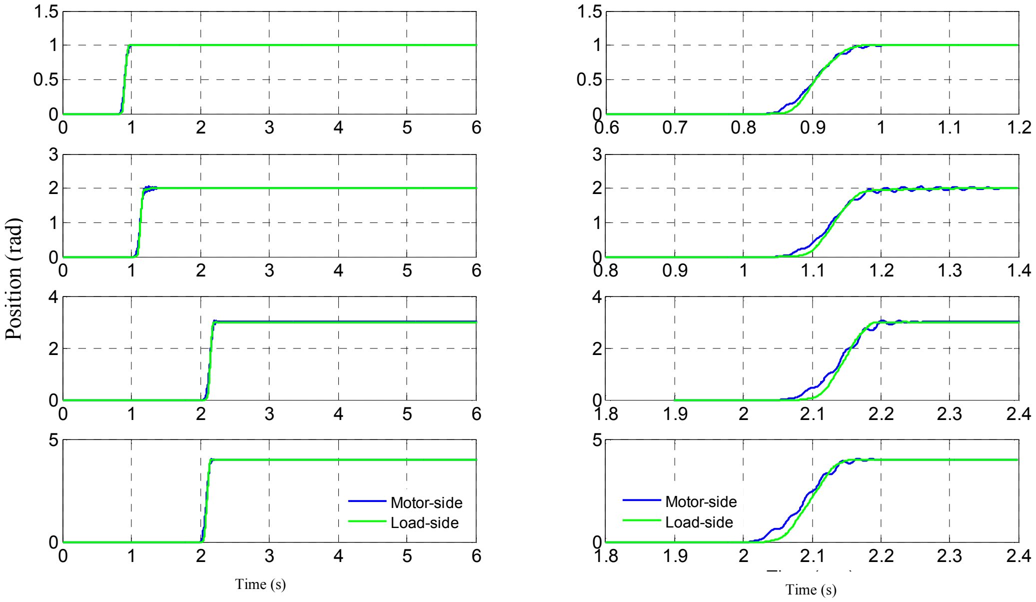

Figure 8.15 Experimentally measured transient position responses for θ_{ref} = 1, 2, 3 & 4 rad

8.6 Summary

To compensate for the nonlinearity of the magnetic coupling's torque transfer characteristic, an approach based on the use of feedback linearization has been developed. The derived control laws and state transformations (diffeomorphisms) result in exact linear behaviour, for both speed and position control, between input and output. Feedback linearization forms an inner control loop that renders the nonlinear input-output dynamics into a linear chain of integrators. With a feedback linearized 'inner loop', an 'outer loop' is designed to produce the overall required dynamics. As previously discussed, the ITAE optimized step response polynomials are used to provide an optimized linear step response over the entire input operating range, prior to the point at which pole-slipping occurs in the magnetic coupling.

Chapter 9

Conclusions and Future Work

9.1 Introduction

The principal objective of this research has been to investigate the design of drive train control systems when incorporating magnetic gear boxes in otherwise mechanically stiff drive trains. A magnetic coupling was designed and integrated into an experimental drive train test rig, consisting of two PMSM electrical machines under the control of a hardware-in-the-loop development platform (dSPACE). The remainder of this chapter provides a summary of the work undertaken, contributions made, and suggestions for further research.

9.2 Summary of research contributions

At the outset of this work no detectable published research could be found that considers the effects of magnetic gear boxes on the control issues of otherwise mechanically stiff drive trains. To analyze control-specific issues, a mathematical model of the specially designed and constructed experimental 1:1 magnetic coupling was derived. This consisted of a classical two-inertia servo-drive model, with a nonlinear torsional spring representing the torque transfer that takes place via the magnetic field. The analytical model derived demonstrated that the experimental magnetic coupling used during this research presented a drive train component of extreme flexibility, that is, very high compliance. Furthermore, the relationship between mechanical displacement angle between the two sides of the magnetic coupling and transmitted torque is fundamentally nonlinear.

Extending the work of O'Sullivan & Bingham [41], analytically determined controller parameter settings, for an ITAE optimized step response, have been derived for speed control and position control servo systems. For both speed and position regulation scenarios, outstanding theoretical (simulated) and experimental (dSPACE) results were achieved, accommodating the high compliance and nonlinear torque transfer characteristic inherent in the magnetic coupling. Furthermore, the concept of 'pole-slipping' was introduced to account for the phenomenon of over-torque slipping that occurs when a magnetic gear is subjected to torque overload. A mechanism to detect pole-slip was developed from an analysis of the feedback/error signal. The identification of a pole-slip 'signature' provided a means for the automatic detection and remediation of a slipping drive train. The developed and presented controller demonstrated the possibility of detection and restart of a slipping drive train in around 100 milliseconds.

A significant advantage of magnetic gears is the ability to act as a non-destructive torque fuse when overloaded. However, a scenario was created that showed how the magnetic coupling could be forced into a pole-slipping regime despite the fact that the steady-state load torque was substantially below the rated pull-out torque of the device. In fact, an experimental scenario involving a simple speed change showed how the magnetic coupling could begin to slip at only 30% of rated torque. This can be viewed as a very significant drawback to the use of magnetic gears. To tackle this problem, a model predictive control (MPC) approach was adopted and an effective control strategy to prevent under-torque pole-slip was demonstrated. The development of an MPC strategy was based on recent advances in the real-time implementation of MPC using explicit model predictive control and multi-parametric programming.

Of particular significance throughout this research was the assumption that only motor-side measurements were available for control purposes, but the states (position/speed) to be controlled were those on the load-side of the magnetic coupling. For a servo position control system with load-side reference, the effect of the magnetic coupling's inherent compliance was demonstrated to induce severe positional errors, potentially up to 30°. To counteract the position errors due to torsion, a dual-observer based approach was developed to correct the load-side set-point position tracking error. In addition, a correction for nonlinearity error was devised due to the linear observer structure utilized. Outstanding theoretical and experimental results have been demonstrated.

The majority of the research undertaken adopted the viewpoint that a linearized approximation of the magnetic coupling's torque transfer characteristic was appropriate, and that excellent theoretical and experimental results could be achieved using linear analysis and linear control techniques. For completeness, a nonlinear approach was also considered. In particular, the nonlinear control law and nonlinear state transformation for perfect input-output feedback linearization of the nonlinear state space model of the magnetic coupling have been derived. Implementation of the derived control law and state transformation produced spectacular results, showing perfect linearization over the entire operating range of the magnetic coupling, and outstanding robustness to parameter variations.

The main purpose of this thesis has been to demonstrate the specific control issues that arise when incorporating magnetic gears in a mechanical drive train. To overcome some of the impediments presented by magnetic gears, classical and advanced control methodologies have been investigated and various theoretical results have been derived for speed control and position control servo systems. Simulation and experimental studies have provided compelling results for the efficacy of these approaches, thereby significantly enhancing the possibility that magnetic gearing can provide a practicable and controllable alternative to mechanical gear boxes, with all the attendant advantages they can bring.

9.2.1 Publications resulting from this thesis

The culmination of the work contained within this thesis, is believed to be the first ever research publications to consider the control issues that arise when incorporating a magnetic gear into a mechanical drive train that would otherwise have been considered mechanically stiff. These publications are,

R. G. Montague, C. Bingham, and K. Atallah, “Servo control of magnetic gears,” *Mechatronics, IEEE/ASME Transactions on*, vol. 17, pp. 269-278, April 2012.

R. G. Montague, C. Bingham, and K. Atallah, “Dual observer-based position-servo control of a magnetic gear”, *Electrical Power Applications, IET*, vol. 5, pp. 708-714, 2011.

R. G. Montague, C. Bingham, and K. Atallah, “Pole-slip prevention in a magnetic gear using explicit model predictive control”, *Mechatronics, IEEE Transactions on*, accepted in revision, Nov 2011;

R. G. Montague, C. Bingham, and K. Atallah, "Magnetic gear overload detection and remedial strategies for servo-drive systems," *Power Electronics Electrical Drives Automation and Motion (SPEEDAM), 2010 International Symposium on*, 2010, pp. 523-528;

R. G. Montague, C. Bingham, and K. Atallah, "Magnetic gear dynamics for servo control," *MELECON - 2010 15th IEEE Mediterranean Electrotechnical Conference*, 2010, pp. 1192-1197;

R. G. Montague, C. Bingham, and K. Atallah, "Characterisation and modelling of magnetic couplings and gears for servo control systems," *Power Electronics, Machines and Drives (PEMD 2010), 5th IET International Conference on*, 2010, pp. 1-6.

9.3 Future work

This research has created a fundamental baseline for the analysis, design, and synthesis of control strategies for drive trains that incorporate magnetic gear boxes and magnetic couplings.

Recommendations to extend the work contained herein are now suggested.

1. The mathematical model of the magnetic coupling has throughout been predicated on zero friction and zero damping. In terms of inherent damping, the experimental coupling used was designed such that the damping term was negligible. An enhancement would be to incorporate a re-designed coupling with some non-negligible damping to further investigate its effects on the control methodologies demonstrated thus far. Furthermore, friction terms for the experimental test rig have been essentially disregarded and not considered in theoretical

analyses or simulations. It may be of interest to consider damping and friction terms in more detail.

2. Torque overload induced pole-slip was investigated for a speed control servo system, with automatic detection and a reconfigurable controller demonstrated to be effective for recovery of a slipping drive train. However, further consideration needs to be given to transient load-side torque overload in a position controlled system. A torque transient that causes the load-side position to slip requires some mechanism from the motor-side to be able to correct the absolute position error. An example might be, say, an antenna positioning system subjected to a wind gust. In this scenario, absolute position registration between motor- and load-side of the magnetic gear could be lost. With only motor-side measurements available this presents a nontrivial problem.

3. Primarily, only the question of *regulation* (stationary set-points) has been considered for both speed and position control of the magnetic coupling. This should be extended to include dynamic output tracking.

4. With a linear model of the magnetic coupling, the use of a linear state observer seems reasonable, provided normal operating conditions do not force the magnetic coupling into the most nonlinear part of the torque transfer characteristic. Although a nonlinear correction term was derived for this condition, it may be prudent to investigate nonlinear state reconstruction.

5. Nonlinear approaches based on feedback linearization produced spectacular theoretical results for linearization of the step response over the entire operating range of the magnetic coupling. However, this is predicated on perfect state feedback of all states, and as reiterated above, the assumption is that only motor-side states are directly measured. Consequently, any implementation of the nonlinear control law and nonlinear state transformation would require the missing load-side states to be reconstructed from a nonlinear state observer. Furthermore, the derived nonlinear control law is of substantial computational complexity and implementation on real-time hardware requires further development and investigation.

6. For both linear and nonlinear models it has been assumed that precise model parameters, such as inertia and friction coefficients, have been available. To generalize the approaches considered so far, the developed models should be extended to include uncertain parameters with an analysis of pertinent robustness issues.

7. Finally, the derived nonlinear control law is based on a Single Input Single Output (SISO) model. This model does not consider the load-side (or any other) torque disturbance. It is therefore necessary to extend the SISO nonlinear model to include the load-side torque disturbance. It may then be possible to derive a disturbance decoupling diffeomorphism and nonlinear state feedback control law that completely decouples (unlikely), or partially decouples, the output from the load torque disturbance. The nontrivial nature of this proposition is considerable.

References

[1] R. L. Norton, *Design of Machinery,* (3rd ed.), McGraw-Hill Professional, 2004.

[2] K. Atallah, S. Calverley, R. Clark, J. Rens, and D. Howe, "A new PM machine topology for low-speed, high-torque drives," in *Electrical Machines, 2008. ICEM 2008. 18th International Conference on*, 2008, pp. 1-4.

[3] D. E. Hesmondhalgh and D. Tipping, "A multielement magnetic gear," *Electric Power Applications, IEE Proceedings B,* vol. 127, pp. 129-138, 1980.

[4] P. O. Rasmussen, T. O. Andersen, F. T. Joergensen, and O. Nielsen, "Development of a high performance magnetic gear," in *Industry Applications Conference, 2003 38th IAS Annual Meeting. Conference Record of the*, 2003, pp. 1696-1702 vol.3.

[5] http://www.magnomatics.com, accessed May, 2011.

[6] R. G. Montague, C.M. Bingham, K. Atallah, "Servo control of magnetic gears," *Mechatronics, IEEE/ASME Transactions on*, vol. 17, pp. 269 -278, April 2012.

[7] R. G. Montague, C. M. Bingham, and K. Atallah, "Magnetic gear overload detection and remedial strategies for servo-drive systems," in *Power Electronics Electrical Drives Automation and Motion (SPEEDAM), 2010 International Symposium on*, 2010, pp. 523-528.

[8] R. G. Montague, C. M. Bingham, and K. Atallah, "Magnetic gear dynamics for servo control," in *MELECON 2010 - 2010 15th IEEE Mediterranean Electrotechnical Conference*, 2010, pp. 1192-1197.

[9] R. G. Montague, C. M. Bingham, and K. Atallah, "Characterisation and modelling of magnetic couplings and gears for servo control systems," in *Power Electronics, Machines and Drives (PEMD 2010), 5th IET International Conference on*, 2010, pp. 1-6.

[10] H. T. Faus, "Magnet gearing," U.S. Patent 2 243 555, May 27, 1941.

[11] J. Pyrhonen, T. Jokinen, V. Hrabovcova, *Design of Rotating Electrical Machines*. Wiley, 2008.

[12] J.F. Gieras and M. Wang (Editors), *Permanent Magnet Motor Technology: Design and Applications, Second Edition*. CRC Press, 2002.

[13] K. Atallah and D. Howe, "A novel high-performance magnetic gear," *Magnetics, IEEE Transactions on,* vol. 37, pp. 2844-2846, 2001.

[14] P. O. Rasmussen, T. O. Andersen, F. T. Jorgensen, and O. Nielsen, "Development of a high-performance magnetic gear," *Industry Applications, IEEE Transactions on,* vol. 41, pp. 764-770, 2005.

[15] K. Atallah, S. D. Calverley, and D. Howe, "Design, analysis and realisation of a high-performance magnetic gear," *Electric Power Applications, IEE Proceedings -,* vol. 151, pp. 135-143, 2004.

[16] F. T. Jorgensen, T. O. Andersen, and P. O. Rasmussen, "The cycloid permanent magnetic gear," *Industry Applications, IEEE Transactions on,* vol. 44, pp. 1659-1665, 2008.

[17] J. Rens, K. Atallah, S. D. Calverley, and D. Howe, "A novel magnetic harmonic gear," *Industry Applications, IEEE Transactions on,* vol. 46, pp. 206-212, 2010.

[18] C. Huang, M. Tsai, and B. Lin, "Development of new magnetic planetary gears for transmission systems," in *Magnetics Conference, 2006. INTERMAG 2006. IEEE International*, 2006, pp. 225-225.

[19] K. Atallah, J. Rens, S. Mezani, and D. Howe, "A novel *pseudo* direct-drive brushless permanent magnet machine," *Magnetics, IEEE Transactions on,* vol. 44, pp. 4349-4352, 2008.

[20] K. T. Chau, C. C. Chan, and L. Chunhua, "Overview of permanent-magnet brushless drives for electric and hybrid electric vehicles," *Industrial Electronics, IEEE Transactions on,* vol. 55, pp. 2246-2257, 2008.

[21] S. L. Ho, N. Shuangxia, and W. N. Fu, "Transient analysis of a magnetic gear integrated brushless permanent magnet machine using circuit-field-motion coupled time-stepping finite element method," *Magnetics, IEEE Transactions on,* vol. 46, pp. 2074-2077, 2010.

[22] K. T. Chau, Z. Dong, J. Z. Jiang, L. Chunhua, and Z. Yuejin, "Design of a magnetic-geared outer-rotor permanent-magnet brushless motor for electric vehicles," *Magnetics, IEEE Transactions on,* vol. 43, pp. 2504-2506, 2007.

[23] N. W. Frank and H. A. Toliyat, "Gearing ratios of a magnetic gear for wind turbines," in *Electric Machines and Drives Conference, 2009. IEMDC '09. IEEE International*, 2009, pp. 1224-1230.

[24] L. N. Jian, K. T. Chau, Z. Dong, J. Z. Jiang, and W. Zheng, "A magnetic-geared outer-rotor permanent-magnet brushless machine for wind power generation," in *Industry Applications Conference, 2007. 42nd IAS Annual Meeting. Conference Record of the 2007 IEEE*, 2007, pp. 573-580.

[25] L. Shah, A. Cruden, and B. W. Williams, "A magnetic gear box for application with a contra-rotating tidal turbine," in *Power Electronics and Drive Systems, 2007 PEDS '07. 7th International Conference on*, 2007, pp. 989-993.

[26] A. Balestrino, A. Landi, and L. Sani, "Disturbance rejection in a rolling mill," in *Control Applications, 1998. Proceedings of the 1998 IEEE International Conference on*, 1998, pp. 207-211 vol.1.

[27] S. Bolognani, A. Venturato, and M. Zigliotto, "Theoretical and experimental comparison of speed controllers for elastic two-mass-systems," in *Power Electronics Specialists Conference, 2000. PESC 00. 2000 IEEE 31st Annual*, 2000, pp. 1087-1092 vol.3.

[28] J. Deur and N. Peric, "Analysis of speed control system for electrical drives with elastic transmission," in *Industrial Electronics, 1999. ISIE '99. Proceedings of the IEEE International Symposium on*, 1999, pp. 624-630 vol.2.

[29] Y. Li and M. Tomizuka, "Robust motion control of mechanical systems with compliance," in *Decision and Control, 1996. Proceedings of the 35th IEEE*, 1996, pp. 2462-2467 vol.3.

[30] K. Yuki, T. Murakami, and K. Ohnishi, "Vibration control of 2 mass resonant system by resonance ratio control," in *Industrial Electronics, Control, and Instrumentation, 1993. Proceedings of the IECON '93., International Conference on*, 1993, pp. 2009-2014 vol.3.

[31] M. Tondos, G. Sieklucki, and A. Pracownik, "Proportional-integral LQ control of a two-mass system," in *Power Electronics and Motion Control Conference, 2006. EPE-PEMC 2006. 12th International*, 2006, pp. 1115-1120.

[32] H. A. Youssef, S. M. El Saied, and O. A. Sebakhy, "Recommended control configurations for DC drives with flexible shafts," in *Control Applications, 1994, Proceedings of the Third IEEE Conference on*, 1994, pp. 691-696 vol.1.

[33] R. Dhaudi, “Robust speed control of rolling mill drive systems using the loop transfer recovery design methodology,” in *Proceedings of IEEE IECON ’91*, 1991, pp. 687-692.

[34] M. S. Tondos, "Minimizing electromechanical oscillations in the drives with resilient couplings by means of state and disturbance observers," in *Power Electronics and Applications, 1993., Fifth European Conference on*, 1993, pp. 360-365 vol.5.

[35] S. J. Dodds and K. Szabat, "Forced dynamic control of electric drives with vibration modes in the mechanical load," in *Power Electronics and Motion Control Conference, 2006. EPE-PEMC 2006. 12th International*, 2006, pp. 1245-1250.

[36] G. Zhang and J. Furusho, "Speed control of two-inertia system by PI/PID control,"

in *Power Electronics and Drive Systems, 1999. PEDS '99. Proceedings of the IEEE 1999 International Conference on*, 1999, pp. 567-572 vol.1.

[37] S. N. Vukosavic and M. R. Stojic, "Suppression of torsional oscillations in a high-performance speed servo drive," *Industrial Electronics, IEEE Transactions on,* vol. 45, pp. 108-117, 1998.

[38] S. J. Dodds, K. Szabat, T. Orlowska-Kowalska, and R. Perryman, "Observer based robust control of an electric drive with a flexible coupling," in *Power Electronics Electrical Drives Automation and Motion (SPEEDAM), 2010 International Symposium on*, 2010, pp. 926-931.

[39] S. Doo-Jin, H. Uk-Youl, and L. Je-Hie, "An observer design for 2 inertia servo control system," in *Industrial Electronics, 1999. ISIE '99. Proceedings of the IEEE International Symposium on*, 1999, pp. 883-887 vol.2.

[40] T. M. O'Sullivan, C. M. Bingham, and N. Schofield, "Observer-based tuning of two-inertia servo-drive systems with integrated SAW torque transducers," *Industrial Electronics, IEEE Transactions on,* vol. 54, pp. 1080-1091, 2007.

[41] T. M. O'Sullivan, C. M. Bingham, and N. Schofield, "High-performance control of dual-inertia servo-drive systems using low-cost integrated SAW torque transducers," *Industrial Electronics, IEEE Transactions on,* vol. 53, pp. 1226-1237, 2006.

[42] M. Kaminski and T. Orlowska-Kowalska, "FPGA realization of the neural speed estimator for the drive system with elastic coupling," in *Industrial Electronics, 2009. IECON '09. 35th Annual Conference of IEEE*, 2009, pp. 2831-2836.

[43] T. Orlowska-Kowalska, M. Kaminski, and K. Szabat, "Mechanical state variable estimation of drive system with elastic coupling using optimized feed-forward neural networks," *Bulletin of the Polish Academy of Sciences,* vol. 56, pp. 239-246, 2008.

[44] T. Orlowska-Kowalska and K. Szabat, "Neural-network application for mechanical variables estimation of a two-mass drive system," *Industrial Electronics, IEEE Transactions on,* vol. 54, pp. 1352-1364, 2007.

[45] A. S. Kulkarni and M. A. El-Sharkawi, "Intelligent precision position control of elastic drive systems," *Energy Conversion, IEEE Transactions on,* vol. 16, pp. 26-31, 2001.

[46] T. Orlowska-Kowalska and K. Szabat, "Optimization of fuzzy-logic speed controller for DC drive system with elastic joints," *Industry Applications, IEEE Transactions on,* vol. 40, pp. 1138-1144, 2004.

[47] T. Orlowska-Kowalska and K. Szabat, "Adaptive fuzzy sliding mode control of a drive system with flexible joint," in *IEEE Industrial Electronics, IECON 2006 - 32nd Annual Conference on*, 2006, pp. 994-999.

[48] T. Orlowska-Kowalska and K. Szabat, "Damping of torsional vibrations in two-mass system using adaptive sliding neuro-fuzzy approach," *Industrial Informatics, IEEE Transactions on,* vol. 4, pp. 47-57, 2008.

[49] K. Szabat and T. Orlowska-Kowalska, "Adaptive control of two-mass system using nonlinear extended Kalman filter," in *IEEE Industrial Electronics, IECON 2006 - 32nd Annual Conference on*, 2006, pp. 1539-1544.

[50] K. Szabat and T. Orlowska-Kowalska, "Application of the extended Kalman filter in advanced control structure of a drive system with elastic joint," in *Industrial Technology, 2008. ICIT 2008. IEEE International Conference on*, 2008, pp. 1-6.

[51] J. Vittek, P. Makys, M. Stulrajter, S. J. Dodds, and R. Perryman, "Comparison of sliding mode and forced dynamics control of electric drive with a flexible coupling employing PMSM," in *Industrial Technology, 2008. ICIT 2008. IEEE International Conference on*, 2008, pp. 1-6.

[52] S. J. Dodds, R. Perryman, et al., “Forced dynamics control of electric drives employing pmsm with a flexible coupling,” *Power Engineering Conference*, *2007. AUPEC 2007. Australasian Universities*.

[53] K. Ogata, *Modern Control Engineering*. Upper Saddle River, New Jersey: Prentice-Hall, 2002.

[54] J. J. D'Azzo and C. H. Houpis, *Feedback Control Systems Analysis & Synthesis*. Tokyo, Japan: McGraw-Hill, 1982.

[55] R. C. Dorf and R. H. Bishop, *Modern Control Systems*. New Jersey: Prentice-Hall, 2010.

[56] M. W. Spong, “Modeling and control of elastic joint robots”, *ASME Journal of Dynamics Systems, Measurements and Control*, vol. 109. pp. 310-319.

[57] S. N. Vukosavič, *Digital Control of Electrical Drives*. New York, USA: Springer, 2007.

[58] M. Close, D. K. Frederick, and J. C. Newell, *Modeling and Analysis of Dynamic Systems*. Hoboken, NJ, USA: John Wiley & Sons, 2002.

[59] J. R. Leigh, *Essentials of Nonlinear Control Theory*. London, UK: Peter Peregrinus, 1983.

[60] H. J. Marques, *Nonlinear Control Systems*. Hoboken, New Jersey: Wiley, 2003.

[61] J. E. Slotine and W. Li, *Applied Nonlinear Control*. New York, USA: Prentice-Hall, 1990.

[62] S. Joe Qin and T. A. Badgwell, "A survey of industrial model predictive control technology," *Control Engineering Practice, Pergamon,* vol. 11, pp. 733-764, 2003.

[63] C. R. Culter and B. L. Ramaker, “Dyanmic matrix contol – a computer control algorithm”, *Presented at the meeting of the American Institute of Chemical Engineers, Houston, Texas*, 1979.

[64] C. E. Garcia and A. M. Morshedi, “Quadratic programming solution to Dynamic Matrix Control (QDMC),” Chemical Engineering Communication, 46:73-87, 1986.

[65] D. W. Clarke, C. Mohtadi, and P. S. Tuffs, “Generalized predictive control. Part I: The basic algorithm. Part II: Extensions and interpretations,” *Automatica*, vol. 23, pp. 137-160, 1987.

[66] N. L. Ricker, “Model-predictive control: state of the art,” *Proc. Fourth International Conference on Chemical Process Control, Padre Island, Texas,* 271-296, 1991.

[67] J. B. Rawlings and K. R. Muske, “The stability of constrained receding horizon control,” *Automatic Control, IEEE Transactions on,* vol. 38, pp. 1512-1516, 1993.

[68] J. M. Maciejowski, *Predictive Control with Constraints*. Guildford, United Kingdom: Pearson Education, 2002.

[69] L. Wang, *Model Predictive Control System Design and Implementation Using MATLAB*. London, UK: Springer, 2009.

[70] S. Boyd and L. Vandenberghe. *Convex Optimization*. Cambridge University Press, 2004.

[71] E. F. Camacho and C. Bordons, *Model Predictive Control*. Springer, New York, 2004.

[72] L. G. Bleris and M. V. Kothare, "Real-time implementation of model predictive control," in *American Control Conference, 2005. Proceedings of the 2005*, 2005, pp. 4166-4171 vol. 6.

[73] M. Kvasnica, *Real-Time Model Predictive Control via Multi-Parametric Programming*. VDM Verlag, 2009.

[74] A. Bemporad, M. Morari, V. Dua, and E. N. Pistikopoulos, "The explicit linear quadratic regulator for constrained systems," *Automatica,* vol. 38, pp. 3-20, 2002.

[75] M. Cychowski, K. Szabat, and T. Orlowska-Kowalska, "Constrained model predictive control of the drive system with mechanical elasticity," *Industrial Electronics, IEEE Transactions on,* vol. 56, pp. 1963-1973, 2009.

[76] D. G. Luenberger, "Determining the state of a linear system with observers of low dynamic order," Ph.D. dissertation, Dept. Elec. Eng. Stanford University, California, 1963.

[77] D. G. Luenberger, "Observing the state of a linear system," *Military Electronics, IEEE Transactions on,* vol. 8, pp. 74-80, 1964.

[78] B. Gopinath, "On the control of a linear multiple input-output systems," *Bell Systems Technical Journal,* vol. 50, pp. 1063-1081, 1971.

[79] M. Vidyasagar. *Nonlinear Systems Analysis, 2nd Edition*. Prentice-Hall, 1993.

[80] A. Isidori, *Nonlinear Control Systems*. Springer-Verlag, New York, 1999.

[81] H.Nijmeijer and A. van der Schaft, *Nonlinear Dynamical Control Systems*. Springer Verlag, Berlin, 1990.

[82] C. I. Byrnes and A. Isidori, “Global feedback stabilization of nonlinear systems,” *24th IEEE CDC*, *Conference on Decision and Control*, pp 1031- 1037, 1985.

[83] L. Hunt, S. Renjeng, and G. Meyer, "Global transformations of nonlinear systems," *Automatic Control, IEEE Transactions on*, vol. 28, pp. 24-31, 1983.

[84] A. N. Zhirabok and A. M. Zhukov, "On the transformations of nonlinear systems," in *American Control Conference*, 1994, pp. 3570-3571 vol.3.

[85] M. Spivak, *A Comprehensive Introduction to Differential Geometry 2e*. Publish or Perish, Inc., Houston, TX, 1991.

[86] J. Zhong-Ping, I. Mareels, and D. Hill, "Robust control of uncertain nonlinear systems via measurement feedback," *Automatic Control, IEEE Transactions on*, vol. 44, pp. 807-812, 1999.

Appendix
Magnetic coupling construction

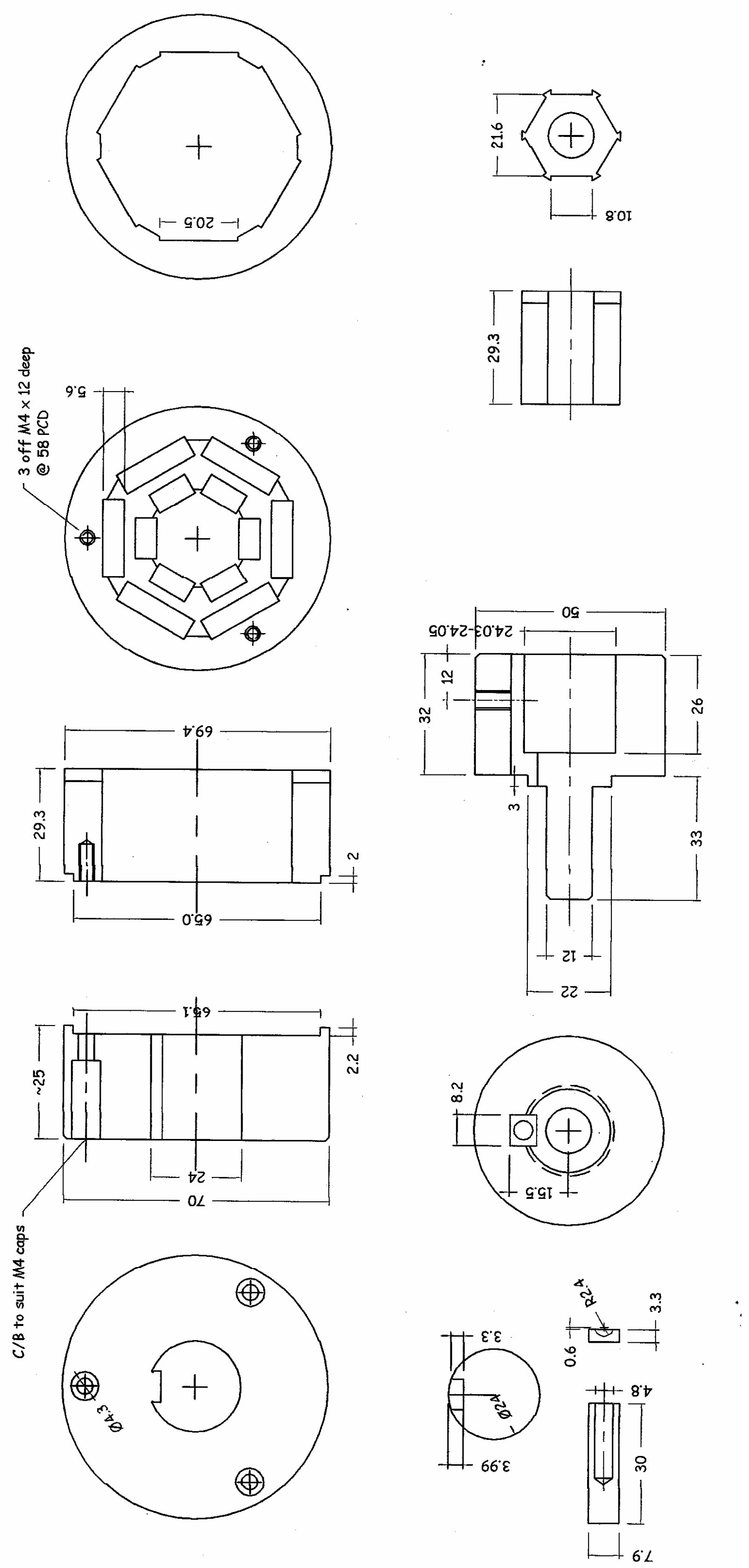
20.5
3 off M4 × 12 deep @ 58 PCD
5.6
21.6
10.8
29.3
69.4
29.3
2
65.0
50
24.03-24.05
32
12
26
3
33
12
22
65.1
~25
2.2
24
70
C/B to suit M4 caps
Ø4.3
8.2
15.5
3.3
Ø2.4
3.99
R2.4
0.6
3.3
4.8
30
7.9

ARNOLD
MAGNETIC TECHNOLOGIES

N38SH

Sintered Neodymium-Iron-Boron Magnets

These are also referred to as "Neo" or NdFeB magnets. They offer a combination of high magnetic output at moderate cost. Please contact Arnold for additional grade information and recommendations for protective coating. Assemblies using these magnets can also be provided.

	Characteristic	Units	min.	nominal	max.
Magnetic Properties	**Br**, Residual Induction	Gauss	12,200	12,350	12,500
		mT	1220	1235	1250
	H_{cB}, Coercivity	Oersteds	11,400	11,700	12,000
		kA/m	907	931	955
	H_{cJ}, Intrinsic Coercivity	Oersteds	20,000		
		kA/m	1,592		
	BHmax, Maximum Energy Product	MGOe	36	38	39
		kJ/m^3	287	299	310

	Characteristic	Units	C //	C ⊥
Thermal Properties	Reversible Temperature Coefficients [1]			
	of Induction, α(Br)	%/°C	-0.12	
	of Coercivity, α(Hcj)	%/°C	-0.55	
	Coefficient of Thermal Expansion [2]	ΔL/L per °Cx10^{-6}	7.5	-0.1
	Thermal Conductivity	kcal/mhr°C	5.3	5.8
	Specific Heat [3]	cal/g°C	0.11	
	Curie Temperature, Tc	°C	340	
Other Properties	Flexural Strength	psi	41,300	
		MPa	285	
	Density	g/cm^3	7.5	
	Hardness, Vickers	Hv	620	
	Electrical Resistivity, ρ	μΩ • cm	180	

Notes:
(1) Coefficients measured between 20 and 150 °C
(2) Between 20 and 200 °C
(3) Between 20 and 140 °C

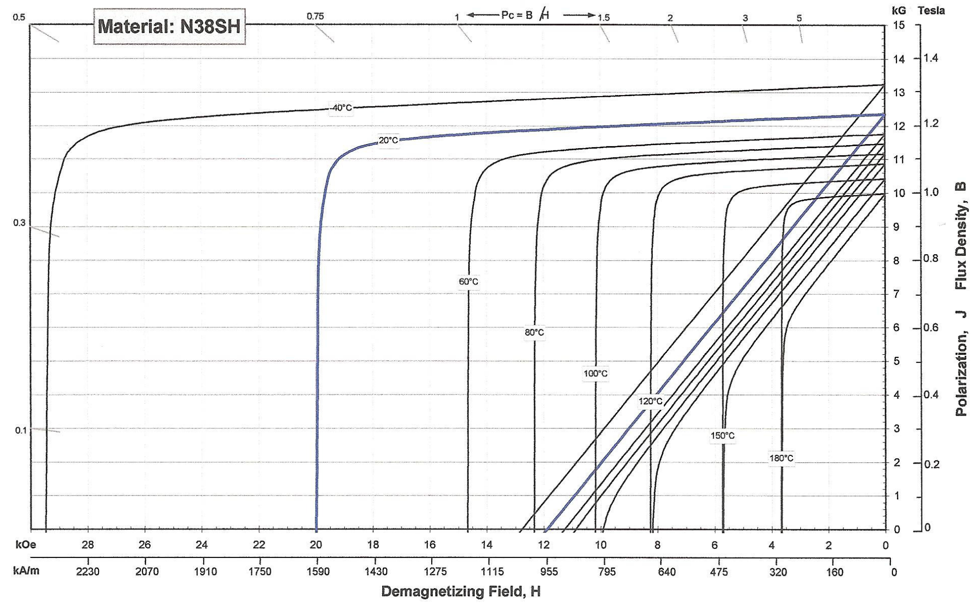

1 kA/m = 12.566 Oe 1 kOe = 79.577 kA/m

Notes The material data and demagnetization curves shown above represent typical properties that may vary due to product shape and size.
Demagnetization curves show nominal Br and minimum Hci.
Magnets can be supplied thermally stabilized or magnetically calibrated to customer specifications.
Additional grades are available. Please contact the factory for information.

770 Linden Avenue, Rochester, NY 14625
Ph: (+1) 585-385-9010
E-mail: info@arnoldmagnetics.com
www.arnoldmagnetics.com

Rev. 100924b